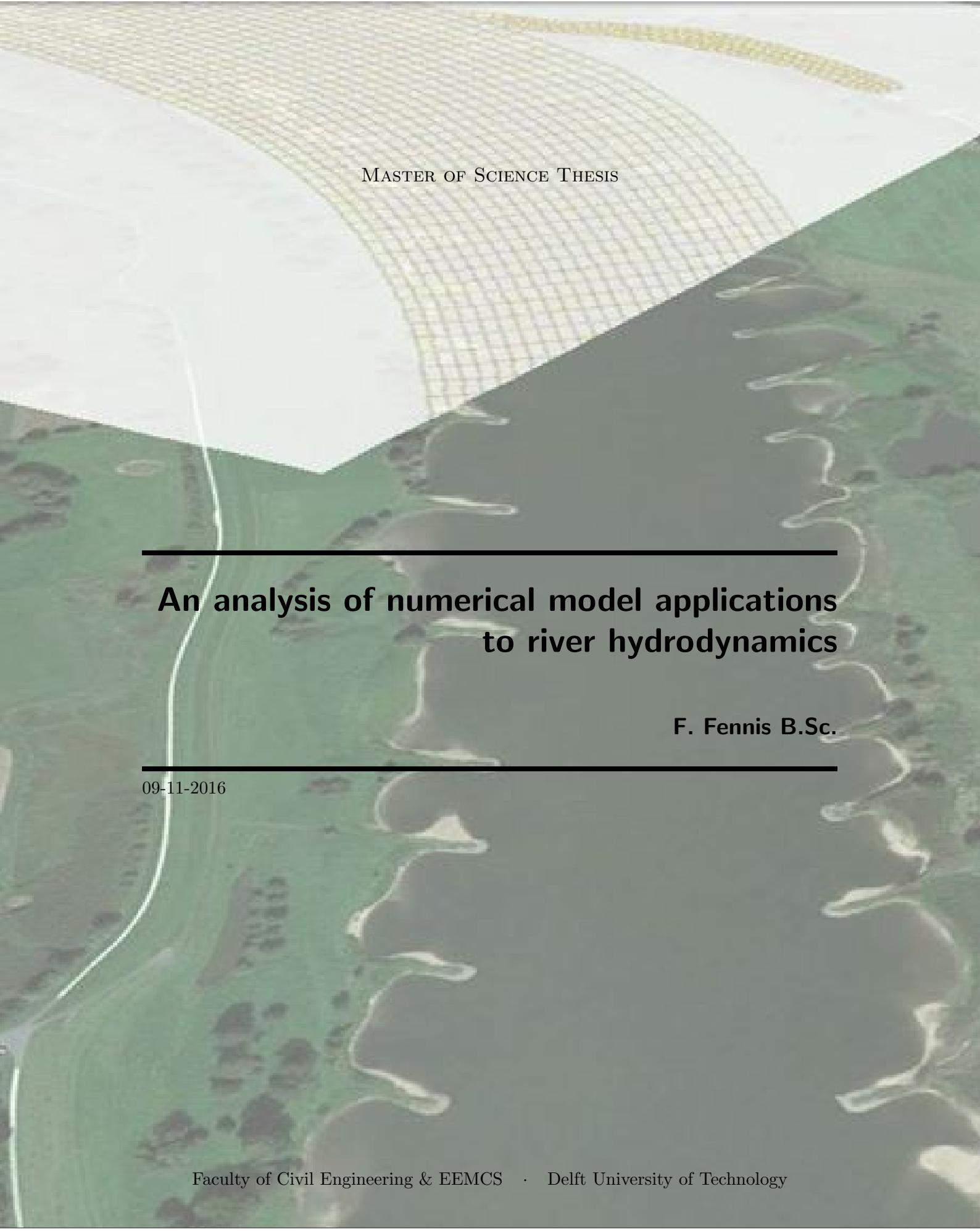

Master of Science Thesis

An analysis of numerical model applications to river hydrodynamics

F. Fennis B.Sc.

09-11-2016

Faculty of Civil Engineering & EEMCS · Delft University of Technology

An analysis of numerical model applications to river hydrodynamics

Master of Science Thesis

For obtaining the degree of Master of Science in Civil Engineering and Applied Mathematics at Delft University of Technology

F. Fennis B.Sc.

09-11-2016

Faculty of Civil Engineering & EEMCS · Delft University of Technology

Delft University Of Technology
Department Of
Applied Mathematics & Hydraulic Engineering

The undersigned hereby certify that they have read and recommend to the Faculty of Civil Engineering & EEMCS for acceptance a thesis entitled **"An analysis of numerical model applications to river hydrodynamics"** by **F. Fennis B.Sc.** in partial fulfillment of the requirements for the degree of **Master of Science**.

Dated: 09-11-2016

Head of department Applied Mathematics: _____
prof.dr.ir. C. Vuik

Head of department Hydraulic Engineering: _____
prof.dr.ir. W.S.J. Uijttewaal

Supervisor: _____
dr.ir. J.L. Korving

Reader: _____
dr. H.M. Schuttelaars

Preface

Hereby I would like to present my master thesis "An analysis of numerical model applications to river hydrodynamics". Starting with my graduation project I knew I wanted to combine the masters Civil Engineering and Applied Mathematics into one project. Witteveen+Bos and Deltares have given me the possibility to combine both studies. Furthermore, Deltares has provided me with all the software I needed. The report consists of multiple parts that starts with a general description. Hereafter part I, that is more focused on the mathematical subjects, is presented. Part II consists of the research of the physical aspects. After these parts, a synthesis is given of both parts in order to conclude this research with a simulation of a river reach.

While reading the report, the reader should keep in mind that this research has lasted for a year. During this year both D-Flow Flexible Mesh and 3Di have been upgraded, hence, some versions used in this research are already outdated. Furthermore, the version of 3Di given by Deltares, 3Di - subgrid Version 0.1.1.1942, is not the most recent version. Each chapter in this report will have the used version stated in the introduction.

Delft, The Netherlands — F. Fennis B.Sc.
09-11-2016

Summary

It is of importance to know how the water is behaving in rivers due to the dangers, such as flooding and eroding of land, it can bring with it. Present day we are still reshaping rivers, building structures in rivers or adjusting them, which results in changes in the hydrodynamics and morphology. In order to obtain more insight in the consequences of these adjustments, it is convenient to use a numerical model to simulate the river hydrodynamics. For the last decades numerical models have been developed that are able to simulate hydrodynamics. Currently, new software packages are proposed that are more efficient in predicting this. Two of these new software packages are D-Flow Flexible Mesh (FM) and 3Di, where 3Di only has the possibility to simulate in 2DH and FM in both 2DH and 3D. Whereas the first is especially designed to model the hydrodynamics of rivers and other flows, the latter is mostly used for the simulation of flooding of land.

Both packages 3Di and D-Flow Flexible Mesh are quite new and came available around the same time. Hence, more insight is needed in all the possible choices that influence the river hydrodynamics. The considered choices in this research are related to grid resolution, boundary conditions, and turbulence models. Based on these choices there are considerations that need to be taken into account, which are the representation of physical processes, accuracy and computational effort. Each of the choices and considerations will have consequences for the depth averaged simulations. This research investigates the importance of these considerations and consequences for the suitability of results for specific problems. The consequences that are of interest in this investigation are convergence, robustness, and validity. In order to obtain more insight in the choices, considerations, and consequences, the differences and similarities of both packages need to be investigated. One of the main differences between these packages is the mesh generation. 3Di generates a Cartesian grid based on the sub-grid method with quadtrees, while FM works with an unstructured grid that combines the curvilinear grid and triangles. Though it also has the possibility to use a Cartesian grid. The other main difference is the including diffusivity term in the shallow water equations of Flexible Mesh. In order to obtain a better understanding of both packages, some test cases are set up before simulating a river reach. In total four test cases have been investigated in order to obtain a better understanding of these packages. The results will be used to set up hypotheses for a more complex case, the

river Elbe. In Table 1 an overview of the test cases is given together with the subject of each study. Though packages such as Flexible Mesh and 3Di are usually not designed to

Test case	Physical aspects	Mathematics
1. Flume experiment	3-dimensional processes Grid comparison	Grid comparison
2. U-bend		Local refinement in one part of the bend
3. Flow over weir	Energy losses	Local refinement as a function of x
4. Turbulent jet	Horizontal viscosity	

Table 1: Overview test cases

simulate lab experiments, Flexible Mesh is quite suitable to simulate these, which is seen in test case 1 "Flume experiment". With the applicable conditions no-/partial slip, the velocity profile of Flexible Mesh agrees better with the velocity profile of the lab experiments, compared to a free slip condition. In this experiment the vertical walls influence the velocity profile significantly, as seen in the test case "Flume experiment". In rivers this condition is not used, and the results of Flexible Mesh and 3Di are quite similar without this condition.

Generating a grid for the river is done in different ways for both packages. Test cases have shown that a curvilinear grid for Flexible Mesh obtains results that are more precise than using a Cartesian grid. In 3Di only a Cartersian grid is possible, but results show that this grid does not limit the results in the same way as in Flexible Mesh. With a high pixel subgrid resolution the results of 3Di appear to converge faster than Flexible Mesh in some cases.

In the test cases it is seen that besides the numerical viscosity, the turbulent viscosity has an effect on the mixing layer, since it both determines the amount of viscosity. Results for 3Di are not as expected in the test case "Turbulent jet", as there is no eddy present, but the flow simply follows the walls.

Overall, it appears that the rate of convergence in 3Di is higher than in Flexible Mesh for the cases that are taken into account. In most cases a high resolution for the pixel subgrid model is used, which has the advantage of a more precise volume balance while it is possible to maintain a coarser grid. Though the rate of convergence is high, the converge itself is more unexpected, which is seen in each case where a variable grid is used. By changing the resolution the results are unexpected, making it more difficult to interpret them.

Furthermore, in both 3Di and Flexible Mesh the placement of transition from a coarse to fine grid is important. When this transition is placed where gradients are present, local errors are introduced. A larger gradient will results in higher errors. It is recommended to place this transition a distance further upstream from the area of interest in order to avoid these errors in that area. When multiple areas of interest are closely together it might be better to refine the complete area in order to avoid unnecessary errors.

Besides some differences, both packages behave quite similar in either physical processes that influence the hydrodynamics or when applying a local refinement. Based on the cases that are solved in this thesis a better overview of the choices in each package is obtained for specific problems, together with the most important considerations and consequences.

Acknowledgements

I wish to thank the following persons:

First of all, my supervisors Hans Korving (Witteveen+Bos), Kees Vuik (TU Delft) and Arthur van Dam (Deltares). Each of them helped me with my report, models, programs, and progress. Learning to work with new programs can be quite difficult, especially when they are just released and not many people have knowledge of them. Luckily, Arthur helped developing Flexible Mesh and knows how to work with 3Di. Thus, whenever there were some troubles with the models, I could come to him and we would look at it together. Kees Vuik, chair of the committee Applied Mathematics and my daily supervisor of TU Delft, and Hans Korving, my supervisor from Witteveen+Bos, helped me a lot with their advice, asking questions about my report/research which kept me sharp, and showed trust in my research. Furthermore, Henk Schuttelaar, thanks for joining my committee with enthusiasm. The first time we talked about it, you instantly had some good ideas that helped me with my research. Frank Platzek, thanks for your contact with the BAW and arranging the data of the river.

I also like to thank Wim Uijttewaal, the chair of the committee of Civil Engineering. Whenever I lost track, or needed some advise, he would help me by remembering me that I should always be critical. He also kept telling me about the path one needs to follow for research, which could be difficult for me.

Furthermore, the companies Witteveen+Bos, Deltares and BAW (Bundesanstalt für Wasserbau) have provided me with much help. Both Witteveen+Bos and Deltares offered me a working space with the needed material. Deltares has also provided me with all the software that was needed for my study. BAW has given me the available data of the river Elbe, which gave me the opportunity to investigate a proper river reach. Hereby I wish to thank you for the possibilities you have given me for my research.

Last but not least, I wish to thank my parents, family, friends, colleagues at Deltares and Witteveen+Bos, and everyone who has been there for me during this time. It has not always been easy, but they were there the whole time to support me. Whether I needed some feed back, a compliment, or just someone who could listen to me at that moment,

I could rely on them. Thank you very much! Without you it would have been a lonely road to take.

Delft, The Netherlands F. Fennis B.Sc.
09-11-2016

Contents

Preface v

Summary vi

Acknowledgements ix

List of Figures xx

List of Tables xxi

Nomenclature xxiii

1 Introduction 1
- 1.1 Problem description . . . 1
- 1.2 Objective . . . 2
- 1.3 Outline . . . 3

2 Literature study 5
- 2.1 Description of the mathematical model . . . 5
- 2.2 Grid generation . . . 6
  - 2.2.1 Grid generation in Flexible Mesh . . . 6
  - 2.2.2 Grid generation in 3Di . . . 6

I Applied Mathematics: The role of grid refinement in the modeling of river hydrodynamics 9

3 Grid comparison of Flexible Mesh and 3Di 11
- 3.1 Flow geometry . . . 11
- 3.2 Different types of grid generation . . . 13
- 3.3 Conclusion . . . 16

4 U-bend with sinusoidal bed **19**
4.1 Flow Geometry . . . 19
4.2 Test case in Flexible Mesh . . . 20
4.2.1 Convergence . . . 21
4.2.2 Wiggles . . . 22
4.2.3 Local refinement . . . 24
4.3 Test case in 3Di . . . 27
4.3.1 Convergence . . . 28
4.3.2 Wiggles . . . 29
4.3.3 Local refinement . . . 31
4.4 Comparing results from both programs . . . 33
4.4.1 Comparison without refinements . . . 33
4.4.2 Streamwise differences in local refinements . . . 35
4.4.3 Transverse differences . . . 36
4.4.4 Wall clock time . . . 36
4.5 Conclusion . . . 38

5 Flow over weir **41**
5.1 Flow geometry . . . 41
5.2 Convergence study . . . 43
5.2.1 Influence of grid placement . . . 50
5.3 Refinement . . . 52
5.3.1 Refinement with triangles in Flexible Mesh . . . 54
5.3.2 Refinement in flow direction in Flexible Mesh . . . 58
5.3.3 Refinement in 3Di . . . 61
5.4 Conclusion and discussion . . . 64

II Hydraulic Engineering: The physical properties of 3Di and Flexible Mesh **67**

6 Mildly curved flow experiment in flume **69**
6.1 Flow geometry . . . 69
6.2 Different types of grid generation . . . 70
6.3 Physical parameters . . . 74
6.3.1 Slip at vertical, closed boundaries . . . 75
6.3.2 Constant turbulent viscosity . . . 76
6.3.3 Secondary flow . . . 76
6.3.4 Elder and Smagorinsky . . . 77
6.4 Results . . . 77
6.4.1 3Di . . . 78
6.4.2 Simulation 1: default . . . 80
6.4.3 Simulation 2: Smagorinsky and no-slip . . . 80

6.4.4 Simulation 3 & 4: Smagorinsky/constant viscosity and partial slip 82
6.4.5 Simulation 5: Elder, Smagorinsky and partial slip 84
6.4.6 Simulation 6: Secondary flow, constant viscosity and partial slip . 84
6.4.7 Analysis for combined results 86
6.5 Conclusion and discussion 90

7 Flow over weir **93**
7.1 Flow geometry 93
7.2 Convergence study 95
7.2.1 Influence of grid placement 102
7.3 Varying model input 103
7.3.1 Friction 106
7.3.2 Friction + bottom slope 108
7.3.3 Including turbulent viscosity 109
7.4 Conclusion 111

8 Turbulent jet **113**
8.1 Numerical viscosity 113
8.2 Simulation 1 114
8.2.1 Flow geometry 114
8.2.2 Results 114
8.3 Simulation 2 116
8.3.1 Results 118
8.4 Conclusion 123

9 Synthesis of both parts **125**

10 Applying the geometry of test case "U-bend" to the test case "Flume experiment" **129**
10.1 Addition of bottom profile and friction for the flume experiment 129
10.2 Conclusion 131

11 River Elbe **133**
11.1 Numerical model 133
11.1.1 Grid generation 134
11.1.2 Calibration 135
11.1.3 Cartesian grid Flexible Mesh 136
11.2 Convergence 138
11.3 Physical processes in groyne fields 140
11.3.1 Energy losses 140
11.3.2 Viscosity 141
11.4 Local refinement 144
11.5 Conclusion 148

12 Discussion **149**

13 Conclusions **151**
13.1 Further research . . . 153

A Description of the mathematical model **157**
A.1 Navier-Stokes equations . . . 157
A.1.1 Conservation of mass . . . 158
A.1.2 Conservation of momentum . . . 158
A.2 Grid generation . . . 159
A.2.1 Structured grid . . . 160
A.2.2 Unstructured grid . . . 161

B Shallow water equations **163**
B.1 Reynolds averaged Navier-Stokes equations . . . 163
B.2 Boundary conditions . . . 164
B.3 Scaling . . . 165
B.4 2D shallow-water equations . . . 166
B.5 Assumptions . . . 167
B.6 Difference in processes in 3Di and Flexible Mesh . . . 170

C D-Flow Flexible Mesh **173**
C.1 Grid generation . . . 173
C.1.1 Connectivity . . . 175
C.1.2 Bed geometry . . . 176
C.2 Discretisation of shallow water equations . . . 178
C.2.1 Spatial discretisation . . . 178
C.2.2 Time discretisation . . . 180

D 3Di **183**
D.1 Quadtrees . . . 183
D.2 Subgrid . . . 184
D.2.1 Integration of the grids . . . 186
D.3 Discretisation of the shallow water equations . . . 188
D.3.1 Spatial discretisation . . . 189
D.3.2 Time discretisation . . . 194

E Derivation of mass and momentum equations **197**
E.1 Conservation of mass . . . 197
E.2 Conservation of momentum . . . 198

F Derivation of the shallow water equations **201**
F.1 RANS equations . . . 201
F.2 Scaling . . . 202
F.3 Depth integration . . . 204

G River Elbe local refinement results **207**

List of Figures

2.1 Combination of curvilinear grid and triangles in FM (Kernkamp et al., 2011a) 7
2.2 Example of grid refinement in 3Di with quadtrees 7

3.1 Set up of flume experiment of (Blokland, 1985) 12
3.2 Multiple grid types used in Flexible Mesh and 3Di 12
3.3 Water levels for a Cartesian grid in FM and 3Di 13
3.4 Velocities for a Cartesian grid in FM and 3Di 14
3.5 Water levels for a Cartesian grid in FM and 3Di with variable pixel sizes . 15
3.6 Velocities for a Cartesian grid in FM and 3Di with variable pixel sizes . . 15
3.7 Water levels for both a Cartesian and curvilinear grid in FM 16
3.8 Velocities for both a Cartesian and curvilinear grid in FM 17

4.1 Dimensions of the U-bend presented in a top view and cross section . . . 20
4.2 Representation of grid and bed profile in FM with a curvilinear grid . . . 20
4.3 Water level inner (lower curves) and outer bend (upper curves) for multiple resolutions 21
4.4 Equilibrium discharge convergence in Flexible Mesh 22
4.5 Zoomed in water levels inner(left) and outer bend (right) of Figure 4.3 . . 22
4.6 Colored lines that indicate where the water levels are plotted 23
4.7 Water levels int he outer bend for multiple max. CFL numbers in Flexible Mesh 23
4.8 Placement of local refinement with transition in the middle of the bend for FM 25
4.9 Water levels for a local refinement 25
4.10 Zoomed in water elvels in the inner (left) and outer bend (right) of Figure 4.9 26
4.11 Comparison of water levels between local refinement 2-3 and uniform grid 26
4.12 Comparison of water levels between local refinement 3-4 and uniform grid 27

4.13 Example of both grid and pixel subgrid in 3Di for U-bend 28
4.14 Part of cross section represented by various pixels for arbitrary $y-$value . 28
4.15 Water level for various pixel sizes with grid size $\Delta x = 54$m 29
4.16 Water level for different grid sizes with a fixed pixel size $\Delta x_p = 1.7$m in 3Di 30
4.17 Discharge for various grid and pixel sizes 30
4.18 Water levels in multiple streamlines where in the outer bend wiggles are visible 31
4.19 Placement of local refinement with water elvels 31
4.20 Comparison of water levels between local refinement 2-3 32
4.21 Water levels of the cross sections in the middle of the bend 33
4.22 Comparison of water levels between local refinement 3-4 33
4.23 Equilibrium discharge convergence in Flexible Mesh and 3Di 34
4.24 Streamwise water levels for both FM and 3Di with a refinement factor 3 . 35
4.25 Differences in water level for both FM and 3Di 35
4.26 Overview of cross sections in U-bend 36
4.27 Transverse water levels with no refinement for both FM and 3Di 37
4.28 Transverse water levels with local refinement for both FM and 3Di 37
4.29 Computational time for all resolutions in 3Di and FM 38

5.1 Example of how a fixed weir is located to the cell faces 42
5.2 Groyne representation for various grid sizes in FM and 3Di 43
5.3 Convergence of discharges in FM and 3Di using a subgrid or supergrid model for various submergence degrees 44
5.4 Energy head in FM and 3Di using a subgrid and supergrid model for $S = 0.95$ 45
5.5 Convergence of discharges in FM and 3Di with an obstacle represented in bathymetry 46
5.6 Energy head in FM and 3Di with variable width in obstacle 47
5.7 Comparison of convergence of discharge for an obstacle with a smooth or sudden expansion 48
5.8 Comparison of energy head for an obstacle with a smooth or sudden expansion 48
5.9 Discharge for groyne with a combination of subgrid and bathymetry . . . 50
5.10 Discharge for groyne with a combination of subgrid and bathymetry in FM 51
5.11 Discharge for groyne with a combination of subgrid and bathymetry in 3Di 52
5.12 Comparison of convergence of discharge with different placements of obstacles in basin in 3Di 53
5.13 Comparison of convergence of discharge for multiple grid sizes and two placements 53
5.14 Groyne representation in FM with a grid size of $\Delta x = 12$m 53
5.15 Two types of refinement in Flexible Mesh 54
5.16 Errors in discharge that arise due to applying triangles in a grid 54
5.17 Velocity and waterlevel gradients in the $x-$direction with $\Delta x = 3$m (top) and $\Delta x = 1.5$m (bottom) 55
5.18 Errors in discharge that arise due to applying triangles in a grid 56

5.19 Three types of refinement using triangles 56
5.20 Comparing discharges for multiple types of refinement with a transition placement that varies in space 57
5.21 Velocities over the $x-$axis for multiple types of refinements with triangles 58
5.22 Equilibrium discharges with a rectangular refining for multiple resolutions and varying transition placements 59
5.23 Velocities over the $x-$axis for multiple types of refinements with rectangles 60
5.24 Equilibrium discharges with multiple refinements at various places 60
5.25 Equilibrium discharges with refinements at various places for several resolutions 61
5.26 Equilibrium discharges with multiple refinements 62
5.27 Velocities over the $x-$axis for multiple types of refinements in 3Di 63
5.28 Top view of several basins presenting eastward velocities 64

6.1 Set up of flume experiment of (Blokland, 1985) 70
6.2 Multiple grid types used in Flexible Mesh and 3Di 71
6.3 Water levels for a Cartesian grid in FM and 3Di 72
6.4 Velocities for a Cartesian grid in FM and 3Di 72
6.5 Water levels for a Cartesian grid in FM and 3Di with variable pixel sizes . 73
6.6 Velocities for a Cartesian grid in FM and 3Di with variable pixel sizes . . 74
6.7 Water levels for both a Cartesian and curvilinear grid in FM 75
6.8 Velocities for both a Cartesian and curvilinear grid in FM 75
6.9 Water levels with multiple grid resolutions in 3Di compared with measurements 79
6.10 Velocities with multiple grid resolutions in 3Di compared with measurements 79
6.11 Water levels for a curvilinear grid in FM and Cartesian grid in 3Di 80
6.12 Velocities for a curvilinear grid in FM and Cartesian grid in 3Di 81
6.13 Water levels in FM where a constant and variable viscosity is applied with free slip conditions 82
6.14 Velocities in FM where a constant and variable viscosity is applied with free slip conditions 82
6.15 Water levels in FM where a constant (2 values) viscosity is applied with partial slip conditions 83
6.16 Velocities in FM where a constant (2 values) viscosity is applied with partial slip conditions 83
6.17 Water levels in FM where a variable (2 values) viscosity is applied with partial slip conditions 84
6.18 Velocities in FM where a variable (2 values) viscosity is applied with partial slip conditions 85
6.19 Water levels in FM where a constant viscosity is applied in combination with secondary flow 85
6.20 Velocities in FM where a constant viscosity is applied in combination with secondary flow 86

6.21 Water level course in time for three observation stations with a low turbulent viscosity set . . . 87
6.22 Variable viscosity calculated with Smagorinsky for all slip conditions . . . 88
6.23 Comparing $\overline{u'v'}$ of numerical results and experimental data by calculating the (relative) 2-norm error . . . 88
6.24 Comparing $\overline{u'w'}$ of numerical results and experimental data by calculating the (relative) 2-norm error . . . 89

7.1 Example of how a fixed weir is located to the cell faces . . . 94
7.2 Groyne representation for various grid sizes in FM and 3Di . . . 95
7.3 Convergence of discharges in FM and 3Di using a subgrid or supergrid model for various submergence degrees . . . 96
7.4 Energy head in FM and 3Di using a subgrid and supergrid model for $S = 0.95$ 97
7.5 Convergence of discharges in FM and 3Di with an obstacle represented in bathymetry . . . 98
7.6 Energy head in FM and 3Di with variable width in obstacle . . . 99
7.7 Comparison of convergence of discharge for an obstacle with a smooth or sudden expansion . . . 100
7.8 Comparison of energy head for an obstacle with a smooth or sudden expansion 101
7.9 Discharge for groyne with a combination of subgrid and bathymetry . . . 102
7.10 Discharge for groyne with a combination of subgrid and bathymetry in FM 103
7.11 Discharge for groyne with a combination of subgrid and bathymetry in 3Di 104
7.12 Comparison of convergence of discharge with different placements of obstacles in basin in 3Di . . . 105
7.13 Comparison of convergence of discharge for multiple grid sizes and two placements . . . 105
7.14 Groyne representation in FM with a grid size of $\Delta x = 12$m . . . 105
7.15 Energy head in FM and 3Di for multiple inflow boundary conditions . . . 106
7.16 Invluence of friction on the results. Forces in cell presented . . . 107
7.17 Velocity and water level gradients with friction on for subgrid models and obstacles presented in bathymetry . . . 107
7.18 Energy head in FM and 3Di using a subgrid and supergrid model for $S = 0.95$ with friction . . . 108
7.19 Forces in cell with friction on and a slope . . . 109
7.20 Energy head in FM and 3Di using a subgrid and supergrid model for $S = 0.95$ with friction and a bottom slope . . . 109
7.21 Velocity and water level gradients with friction and a bottom slope for subgrid models and obstacles presented in bathymetry . . . 110
7.22 Top views of basins with a variable viscosity calculated with Smagorinsky 111
7.23 Energy head in FM and 3Di using a subgrid and supergrid model for $S = 0.95$ with friction, a turbulent viscosity model and a bottom slope . . . 111

8.1 Top view of flow geometry of test case “Turbulent jet” . . . 114
8.2 Difference between an instantaneous and time-averaged flow field . . . 116

8.3 Velocity profiles at cross sections $x = 3, 6, 9$m for 3Di and FM (both with and without a turbulence model) with an open boundary 117
8.4 Top view with eastward velocities in 3Di 118
8.5 Top view with eastward velocities in FM 119
8.6 Velocity profiles at cross sections $x = 3, 6, 9$m for 3Di and FM (both with and without a turbulence model) with a partly open boundary 121
8.7 Top view with northward velocities in FM 122

10.1 Water levels in 3Di for multiple resolutions with varying bed profile and friction coefficient 130

11.1 Bathymetry of river Elbe with indicated domain of interest 134
11.2 Steamwise velocities (upper figure) and water levels (bottom figure) in main channel with n = 0.022 135
11.3 Steamwise velocities (upper figure) and water levels (bottom figure) in main channel with n = 0.03 136
11.4 Steamwise velocities (upper figure) and water levels (bottom figure) for a curvilinear and Cartesian grid in FM 137
11.5 Bathymetry of the Elbe with the groyne fields, where measurements are taken, indicated 138
11.6 Velocity in indicated groyne fields of Figure 11.5 for a curvilinear (curv) and Cartesiant (cart) grid in FM 138
11.7 Steamwise velocities and water levels in main channel for FM and 3Di . . 139
11.8 Bathymetry of river Elbe with an arrow indicating the $x-$axis location in Figure 11.9 141
11.9 Plotted energy head and bottom level at the arrow of Figure 11.8 141
11.10Plotted velocities of measurements in indicated groyne fields 142
11.11Differences between a turbulent model with a constant viscosity and no turbulent model 143
11.12Turbulent viscosity plotted in part of the river based on two options . . . 144
11.13Bathymetry of the Elbe with placement of transitions 145
11.14Differences between a fine uniform grid and a grid with local refinements . 146
11.15Differences between a fine uniform grid and a grid with local refinements . 147
11.16Plotted energy head and bottom level at the arrow of Figure 11.8 147

A.1 Coordinate system 157
A.2 Grid cell definitions 159
A.3 Admitted and nonadmitted cells 160
A.4 Layout of grid points in a structured grid 160
A.5 Sub-grid with quadtrees 161
A.6 Unstructured grid 161

B.1 Secondary flow in a bend 169
B.2 Helical flow (Jirka and Uijttewaal, 2004) 169

C.1 Net (domain discretisation) . . . 174
C.2 Perfect orthogonality (left) and perfect smoothness (right) . . . 174
C.3 Small flowlinks . . . 175
C.4 Behaviour of the flow when a flowlink misses . . . 175
C.5 Example of notations (Deltares, 2015a) . . . 176
C.6 Flow area A_{uj} and face-based water depth h_{uj} (Deltares, 2015a) . . . 177
C.7 Control volumes of triangular grid (Kernkamp et al., 2011b) . . . 179

D.1 Grid cell numbering in two layers . . . 183
D.2 Grid cell numbering . . . 184
D.3 Coarse cell with sub-grid . . . 185
D.4 Coarse grid sub-domains (Stelling, 2012) . . . 185
D.5 Discharges for momentum transport (Stelling, 2012) . . . 190

E.1 Fluid particle . . . 197

G.1 Differences between refinement 2 and uniform grid for 3Di . . . 207
G.2 Differences between refinement 3 and uniform grid for 3Di . . . 208
G.3 Differences between refinement 2 and uniform grid for Flexible Mesh . . . 208
G.4 Differences between refinement 3 and uniform grid for Flexible Mesh . . . 209

List of Tables

1 Overview test cases viii

1.1 Overview test cases 4

3.1 Values of the physical domain 11

4.1 Values of the physical domain 19
4.2 Velocity values 24

6.1 Values of the physical domain 69
6.2 Implemented parameters in simulations 78

8.1 Overview of the simulated models 116

9.1 Overview test cases 125

11.1 Definition of colors in Figure 11.10 142

Nomenclature

Latin Symbols

g	Gravitational acceleration	$[ms^{-2}]$
t	Time	$[s]$
u	Velocity x-direction	$[ms^{-1}]$
v	Velocity y-direction	$[ms^{-1}]$
w	Velocity z-direction	$[ms^{-1}]$
A	Cross sectional area	$[m^2]$
A_{uj}	Flow area	$[m^2]$
B	Width	$[m]$
bob	Face-based bed levels	$[m]$
C	Chezy number	$[m^{1/2}s^{-1}]$
c_f	Friction coefficient	$[-]$
C_s	Smagorinsky coefficient	$[-]$
E	Energy head	$[m]$
f	Coriolis parameter	$[rads^{-1}]$
Fr	Froude number	$[-]$
$\overline{f_{\text{vis}}}$	Viscous force	$[kgm^{-2}s^{-2}]$
h	Water depth	$[m]$
h_{uj}	Face-based water depth	$[m]$
i_b	Bed slope	$[-]$
k_s	Wall roughness	$[m]$
L	Crest width	$[-]$

n	Manning coefficient	$[m^{-1/3}s]$
P	Wet perimeter	$[m]$
p	Pressure	$[Pa]$
p_a	Atmosphere pressure	$[Pa]$
Q	Discharge	$[m^3s{-}1]$
R	Hydraulic radius	$[m]$
Re	Reynolds number	$[-]$
Ro	Rossby number	$[-]$
S	Submergence degree	$[-]$
S_f	Friction slope	$[-]$
∇^S	Symmetric operator	$[-]$
T	Lateral stresses	$[Pa]$
Δt	Time step	$[s]$
u^*	Turbulent shear velocity	$[ms^{-1}]$
$\overline{u'v'}$	Turbulent shear stress	$[m^2s^{-2}]$
V	Volume	$[m^3]$
w_{uj}	Face width	$[m]$
Δx	Grid size	$[m]$
z_b	Bottom level	$[m]$
z_c	crest heigth	$[m]$
z_i	Node-based bed levels	$[m]$

Greek Symbols

ϵ	Roughness height	$[m]$
ζ	Water level	$[m]$
κ	Von Karman constant	$[-]$
μ	Dynamic viscosity	$[kgs^{-1}m^{-1}]$
ν	Kinematic viscosity	$[m^2s^{-1}]$
ν_N	Numerical viscosity	$[m^2s^{-1}]$
ν_t	Turbulent viscosity	$[m^2s^{-1}]$
ρ	Density	$[kgm^{-3}]$
τ	Shear stress	$[Pa]$
ϕ	Latitude	$[-]$
Ω	Rotation rate of the Earth	$[rads^{-1}]$

Other Symbols

$\mathcal{I}$	Set that contains mesh nodes
$\mathcal{J}$	Set that contains vertical faces

Chapter 1

Introduction

It is of importance to know how the water is behaving in rivers due to the dangers, such as flooding and eroding of land, it can bring with it. Present day we are still reshaping rivers, building structures in rivers or adjusting them, which results in changes in the hydrodynamics and morphology. In order to obtain more insight in the consequences of these adjustments, it is convenient to use a numerical model to simulate the river hydrodynamics. For the last decades numerical models have been developed that are able to simulate hydrodynamics. Currently, new software packages are proposed that are more efficient in predicting this. Two of these new software packages are D-Flow Flexible Mesh (FM) and 3Di. Whereas the first is especially designed to model the hydrodynamics of rivers and other flows such as in estuaries, the latter is mostly used for the simulation of flooding of land (for example due to dike breaches). 3Di is thus not particularly developed to simulate the hydrodynamics of rivers, which should be kept in mind.

1.1 Problem description

The usage of numerical model applications results usually in many choices that have to be made. Based on these choice there are considerations that need to be taken into account. Both these choices and considerations will have influence on the river hydrodynamics. With two new packages available that can simulate hydrodynamics, the choices and possibilities for each package should be clear. When multiple numerical model applications are considered the similarities and differences should be known.

One of the differences between 3Di and Flexible Mesh is the mesh generation. 3Di generates a structured grid based on the sub-grid method with quadtrees, while Flexible Mesh works with an unstructured grid that combines a curvilinear grid with triangles. Both kind of grid combinations are not often used in river simulations, which distinguish these tools from others. From a mathematical point of view these differences between the grids are interesting. Different grids might lead to dissimilar results and the question would be, which of these grids produces a more realistic performance in what situation.

Even though the packages are new, the grids they use are not. The advantage of these grids is that there is the possibility to refine the grid at certain areas without having this refinement over the whole computational domain. As a result, the computational time is less than when the whole domain has to be refined. Studies of the refinement of these grids on rivers over the complete computational area have been done by Hagen (2014) for Flexible Mesh and Stelling (2012) for 3Di. These studies did not include the transition from a coarse to finer grid in one simulation. The transition can result in different hydrodynamics compared to the results when a grid is refined over the complete computational area. Consequences might be that the results are not quite reliable at these local areas.

Considering the hydrodynamics it is important that properties such as turbulence, diffusivity etc. are as best processed as possible. Hence, the physical aspects in a simulation should be close to reality. How well these aspects are simulated might depend on the type of grid that is used as well, which relates this subject to the mathematical part. It can be difficult to simulate this, hence, in existing numerical models some used values are physically not realistic, even though the result might be. However, in that case the resulting simulation is not suitable for other situations or predicting in a precise way what can happen in the future. Since both Flexible Mesh and 3Di are new packages it is not known how well this is done.

1.2 Objective

Both packages 3Di and D-Flow Flexible Mesh are quite new and came available around the same time. Hence, more insight is needed in all the possible choices that influence the river hydrodynamics. The considered choices in this research are related to grid resolution, boundary conditions, and turbulence models. Based on these choices there are considerations that need to be taken into account, which are focused on the representation of physical processes, accuracy and computational effort in this thesis. Each of the choices and considerations will have consequences for the depth averaged simulations. This research investigates the importance of these considerations and consequences for the suitability of results for specific problems.

The general research question will be

Which considerations and consequences for simulations, that follow from the choices in numerical model applications, are important for the suitability of results given a specific problem?

The thesis consists of two parts. In the first part the focus is more on mathematical subjects, while the second part zooms in on the hydrodynamics. Both parts distinguish D-Flow Flexible Mesh and 3Di, so the conclusions of each part can be used to answer the general research question.

The objective of the first part is to find out how local grid refinements influence the results of Flexible Mesh and 3Di. It is of importance to know how well the results are in comparison with reality, especially in the area of interest where a local refinement will be applied. This has led to the following research question:

"How do local grid refinements influence the modeling results of river hydrodynamics?"

with subquestions

- What are the differences between the results of Flexible Mesh and 3Di due to dissimilar grid types?
- Are the results dependent on the placement of the transition between grid sizes?
- What influences the possible differences between uniform and local refinements?

The second part will investigate the modeling of physical aspects. The basic equations of both 3Di and Flexible Mesh are the shallow water equations. Instead of solving 3-dimensional simulations, the depth-averaged shallow water equations are solved, which are 2-dimensional horizontal (2DH) equations. Solving a 3-dimensional problems is often quite time consuming, thus, the shallow water equations are usually used for simulations when 3D processes are less important. In 3Di it is only possible to simulate in 2DH, while in Flexible Mesh both 2DH and 3D are possible. In order to have a better comparison, all simulations are done with 2DH equations. The main difference in the shallow water equations between Flexible Mesh and 3Di is the diffusion term. This term is included in the equations of Flexible Mesh. In cases where diffusion is an important aspect, it will be interesting to investigate how this difference influences the results. This led to the following research question:

"Which processes are important for the suitability of numerical model applications for a specific problem?"

with subquestions

- What assumptions are done to obtain the equations used in the numerical models?
- What are the consequences of these assumptions?
- If the results differ in both models, where do these differences come from?

1.3 Outline

In order to obtain a better understanding of both numerical models, some test cases are set up before simulating a river. In total four test models will be investigated: a flume experiment, a U-bend with sinusoidal profile, a rectangular channel with a weir and a turbulent jet. In Table 1.1 an overview of the test cases is given together with the research subject of each study. With an exception of the turbulent jet, each model consists of a convergence study as starting point. In each model the water levels and velocities are investigated. In test case 3, the energy head, which is dependent on the water level and velocity, will be taken into account as well.

With the focus on software packages 3Di and D-Flow Flexible Mesh, multiple cases are simulated in order to analyze the results based on the made choices. Before these test

Test case	Physical aspects	Mathematics	Chapter
1. Flume experiment	3-dimensional processes Grid comparison	Grid comparison	3 & 6
2. U-bend		Local refinement in the middle of the bend	4
3. Flow over weir	Energy losses	Local refinement as a function of x	5 & 7
4. Turbulent jet	Horizontal viscosity		8

Table 1.1: Overview test cases

cases are investigated, a literature study is presented in Chapter 2. Differences in the equations and grid types of Flexible Mesh and 3Di are emphasized, since mainly these differences determine possible dissimilarities in the results between both programs. Part I (mathematics), consisting of Chapter 3 up to Chapter 5, describes three test cases to investigate the grid differences and local refinements, see Table 1.1. Chapter 6 to 8 belong to part II (physical aspects) that also consists of three test cases. Two of them are the same as in part I, where the focus is on the physical processes instead of the local refinement. In Chapter 9 a synthesis of both parts is given, where the results of the test cases help to set up a hypothesis of the river results. Since some uncertainties have come to the surface in test case 1, it is combined with the geometry of test case 2 to investigate its influence on the results and gain more insight of how the uncertainties arise. These results are given in Chapter 10. Hereafter the river is being simulated. All conclusions of the previous parts are taken into account and will help with the interpretation of the results. This thesis ends with a conclusion and recommendation of the research, after the discussion that is given in Chapter 12.

Chapter 2

Literature study

This chapter describes the differences in the equations and grid types of Flexible Mesh and 3Di. In Chapters 3-8 test cases will be simulated and analyzed. In order to obtain a better understanding of the results, the (dis)similarities between both packages should be known. Section 2.1 will compare the mathematical model of both packages, while in Section 2.2 the grid generation is considered.

2.1 Description of the mathematical model

Though both 3Di and Flexible Mesh are based on the shallow water equations for the mathematical model, there is one main difference between these equations in both packages. The starting point of simulating rivers is the Navier-Stokes equations, which describe the evolution of a fluid. These equations govern the motion of a viscid fluid and describe the conservation of mass and momentum. The shallow water equations that are used in 3Di and D-Flow Flexible Mesh are derived from the Navier-Stokes equations. In order to derive the shallow water equations various assumptions have to be done. Making these assumptions means that some 3-dimensional processes are not implemented in the numerical models, or are not represented in a correct manner. All assumptions are explained in detail in Appendix B. The resulting equations, the shallow water equations, are presented in Equation (2.1)-(2.3). Whereas the continuity equations is similar for both models, the momentum equation differs. On the right hand side of Equation (2.3) an extra term can be found, which is the diffusion term. Chapter 8 consists of a test case where a turbulent jet is simulated. In this test case the differences due to inclusion of diffusion in Flexible Mesh will become clear.

$$\frac{\partial h}{\partial t} + \frac{\partial uh}{\partial x} + \frac{\partial vh}{\partial y} = 0 \tag{2.1}$$

$$\text{3Di } x-\text{direction} \quad \frac{\partial u}{\partial t} + u\frac{\partial u}{\partial x} + v\frac{\partial u}{\partial y} + g\frac{\partial \zeta}{\partial x} + \frac{c_f}{h}u\|u\| = 0 \tag{2.2}$$

$$\text{FM } x-\text{direction} \quad \frac{\partial u}{\partial t} + u\frac{\partial u}{\partial x} + v\frac{\partial u}{\partial y} + g\frac{\partial \zeta}{\partial x} + \frac{c_f}{h}u\|u\| = \frac{1}{h}\nabla \cdot \left(\nu h \left(\nabla u + \nabla u^T\right)\right) \tag{2.3}$$

2.2 Grid generation

Besides the difference in the shallow water equations as described in Section 2.1, the grid generation of both packages differs. In Flexible Mesh multiple options are available including a Cartesian and curvilinear grid and triangles (Deltares, 2015a). 3Di uses a Cartesian grid in combination with flow solvers (quadtree, subgrid pixel) (Stelling, 2012) in order to counteract the disadvantages of this type of grid. In Sections 2.2.1 and 2.2.2 these grid generations are explained in more detail.

2.2.1 Grid generation in Flexible Mesh

Flexible Mesh works with multiple grid types, which can be subdivided into a structured and unstructured grid. A Cartesian and curvilinear grid belong to the structured class, while using grid with shapes such as triangles, pentagons, etc. belong to the unstructured grid class. More information about these grids can be found in Appendix A. Generating a curvilinear grid can be complicated compared to a Cartesian grid. There are two important properties that have to be taken into account. These are orthogonality and smoothness. The orthogonality is measured by taking the cosinus of the angle between the netlink and flowlink, see Appendix C for definitions. Smoothness is defined by the ratio of two adjacent cell areas. In a perfect grid generation both of these parameters would be equal to one. Flexible Mesh has the possibility to combine a curvilinear grid, or a Cartesian grid, with other grid shapes such as the triangles. This results in a grid that is completely unstructured, whereas a curvilinear grid alone is structured. When there are complex geometries present in a river (or somewhere else), the triangles can be used to simulate this easier than a curvilinear grid alone. Where the geometry is less complex a curvilinear grid can be used which has the advantage of a faster computational time and using less memory than working with only a triangular grid.

2.2.2 Grid generation in 3Di

In 3Di a Cartesian grid is used in combination with a sub-grid method, and can be refined by using the quadtree method. A Cartesian grid is often the most simple grid that can be used for simulating a numerical model. It has many advantages. One of them is the simplicity. The numerical equations that are involved are quite simple and the generation of a grid is easier and quick compared to other grids. In the past years disadvantages are partly removed by using flow solvers that have the ability to manage arbitrary and

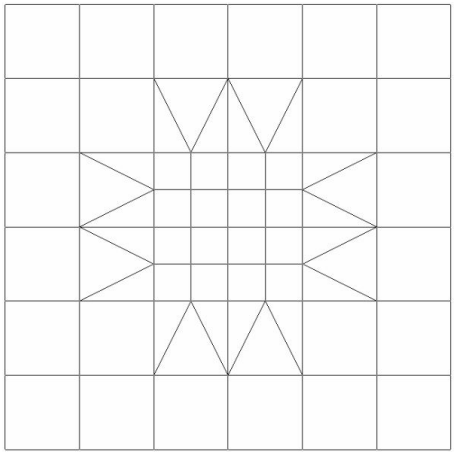

Figure 2.1: Combination of curvilinear grid and triangles in FM (Kernkamp et al., 2011a)

moving boundaries. 3Di uses a sub-grid method that is arranged as stated by quadtrees (Stelling, 2012), see Figure 2.2. A quadtree grid distinguishes itself from other grids due to the fact that each square cell can be subdivided into four child cells. Each of these child cells will be of equal size. Hence, a grid using this method can be refined in an easy way. Another change in the flow solver that is used to remove the disadvantages of the Cartesian grid is using a digital element model (DEM), which is a second grid with a higher resolution. In this way it is possible to use detailed bathymetry data. This second grid contains the bottom values, while the calculations of the water levels and velocities are done on the coarse grid. This second grid, also called subgrid, will always have a higher resolution, since at least 4 pixels are needed in one grid cell.

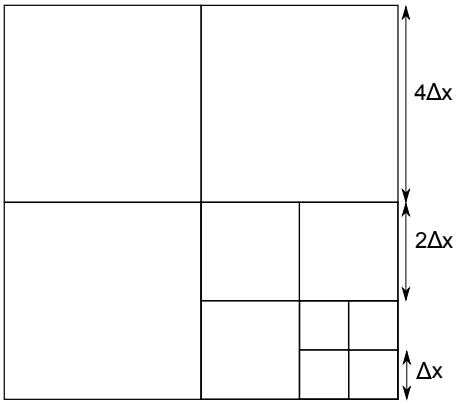

Figure 2.2: Example of grid refinement in 3Di with quadtrees

Part I

Applied Mathematics: The role of grid refinement in the modeling of river hydrodynamics

Chapter 3

Grid comparison of Flexible Mesh and 3Di

The research of part I is about the influence of local refinement. However, before considering these local refinements, a first research is done to the influence of the different types of grid. 3Di has standard a Cartesian grid (which is structured). In Flexible Mesh there are multiple options as is seen in Chapter 2. In this chapter both a curvilinear and Cartesian grid will be used to see how these grids influence the results. Both of them are compared to the results with 3Di. Only a convergence study will be performed in this chapter, hence, no local refinements are done yet. This will be applied in the upcoming chapters. The version used of D-Flow Flexible Mesh in this chapter is D-Flow FM Version 1.1.148.41897. For 3Di this is subgrid Version 0.1.1.1942.

3.1 Flow geometry

Specifications of the flume geometry, which originates from Blokland (1985), are given in Table 3.1. In this table is C the Chezy coefficient, i_b the bottom slope in streamwise direction, B the width and R the radius of either the inner or outer bend. The cross section profile of this flume is a rectangular. Furthermore, in the streamwise direction there is no bottom slope.

R_{in} [m]	R_{out} [m]	B [m]	i_b	C [$m^{1/2}s^{-1}$]
3.85	4.35	0.5	0	60

Table 3.1: Values of the physical domain

Boundary conditions are chosen based on the available data from Blokland (1985). At the inflow a discharge boundary condition is given, while at the outflow a water level boundary condition is placed. The first is set at $Q_{in} = 6.44$l/s, the average discharge that is measured. The water level is equal to the water depth in this case, since the bottom

level is placed at $z = 0$. The water depth is known at certain points by measurements. Further, the hydraulic gradient is around $0.5 \cdot 10^{-3}$, which gives the possibility to calculate the outflow boundary condition. It gives a value of $\zeta_{out} = 0.045$m.

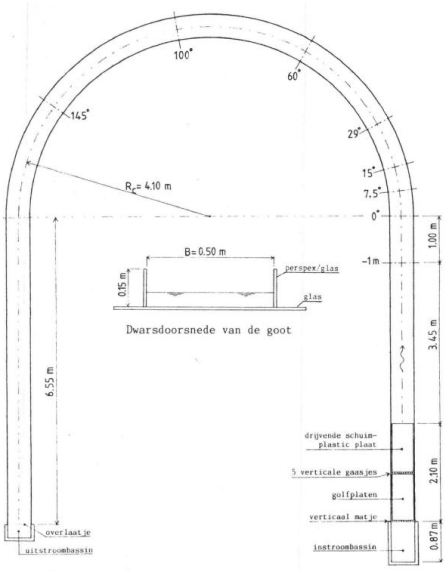

Figure 3.1: Set up of flume experiment of (Blokland, 1985)

Figure 3.1 presents a display of the set up of the flume used in the experiment. Places where measurements have been taken are shown. These measurements are done in eight cross sections, each at a different place in or in front of the bend. With this data both programs can be validated. Though it should be kept in mind that these measurements can always contain some errors.

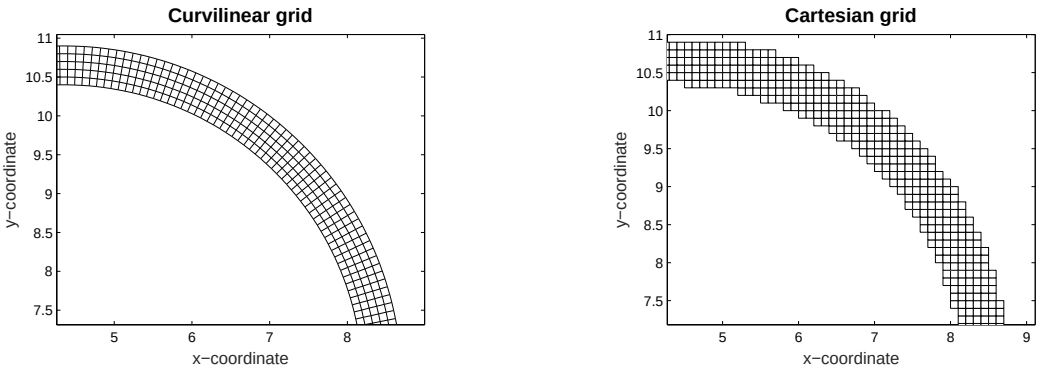

(a) Curvilinear grid (b) Cartesian grid

Figure 3.2: Multiple grid types used in Flexible Mesh and 3Di

3.2 Different types of grid generation

In order to compare the test case results with the available data, results from the same cross sections as in the experiment (Figure 3.1) are used for comparison, where three different grid sizes are used. The coarsest grid has 5 cells in the width, while the finest grid has 20 cells in the width. Thus, with each refinement a cell is half the size of the grid cell in both $y-$ and $x-$direction. The coarsest grid of both types is presented in Figure 3.2, where the differences between a curvilinear and Cartesian grid are clearly visible. For Flexible Mesh both types of grid are used in this chapter, while for 3Di a Cartesian grid is used, which is the only option. The first simulation will be using a Cartesian grid of both Flexible Mesh and 3Di.

When investigating the result of different grid generation of both packages, the numerical models should be as similar as possible. It is seen in Chapter 2 that the shallow water equations differ. In the momentum conservation equation of 3Di the diffusivity term is missing. This term is dependent on the turbulent viscosity, which can be set to zero in Flexible Mesh. By doing so, the shallow water equations are equal to each other. How these equations are implemented in the packages is still different, but this cannot be changed. Hence, differences are in the implementation and grid generation at this point.

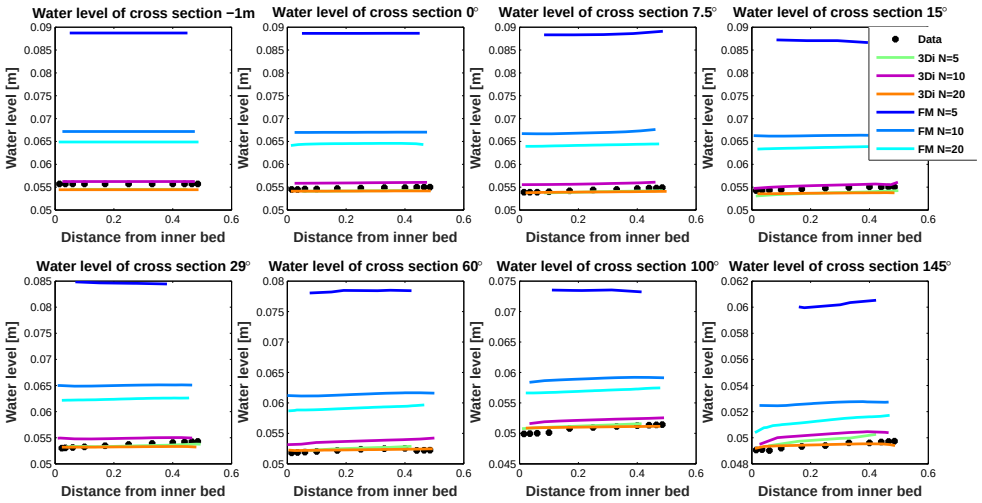

Figure 3.3: Water levels in cross sections indicated in Figure 3.1 for a Cartesian grid in FM and 3Di for multiple grid resolutions

It can be seen in Figure 3.3, where the water levels are plotted, that the results of a Cartesian grid in Flexible Mesh are far of the experimental data, while for 3Di they are quite agreeable. Considering the water levels of the simulation where $N = 5$ in Flexible Mesh, they are more than 50% higher than the experimental data. Due to the mass balance, the velocity is much lower than this data. Increasing the resolution of this grid results in differences of the water levels that are less than 20%. This opposite to the results of 3Di, where the water levels for each of the resolutions are close to the experimental data. With the pixel subgrid model, the volume balance can be calculated in more detail. For this simulation only one pixel subgrid size is used, where $N_p = 40$ in the width, even

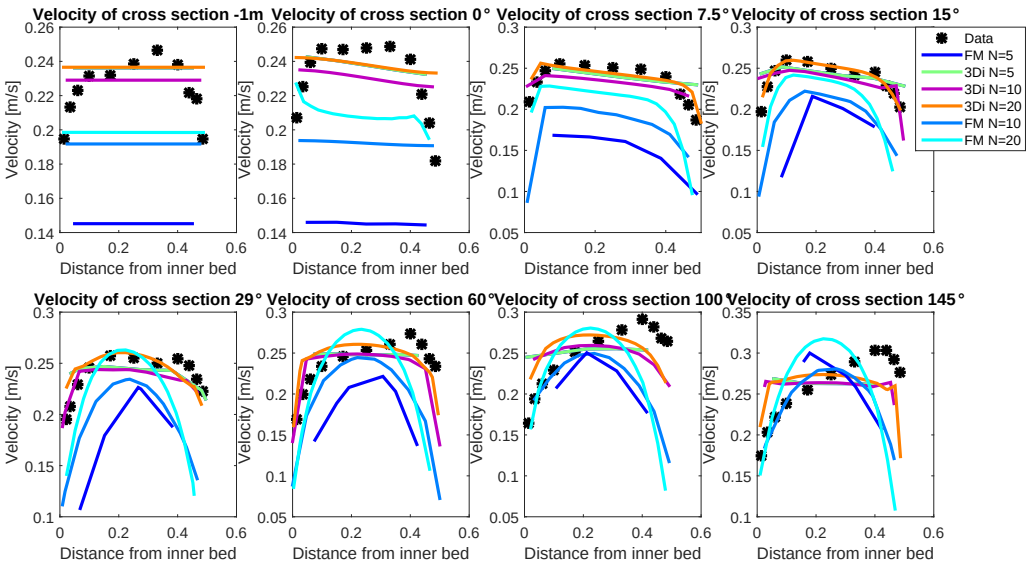

Figure 3.4: Velocities in cross sections indicated in Figure 3.1 for a Cartesian grid in FM and 3Di for multiple grid resolutions

for $N = 5$. Hence, no matter the grid size, the volume balance is always calculated with this subgrid.

In order to investigate whether the results of 3Di are closer to the data than Flexible Mesh due to the high subgrid resolution, a pixel size of $N_p = 10$ is taken for $N = 5$ instead of $N_p = 40$. Presented in Figure 3.5 and Figure 3.6 are the results of Flexible Mesh with a Cartesian grid, 3Di with $N = 5$ and $N_p = 10$ and $N_p = 40$. Although the water levels of $N_p = 10$ are closer to the results of Flexible Mesh, the difference is still quite large. Especially with $N = 5$ of Flexible Mesh. The profiles of the velocities are in some cross section more similar to Flexible Mesh: on the outsides it is lower, while with a higher pixel resolution it is more a linear line. Thus, even though the grid with pixels is more similar to the coarsest grid of Flexible Mesh, the results are still more precise when compared to the data. So apparently the Cartesian grid of 3Di with pixels is more suitable to use than a Cartesian grid in Flexible Mesh for this specific problem.

Not only the water levels of the results of both packages differs, the shape of the velocity profile is in the bend quite dissimilar. In front and in the beginning of the bed these profiles are (almost) linear. As the angle increases the velocities get smaller near the edges of the flume. In both programs there is however free slip, so the velocity is not zero near the walls. Considering Figure 3.8, where the curvilinear and Cartesian grid of Flexible Mesh are compared, it can be seen that the velocity profile for a curvilinear grid is still linear in the bend. Hence, it is due to the Cartesian grid that these velocities are lower near the wall. A Cartesian grid has a staircase profile for bends, where the velocity cannot follow the boundaries of the real flume. As a result, the velocities are low in these cells adjacent to the boundary. The shapes of these velocity profiles differ between 3Di and Flexible Mesh. It appears that the velocity over the entire cross section in Flexible Mesh is influenced by the staircase bend (based on the parabolic shape), while for 3Di the shape is still linear in the middle. Since all input values that can be influenced are the

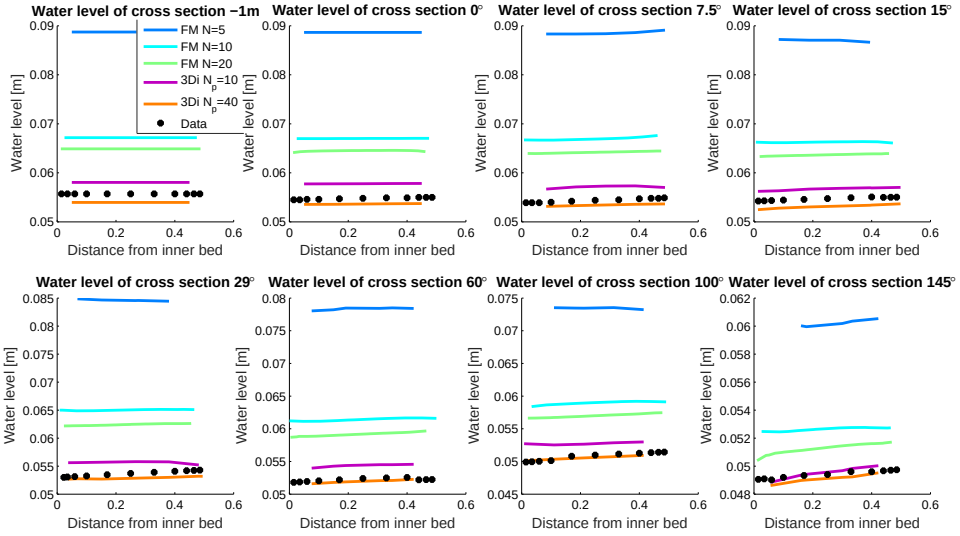

Figure 3.5: Water levels in cross sections indicated in Figure 3.1 for a Cartesian grid in FM and 3Di for multiple grid resolutions with variable pixel sizes in 3Di

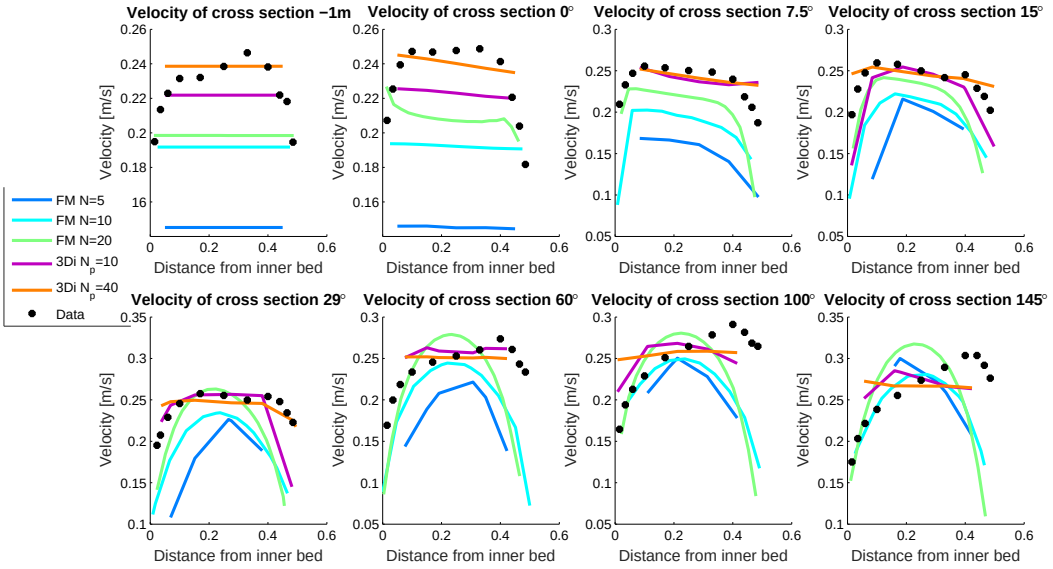

Figure 3.6: Velocities in cross sections indicated in Figure 3.1 for a Cartesian grid in FM and 3Di for multiple grid resolutions with variable pixel sizes in 3Di

same, it is most likely that it is the result of how the mathematical model is implement in both packages.

Next the curvilinear and Cartesian grid are compared. Both grids are built in Flexible Mesh, thus except the grid all processes and equations are the same. Just as before, the water levels and velocities are compared for both grids, see Figure 3.7 and Figure 3.8.

Opposite to a Cartesian grid in Flexible Mesh, the result of a curvilinear grid have almost

the same value as the given data. It is seen before that for a Cartesian grid with $N = 5$ results are far off the experimental data. For a curvilinear grid, all the results of different resolutions are closely together. Considering the water levels, Figure 3.7, these results coincide with the experimental data for each cross section. However, for the velocity profiles it is another case. In the first four cross sections, the results agree with the experimental data, except near the wall. The latter occurs due to using a free slip condition, instead of a no-slip condition. After these first cross sections, the values of the velocities are still quite agreeable, but the shape not anymore. Since many 3-dimensional physical processes as secondary flow are not taken into account, one cannot expect these results to match the given data.

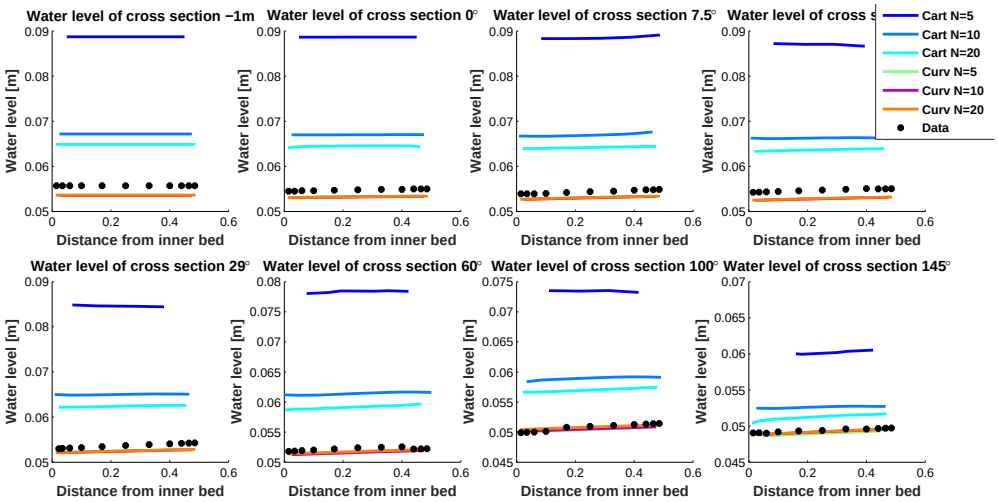

Figure 3.7: Water levels in cross sections indicated in Figure 3.1 for both a Cartesian and curvilinear grid in FM and 3Di for multiple grid resolutions

3.3 Conclusion

Two types of grids have been compared in this chapter, a Cartesian and curvilinear grid. The results for these grids in each package were different, either in the water levels or velocities. A Cartesian grid in Flexible Mesh when simulating bends is not recommended. Although a higher resolution led soon to a much better approximation of the water levels and velocities, the errors are still higher than when applying a curvilinear grid. Although 3Di uses a Cartesian grid as well, the results are closer to the experimental data than Flexible Mesh. With a pixel subgrid that has the minimum resolution ($N_p = 10$), the differences with the experimental data are smaller than using Flexible Mesh. Using a higher resolution for the pixels improves the results quite a lot, while the sizes of the grid can be kept the same. Using a smaller grid size, while having the same resolution of pixels led only to a small improvement of the results. Thus, for similar results the computational time can be lowered due to this approach. In the next chapter another bend is modeled. Instead of a flat bottom, there is a slope in the streamwise direction and a sinusoidal profile in the cross section. For above reasons a curvilinear grid is used for Flexible Mesh.

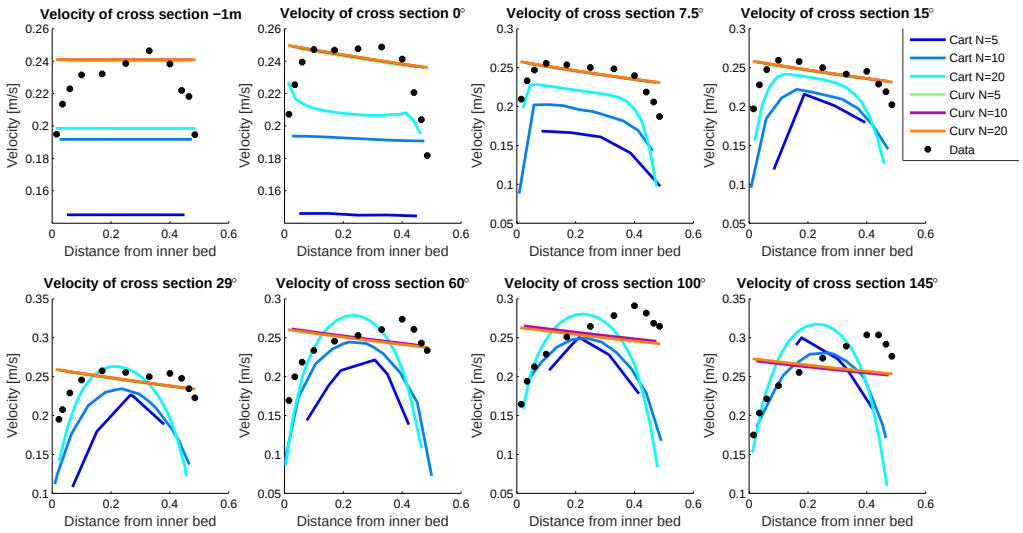

Figure 3.8: Velocities in cross sections indicated in Figure 3.1 for both a Cartesian and curvilinear grid in FM and 3Di for multiple grid resolutions

Chapter 4

U-bend with sinusoidal bed

The second test case that is considered is a U-bend with a sinusoidal bed. The test cases that are done, represent simple situations of flows that appear in rivers. By simulating these test cases first, both packages can be understood. This will lead to a better understanding of the results for a river. This specific test case is an example that is made by Stelling (2012). It consists of testing convergence with different water levels in 3Di. It is recreated for both Flexible Mesh and 3Di, to make sure the same values are used. In this chapter the flow geometry is given first. Followed by the simulation in Flexible Mesh and 3Di, where both a uniform grid is used and local refinements are applied. Hereafter a comparison of these results is done. This chapter ends with a conclusion of the results obtained for this test case. These simulations are performed with D-Flow FM version 1.1.148.41897, file format 1.05 and 3Di - subgrid Version 0.1.1.1942.

4.1 Flow Geometry

The geometry of the U-bend originates from Stelling (2012). Specifications of its domain are given in Table 4.1, where n is the Manning coefficient (determines the value of the friction coefficient), i_b the bed slope in streamwise direction, B the width of the river and R the radius of either the inner or outer bend. In order to study the effect of nonlinear variations in bed level, the profile is a quarter sinusoidal function (Figure 4.1b) in the cross section. Figure 4.1b shows this profile when one looks in the direction of the red arrow in the figure left of it.

R_{in} [m]	R_{out} [m]	B [m]	i_b	n
107	320	213	$2 \cdot 10^{-4}$	0.026

Table 4.1: Values of the physical domain

The boundary conditions are prescribed water levels for both inflow and outflow. At the inflow it is $\zeta_{in} = 0$ m and at the outflow $\zeta_{out} = -0.3901$ m. The latter is calculated by multiplying the bottom slope i_b with the total length of the bend in streamwise direction.

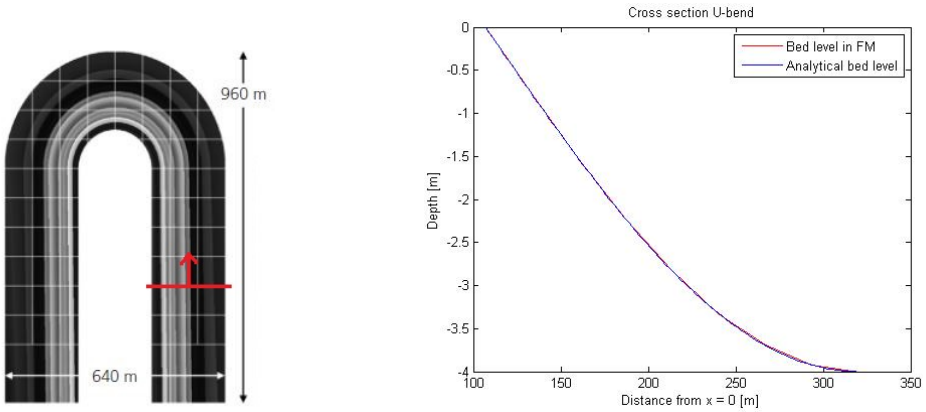

(a) Top view, Stelling (2012)

(b) Cross-section

Figure 4.1: Dimensions of the U-bend presented in a top view and cross section

4.2 Test case in Flexible Mesh

This bend is simulated with multiple grids. The starting point is a curvilinear grid with 8 grid cells in the cross direction, 12 cells in the streamwise direction of the straight parts and 15 in the bend. The latter is chosen such that the length of the cells in the middle of the bend are more or less the same as in the straight parts. The grid is 4 times refined such that each refinement gives a cell that is a quarter of the previous cell. Hence, in both directions it is half the size of the previous cell.

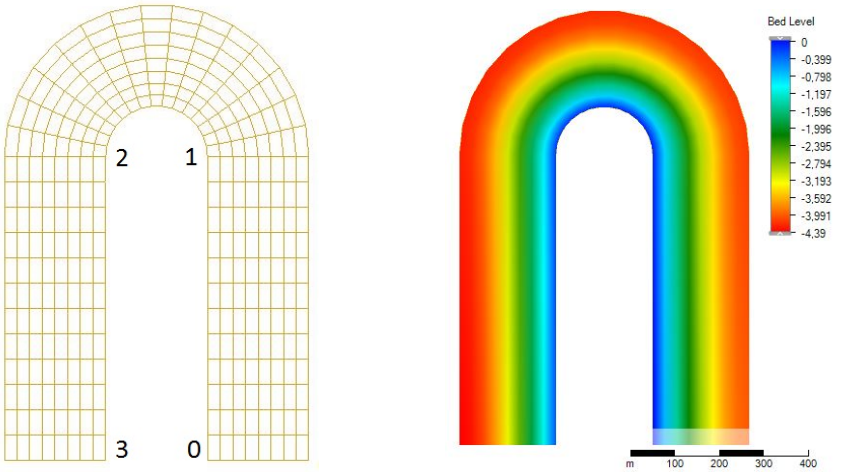

(a) Coarsest grid

(b) Bottom profile

Figure 4.2: Representation of grid and bed profile in FM with a curvilinear grid

The bottom profile is, as said before, a quarter of a sinus function as given in Figure 4.1b. Figure 4.1b also shows the linear representation of the bed level in Flexible Mesh (red line). It can be seen that this line lies almost completely on the analytical function,

except at the deeper part with the steeper slope. However, when the grid is refined, this will coincide even better. In Matlab, sample points are made that can be interpolated on a grid. The result can be seen in Figure 4.2b. Each corner of a cell has a certain value. In between these points a linear relation is determined such that the bottom represents the sinus in quite a good way.

4.2.1 Convergence

In this part a closer look is taken at the convergence for this test case. Figure 4.3 shows the water level of all refinements that are simulated. The legend gives the refinement factor, where refinement factor 1 is the coarsest grid, hence, no refinement is done there. The $x-$axis represents the dimensionless distance. This makes it easier to plot both the outer (top line) and inner bend (bottom line) in one figure. The distance 0 - 1 corresponds to the right straight part, 1 - 2 the bend, and 2 - 3 the left straight part, see Figure 4.2a for a better understanding. Thus, the water flows from the right part to the left part in the physical situation. Besides the water levels the discharge is also analyzed, see Figure 4.4. In the test case three cross sections were considered to measure the discharge. One of them was placed in front of the bend, the second in the bend, and the last after the bend. This is done to conclude that the flow was steady and enough time had passed to view the results. All the cross sections had the same results after some spin up time, confirming that the simulation has become steady.

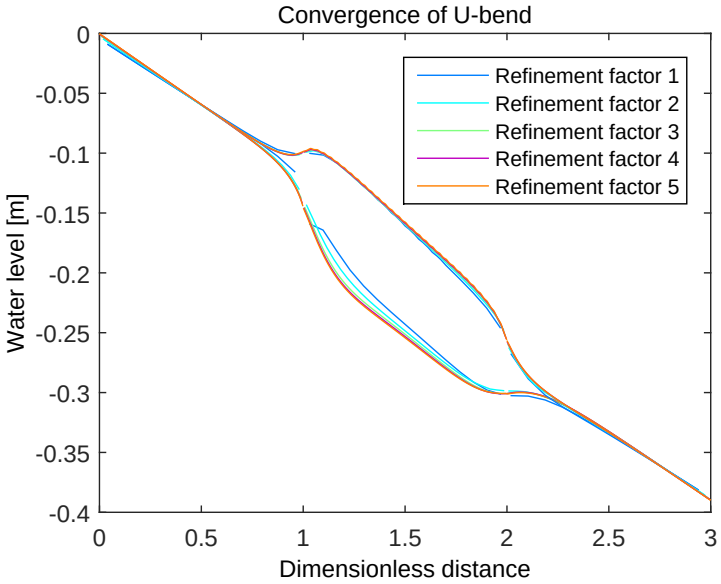

Figure 4.3: Water level inner (lower curves) and outer bend (upper curves) for multiple resolutions

In both Figure 4.3 and Figure 4.4 it can be seen that the test case converges when the grid size decreases, though there appear some uncertainties in the water level at the outer bend. Except for the inner bend it looks as if the water levels are almost the same for every grid. If we zoom in at both the inner and outer bend details are revealed. Figure

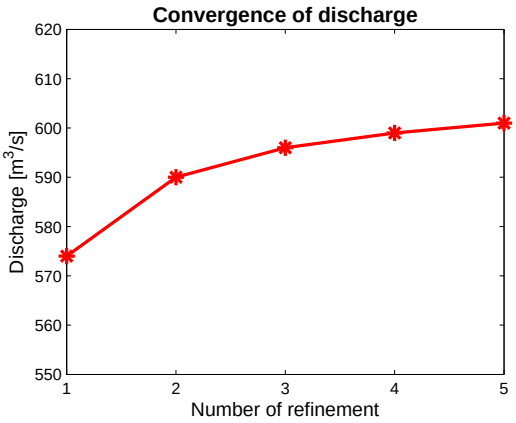

Figure 4.4: Equilibrium discharge convergence in Flexible Mesh

4.5a zooms in on the inner bend, which seems converging. With each refinement the differences get less. Figure 4.5b zooms in on the outer bend.

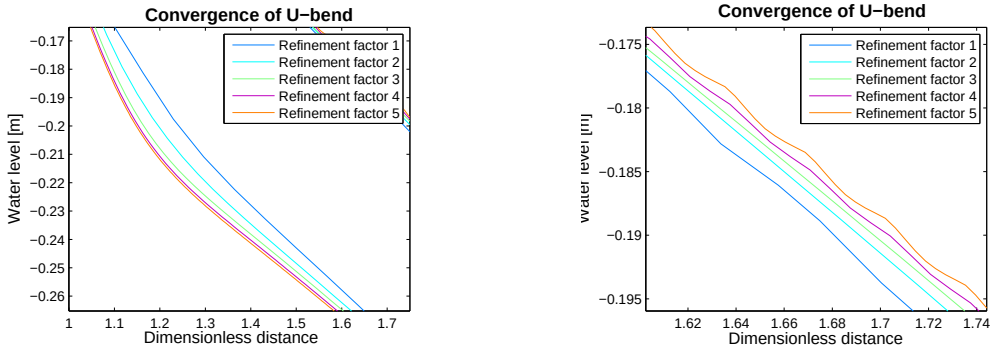

(a) Part of the inner bend

(b) Part of the outer bend

Figure 4.5: Zoomed in water levels inner(left) and outer bend (right) of Figure 4.3

In Figure 4.3 it seems that all lines are lying well on each other. However, by having a closer look some wiggles can be seen for multiple lines. The wiggles that are the most noticeable are the ones belonging to refinement factor 5, hence, the grid with the highest resolution. One would expect that the wiggles will disappear when the grid is refined. In this case the opposite appears to happen with refinement factor 5. These wiggles will be further investigated in Section 4.2.2.

4.2.2 Wiggles

In Figure 4.5b some wiggles were discovered in the outer bend when looking at the highest resolution. The polygon that intersects with the flow links of the U-bend is given at Figure 4.6, the red line. However, when researching the instabilities that have been found we limit ourself to the finer grid (refinement factor 4). With the wiggles appearing in the outer bend, it is interesting to plot the water levels that are closer to the outer boundary.

The blue line represents the new polygon that is used when plotting water levels in this part.

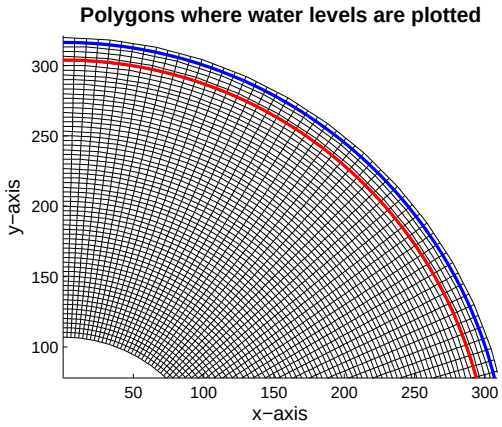

Figure 4.6: Colored lines that indicate where the water levels are plotted

When plotting the water levels at this new polygon, the results show that the wiggles get larger. Where in Figure 4.5b almost no wiggles occur for refinement factor 4, Figure 4.7 shows quite large wiggles. The line belonging to CFL number (defined as $\frac{u\Delta t}{\Delta x}$) 0.7 can be compared with the other figures, since this value has been used there. However, it is the maximum value that may occur, so it can be smaller than the given 0.7.

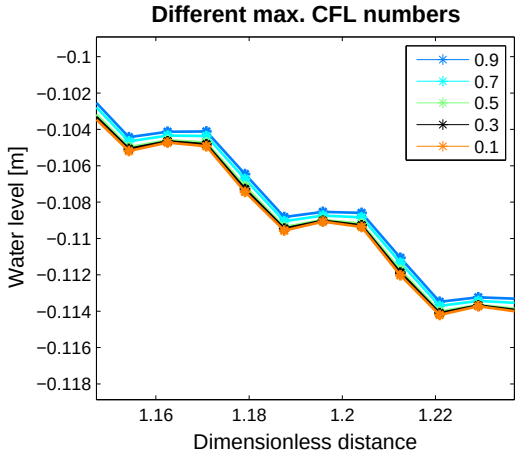

Figure 4.7: Water levels int he outer bend for multiple max. CFL numbers in Flexible Mesh

The wiggles that arise have an unknown origin. Usually if there are wiggles, these can arise due to a small grid size, or a large timestep. Both factors result in large CFL number. Of course, velocity also influences this factor, but this is not always controllable. It can explain why there are only instabilities in the outer bend. With a typical profile that can occur in a river, the velocity profile is as follows: in the inner bend it is smaller, while going near the outer bend it gets higher. So, the highest velocities are in the outer bend. The maximum and minimum values of the velocities are presented in Table 4.2. u is the velocity in the $x-$direction, and v in the $y-$direction. Hence, in the straight parts v is directed in the streamwise direction.

Variable	Outer bend	Inner bend
u_{min}	-1.2016 m^3/s	-0.1636 m^3/s
u_{max}	0.0016 m^3/s	0.0012 m^3/s
v_{min}	-1.4811 m^3/s	-0.1772 m^3/s
v_{max}	1.3037 m^3/s	0.3060 m^3/s
dx	8.4 m	2.9 m

Table 4.2: Velocity values

Table 4.2 shows that there is a difference between the grid size values of a factor 3. But, the difference between the velocities u (more or less streamwise direction in the middle of the bend) is more than a factor 6. Thus, the velocity differences might give an explanation why there are instabilities in the outer bend, while they do not occur in the inner bend. Since the grid size and velocity will not change, the only option is to lower the maximum value of the CFL number or the time step. When the maximum CFL number is lowered, Flexible Mesh will choose a lower time step in order to lower the CFL number. So, it is not needed to change the time step manually. Results of lowering the maximum CFL number are given in Figure 4.7. Notice that the size of the wiggles stay the same, while the water level is lowering by perhaps a millimeter. Changing the CFL numbers did not have the desired result. This either means that the maximum value of the CFL number is not reached at all, or that the problem lies somewhere else. In the future, this question will be further investigated.

4.2.3 Local refinement

The next step is applying local grid refinements in the domain. The effect of the changed grid resolution is studied. Resolution of the grid changes half way of the domain, see Figure 4.8. The local refinements are done at both sides to find out whether the results will differ when the water is flowing into a refinement in a bend or flow out a refinement. To observe the results, the same streamwise polyline (as in Section 4.2.1) is used to compare the water levels. Preferably one would have that the transition from one grid size to the other has no influence on the results.

The results differ not that much when either the refinement is at the left or right half. It is very good mirrored from each other, hence, looking only at one of the refinements is a good starting point. Later, for two grids without refinement, both refinements are compared with these two grids to look precisely at all errors that arise. Figures 4.9-4.11a are made from the simulation where the fine grid is at the left half.

Though over the entire domain the results appear to be valid, there arise some deviations in the water levels locally at the jump of one grid size to the other. Around distance 1.5 the refinement is done. Figure 4.9 presents the water levels belonging to this simulation. It clearly shows that there are some deviations that have not been present in Figure 4.3, where a uniform grid is used. The water level suddenly drops and rises before continuing as a smooth line. Zooming in on the outer and inner bend, Figure 4.10, shows that these drops and rises are larger in the outer bend than the inner bend. Looking at the grid and Table 4.2, the size of a cell differs a factor three in the inner and outer bend. Hence, because the cell size in the outer bend is much larger, the error is larger as well. When

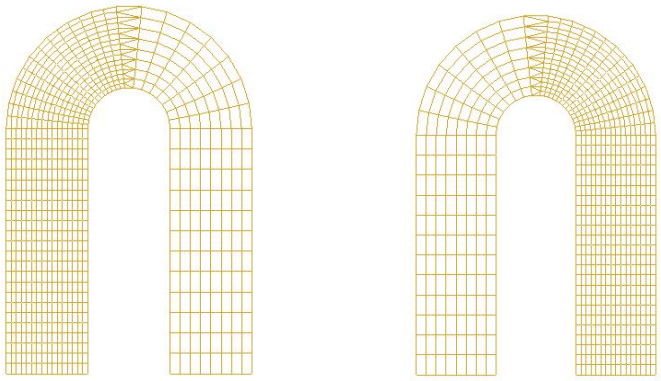

(a) Coarse grid right, fine grid left

(b) Coarse grid left, fine grid right

Figure 4.8: Placement of local refinement with transition in the middle of the bend for FM

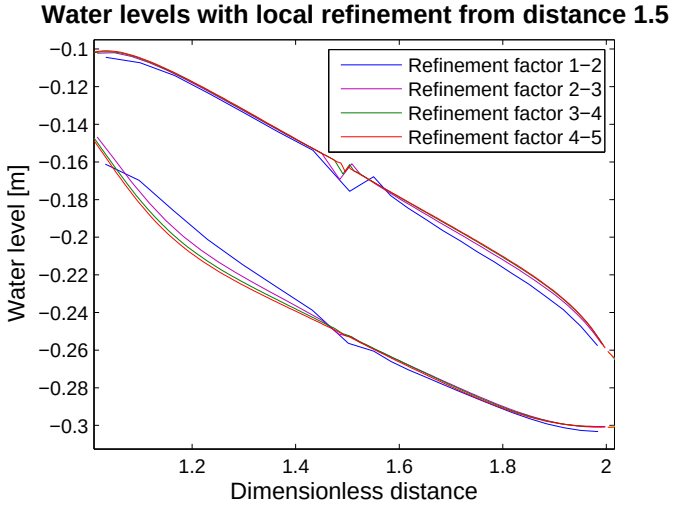

Figure 4.9: Water level inner (lower curves) and outer bend (upper curves) for multiple resolutions for a local refinement on the left and transition in the middle

the cells become smaller, these errors will shrink (as can be seen for different grid sizes in the figure).

Besides these errors in the transition of one grid to the other the results are plausible. The next step is to check whether this is the case. The results of these refinements are compared with uniform grids. The simulation with refinement factor 3-4 is compared with both grids that have only refinement factor 3 and 4. The same is done with the simulation where a refinement factor 2-3 is used.

Figure 4.11 shows the comparison of refinement factors 2 and 3. In the outer bend the water levels do not differ much. All three of them lie closely together. Zooming in shows that the small difference is that the red line (local refinement) lies closer to the one that belongs to refinement factor 3 (green line). First thoughts would be that before the refinement it lies closer to the blue line, and after refinement to the green line. This is in

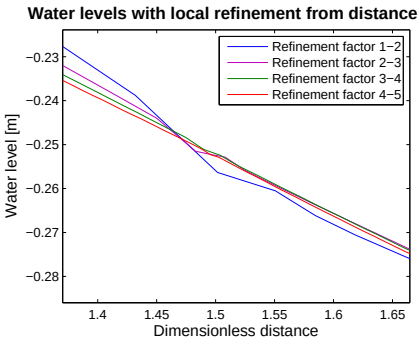

(a) Inner bend

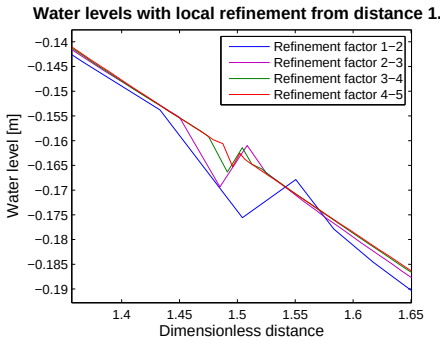

(b) Outer bend

Figure 4.10: Zoomed in water elvels in the inner (left) and outer bend (right) of Figure 4.9

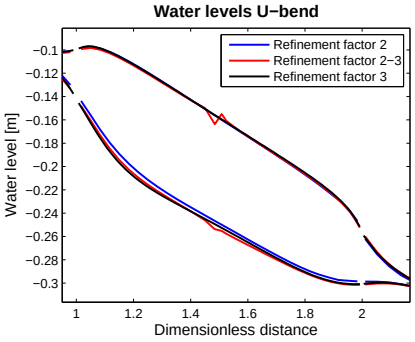

(a) Both inner and outer bend

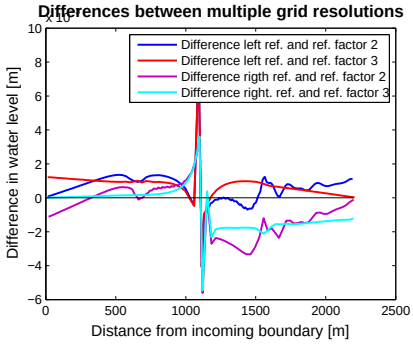

(b) Differences at the outer bend, both left and right refinement

Figure 4.11: Comparison of water levels between local refinement 2-3 and uniform grid with factors 2 and 3 in FM

both the outer and inner bend not the case. Also in the inner bend it lies before and after the refinement closer to the green line. This would mean that the local refinement has a positive influence on the results. It might also mean that due to the local refinement some errors are made there that are carried upstream to the coarser grid. Figure 4.11b gives the differences in meters for both refinements (right and left half refined). The other figure already showed that the differences were small, which is confirmed in this figure. They are of the order of millimeters, with the largest error at the refining for both refinements.

Now the other refinements are compared to see if the same properties appear. Figure 4.12 shows the water levels of these refinements. Like the previous comparison, also here in the outer bend the results are not that different from each other. There is however one thing that is noticeable. Whereas the results of refinement factor 4 show some beginning wiggles as were showed in Section 4.2.2, these are missing in the local refinement grid. This might be due to the fact that the bend starts with refinement factor 3 instead of 4. In the inner bend the water levels are as one would expect. Before the local refinement, the water levels are closer to refinement factor 3, while after the local refinement they are closer to 4.

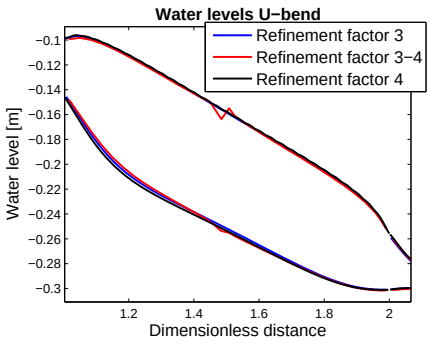

(a) Comparison of refinement factor 3-4 with no local refinement in the bend

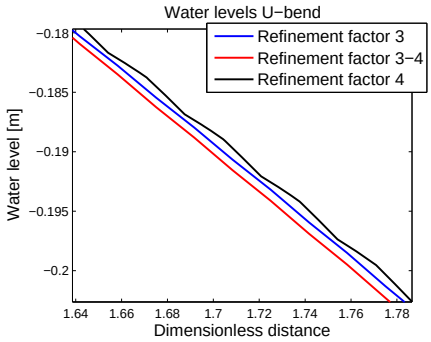

(b) Outer bend

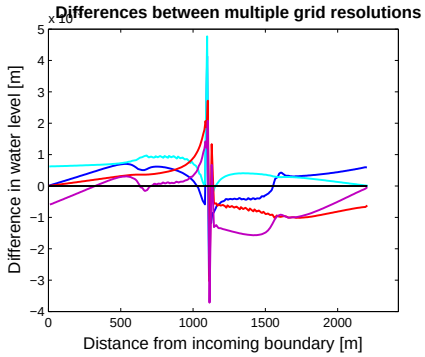

(c) Differences at the outer bend, both left and right refinement

Figure 4.12: Comparison of water levels between local refinement 3-4 and uniform grid with factors 3 and 4 in FM

4.3 Test case in 3Di

In 3Di a Cartesian grid is used in combination with a sub-grid method, and can be refined by using the quadtree method. A Cartesian grid is often the most simple grid that can be used for simulating a numerical model. Figure 4.13a shows how the coarsest grid is defined for the U-bend in 3Di. Besides the grid, boundaries of the physical model are plotted in the same figure. This gives a clear idea what the disadvantages are of a Cartesian grid. To counteract these, 3Di has a subgrid that contains the bottom levels, see Figure 4.13b. Even though the grid is very coarse, with these pixels the depth is simulated more realistically. In grid cells that are partly white no value is defined, hence, it is not taken into account when calculating the volume of water in a cell.

Just as the grid size, the pixel size is also possible to choose. When simulating something in reality the minimum pixel size will depend on a available bathymetry resolution. In this simulation both the grid and pixel size are taken as a variable to investigate their effects. One of the things to keep in mind is that a quadtree must contain at least four subgrid cells.

Further, each refinement means that a grid cell is a quarter of the previous cell. Doing 4

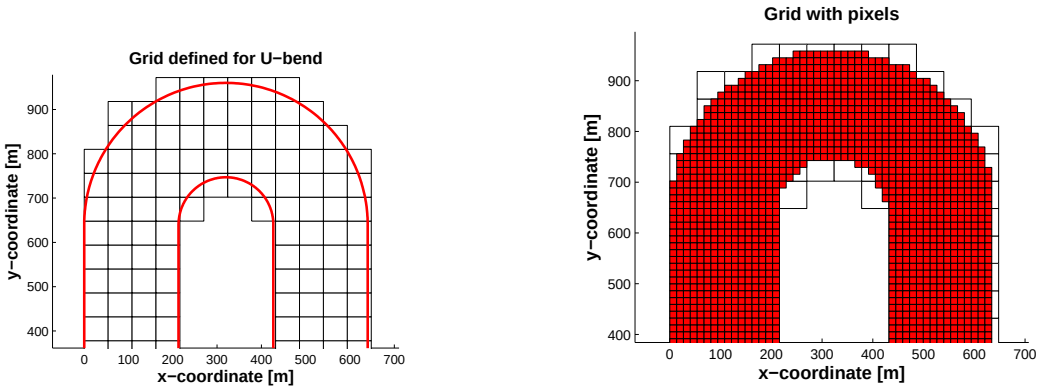

(a) Coarsest grid defined for U-bend

(b) Subgrid with pixels

Figure 4.13: Example of both grid and pixel subgrid in 3Di for U-bend

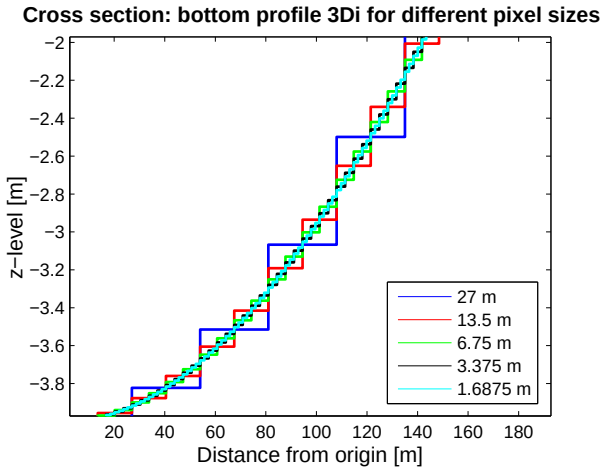

Figure 4.14: Part of cross section represented by various pixels for arbitrary $y-$value

refinements like the simulation in Flexible Mesh gives as value for the minimal grid and pixel size, 3.375m and 1.6875m. The coarsest grid size is 54m which must have a pixel with maximum size 27m. Using different pixel sizes has quite an influence on the bottom profile as shown in Figure 4.14. This figure displays a zoomed in part of an arbitrary cross section made for a certain y-coordinate between 0 and 640, hence, in the straight part.

4.3.1 Convergence

The starting point in simulating with 3Di is to investigate the influence of different pixel sizes. The grid size will be fixed at $dx = 54$m, while the pixel size will differ with the values as in Figure 4.14. It is expected that even with a coarse grid the results can be very appealing when the pixel size is very small. Results are given in Figure 4.15. With the minimal amount of pixels in a cell ($dx_p = 27$m) the results are not represented correctly. In the bend the water levels are fluctuating over the length, which is due to

the combination of both a coarse grid and subgrid. However, these fluctuations appear to vanish when the subgrid resolution is increased. This demonstrates that the pixel size has a great influence on the results, where a smaller pixel size results in a plausible result even though the grid is coarse.

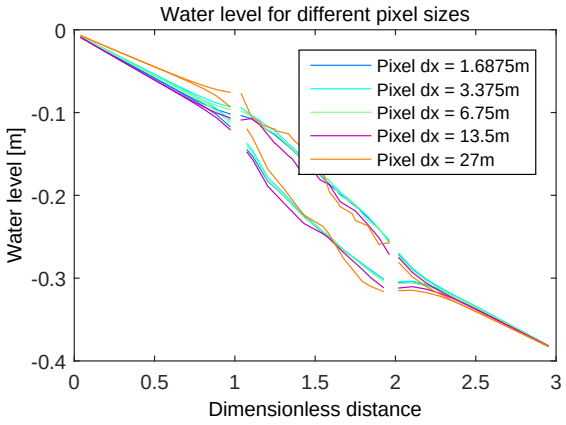

Figure 4.15: Water level for various pixel sizes with grid size $\Delta x = 54$m

The next step is varying the grid size. The pixel size is chosen as the smallest value, 1.6875m. In this way the same pixel size can be used for every grid size and is the latter the only variable. Figure 4.16 presents the results. The height dy is more or less chosen the same, but this means that dx is almost twice as large than in Flexible Mesh, since these are squared cells. In Section 4.4 both results will be compared.

Considering the results of only 3Di in Figure 4.16, it can be seen that the water levels are converging as well as the discharge seen in Figure 4.17. The graph in Figure 4.17 differs from other graphs seen so far. It consist of two $x-$axes, where one represents the grid size and the other the pixel size. Hence, both axes together present the combination of grid and subgrid used. It appears that the discharge converges, though one of the values seems a bit off. At $dx = 54$m with the smallest pixel size the discharge is suddenly a bit lower. Since the following values are increasing again, one would expect that this value would either be more or less the same or higher than the previous pixel size. The same occurs at $dx = 3.375$m in combination with $dx_p = 1.5875$m. However, this difference is minimal and might be the result of truncation errors.

4.3.2 Wiggles

Since there are some unexpected wiggles in the outer bend when using Flexible Mesh, it is interesting to investigate if the same happens in 3Di. In Section 4.3.1 no wiggles are found. Even not with the largest refinement factor which has been the case in Flexible Mesh. However, this does not mean that there are no wiggles closer to the outer boundary. Starting with the results of the largest refinement factor, the water levels are shown in Figure 4.18a. It is clear that there are again wiggles visible. However, they are not only present with refinement factor 5, but also with refinement factor 4 (Figure 4.18b). Although the other results are not presented, the results of refinement factor 2 and 3 are comparable with Figure 4.18. Without refinement (factor 1), the wiggles seem to be

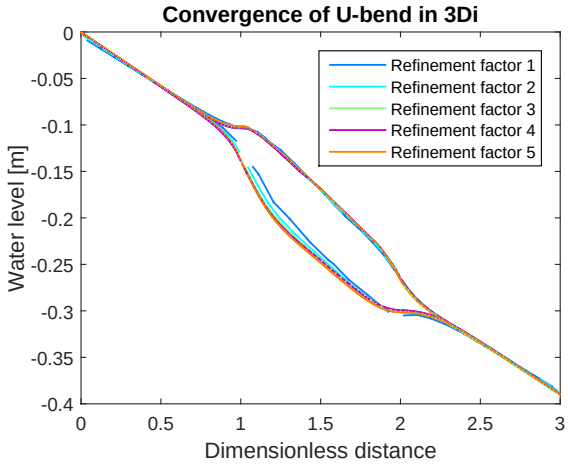

Figure 4.16: Water level for different grid sizes with a fixed pixel size $\Delta x_p = 1.7$m in 3Di

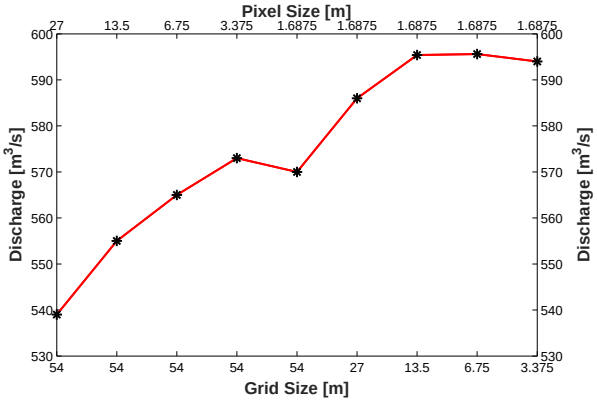

Figure 4.17: Discharge for various grid and pixel sizes. The bottom $x-$axis represents the grid size and the upper $x-$axis the pixel size.

absent. What is noticeable is the fact that these wiggles only appear in the most outer streamline and a bit at the inner streamline (although it represents itself there as missing gaps that are not easy to see in the figures).

In 3Di the grid consists of two layers, grid cells and pixels. Disadvantages of using grid cells that do not fit exactly over the physical model, as was seen in Figure 4.13b, are partly counteracted by these pixels. Parts of a grid cell have therefore pixels that have "no-values". These are not taken into account when calculating water volumes, which is calculated as the sum of all water depths times the pixel size. In a bend there are forces directed towards the outside of the bend resulting in a higher water level in the outer bend compared with the inner bend, see Figure 4.21. The outer grid cells in this bend do not fit exactly with this physical boundary, as said before. So there are quite a few pixels that have "no-value" in these cells, hence, these are not taken into account. If a relatively high amount of water has to be spread over a less number of pixels than in these pixels the water level will be higher than neighbor cells. This can explain the wiggles and why they are only in the most outer streamline. So even though both in Flexible Mesh and 3Di wiggles are present, the origin appears to be completely different.

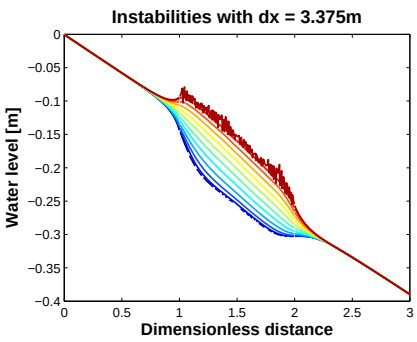

(a) Wiggles with grid size $dx = 3.375$m

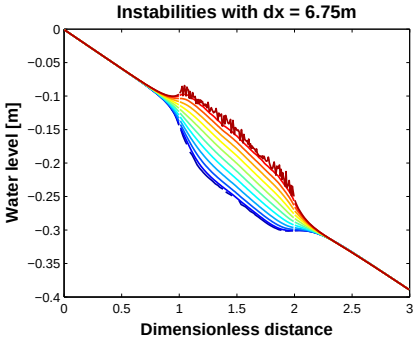

(b) Wiggles with grid size $dx = 6.75$m

Figure 4.18: Water levels in multiple streamlines where in the outer bend wiggles are visible

4.3.3 Local refinement

The next step is to apply local grid refinements in the domain, where the effect of the changed grid resolution is studied. Resolution of the grid changes half way of the domain, see Figure 4.19a. One of the simulations has a higher resolution at the left part, while the other at the right part. The refinements are done at both sides to investigate whether the results will differ when the water is flowing into a refinement in a bend or flowing into a coarser grid. To observe the results, the same streamwise polyline as in Section 4.3.1 is used to compare the water levels. In a perfect situation the transition from one grid size to the other has no influence on the results. Halfway the bend a transition is done by using quadtrees, explained in Section 2.2.2.

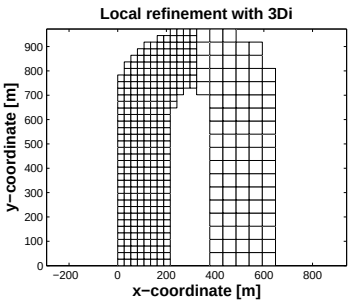

(a) Local refinement in 3Di

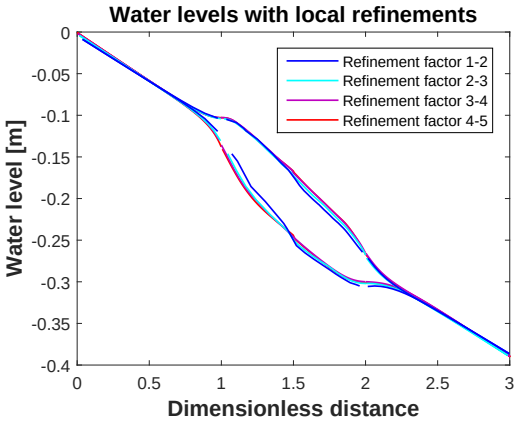

(b) Water levels using local refinement

Figure 4.19: Placement of local refinement with transition in the middle of the bend for 3Di and the water levels in the inner and outer bend when applying a local refinement.

In Figure 4.19 it can be seen that the water level, at the point where the jump from one grid size to the other is, deviates compared with a uniform grid. The results of the local

refinement with factors 2-3 and 3-4 are considered in these figures. These have also been studied for Flexible Mesh. Since refinement factor 1 is too coarse, and factor 5 takes too much time to obtain these results which do not differ much from factor 4. Starting with factors 2-3, Figure 4.20 presents the difference in water levels when one uses local refinement of only factor 2 or 3.

For example, the blue line in this figure is the result of subtracting the water levels using only refinement factor 2 from water levels using a grid as in Figure 4.19a with factor 2 and 3, with the refinement on the left side. In order to see the correct differences over a polygon with local refinement, one has to follow two lines. The first half of the distance one of these lines needs to be followed and the second half the other line. So, if the refinement is done at the left half, one looks first at the blue line and halfway to the light blue line.

Refining either left or right does not matter much, since the lines are both horizontal and vertical symmetric. Important is the observation that differences appears to increase starting from the incoming boundary up to where the local refinement begins. After this point where the grid size is changed, these differences shrink to the point where a boundary is met to zero.

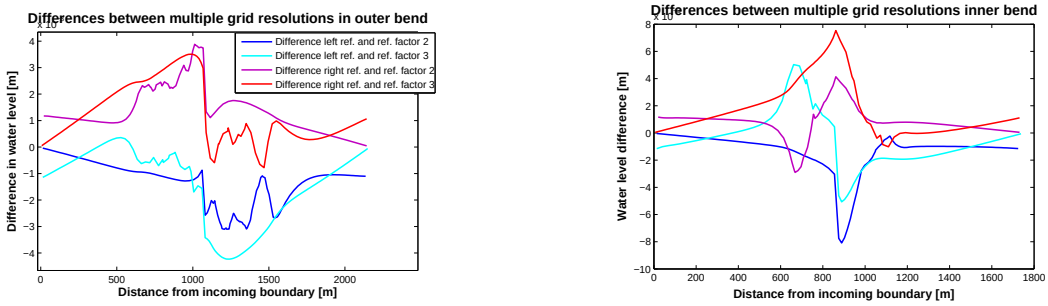

(a) Outer bend

(b) Inner bend

Figure 4.20: Comparison of water levels between local refinement 2-3 and uniform grid with factors 2 and 3 in 3Di

The order of difference is also different when looking at the inner or outer bend. In the outer bend there is a maximum difference around 4mm, while at the inner bend this is 8mm. Figure 4.19b already showed that the influence of a refinement is larger in the inner bend than outer bend. Comparing water levels of a cross section half way the bend as in Figure 4.21 shows that there is a small difference between using no refinement or local refinement. Thus, using a refinement gives quite some other results than using no refinement.

Using a grid with higher resolutions results is smaller deviations, both locally at the jump and over the entire domain. Figure 4.22 presents the results with a refinement factor 3-4. These figures are composed in the same way as Figure 4.20. So, wiggles that are seen in these figures can be neglected. They can appear because water levels of different grid resolutions are subtracted from each other. These results differ both in shape as in order of differences with the previous results. The latter is smaller, which is understandable. One would expect better results with a smaller grid size. Further, the shape of these lines seems better in some cases. When the refinement is on the right side (red line and purple

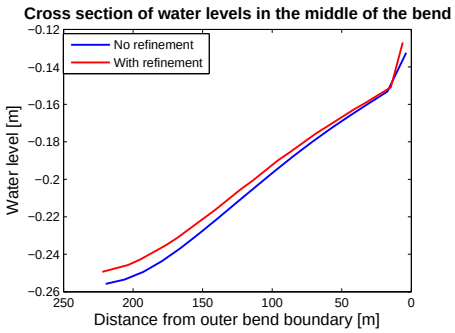

Figure 4.21: Water levels of the cross sections in the middle of the bend

line) it results in a line that stays much closer to the y-axis (around zero-point) for a longer time before it suddenly rises. With a refinement on the left side this is not the case and the results are more as in the previous example. From this it can be concluded that a finer grid gives less errors when refining the grid and in this case it appears to matters at which side the refinement is done.

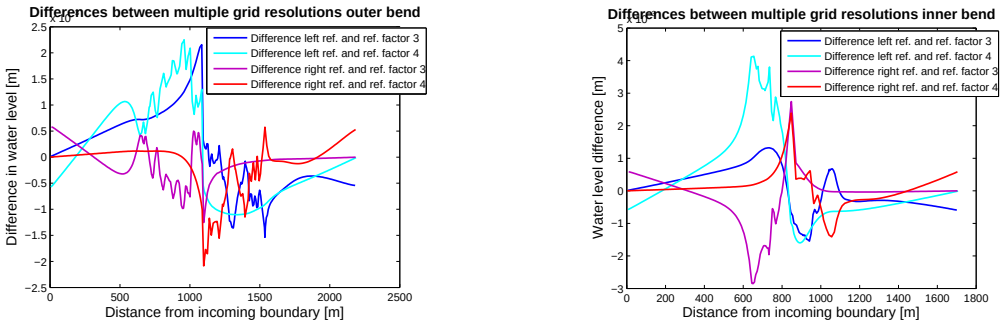

(a) Outer bend

(b) Inner bend

Figure 4.22: Comparison of water levels between local refinement 3-4 and uniform grid with factors 2 and 3 in 3Di

4.4 Comparing results from both programs

With both packages investigated separately, this section will combine the results. First the results of both packages are compared without applying local refinements. Hereafter the results in streamwise and transverse direction are compared when local refinements are applied. In the end a comparison of the wall clock times of both packages is performed.

4.4.1 Comparison without refinements

The first step is to compare the results from both packages without applying local refinement. Figure 4.23 presents the values of measured discharge in a cross section. Both have already been given separately in the previous sections. There is some difference between these values for each refinement factor, but these differences get higher when the

resolution gets higher. Whereas the discharge in Flexible Mesh seems to converge to a value around 605m^3/s, it reaches a value of 595m^3/s in 3Di for refinement factor 3 and 4 where after is drops a bit when the factor is higher.

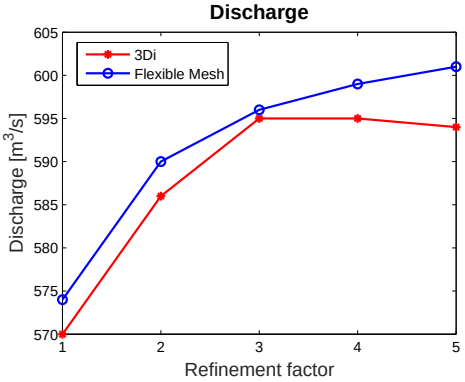

Figure 4.23: Equilibrium discharge convergence in Flexible Mesh and 3Di

In order to estimate the error in the numerical estimation, the Richardson Extrapolation can be used (Vuik et al., 2006). Assuming that the error can be approximated by

$$M - N(dx) = K_1 dx^{a_1} + K_2 dx^{a_2} + ..., \tag{4.1}$$

an estimation of a_1 can be obtained. Since, with dx small enough all terms on the right hand side, with exception of the first, can be neglected. Letting M be the exact solution, and N(dx) the numerical estimation with a grid size of dx, the error can be estimated. Vuik et al. (2006), Section 3.6 explains this in more detail. The exact value is approximately 600m^3/s for Flexible Mesh, and 607m^3/s for 3Di. However, the convergence of 3Di makes the Richardson Extrapolation not quite suitable to use. Instead of increasing with every lower grid size, it decrease after a certain refinement factor. For this reason, the refinement factors 1, 2, and 3 are used in order to estimate M, the exact value.

For further comparison refinement factor 3 is used, since for this factor the discharge are almost the same. If this is not the case, it would be harder to make a fair comparison. For this refinement the water levels are observed in a streamwise direction. They are also researched in the transverse direction, however, this is treated in Section 4.4.3, where it is also analyzed with a local refinement.

Comparing the water levels, which are illustrated in Figure 4.24, there are no large differences. The lines are close together, perhaps at some places a few millimeters difference. The main distinctness is in the streamlines closest to the inner and outer bend. 3Di contains the instabilities which were discussed in Section 4.3.2, whereas Flexible Mesh has smooth lines for each streamline. When a higher resolution was chosen, the results of Flexible Mesh would also contain instabilities close to the outer bend as seen in Section 4.2.2.

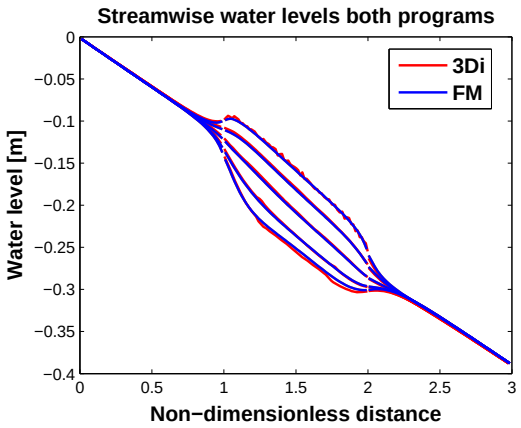

Figure 4.24: Streamwise water levels for both FM and 3Di with a refinement factor 3

4.4.2 Streamwise differences in local refinements

In previous sections the influence of applying local refinements were studied for each package on its own. In this section the results are combined. To get a clearer overview these results are presented as follows. The water levels that are illustrated in Figure 4.25 are taken at the middle of the width of the simulation. Each line presents the difference of the results with local refinement and the one without. Considering the blue line of Figure 4.25a, this line is composed of two parts. The first half of the line is the outcome of subtracting the water level of the results with refinement factor 3 with the results with local refinement 3-2. While at the second half of the line the results with refinement factor 2 are subtracted from the results with local refinement 3-2. Thus, one line illustrates the differences of the results with local refinements with the results without refinement.

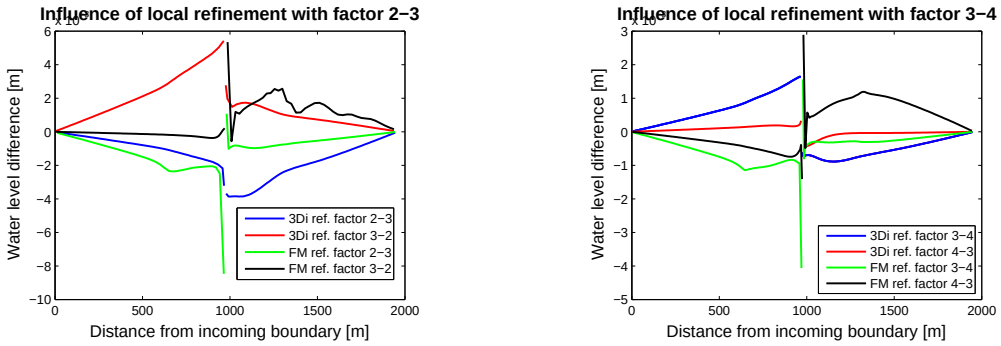

(a) Refinement factor 2-3

(b) Refinement factor 3-4

Figure 4.25: Differences in water level for both FM and 3Di between a uniform and local refined grid for multiple refinement factors

For both packages applies that a higher resolution leads to a lower difference. This can be seen in the order of difference in both figures, but also for each line this is visible. A lower difference can be seen when the local refinement applies a higher resolution. Whether this is on the right or left side does not matter. Observing each line separately shows that one half of the line has a noticeable smaller difference, the part with the highest resolution.

A final point to notice is the fact that when applying a local refinement in Flexible Mesh result in a more sudden peak at the place of refinement, while 3Di gradually obtains a higher differences.

4.4.3 Transverse differences

Comparing the transverse water levels for both packages, with and without local refinements, shows only small differences between the results. Figure 4.26 presents the cross sections that are used in the upcoming figures. Cross section 1 is represented by the red line most right and under, cross section 6 most left and under. In between are cross sections 2-5 in the order of going from 1 to 6.

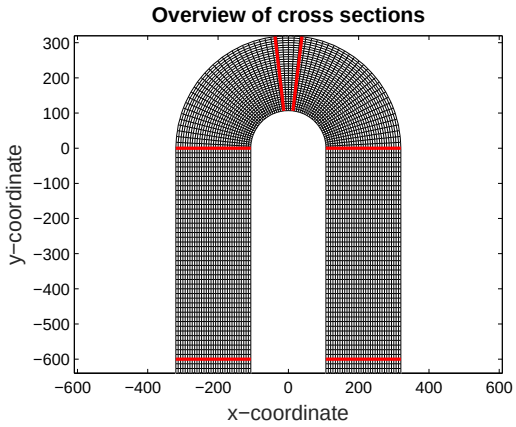

Figure 4.26: Overview of cross sections in U-bend

First the transverse water levels are compared without refinement. The same refinement factor is used as in Section 4.4.1, factor 3. With this factor the discharge is for both packages almost equal. Results for each cross section are presented in Figure 4.27.

Noteworthy is the fact that in cross section 1 the water levels in 3Di are higher, whereas it is the other way around in cross section 6. At the cross sections in between one sees the transition of this. In this transition the differences are a bit higher between the two packages, of the order 10^{-3}m in cross section 5 for example. In cross section 2, 3, and 4 these differences appear mostly in the inner bend. As if forces in the outward direction are a bit higher in 3Di than in Flexible Mesh.

The second part of looking at transverse water levels is applying local refinement. The right half of the bend has refinement factor 3, and the left half factor 4. Again, differences between both results are minimal. The shape of these lines are almost the same as without refinement. Since refinements are applied in the streamwise direction this would be expected.

4.4.4 Wall clock time

The previous sections about convergence showed that refining the grid gives a more precise result. However, using a grid with a higher resolution results in a longer simulation time.

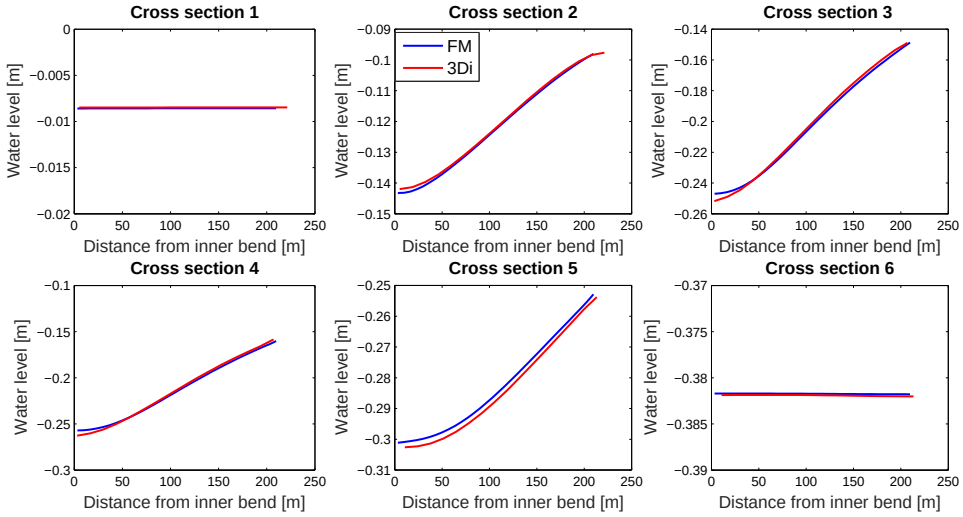

Figure 4.27: Transverse water levels with no refinement for both FM and 3Di in the indicated cross sections of Figure 4.26

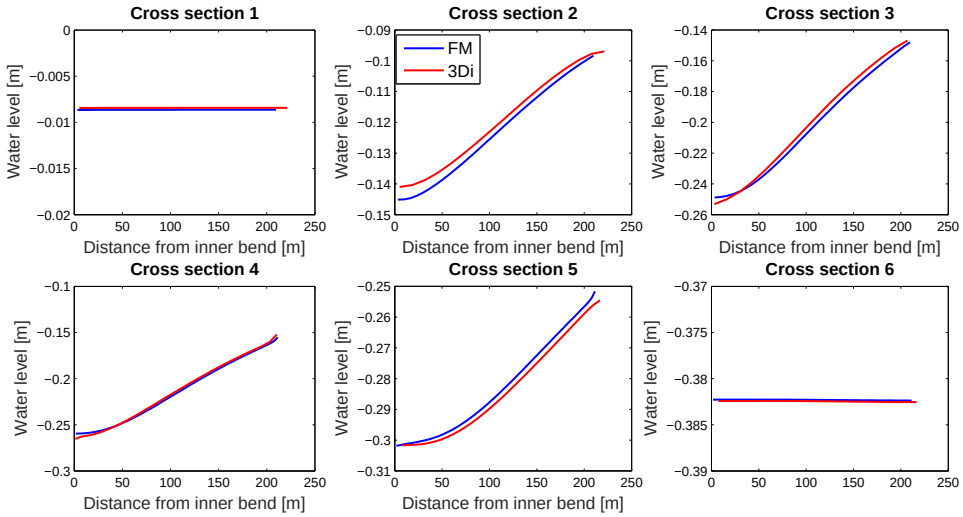

Figure 4.28: Transverse water levels with local refinement for both FM and 3Di in the indicated cross sections of Figure 4.26

This section examines the wall clock time of the simulations done in the previous sections for both Flexible Mesh and 3Di. These times are measured in seconds and do not include the time of plotting and writing the files. The simulation time is for each run equal to 64800 seconds (18 hours). This time is chosen such that the flow has the possibility to become steady and that effects of spinning time are not visible.

The blue dots in Figure 4.29a present the wall clock time of each simulation that is done in Flexible Mesh. The number of refinement factor gives how often the grid is refined. When it is not an integer number the grid is only half refined on the left half of the bend. Thus, refinement factor 1.5 represents the grid in Figure 4.8a. The red stars represent the

wall clock times of simulations done in 3Di. Before observing the results one note should be made beforehand. The time step in each program is determined in another way. In Flexible Mesh the time step is determined from the maximum CFL number that is set manually. Its standard value is 0.7. In 3Di one has to set the time step manually. Since the grid cell sizes are for each refinement larger than in Flexible Mesh, the same time step is taken but rounded up. So, for example, if in Flexible Mesh the time step is 25.8s, it is 30s for 3Di. For each refinement this is done. Results of the total wall clock time for each simulation is illustrated in Figure 4.29a. Since the number of time steps differs per program, the wall clock time divided by the number of these time steps is also compared. This gives the average wall clock time that is needed for each step in Figure 4.29b. The lines in each of these figures are fitted lines through the dots and stars.

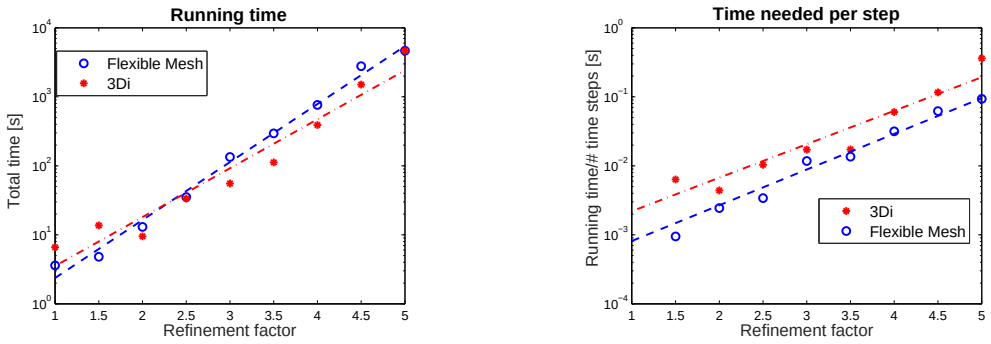

(a) Wall clock time

(b) Wall clock time divided by total number of time steps

Figure 4.29: Computational time for all resolutions in 3Di and FM

The wall clock times for FM are higher than in 3Di after refinement factor 2.5. Before this factor it is the other way around. However, comparing the wall clock time divided by total number of time steps results in the fact that 3Di is relatively slower per time step than Flexible Mesh. It should be noted that comparing wall clock times is not always precise. Running a simulation on different computers or using other programs at the same time result in a higher or lower wall clock time. Thus, these wall clock times can be a bit inaccurate.

One of the other things that these wall clock times do show is the fact that it is easy to see what the costs are if one uses a very fine grid. Thus, a higher resolution results in a longer wall clock time. Refining only part of the bend results in less running time. So if there are parts that are interesting to look at it will pay off to only refine these parts, keeping in mind the errors of a refinement as shown in the previous section.

4.5 Conclusion

While the complete thesis focus on the multiple choices, which are grid resolution, turbulence models, and boundary conditions, this chapter focus on the grid resolutions only. Of course, for each simulations boundary conditions are needed, in this case *overgenomen* from Stelling (2012). For both 3Di and Flexible Mesh multiple grid resolutions have been

used, either for a uniform grid or a grid with local refinements. For each grid resolution the computational time, accuracy and the representation of physical processes should be considered. The latter will not be taken into account for this part.

The convergence of 3Di and FM differs slightly from each other. Flexible Mesh appears to converge to a value higher than 3Di. However, based on the Richardson extrapolation this value should be lower. Furthermore, 3Di seems to have reached its limit at a certain refinement factor. However, after this factor it diverge from this limit value. Though it differs only minimal with the value from the previous refinement factor it might be the result of truncation errors.

Applying a local refinement in the simulations resulted in local differences at the transition of a coarse to fine grid. It is also seen that the there are small water level differences over the entire domain visible when comparing the simulations with a local refinement to ones with a uniform grid. These differences are only of the order $\mathcal{O}(10^{-3})$, hence, are not that significant.

With this second test case it has become clear that both Flexible Mesh and 3Di work in a different way. The main difference is the grid, which has a great influence on the results. While working with this test case some questions came up that were not possible to answer. Some further research is needed if one wants to solve these. One of the uncertainties is the wiggles in Flexible Mesh that became visible in Section 4.2.2. With a higher resolution wiggles arise near the outer bend without explanation. The CFL number has a limited value which cannot be exceeded. Since the wiggles are numerical and not physical, something in either the core goes wrong or some values are not correct that are entered manually.

The other observation that is difficult to understand, is the convergence of discharge when simulating in 3Di. With refinement factor 3 and 4 it reaches its maximum discharge that is measured, while with refinement factor 5 it goes down a bit. If it would be converged one would expect the same value and otherwise a bit higher, but not a lower value. When varying the pixel size the same happens. As if with a larger pixel or grid size the discharge is overrated. In other test cases there is data available from experiments to compare the numerical values with. This should give a clear overview whether 3Di or Flexible Mesh gives a better value for the numerical results. If this happens in other cases as well, then these values can be used to obtain more insight.

Chapter 5

Flow over weir

Before simulating part of the river Elbe with Flexible Mesh and 3Di, another test case is done. A straight channel with a weir is considered. This weir is set up with two different methods. The first method uses a supergrid model, where the weir is represented in the bathymetry. The second method consists of a subgrid model. With an extra input file the weir can be placed anywhere and a special numerical scheme is applied for horizontal advection. With an analytical solution, where hydrostatic pressure is assumed, the results of both 3Di and Flexible Mesh are compared. With these results a convergence test is done, followed by refining the grid locally at various locations. This chapter ends with a conclusion and discussion that can be used for the simulation of the river Elbe. These simulations are performed with D-Flow FM Version 1.1.148.41897, and 3Di - subgrid Version 0.1.1.1958

5.1 Flow geometry

In order to study the influence of the grid refinement on the results, the set up of this case is as simple as possible. Hence, friction and viscosity are not taken into account. Furthermore, the bottom does not have a slope and the cross section of the channel is rectangular. The water flows due to the difference in water levels at the boundary conditions. The water level on the left side of the channel is fixed at 3m, while at the right side it changes in time. Its starting point is 2.95m. Each time interval of 3 hours it goes down by 0.05m until it reaches 2.75m. This results in different submergence degrees, hence, different flow regimes. The interval for each water level is chosen such that the model has enough time to become steady. Different flow regimes can be established with the Froude number, which is a dimensionless number that describes the ratio between inertia and gravitational forces.

$$Fr = \frac{U}{\sqrt{(gh)}} \tag{5.1}$$

with U the velocity, g the gravitational acceleration and h the water depth in the open channel flow. If $Fr > 1$ the flow is supercritical (fast rapid flow), while if $Fr < 1$ it is subcritical (slow flow). With a submergence degree of 0.8 and 0.75 the flow on top of the weir is supercritical. For the other degrees this is subcritical.

In the middle of the channel a groyne is placed. This can be done for both packages in two different ways. In one of the options, a groyne is represented in the bathymetry, while for the other option an extra input file is needed with the location of a fixed weir and the crest height. The energy loss is then calculated at that location with a special numerical scheme. When a groyne is captured by enough grid cells, and it is represented in the bathymetry it is called a supergrid model. Usually a minimum of three grid cells on the crest is needed to solve the hydrodynamics in a detailed way. Otherwise it is better to use the extra input file, which is called subgrid modeling. When using 3Di, a third option is used which is subgrid pixel modeling. As seen in the previous chapter, a minimum of four pixels in one grid cell is needed. With these pixels the volume inside a grid cell can be calculated more precisely. The influence of these pixels will become more clear in Section 5.3, where the size will vary in each model.

It should be noted that when a weir is placed exactly in the middle of a cell, it is placed on both sides of the cell instead of just one, see Figure 5.1. A fixed weir is not solved at the given location, but it is placed near the closest face of a cell and solved there (Deltares, 2015a), see Figure 5.1. This is done so that no computational cells are cut by a weir, which makes the computation easier. In this case, it resulted in an error of 30% when the weir is placed in the middle of a cell with $dx = 12$m. So, if by accidence the weir is placed in the middle of a cell, this results in quite an error. This can be fixed by replacing the weir just a few centimeters. This will result in the top figure of Figure 5.1 instead of the bottom figure, where the cell is surrounded by the fixed weir.

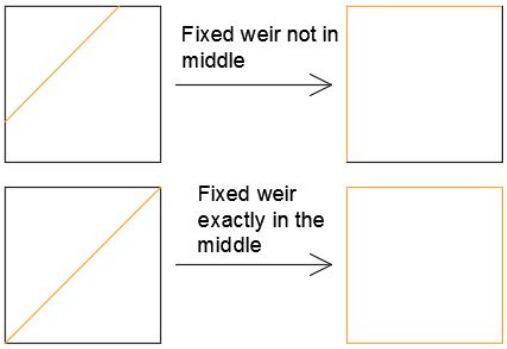

Figure 5.1: Example of how a fixed weir is located to the cell faces

The groyne that is used, has a crest height of 2 meters, a crest width of 3m and is in total 15m long with a slope of 1:3. Figure 5.2 shows how the groyne is presented in both Flexible and 3Di when using a grid size of $dx = 6$m and $dx = 3$m and how it is in reality (black line). In this figure the minimum amount of pixels is used in 3Di to represent the bathymetry. If a higher resolution is available of the bottom one can use more pixels per grid cell. Due to these pixels the bottom of 3Di is better represented than when using Flexible Mesh. Another difference between the two figures is that the figure of Flexible Mesh contains two lines, a blue and red line. The latter is used in calculations for the

volume, while the flow area and friction term depend on the values of the blue line.

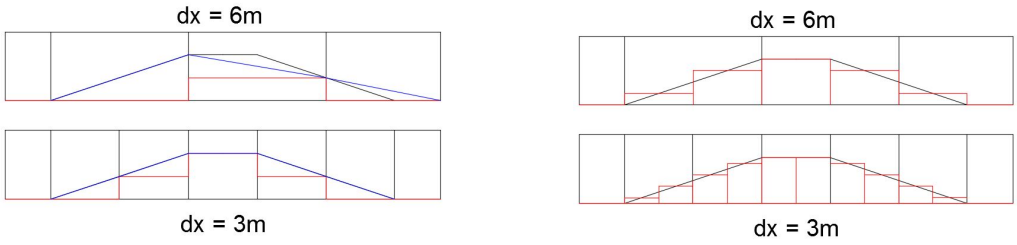

(a) Groyne representation FM

(b) Groyne representation 3Di

Figure 5.2: Groyne representation for various grid sizes in FM and 3Di

Weirs can be distinguished in roughly two types, a short-crested and broad-crested weir. With the latter streamlines on top of the weir have enough space to become parallel to each other, which gives that a hydrostatic pressure distribution (linear pressure relation $p = \rho g h$) can be assumed. In case of a short-crested weir the streamlines stay curved, hence, this kind of pressure distribution is not valid. If one does assume this distribution, then the velocity on top of the crest can be underestimated in case of a constant discharge. To decide which type of weir it is, one has to calculate the ratio H_w/L, where H_w is the energy head above the weir and L the width of the crest. Although it differs per source between which values this ratio should be, the smallest upper limit found so far is (Boiten and Pitlo, 1982), $0.075 \leq H_w/L \leq 0.45$. It is expected, based on analytical calculations, that the energy head is around $1 - 1.1$ on top of the weir. This would give, in case of $H_w = 1.1$, $H_w/L = 0.36$, which is below the upper limit. However, since it is close to the upper limit and per source this upper limit is different, it might be that this value is too high in order for the hydrostatic pressure distribution to be valid.

In order for the hydraulic assumption to be valid in the simulation, at least 5 cells on the crest of the weir are needed in order to create straight streamlines. For this case only one of the grid sizes that is used, satisfies this condition. It is also recommended to use this amount of cells on the crest in order to obtain a accurate answer (van Kester, 2015) In the maintaining part of this chapter simulating obstacles in the bathymetry will be called supergrid modeling to make it easier to distinguish between the two types of modeling. However, usually it is supergrid modeling if at least 5 cells on top of the crest are used to simulate the obstacle.

5.2 Convergence study

Starting point for this test case is a convergence study. In both cases the same sizes in grid cells are used: $dx = 12$, $dx = 6$, $dx = 3$, $dx = 1.5$ and $dx = 0.75$ meter. For 3Di some extra runs are done with different pixel sizes. These pixel sizes for grid cell $dx = 12$m, could differ from $dx_p = 6$m (largest value) and $dx_p = 0.75$m (smallest value). First comparisons are done with a fixed pixel size of $dx_p = 0.75$m (or $dx_p = 0.375$m if $dx = 0.75$m) and a varying grid size for 3Di and FM. In Section 5.2.1 pixel sizes will be varied as well. Results of the discharges for the convergence study are given in Figure 5.3. When using a grid size of $dx = 3$m, or smaller, the groyne is represented correctly in

length and shape (for friction and flow area). Of course, this groyne is chosen such that it fits precisely in these cells. In this case the crest of the groyne is always on a cell face. This gives a better idea of the influence of the grid cells around a groyne or other obstacle. In the next section the results are compared if the groyne is placed 6 meters further to the right. When modeling a random river, the grid is usually not perfect aligned around obstacles, so this will show how the placement of a grids influence the result.

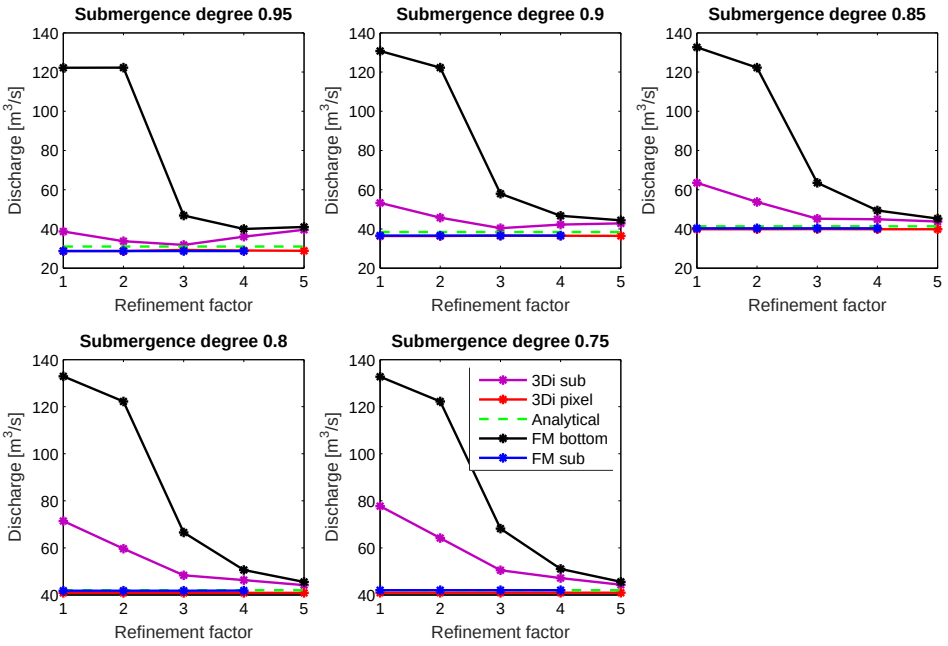

Figure 5.3: Convergence of discharges in FM and 3Di using a subgrid or supergrid model for various submergence degrees

It can be seen in Figure 5.3 that though the models converge, they conerge to another value than the analytical value. Considering the figure that belongs to a submergence degree of 0.95, it can be seen that it appears that the lines belonging to a supergrid model converge to the analytical value. However, the discharge of the purple line that belongs to the simulations in 3Di, increases again when a higher refinement factor than 2 is applied. The same seems to happen in FM (black line), although it is almost negligible and it happens with a higher refinement factor than 4. Both cases appear to converge to another value than the analytical value. In order to find the cause, the most important processes of this case need to be known. With a sudden decrease in the bottom there will be a detachment point, which means that there will be energy losses. Thus, we will take a closer look at the energy head of this model in the $x-$direction. Roughly the model can be split into three parts, before the weir, on top of the weir and behind the weir. For the first two parts energy conservation should apply, while for the last two parts it is momentum conservation. In the figure below the energy head is presented. At $x = 162$, the slope of the weir starts until $x = 168$, where the crest begins. At $x = 171$ an expansion starts until $x = 177$. From here on the bottom will be flat again.

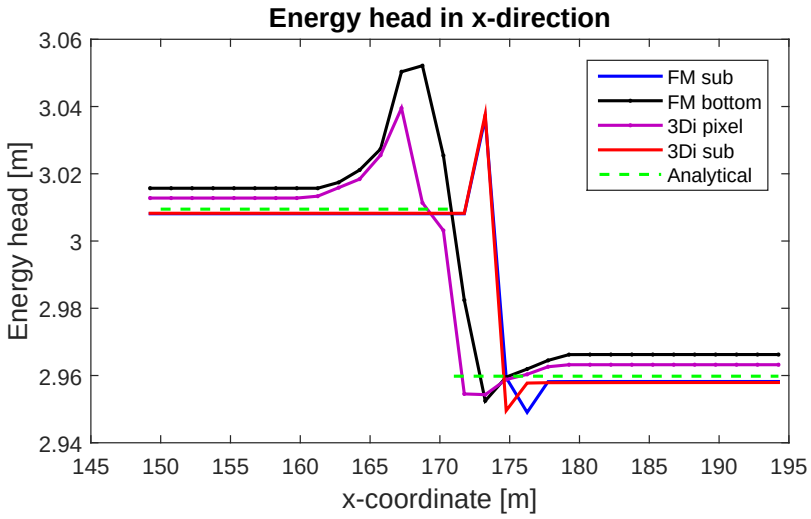

Figure 5.4: Energy head in FM and 3Di using a subgrid and supergrid model for $S = 0.95$

The energy head is calculated as follows,

$$E = h_1 + \frac{u_1^2}{2g} = h_2 + z_c + \frac{u_2^2}{2g}, \tag{5.2}$$

where h_1 and u_1 are respectively the water level and velocity in front of the weir, h_2 and u_2 are on top of the weir and z_c is the crest height. Both of the super- and subgrid models the energy head is plotted, together with the analytical value in Figure 5.4. Results of this figure are from simulations with $dx = 1.5$m.

Though it is physically not possible, an energy increase is seen for all types of simulations in Figure 5.4. Immediately it can be seen that the energy head has an increase at the point where the weir starts. As said before, between part 1 and 2 there should be energy conservation, so both packages introduce energy. For both packages it can be due to the discretization fo the advection term. According to Stelling and Duinmeijer (2003) an increase of energy can occur, when the wrong type of conservation is used. Over the entire area a conservation of momentum is assumed, where at some points, such as contractions, another balance is needed. When using the subgrid method, another advection scheme will be locally used. It is explained in Section 5.1 that fixed weirs are placed to the nearest face of a cell. At this face conservation of energy is applied between the two neighbor cells instead of momentum. The local energy loss after the weir is calculated with the velocities in front and after the weir (Deltares, 2015a). For Flexible Mesh and 3Di the energy heads of subgrid modeling are quite the same. Hence, in both programs a certain energy increase can be seen, even though energy conservation is applied. This is due to the interpolation of velocities that is done. Both Flexible mesh and 3Di use a staggered grid, hence, water levels are solved on the cell center and velocities on the cell faces. When these results are plotted the velocities are interpolated to the cell centers. Resulting in having both velocities and water levels at the cell centers. Interpolating the velocities can result in values that are not correct with the water level in the cell center, which results in an over- or underestimated energy head. Stelling and Duinmeijer (2003) has done research about these staggered conservative schemes.

Another noticeable point is that for each grid size when modeling the groyne with a fixed weir (subgrid), the discharge is almost the same. Differences are of the order 10^{-2}, hence negligible. For both 3Di as Flexible Mesh this is the case. While the results of modeling the weir in the bathymetry is dependent on the grid size, the subgrid method is always applicable since it is independent of the cell sizes. Usually the resolution of a grid in rivers is never high enough to capture obstacles such that supergrid modeling is possible. Thus, in these cases it is better to implement fixed weirs. In order to get more insight in the energy losses and gains, three other variations of the previous cases are simulated. Each of them are explained together with their results.

Groyne with a wider basis

The first variation of the previous model is a groyne with a variable width. Together with the original width, five weirs are simulated. Each weir has the same height, but the width, hence slope, is different. With a lower slope the velocity differences between two cells in the $x-$direction are lower, hence, the advection term becomes smaller for each cell, since the cell sizes will be the same. This might result in a lower energy increase than before.

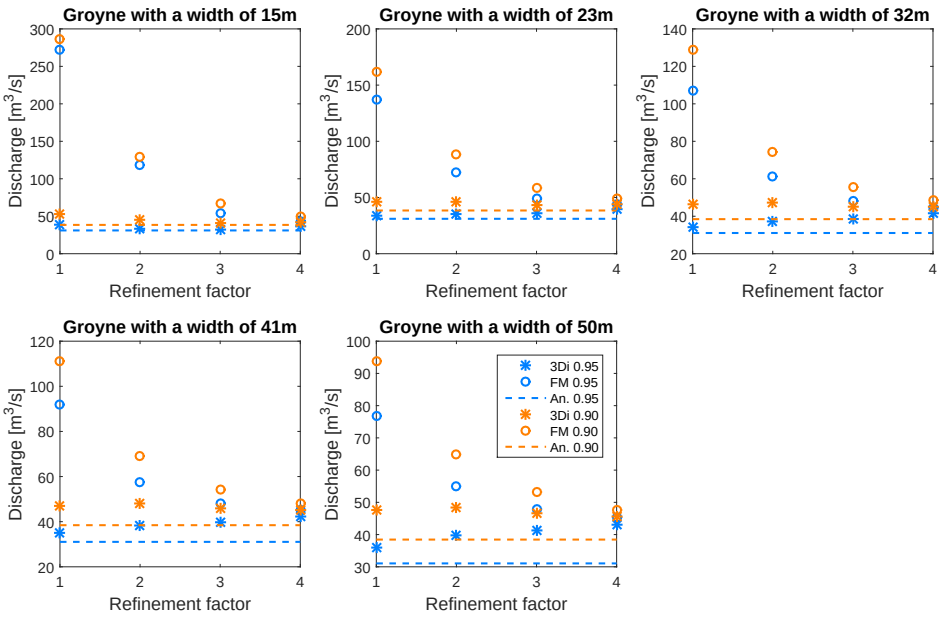

Figure 5.5: Convergence of discharges in FM and 3Di with an obstacle represented in bathymetry for $S = 0.95$ and $S = 0.9$ for various width

While the results appear to converge faster for a groyne with a wider basis, this variation does not have much influence on the energy increase. The results are obtained with a submergence degree $S = 0.95$ and $S = 0.90$, to see if this variable has some influence on them. In Figure 5.3 it is seen that the convergence is different between these two submergence degrees. With $S = 0.95$ the discharge decreases up to a certain refinement factor, where after it increases. As said before, with a wider groyne the slope is smaller. Additional to this, more grid cells capture the groyne when it is wider. As a result the

convergence of the discharge goes faster than when having the original width, see Figure 5.5. The presumption that the values seem to converge to another value seem true for both submergence degrees. For $S = 0.95$ the discharge converges to a value around $Q = 44\text{m}^3/\text{s}$, both for 3Di and Flexible Mesh, which is about 40% off with the analytical value. Since the discharges of 3Di increase even more than before, it can be expected that the energy level increases as well. Figure 5.6 presents the energy heads of both Flexible Mesh and 3Di. For 3Di the energy increase is mostly spread over the entire length. Hence, the velocity is overestimated for the whole model. On the other hand, for Flexible mesh the peaks decreases a bit. Over most of the length the energy does not depend much on the groyne's width. Although varying the width has some influence on the energy head, it does not prevent the energy increase.

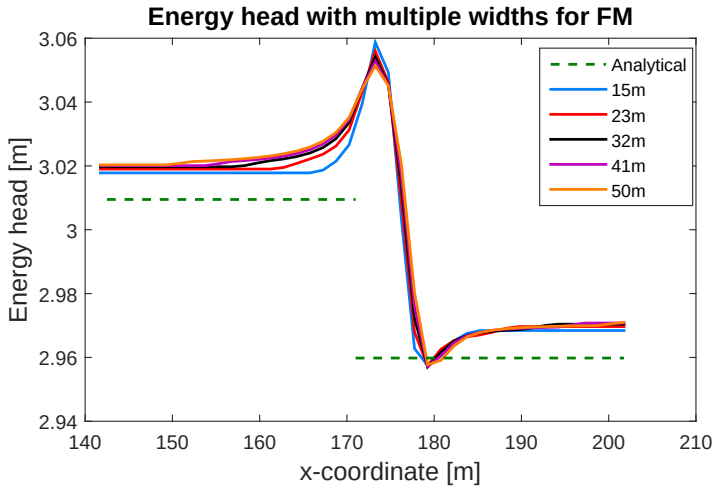

(a) Flexible Mesh

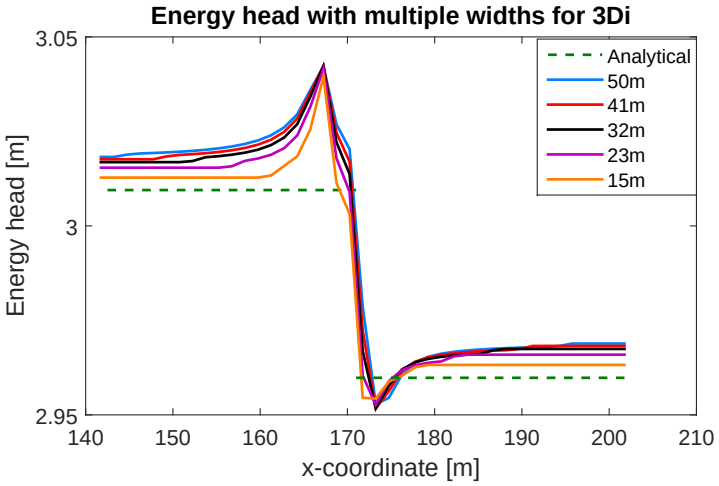

(b) 3Di

Figure 5.6: Energy head in FM and 3Di with an obstacle represented in bathymetry for $S = 0.95$ and $S = 0.9$ for various width

Groyne with a sudden expansion

This case is almost the same as the previous variation, hence, there are multiple widths of the weir simulated and the height is the same. The only difference is that the weir has a sudden expansion instead of gradually expanding slope. Whereas the previous simulations investigated the effect of a slope's steepness, this case will take into account the effects of a sudden expansion. Usually when experimenting with flow over a weir, it ends with a sudden expansion. The analytical value is based on this type of weir. Using this sudden expansion results in a simulation that is more similar to the analytical approach.

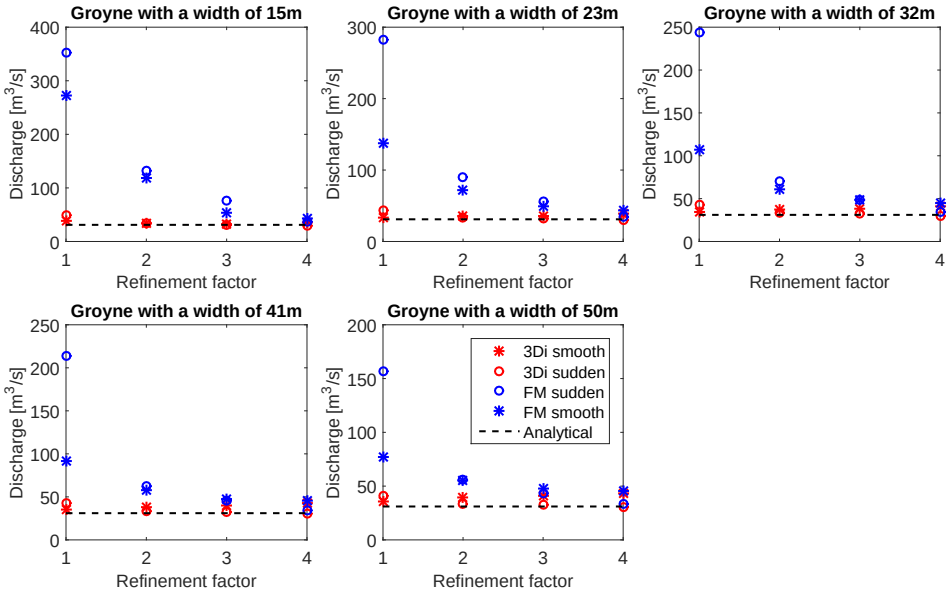

Figure 5.7: Comparison of convergence of discharge in FM and 3Di for an obstacle with a smooth or sudden expansion for $S = 0.95$ and varying width

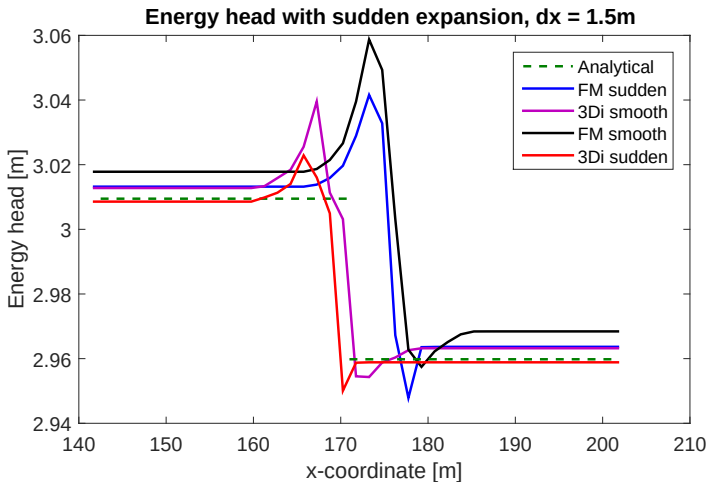

Figure 5.8: Comparison of energy head in FM and 3Di for an obstacle with a smooth or sudden expansion for $S = 0.95$ and varying width

Having a sudden expansion agrees more with the analytical values than the other simulations, considering the discharge. Comparing the smooth and sudden expansion, it can be seen (especially with a width of 50m) that the discharge converges more to the analytical value for both packages. For a refinement factor of 4 the difference between two numerical values (smooth and sudden) is about 40% ($(x_{smooth} - x_{sudden})/x_{smooth}$). Considering the energy over the length, it can be seen that the peak is smaller for a sudden expansion than a smooth expansion. Not only this peak is a bit smaller, but the energy head over the length is lower with a sudden expansion. Both for Flexible Mesh and 3Di it is closer to the analytical value. Even though there is still an increase of energy locally at the groyne, hence, the velocities and/or water levels do not agree with the analytical values, they are more agreeable over the rest of the length. Physically it is expected that more energy is lost with a sudden expansion. In these cases, the energy losses in front and after the groyne are the same everywhere, but locally at the groyne from the highest to lowest energy peak, energy losses are higher with a smoother bottom. With the depth-averaged equations in a simulation it is more difficult to distinguish depth variations, which can results in a under or overestimation of energy loss.

Combination of fixed weirs and use of bathymetry

Whereas the previous variations were a continuation of the research of energy increase, this case will combine both fixed weirs and usage of bathymetry (subgrid and supergrid). When simulating rivers its bathymetry is either interpolated in the net nodes (Flexible Mesh) or it is needed in a special file where the pixel sizes and heights are defined(3Di). Either way, the groynes and other obstacles are present in the grid. With a coarse grid these obstacles can be too small to be noticed for the cells, hence, a subgrid model is needed to correctly represent these. In case of a finer grid it is possible that these obstacles are better represented by the grid. Local refinements can already result in a better represented obstacle in the bathymetry without having to refine the entire grid. In some cases one also wants to use a subgrid model to obtain energy conservation, as energy conservation is not valid otherwise. For both a coarse and fine grid both types of modeling are used to investigate the effects of this combination. The fixed weir is positioned at two different places when combining bathymetry with subgrid modeling. In one of the simulations it is placed at the first face of the cell where the crest begins. In the other on the second face. For $dx = 1.5$m this gives that the face is placed at the beginning of the crest and in the middle. For lower resolutions they are placed at the end or even on the slope after the crest.

Figure 5.9 shows that the equilibrium discharge, when combining both a supergrid and subgrid model, depends on the grid resolution and placement of the fixed weir. This is especially the case for 3Di. Results of both programs when combining both models gives quite different results. For Flexible Mesh the differences between placement of the fixed weir is not that significant, but the discharges for 3Di are much lower than expected. Placing a fixed weir at the beginning of the crest gives for both packages results that are near the values of only a subgrid model. Placing it at the second cell discharges are suddenly below $20\text{m}^3/\text{s}$ in 3Di. The main difference between these programs are the pixels that are present in 3Di to calculate the volume more precise. Whereas for Flexible Mesh the volume is calculated with the lowest bottom point in a cell. Thus, in Flexible Mesh

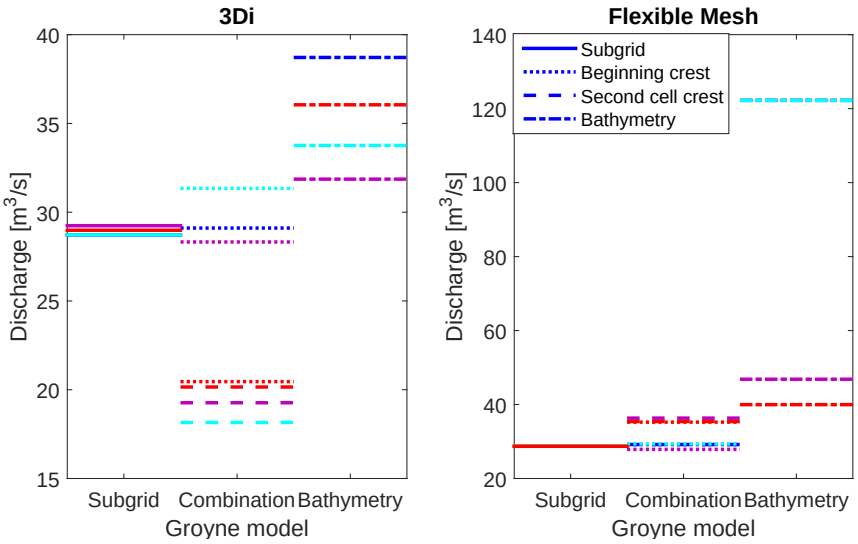

Figure 5.9: Discharge for groyne with a combination of subgrid and bathymetry compared with both models separately: blue = refinement 1, purple = refinement 2, light blue = refinement 3, red = refinement 4

the volume is probably overestimated, which might result in a higher estimation of the discharge compared to 3Di. If we look at the energy heads for $dx = 3$ and 1.5m, it can be seen that for 3Di the velocities are underestimated as well. The energy head is below the analytical value. Also the peak is smaller for certain placements of the fixed weir in combination with the bathymetry. The same applies for Flexible Mesh.

It can be concluded that for small grid sizes the placement of a fixed weir is more important than when a lower resolution is used. The bathymetry influences the results far more when a high resolution is used. For grid sizes a limit can be established, where it can be determined when it is more convenient to use only a supergrid model, or both a supergrid and subgrid model.

5.2.1 Influence of grid placement

In the first simulations the placement of the groyne has been such that the crest was adjacent to at least one face of a cell for all refinements. However, this is not always the case when modeling. Usually one does not have the luxury to place each obstacle at the face of a cell. To show the difference of results with different placements, the groyne is placed 6 meters to the right. Although the results of Figure 5.12 are only for 3Di, the same occurs in Flexible Mesh.

Figure 5.13 clearly shows the difference for the pixel resolution for both placements. This figure shows how the discharge depends on the pixel sizes for both placements.

It can be seen that for grid sizes, except for $dx = 12$m, the equilibrium discharges are closely together when varying pixel sizes. For $dx = 12$m, the values seem to be far of the analytical value with increasing pixel resolution for placement 2. While expecting for a higher pixel resolution a discharge that is closer to the analytical value shown in

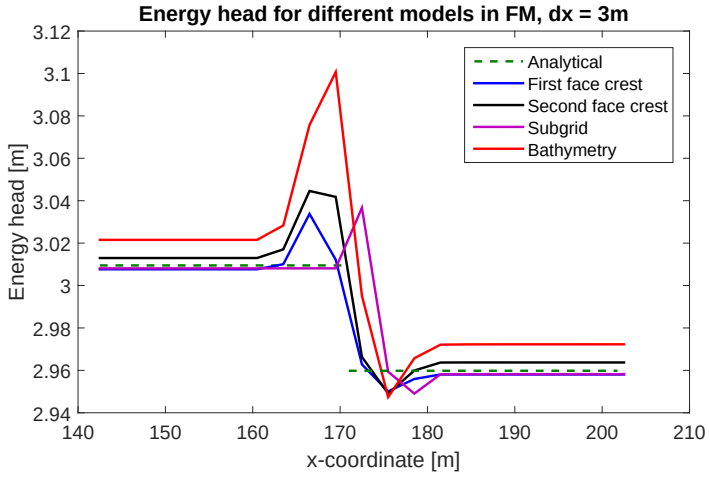

(a) $dx = 3\text{m}$

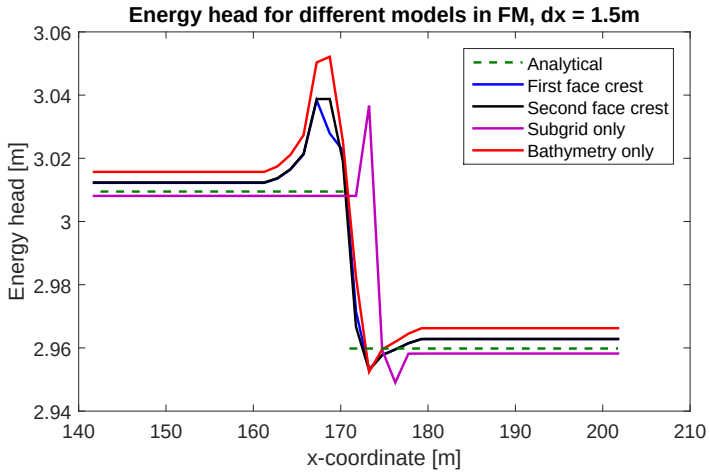

(b) $dx = 1.5\text{m}$

Figure 5.10: Discharge for groyne with a combination of subgrid and bathymetry compared with both models separately for Flexible Mesh

Figure 5.3, it is not the case. With a lower resolution the groyne is better simulated than a higher resolution. With a grid size of $dx = 12\text{m}$, where most of the groyne is placed exactly inside one grid cell, the groyne is not taken into account for all calculations. With the computation of the volume each pixel cell is used, but for the flow area only the pixels that are adjacent to the face of the cell are used. So, when an obstacle like this groyne is placed as in Figure 5.14, it will seem as if there is just a small obstacle when computing the flow areas. This will lead to an overestimation of the discharge. This is why the results in Figure 5.12, for $dx = 12\text{m}$, are so different. One of the possibilities in 3Di is that one can give a refinement threshold. This is the maximum bathymetry difference between pixels that is allowed before 3Di will automatically refine the cells. For this simulation, locally refinements are turned off, hence, it is not applied.

Results of placement 1, where the crest of the weir is placed at a cell face, show that discharges for different pixel sizes are closer together than before. Also, for increasing

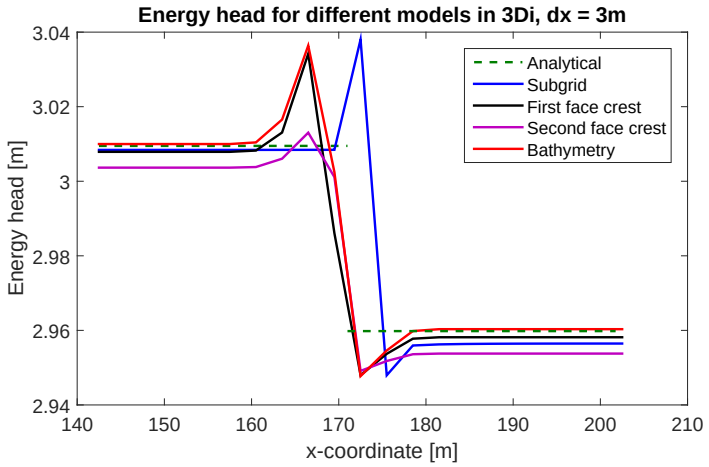

(a) $dx = 3$m

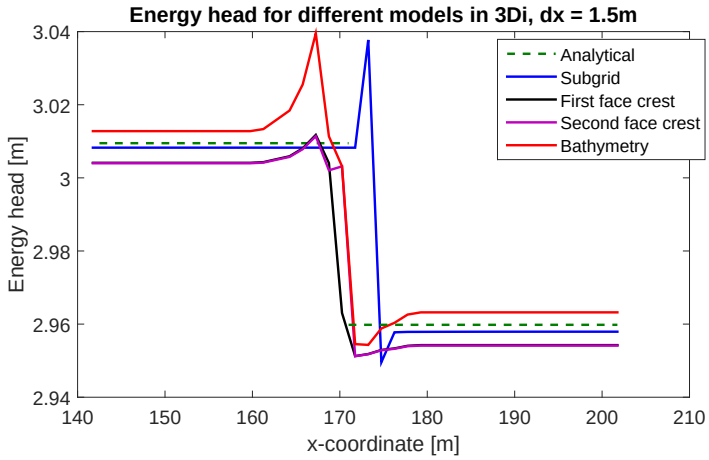

(b) $dx = 1.5$m

Figure 5.11: Discharge for groyne with a combination of subgrid and bathymetry compared with both models separatelyfor 3Di

pixel resolution the discharge is closer to the analytical value. Thus, it is recommended to not use one cell size, but use at least two sizes in combination with using the option mentioned before about a refinement threshold. Unless the placement of obstacles can be influenced.

5.3 Refinement

In Chapter 4 the refinement is done in the middle of the bend such that in front of the refinement the cells are four times as big as the onces after the refinement. Using 3Di, there is no other option when refining the grid. However, using Flexible Mesh there are other options available. Figure 5.15 shows two other possible options.

The option with triangles (top figure) refines in this example only in the $y-$direction. The reason for only refining in the $y-$direction at the moment, is to find out how the

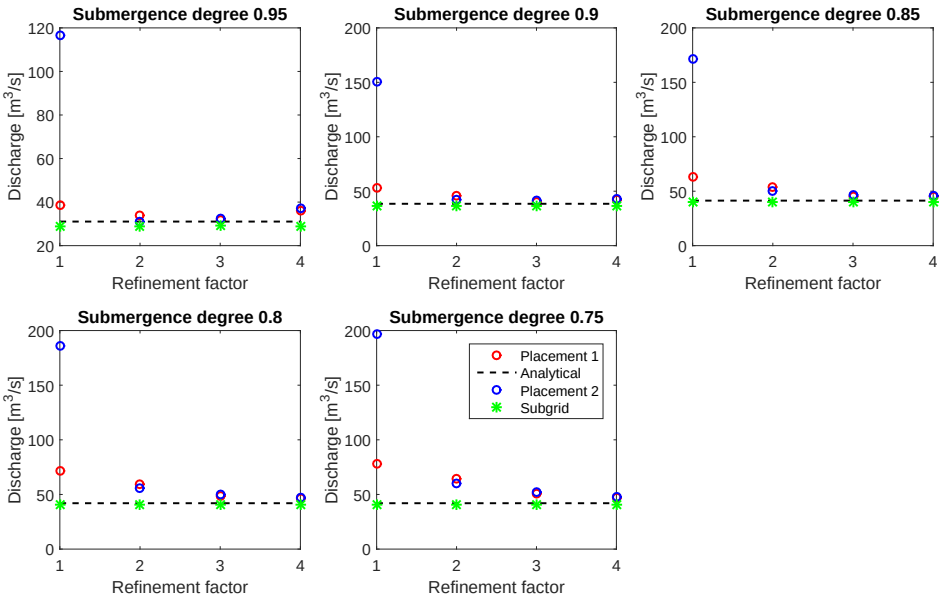

Figure 5.12: Comparison of convergence of discharge with different placements of obstacles in basin in 3Di

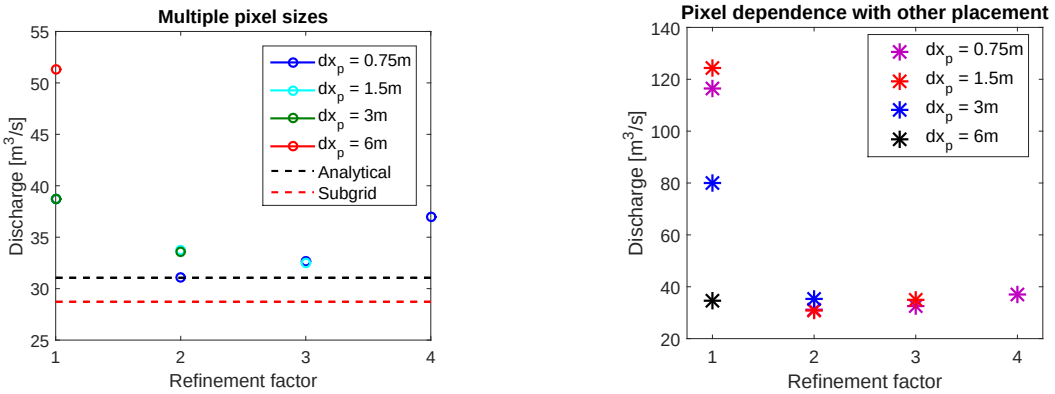

(a) Placement 1 (b) Placement 2

Figure 5.13: Comparison of convergence of discharge for multiple grid sizes and two placements

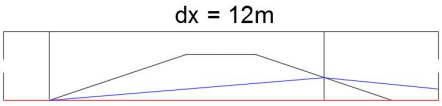

Figure 5.14: Groyne representation in FM with a grid size of $\Delta x = 12$m

triangles influence the results. Since the model is quasi-1D, there are no variations in the $y-$direction. So, any refinement in this direction should not influence the results. The second option is refining without triangles and only refine in the $x-$direction. Hence, all

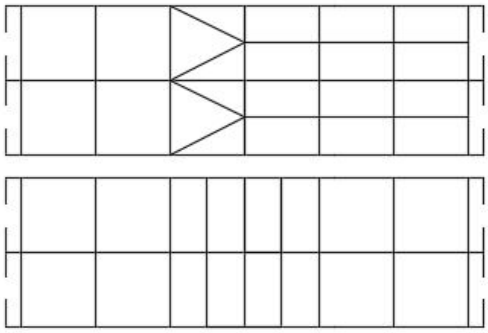

Figure 5.15: Two types of refinement in Flexible Mesh

changes that occur will be due to the use of triangles.

5.3.1 Refinement with triangles in Flexible Mesh

The first refinement that is done, contains triangles and refines only in the $y-$direction. This will give a better overview of the influence of triangles on the results, and when their influence is the highest. This triangle refinement is done with grid sizes $dx = 12$, 6, 3 and 1.5m on multiple places. The three main placements are in front of the groyne, on top of the groyne and behind it.

Refining with triangles results in errors that are highest on and near the weir, where the largest gradients are. Results of Figure 5.16 and 5.17 show that only refining on top of the groyne or directly near it influences them, as can be seen in Figure 5.16 and Figure 5.18. The red line represents the start and end location of the groyne. In between these lines, for Figure 5.18 also just outside, one can see that the difference between the discharge when using a refinement, and the discharge with a uniform grid, is the highest. This can

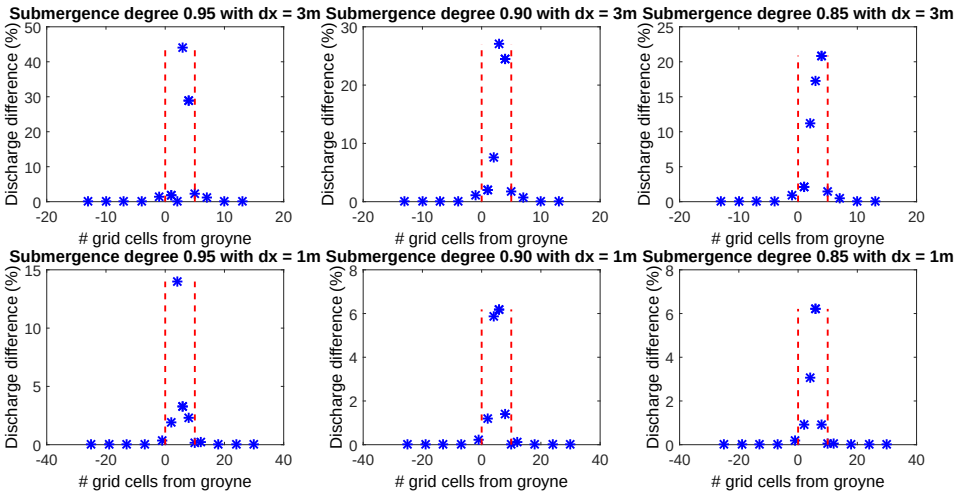

Figure 5.16: Errors in discharge that arise due to applying triangles in a grid for multiple submergence degrees with $dx = 3m$ (top) and $dx = 1.5m$ (bottom)

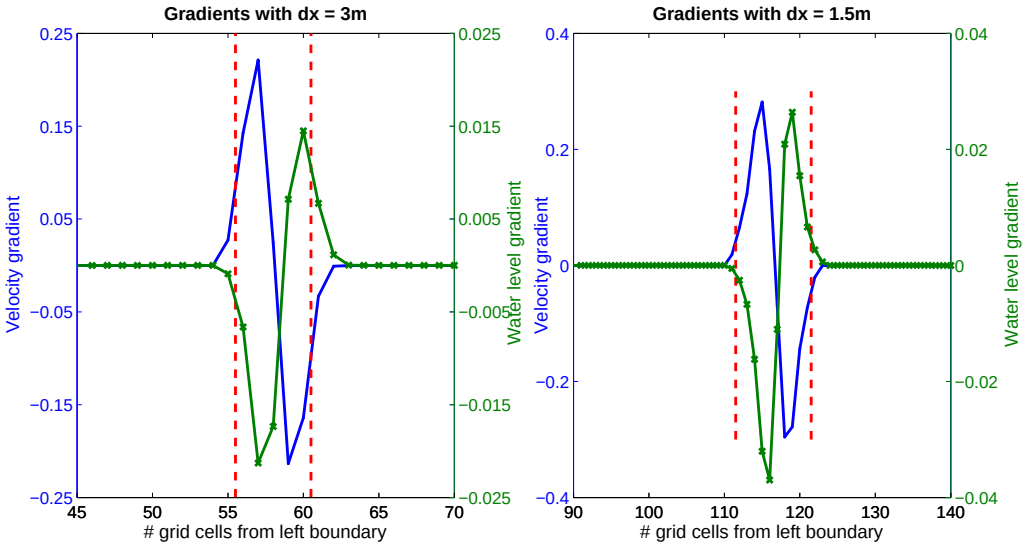

Figure 5.17: Velocity and waterlevel gradients in the $x-$direction with $\Delta x = 3$m (top) and $\Delta x = 1.5$m (bottom)

be explained with Figure 5.17, which presents the velocity and water level gradients. The groyne results in a change of velocity in the $x-$direction. Also, the water levels change a bit, though the gradients are an order smaller than the velocity gradients. So, refining the grid with triangles at a place with high gradients can result in errors. When using a coarse grid, $dx = 12$ and 6m, it can be seen that the errors also occur further off the groyne compared with a finer grid. The coarse cells are not capable of capturing the groyne precisely in an integer number of cells. In this case, there is a groyne of 15m. For cells with $dx = 6$, three cells are needed, and with $dx = 12$m, two cells, resulting in a groyne of respective 18 and 24m when implemented in the bathymetry. Hence, the velocity gradients are occurring further to the right and the left in both cases.

Comparing all grid sizes, it can be concluded that the coarser a grid is, the higher the error will become with triangles. Furthermore, refining at a velocity gradient will result in an error. The higher this gradient is, the larger the error will be. Refining in a flow with no gradients has no influence on the results.

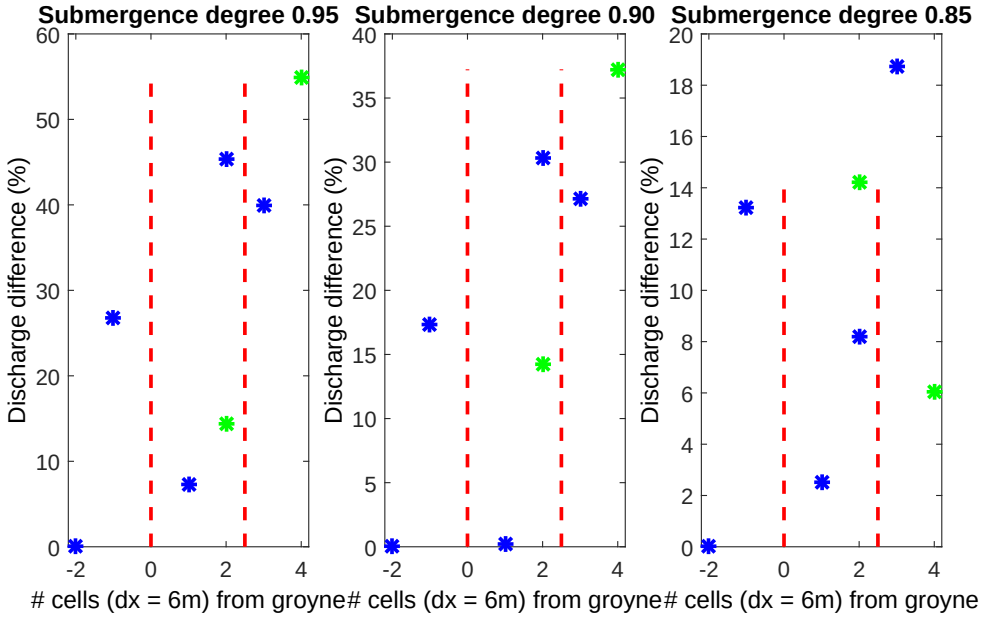

Figure 5.18: Errors in discharge that arise due to applying triangles in a grid for multiple submergence degrees with $dx = 12m$ (green dots) and $dx = 6m$ (blue dots)

Using triangles as refinement it is also possible to refine both in the $x-$ and $y-$direction, instead of in one direction. In Section 5.3.2 the refinement will be done in the $x-$direction only without the use of triangles. There are three types of refinement possible when using triangles. These types can be seen in Figure 5.19. Type 2 is the one used before, and the other two types include refinement in the $x-$direction.

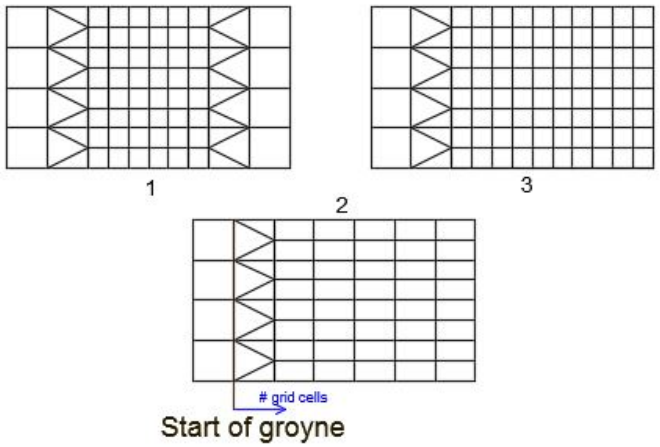

Figure 5.19: Three types of refinement using triangles

These three types of refinement are only done on top of the groyne, since it is seen that

refinement in front or far behind the groyne has no influence on the results. Figure 5.19 shows how the counting of the number of cells is done. These types of refinement are only done for $dx = 3$m. Hence, the size of the grid cells when refining in both directions is $dx = 1.5$m. Figure 5.20 presents the equilibrium discharges that are found from each refinement. This refinement is done five times, from cells 1 to 5 from the beginning of the groyne and also for three different submergence degrees. The black line in the figure represents the discharge belonging to a uniform grid with $dx = 3$m, and the red line to $dx = 1.5$m. This can show whether the equilibrium discharge belongs more to one or the other, or contains many errors. Using the results of the previous refinement, one would expect that the largest errors occur when the triangles are placed around the middle of the groyne. Indeed, it can be seen that the green line, which belongs to the refinement done in the middle of the groyne, is the furthest away from both the black and green line. Which gives that an error arises in this model. Since for type 2, no refinement in the $x-$direction takes place, the deviation is coming from the triangle refinements. When using type 1 or 3, it can be seen that the error is less high. This is do to the refinement in the $x-$direction. The equilibrium discharge is getting closer to the red line. It can be noticed that the results for type 1 and 3 are the same. Apparently the second time that the triangles are used to go back to the coarse grid, are not causing errors. Since it is made coarser after the groyne, there are no velocity gradients, hence no errors arise. If the whole groyne is refined, as if when the triangles are placed on the first cell, the equilibrium discharge is almost the same as when using a fine uniform grid. This can save much computational time if this can be applied.

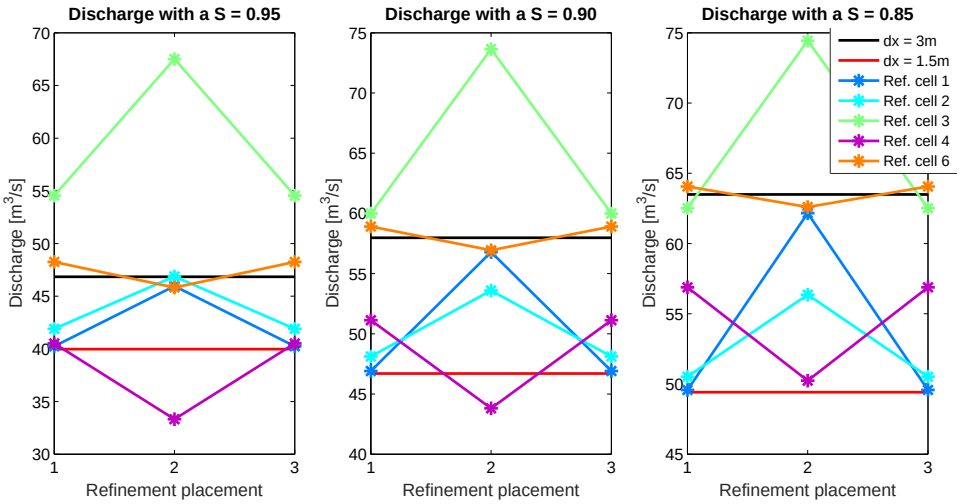

Figure 5.20: Comparing discharges for multiple types of refinement with a transition placement that varies in space

The results of type 1 and 3 are similar to the results of type 2, with the excaption that the discharge of the first types can be more precise due to the refinement in the $x-$direction. Figure 5.21 represents the velocities in the cell centers in the $x-$direction, the top figure with the refinement in the first cell and the bottom in the middle cell. The largest difference in values is between refining in the first and middle cell of the groyne as seen before. This figure shows where these errors arise. In the top figure it can be

seen that around $x = 112$m the values that belong to the refinements are off, whereas at other places it is almost the same as the values with no refinement. This place is exactly where the triangles are placed for the refinements. Considering the bottom figure, it can be seen that the velocities belonging to the grids with refinement are higher than the ones without. Which can also be seen in Figure 5.20, the green line. Thus, placement of the refinement has a huge influence on the results. Insight of the problem is convenient if one wants to use refinements. In this way the velocity gradients can be more or less taken into account, which results in less numerical errors.

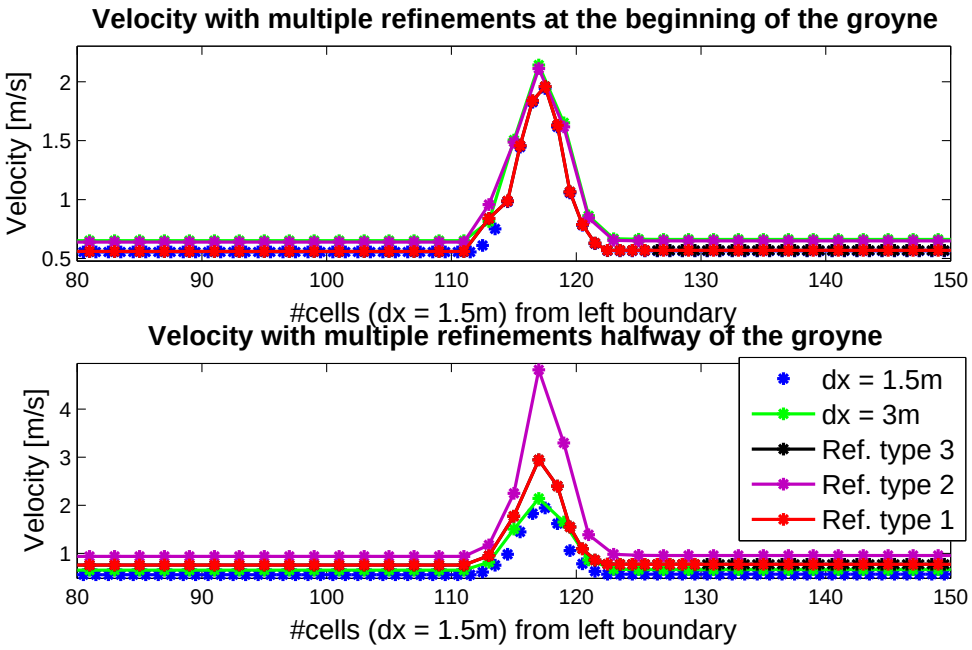

Figure 5.21: Velocities over the $x-$axis for multiple types of refinements with triangles compared to velocities with a uniform grid in FM

5.3.2 Refinement in flow direction in Flexible Mesh

Section 5.3.1 has been about refining a grid in Flexible Mesh using triangles. This section will be about refinement in the $x-$direction only, without the use of triangles. The approach is a bit different than Section 5.3.1, since it is not possible to calculate the errors as before. Instead, the equilibrium discharge is plotted of the grids containing refinement (dots) and the uniform grids (lines). This can be seen in Figure 5.22. The refinement is only done just in front and on top of the groyne, since it is seen in Section 5.3.1 that refining far in front and after the groyne does not influence the results.

When the refinement includes the entire groyne, the equilibrium discharge is similar to the discharge of a uniform, fine grid, while otherwise some differences arise. This can be seen in the second and third figure from the left in Figure 5.22. If the refinement is done at cell 1, the complete groyne is refined. In case it is not completely refined, the equilibrium discharge of a grid with refinement is different than both uniform grids. It can either be lower or higher, or in between the discharge of both uniform grids. This

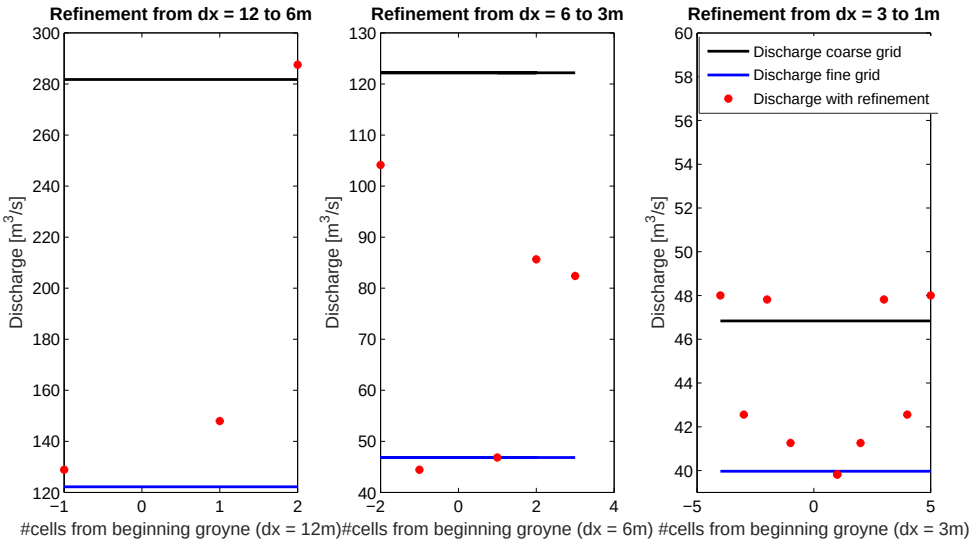

Figure 5.22: Equilibrium discharges with a rectangular refining for multiple resolutions and varying transition placements

makes it a bit more difficult to predict whether it is near the correct value. Figure 5.23 shows the velocities that belong to the refinements $dx = 6$ to 3m and $dx = 3$ to 1.5m. Two refinements are taken into account, namely the one that gives the smallest difference with the fine uniform grid, and the largest difference. Considering the velocity belonging to the grid with the smallest error, it can be seen that the velocity is similar over the whole length as the fine uniform grid in both cases. However, this does not apply for the velocities where the discharge has the largest difference. In the top figure the velocity is between the velocities of the uniform grid. Of course, this can be expected, since the discharge is also in between the other values. The velocity values of the bottom figure are more interesting. They are the same as the velocities belonging to the coarse grid, except at the groyne where the refinement is. Here they are overestimated at first where the jump from a coarse to fine grid is, where after a bit underestimated. This might be due to the high velocity gradients that are on the groyne.

The last refinement that is done in the $x-$direction, is a double and short refinement. The first means that there is a coarse grid, in this case $dx = 6$m, followed by a refinement to $dx = 3$m in one cell and a second refinement to $dx = 1.5$m after the first. The left figure of Figure 5.24 shows the results of this refinement.

It can be seen that with the right placement the same equilibrium discharge as the finest grid can be reached, whereas the surrounding grid is twice as coarse. This could save much computational time. However, the right placement is thus important.

The short refinement contains refining that is less than 5 cells when $dx = 3$m. In the previous refinements the number of cells is chosen such that at least 15m, the width of the groyne, is refined. The right figure of Figure 5.24 shows the results of this refinement. The discharge values are closest to the fine uniform grid when the most cells (three) are refined. Unlike all the other cases, the same value as the uniform grid is never reached. Hence, from this it can be concluded that refining the whole structure is an important

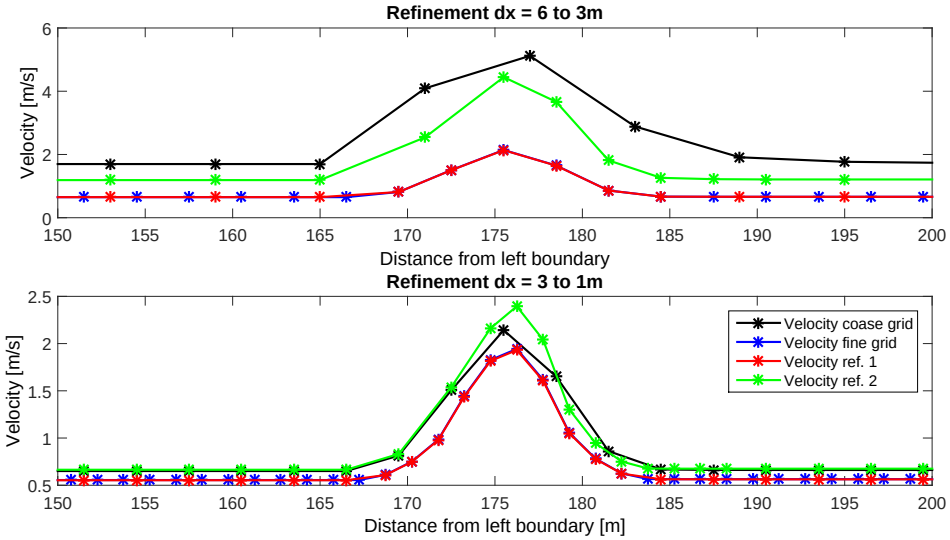

Figure 5.23: Velocities over the $x-$axis for multiple types of refinements without triangles compared to velocities with a uniform grid in FM

point.

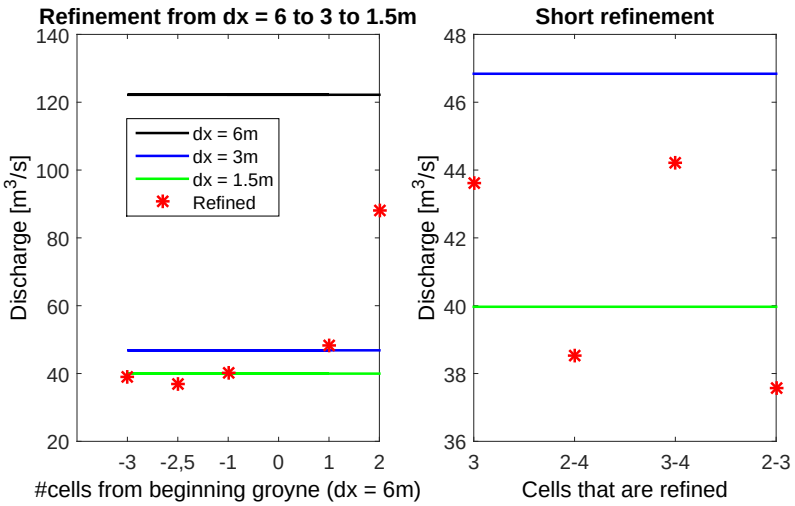

Figure 5.24: Equilibrium discharges with multiple refinements at various places

5.3.3 Refinement in 3Di

In 3Di it is only possible to refine in one way, and that is with quadtree cells. Using Flexible Mesh it is possible to choose whether one wants to refine in the $x-$ or $y-$direction, or both. However, with the quadtree method a grid is refined in both directions. In this section the focus is only on refining the model in 3Di. The refinement is done in the same way as in the Section 5.2.1 and 5.2.2 with Flexible Mesh. Just in front of the groyne and on the groyne itself, the grid is refined one level. This is done for both $dx = 12$, 6 and 3m. Hence, the finest grid is $dx = 1.5$m and the coarsest $dx = 12$m. Results of these refinements are plotted in Figure 5.25. The green dots represent a refinement extended till the right boundary. On the other hand are the red dots. This refinement is done only 5 of the coarsest cells to the right.

Just as in Flexible Mesh, the location of transition from one grid size to another, influences the results. Considering the green dots in Figure 5.25, where the refinement starts just in front of the groyne, it can be seen that the results are similar to discharge of the finest grid. Refining on top of the groyne has as consequence that the discharge is neither similar to the fine or coarse grid. It appears most of the times between the two discharges belonging to a uniform grid as some transition from one to the other. What stands out is the fact that quite some results are outside this area. This applies for both the green as the red dots.

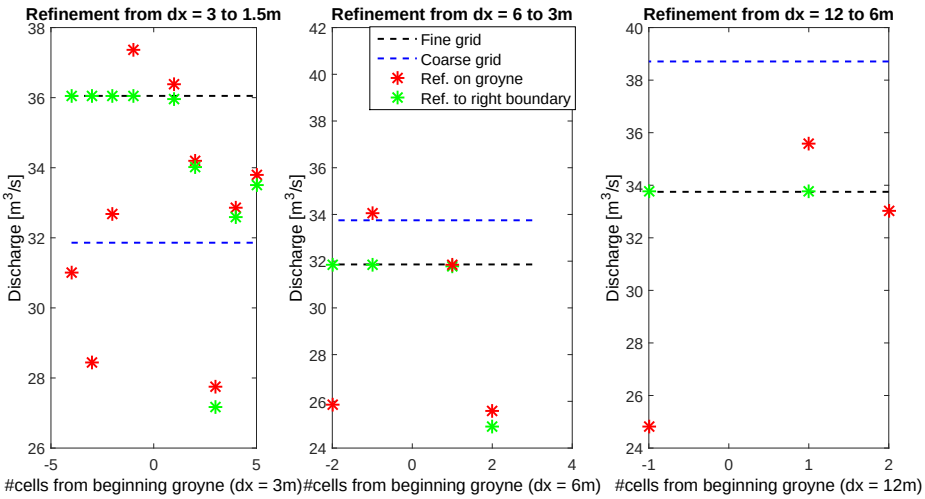

Figure 5.25: Equilibrium discharges with refinements at various places for several resolutions

Figure 5.25 already showed that refining just in front of the grid until the right boundary gives the same results as using a uniform fine grid. One would expect that refining after the groyne would result in the opposite. The discharge is expected to be the same as the coarse grid. This can be seen in Figure 5.26. 12 meters after the groyne (not after the beginning of the groyne but the end), a refinement is applied until the right boundary every 25m. The same is done in front of the groyne 12 meters from the beginning of the groyne. Exactly what is expected happens as shown in the figure. The dashed lines represents discharges belonging to a uniform grid, while the dots to a refined grid. There are no difference between the discharges when varying in the $x-$direction either in front

or behind the groyne. Hence, refining with a constant water level or velocity results in no error.

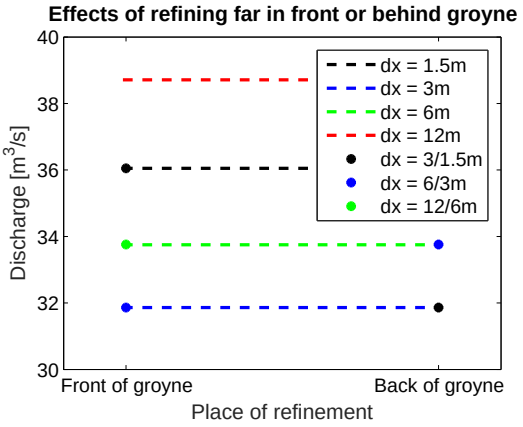

Figure 5.26: Effects on equilibrium discharges when the transition of a refining is either far in front or behind an obstacle

By analyzing the results of the local refinements in 3Di, it is noticed that in some simulations velocities are physically not correct. In Section 5.3.1, where a refinement with triangles is applied in Flexible Mesh, it is seen that there is no difference in the results whether the refinement is all the way until the right boundary or just a small part when placing a refinement on the groyne. This is because the part that contains the gradients has the same grid sizes, either coarse or fine. However, considering Figure 5.25 again, it seems that it is not the case for 3Di. Differences in discharges are caused due to velocities as seen before. Figure 5.27 presents velocities that belong to the refinement $dx = 3$ to 1.5m, where cells 1 to 5 are refined (starting point the beginning of the groyne). At first sight it appears that the orange line, which belongs to a refining at cell 5, is too high after the groyne. Especially compared with the other velocities. To get a better insight in this, the top views of velocities for these refinements are plotted in Figure 5.28. It shows that there is variation in the $y-$direction, which should not happen, since it is a quasi-1D problem. Both figures have these variations. However, with exception of the most upper rectangular basin, it appears that these variations vanish when the grid is coarse again. Based on these top views it seems that the largest errors occur when refining on cell 3 and 5. But, founded on the equilibrium discharge from Figure 5.25 one would agree with cell 3, but not cell 5. However, if we look at the velocities it can be noticed that at some points it is negative, which might explain why the equilibrium discharge is not agreeable with what to expect, since this discharge does not appear to be off.

This type of refinement agrees most with the rectangular refinement of Flexible Mesh. If we consider Figure 5.22, one can see that the results are similar. Though the values are in the opposite direction going away from the uniform value. So, both programs seem to be sensitive to gradients in the model. Whereas in Flexible Mesh the velocities and water levels will only vary in the $x-$direction, they will also vary in the $y-$direction when using 3Di. Although the water levels will vary just slightly, due to the fixed water level boundary conditions, the velocities can differ up to a factor 2 in the $y-$direction, which seems not correct. In previous parts, some bugs in the program of 3Di are found. It might be possible that these are present here as well.

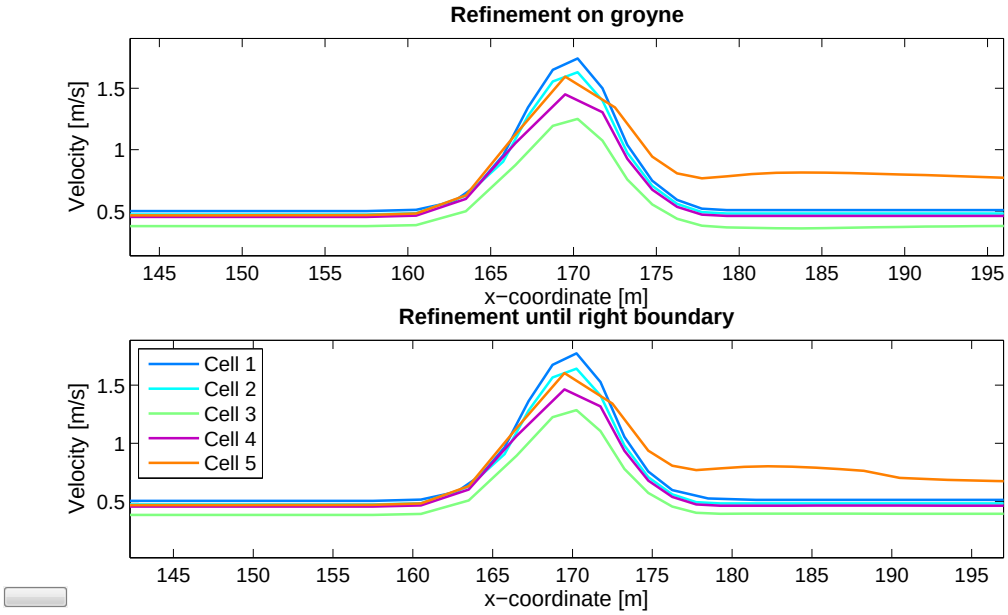

Figure 5.27: Velocities over the $x-$axis for multiple types of refinements compared to velocities with a uniform grid in 3Di

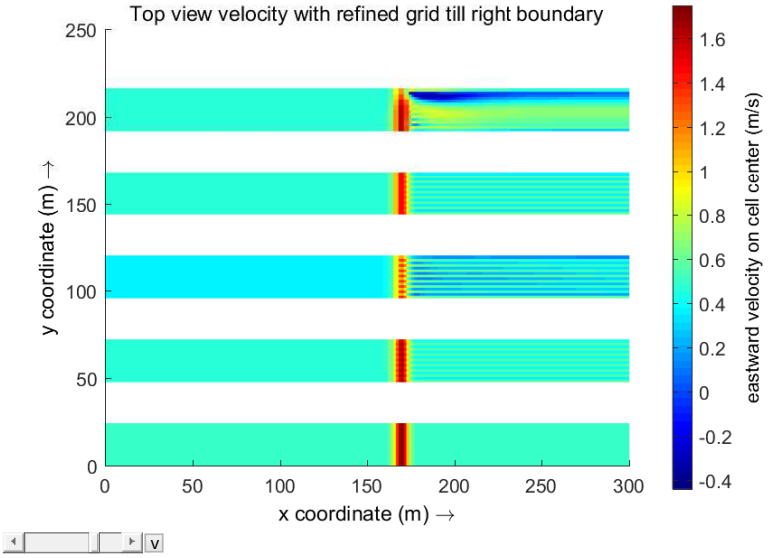

(a) Refinement to the right

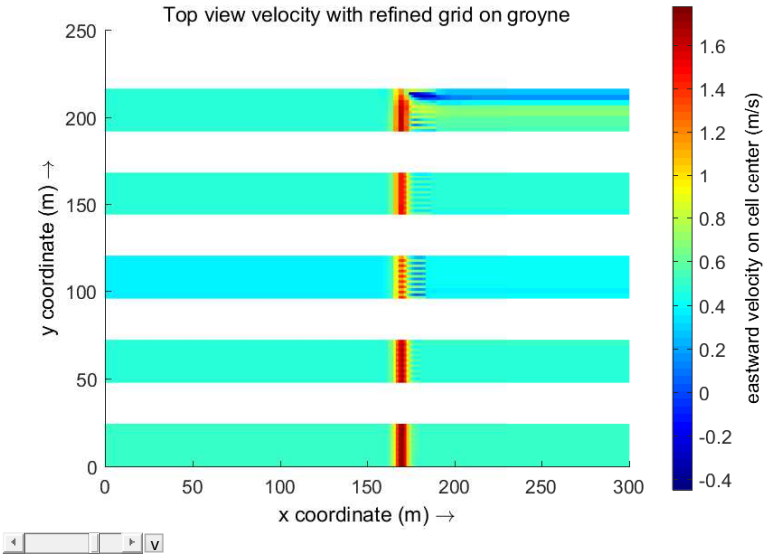

(b) Refinement on groyne

Figure 5.28: Top view of several basins presenting eastward velocities using either a local refinement on 5 cells in the $x-$direction or all the way to the right boundary

5.4 Conclusion and discussion

Investigating the convergence of the test cases in 3Di and Flexible Mesh, shows the energy increase at the weir in both packages. With a conservation of energy in front and on top of the weir and momentum on top and behind the weir, an analytical value has been determined. 3Di and Flexible Mesh have showed convergence to a higher value than this analytical value. Combining both supergrid and subgrid models, resulted in a smaller

difference. When the river is simulated, this combination will be used as well, since the grid will be too coarse to only use bathymetry and the obstacles will not be correctly represented. The groynes in this simulation will only be partly overflowed, hence, it is expected that these differences will be even smaller. Hence, it will not have a high influence on the results. When plotting the energy head over the $x-$direction, it shows that from the beginning of the weir the energy head increases. According to Stelling and Duinmeijer (2003) an increase of energy can occur, when the wrong type of conservation is used. Over the entire domain a conservation of momentum is assumed, while only conservation of energy is applied when a subgrid model is used. It might also be the result of wrongly assuming a hydrostatic pressure. For further research it is recommended to create a weir where the hydrostatic pressure is valid to investigate the origin of the energy increase.

By changing the geometry of the weir (lower slope, sudden expansion) the energy increase is slightly brought down. Combining both the bathymetry and subgrid model resulted in lower energy increases for all simulations. This is because the subgrid model assumes conservation of energy at the first part of the weir instead of conservation of momentum over the entire model. The grid size influence the results in this situation as well. As soon as the resolution is high enough to represent the weir in high detail in bathymetry, this combination can result in an underestimated discharge. This is due to the way how the subgrid model is implemented. It is depended on the grid size and its surrounded bathymetry. When a fixed weir is placed on top of the weir, where on one side the bottom level is still equal to the crest height, this value is used for the calculation of the depth. This results in an underestimation of this value.

Flexible Mesh has the option to refine in three different ways, only in either the $x-$ or $y-$direction or both. With this quasi-1D model, where only variations in the $x-$direction are found, the differences arising due the usage of triangle grid cells could be investigated. Results show that placing a local refinement, whether one uses triangles or not, gives rise to errors. Locally these errors are highest. The same can be seen for 3Di, although locally refining can be done in only one way. Placing these refinements at variant locations, show that the velocity or water level gradient is an important factor. A higher gradient results in a larger local error. Thus, it is recommended to place a local refinement where these gradients are the lowest, since they are almost always present in a river.

The focus of this chapter has been mainly about a submergence degree of 0.95. To get a better idea of the result it is recommended to also investigate other degrees, especially the ones with another flow regime.

Part II

Hydraulic Engineering: The physical properties of 3Di and Flexible Mesh

Chapter 6

Mildly curved flow experiment in flume

Part II, the hydrodynamical part, focuses on the physical aspects. The first test case of this part is based on the experiment of Blokland (1985). With measurement data available it is possible to compare the results of the simulations. This gives a better view of the capabilities of both packages. This chapter starts with a description of the flow geometry. Hereafter a first research is done to the influence of the different types of grid. 3Di has standard a Cartesian grid (which is structured). In Flexible Mesh there are multiple options as is seen in Chapter 2. In this chapter both a curvilinear and Cartesian grid will be used to see how these grids influence the results. Subsequently some theoretical background of the possible physical parameters that can be used is given, where after both packages are compared with experimental data using these parameters. The chapter ends with a conclusion. These simulations are performed with D-Flow FM version 1.1.148.41897, file format 1.05 and 3Di - subgrid Version 0.1.1.1942.

6.1 Flow geometry

Specifications of the flume geometry, which originates from Blokland (1985), are given in Table 3.1. In this table is C the Chezy coefficient, i_b the bottom slope in streamwise direction, B the width and R the radius of either the inner or outer bend. The cross section profile of this flume is a rectangular. Furthermore, in the streamwise direction there is no bottom slope.

R_{in} [m]	R_{out} [m]	B [m]	i_b	C [$m^{1/2}s^{-1}$]
3.85	4.35	0.5	0	60

Table 6.1: Values of the physical domain

Boundary conditions are chosen based on the available data from Blokland (1985). At the inflow a discharge boundary condition is given, while at the outflow a water level

boundary condition is placed. The first is set to $Q_{in} = 6.44$l/s, the average discharge that is measured. The water level is equal to the water depth in this case, since the bottom level is placed at $z = 0$. The water depth is known at certain points by measurements. Further, the hydraulic gradient is around $0.5 \cdot 10^{-3}$, which gives the possibility to calculate the outflow boundary condition. It gives a value of $\zeta_{out} = 0.045$m.

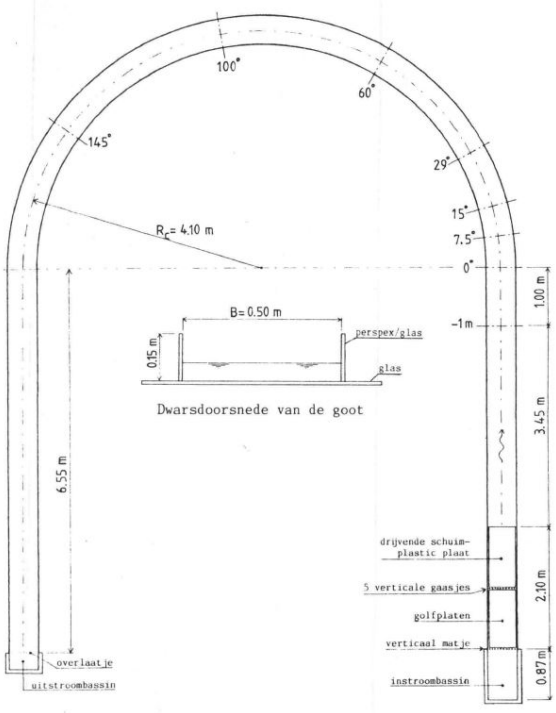

Figure 6.1: Set up of flume experiment of (Blokland, 1985)

Figure 6.1 shows a display of the set up of the flume used in the experiment. Also, places where measurements were taken are shown. It can be seen that there are eight cross sections where measurements were done. Each at different places in the bend. With this data both programs can be validated. However, it should be kept in mind that there can be errors in the measurements as well.

6.2 Different types of grid generation

In order to compare the test case results with the available data, results from the same cross sections as in the experiment (Figure 6.1) are used for comparison, where three different grid sizes are used. The coarsest grid has 5 cells in the width, while the finest grid has 20 cells in the width. Thus, with each refinement a cell is half the size of the grid cell in both $y-$ and $x-$direction. The coarsest grid of both types is presented in Figure 6.2, where the differences between a curvilinear and Cartesian grid are clearly visible. For Flexible Mesh both types of grid are used in this chapter, while for 3Di a Cartesian grid is used, which is the only option. The first simulation will be using a Cartesian grid of both Flexible Mesh and 3Di.

When investigating the result of different grid generation of both packages, the numerical models should be as similar as possible. It is seen in Chapter 2 that the shallow water equations differ. In the momentum conservation equation of 3Di the diffusivity term is missing. This term is dependent on the turbulent viscosity, which can be set to zero in Flexible Mesh. By doing so, the shallow water equations are equal to each other. How these equations are implemented in the packages is still different, but this cannot be changed. Hence, differences are in the implementation and grid generation at this point.

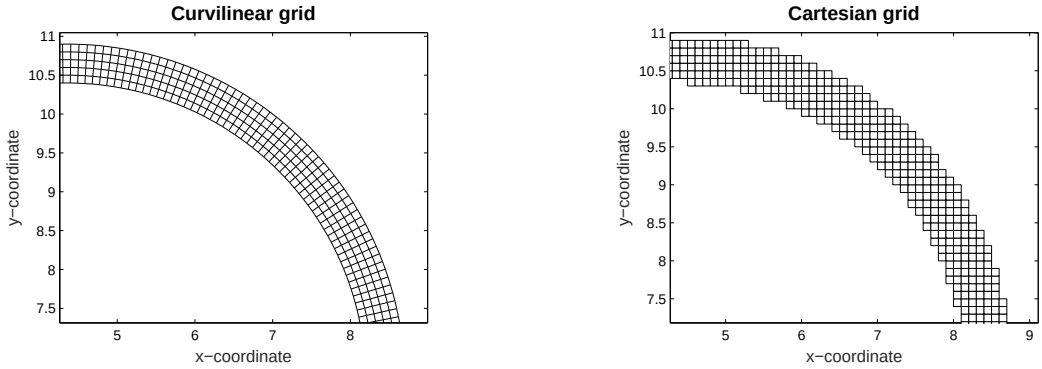

(a) Curvilinear grid (b) Cartesian grid

Figure 6.2: Multiple grid types used in Flexible Mesh and 3Di

It can be seen in Figure 6.3, where the water levels are plotted, that the results of a Cartesian grid in Flexible Mesh are far of the experimental data, while for 3Di they are quite agreeable. Considering the water levels of the simulation where $N = 5$ in Flexible Mesh, they are more than 50% higher than the experimental data. Due to the mass balance, the velocity is much lower than this data. Increasing the resolution of this grid results in differences of the water levels that are less than 20%. This opposite to the results of 3Di, where the water levels for each of the resolutions are close to the experimental data. With the pixel subgrid model, the volume balance can be calculated in more detail. For this simulation only one pixel subgrid size is used, where $N_p = 40$ in the width, even for $N = 5$. Hence, no matter the grid size, the volume balance is always calculated with this subgrid.

In order to investigate whether the results of 3Di are closer to the data than Flexible Mesh, a pixel size of $N_p = 10$ is taken for $N = 5$ instead of $N_p = 40$. Presented in Figure 6.5 and Figure 6.6 are the results of Flexible Mesh with a Cartesian grid, 3Di with $N = 5$ and $N_p = 10$ and $N_p = 40$. Although the water levels of $N_p = 10$ are closer to the results of Flexible Mesh, the difference is still quite large. Especially with $N = 5$ of Flexible Mesh. The profiles of the velocities are in some cross section more similar to Flexible Mesh: on the outsides it is lower, while with a higher pixel resolution it is more a linear line. Thus, even though the grid with pixels is more similar to the coarsest grid of Flexible Mesh, the results are still more precise when compared to the data. So apparently the Cartesian grid of 3Di with pixels is more suitable to use than a Cartesian grid in Flexible Mesh for this specific problem.

Another interesting point are the velocity profiles in the cross section of the bend. In front and in the beginning of the bed these profiles are (almost) linear lines. As the

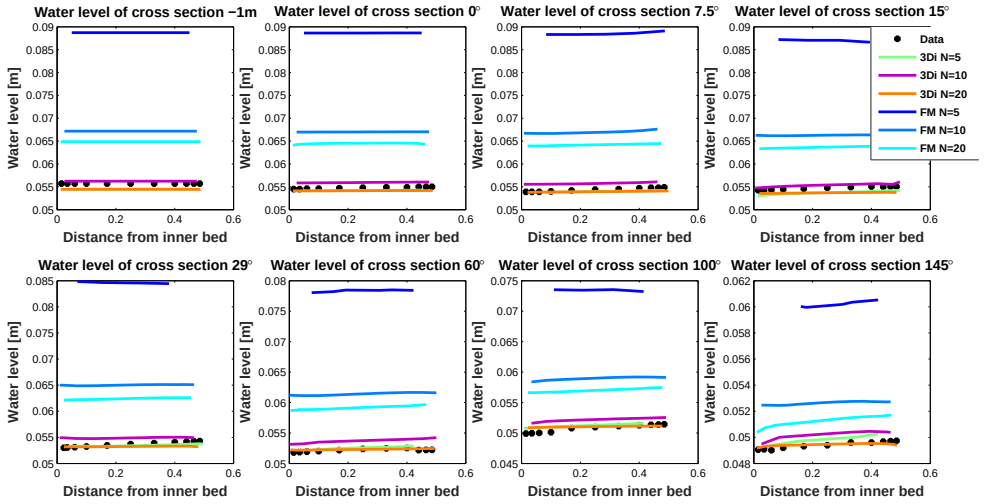

Figure 6.3: Water levels in cross sections indicated in Figure 6.1 for a Cartesian grid in FM and 3Di for multiple grid resolutions

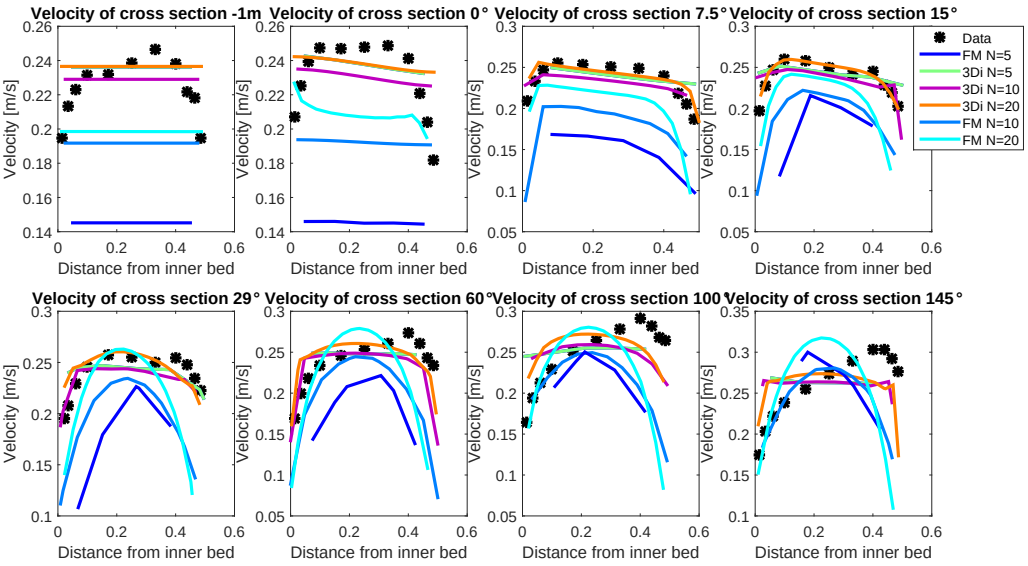

Figure 6.4: Velocities in cross sections indicated in Figure 6.1 for a Cartesian grid in FM and 3Di for multiple grid resolutions

angle increases the velocities get smaller near the edges of the flume. In both programs there is however free slip, so the velocity is not zero near the walls. If we take Figure 6.8, where the curvilinear and Cartesian grid of Flexible Mesh are compared, it can be seen that the velocity profile for a curvilinear grid is still linear in the bend. Hence, it is due to the Cartesian grid that these velocities are lower near the wall. Of course, this is easy to understand. A Cartesian grid has a staircase profile for bends, where the velocity cannot follow the boundaries of the real flume. As a result, the velocities are low in these cells adjacent to the boundary. The shapes of these velocity profiles differ between 3Di

and Flexible Mesh. It cannot be explained why this is the case, but it appears that the velocity over the entire cross section in Flexible Mesh is influenced by the staircase bend (based on the parabolic shape), while for 3Di the shape is still linear in the middle. This might be the result of the different advection schemes that are used in both programs, but it can not be said for sure.

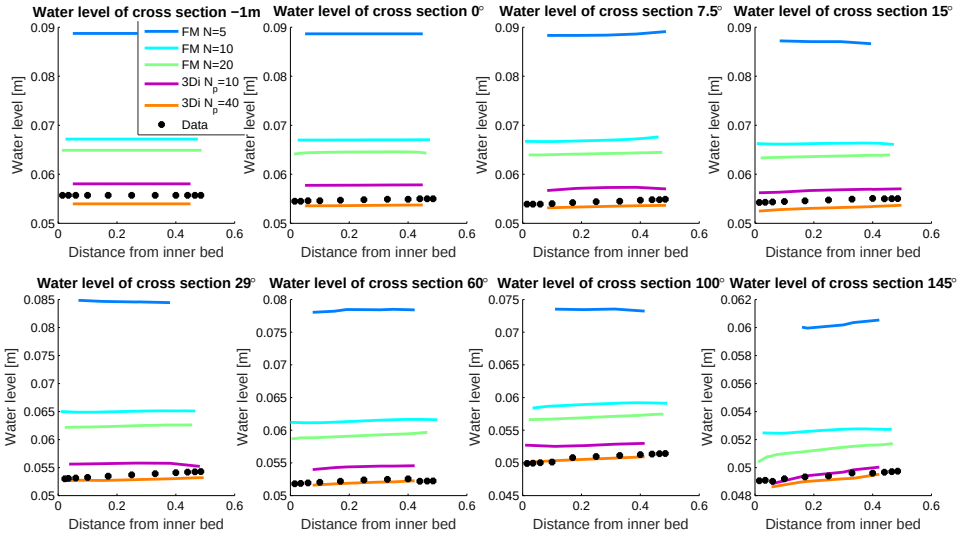

Figure 6.5: Water levels in cross sections indicated in Figure 6.1 for a Cartesian grid in FM and 3Di for multiple grid resolutions with variable pixel sizes in 3Di

Although 3Di uses a Cartesian grid as well, the results are closer to the experimental data than Flexible Mesh. This might be the result of the pixel subgrid model that is also present. If the resolution of these pixels is lower, for example from $N_p = 40$ to $N_p = 10$, the results might be more like the ones of Flexible Mesh when using a Cartesian grid. Presented in Figure 6.5 and Figure 6.6 are the results of Flexible Mesh with a Cartesian grid, 3Di with $N = 5$ and $N_p = 10$ and $N_p = 40$. Although the water levels of $N_p = 10$ are closer to the the results of Flexible Mesh, the difference is still quite large. Especially with N = 5 of Flexible Mesh. The profiles of the velocities are in some cross section more as the ones of Flexible Mesh. On the outsides it is lower, while with a higher pixel resolution it is more a linear line. Thus, even though the grid with pixels is more similar to the coarsest grid of Flexible Mesh, the results are still more precise if we compare them to the data. So apparently the Cartesian grid of 3Di with pixels is more suitable to use than the one in Flexible Mesh.

Not only the water levels of the results of both packages differs, the shape of the velocity profile in the bend is quite dissimilar. In front and in the beginning of the bed these profiles are (almost) linear. As the angle increases the velocities get smaller near the edges of the flume. In both programs there is however free slip, so the velocity is not zero near the walls. Considering Figure 3.8, where the curvilinear and Cartesian grid of Flexible Mesh are compared, it can be seen that the velocity profile for a curvilinear grid is still linear in the bend. Hence, it is due to the Cartesian grid that these velocities are lower near the wall. A Cartesian grid has a staircase profile for bends, where the velocity cannot follow the boundaries of the real flume. As a result, the velocities are low in these

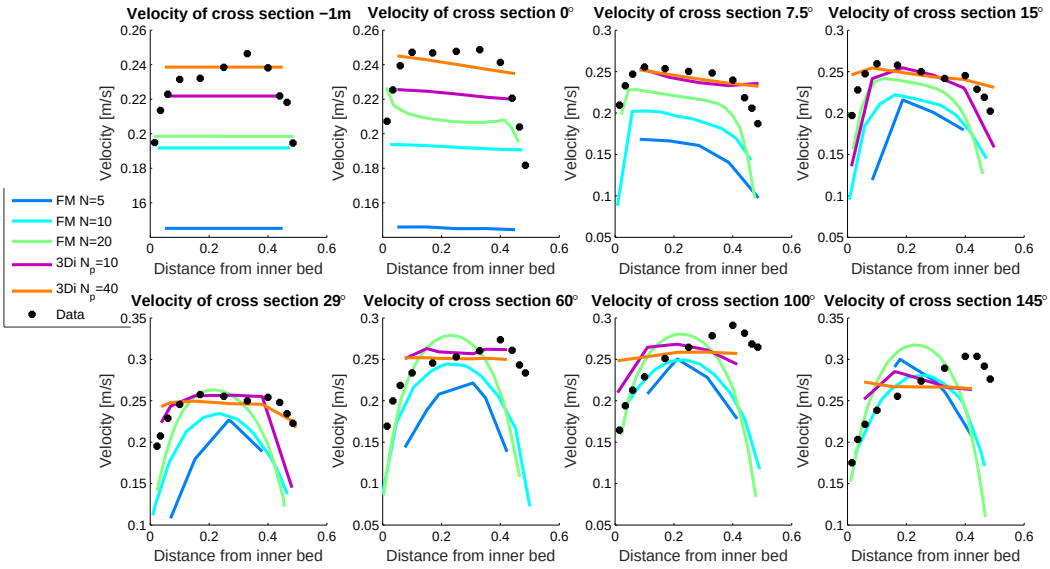

Figure 6.6: Velocities in cross sections indicated in Figure 6.1 for a Cartesian grid in FM and 3Di for multiple grid resolutions with variable pixel sizes in 3Di

cells adjacent to the boundary. The shapes of these velocity profiles differ between 3Di and Flexible Mesh. It appears that the velocity over the entire cross section in Flexible Mesh is influenced by the staircase bend (based on the parabolic shape), while for 3Di the shape is still linear in the middle. Since all input values that can be influenced are the same, it is most likely that it is the result of how the mathematical model is implement in both packages.

Next the curvilinear and Cartesian grid are compared. Both grids are built in Flexible Mesh, thus except the grid all processes and equations are the same. Just as before, the water levels and velocities are compared for both grids, see Figure 3.7 and Figure 3.8.

Opposite to a Cartesian grid in Flexible Mesh, the result of a curvilinear grid have almost the same value as the given data. It is seen before that for a Cartesian grid with $N = 5$ results are far off the experimental data. For a curvilinear grid, all the results of different resolutions are closely together. Considering the water levels, Figure 3.7, these results coincide with the experimental data for each cross section. However, for the velocity profiles it is another case. In the first four cross sections, the results agree with the experimental data, except near the wall. The latter occurs due to using a free slip condition, instead of a no-slip condition. After these first cross sections, the values of the velocities are still quite agreeable, but the shape not anymore. Since many 3-dimensional physical processes as secondary flow are not taken into account, one cannot expect these results to match the given data.

6.3 Physical parameters

In this section the physical parameters that are implemented in Flexible Mesh are explained. Since the friction coefficient is fixed by the experiment, there are no parameters

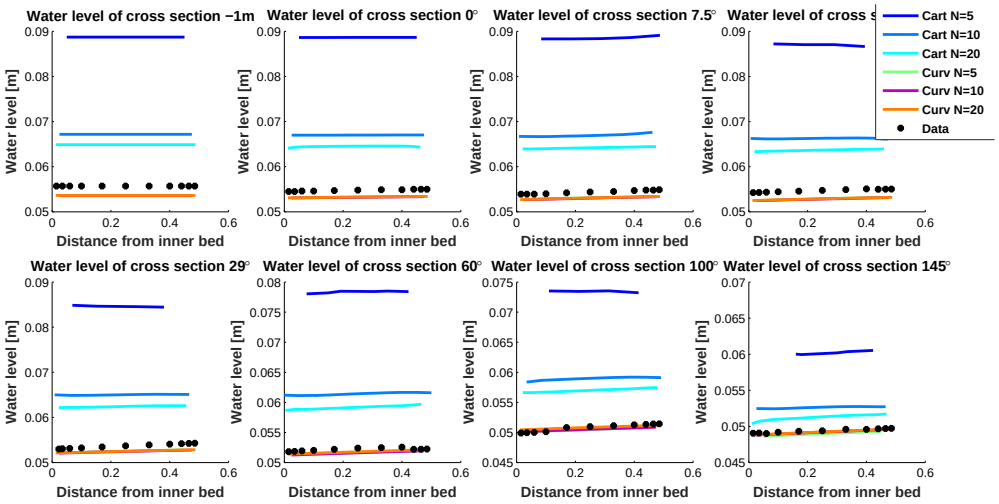

Figure 6.7: Water levels in cross sections indicated in Figure 6.1 for both a Cartesian and curvilinear grid in FM and 3Di for multiple grid resolutions

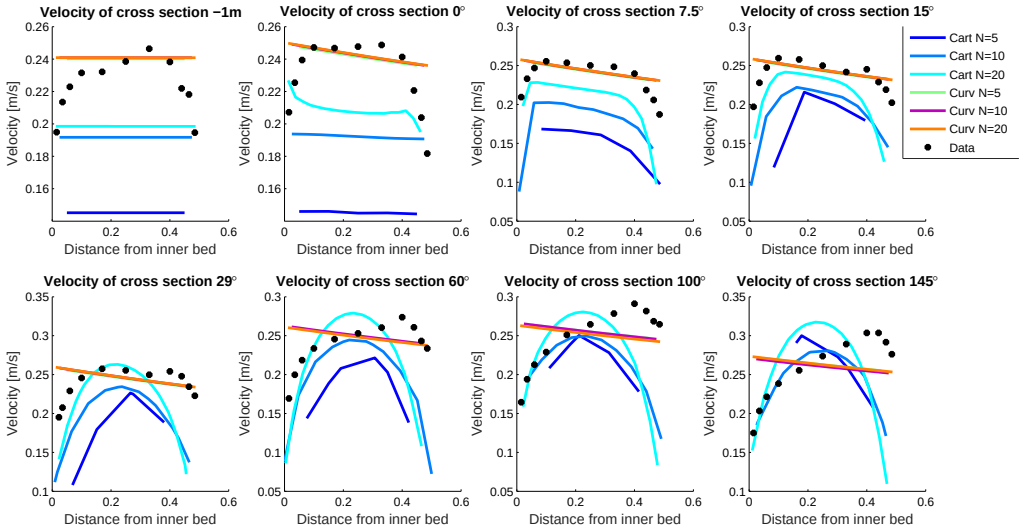

Figure 6.8: Velocities in cross sections indicated in Figure 6.1 for both a Cartesian and curvilinear grid in FM and 3Di for multiple grid resolutions

in 3Di that can vary. For Flexible Mesh multiple parameters can be changed, and each of them is shortly introduced.

6.3.1 Slip at vertical, closed boundaries

At solid boundaries a no-slip conditions applies. Hence, the velocity of the flow that is in direct contact with the solid boundary is zero respectively to the boundary. With the shallow water equations a logarithmic velocity profile over the depth is assumed, where the velocity is zero at the bottom. When a flume experiment such as this one is simulated,

the same no-slip condition should apply at the vertical, closed boundaries. In such an experiment the vertical boundaries has a large influence on the velocity profile, whereas in a river this is of less importance due the lack of vertical boundaries. However, in 3Di this option is not available. By default a free slip condition is applied. Flexible Mesh has the possibility, besides a free slip condition, to use a partial and no-slip condition. When using the partial slip condition one has to set a value for the wall roughness k_s. The following equation can be used to calculate this value,

$$C = (32 \cdot g)^{0.5} \log_{10} \frac{12}{k_s/R}, \tag{6.1}$$

or, rewriting the equation,

$$k_s = 12 \cdot R / \left(10^{C/\sqrt{32 \cdot g}}\right) \tag{6.2}$$

With R the hydraulic radius and C the Chezy value, which is known from Blokland (1985). Using the above formula k_s can be calculated, which is $k_s = 0.2$mm for this particular case.

6.3.2 Constant turbulent viscosity

Flexible Mesh has the option to implement a constant value for the turbulent viscosity. By default this value is set to $1\text{m}^2/\text{s}$, which is usually much higher than it would be in practice. A quick estimation for the turbulent viscosity can be obtained by $\nu_t \approx 1.6 \cdot 10^{-3} h u_m$. Another possibility is the usage of an Elder or Smagorinsky model that calculates the turbulent viscosity, which then depends on space and time. These approximations are explained in Section 6.3.4.

With the bottom shear stress that is calculated it is possible to get a value of the turbulent shear stress $\overline{u'w'}$. The computed value can then be compared with the experimental mean value of Blokland (1985). When the turbulent viscosity is known from the results or input as well, then together with the known velocity of the simulation, the following equation can be solved,

$$\overline{u'v'} = \nu \frac{\partial \bar{u}}{\partial y}, \tag{6.3}$$

which results in another turbulent shear stress $\overline{u'v'}$. This can be compared with the experimental values as well.

6.3.3 Secondary flow

One of the important processes when considering a bend, is secondary flow. This process results from the unbalance between centrifugal and pressure forces in an intersection. Due to secondary flow more momentum is transported to the outer part of the bend resulting in a higher velocity at this part than the inner bend. If it is not taken into account it

would mean that the flow velocity at the outer bend is underestimated, while the velocity at the inner bend is overestimated. By usage of a parametrization in Flexible Mesh, it is possible to take the effects of a secondary flow into account. A more detailed description of this approach can be found in Deltares (2015a).

6.3.4 Elder and Smagorinsky

The importance of 3-dimensional processes depends in some cases on the grid resolution. Using a coarse grid, it might be possible to exclude the 3-dimensional processes, since they will be averaged out. However, when the resolution of a grid becomes higher, these 3-dimensional processes need to be approximated (Madsen et al., 1988). The eddy viscosity is one of the processes that is depended on the grid size. In case that the grid size is larger than the water depth, the sub-grid eddy viscosity is less important, since it is limited due to friction dominated eddies. However, when the grid size is smaller than the water depth, this does not apply anymore (Madsen et al., 1988). In these cases it is better to use additional expression that represent sub-grid processes. Elder (1959) derived an expression for depth-averaged flows to take this eddy viscosity into account, which is as follows for a 2-DH model,

$$\nu_t = \frac{1}{6}\kappa u^* H. \tag{6.4}$$

u^* is the turbulence shear velocity, H the water depth and κ the Von Karman constant ($\approx$ 0.4). Besides an expression when averaging over depth, another one is also needed due to horizontal averaging over a grid cell when it is of the same order as the water depth. This will result in additional dispersion and eddy viscosity. This is done with the Smagorinsky sub-grid model. An extra term is added in the equations that contains the stresses due to phenomena that take place on scales smaller than the grid size (Smagorinsky, 1963).

$$\tau_{ij} = \nu_t \left(\frac{\partial \bar{v}_i}{\partial x_j} + \frac{\partial \bar{v}_j}{\partial x_i} \right), \tag{6.5}$$

with the sub-grid viscosity ν_t defined as

$$\nu_t = (C_s \Delta_f)^2 \sqrt{2 S_{ij} S_{ij}}, \qquad S_{ij} = \frac{1}{2} \left(\frac{\partial \bar{v}_i}{\partial x_j} + \frac{\partial \bar{v}_j}{\partial x_i} \right), \tag{6.6}$$

where C_s is the Smagorinsky constant, usually between 0.1 and 0.2, Δ_f the grid size.

6.4 Results

In order to compare the simulation results with the available data, the same cross sections as in the experiment (Figure 6.1) are used for comparison. In total six different simulations are taken. Each of them has other physical parameters that are implemented, see Table 6.2. In Section 6.2 a comparison has been done with simulations in Flexible Mesh and 3Di, using multiple grid types. The turbulent viscosity in Flexible Mesh has been set to

zero in these cases, in order to obtain a fair comparison. Hence, this simulation will not be repeated in the upcoming sections. Since the results of using a curvilinear grid agreed better with the experimental data, only this grid is applied in the next simulations.

In most simulations a grid with 10 cells in the width will be used. Two exceptions are the simulation in 3Di, where more insight needs to be obtained in the convergence after Section 6.2, and the default simulation in Flexible Mesh. The coarsest grid of both programs is presented in Figure 6.2. The differences between grid generation of both packages is clearly visible here.

Options	Simulation					
	1	2	3	4	5	6
No slip		X				
Partial Slip			X	X	X	X
Secondary Flow						X
Elder					X	
Smagorinsky		X	X		X	
Viscosity	X			X		X

Table 6.2: Implemented parameters in simulations

Table 6.2 presents the multiple simulations that are done. When there is a "X" mark in a cell it means that this parameter is used. Each of the results is investigated separately. Simulation 1 is an exception for this, where 3Di is already compared with Flexible Mesh. Both simulations use their default values in this case (3Di has no variable parameters), which shows how the most simple cases are compared with the experimental data. After this all the obtained results are analyzed with each other. This will provide insight in the influence of these physical parameters.

6.4.1 3Di

In Section 6.2 a convergence test has been done for 3Di and Flexible Mesh in order to compare the results for a Cartesian grid. In order to obtain more insight in this convergence of 3Di, three extra resolutions are taken into account. In Section 6.2 the number of cells in the width have been $N = 5$, $N = 10$, and $N = 20$. Since the water levels belonging with $N = 10$ turned out to be higher than both $N = 5$, and $N = 20$, these new resolutions are needed to investigate this. Figure 6.9 and 6.10 present respectively the water levels and velocity of multiple cross sections.

Though more insight is obtained in the convergence of 3Di, it is still unpredictable how the water levels and velocities behave per resolution. Considering the water levels in Figure 6.9 one can see that the water levels are increasing with higher resolution up to $N = 10$. Hereafter the water levels start to decrease. Applying the highest resolution $N = 40$ even gives the results that are most deviated from the experimental data, while one would expect them to be closest to the data. This might be the result of 3Di converging to another value, which is slightly lower than the given data.

Another noticeable point is the velocity profile difference between the numerical results and the measurements. For the first few cross sections the profile resembles the measure-

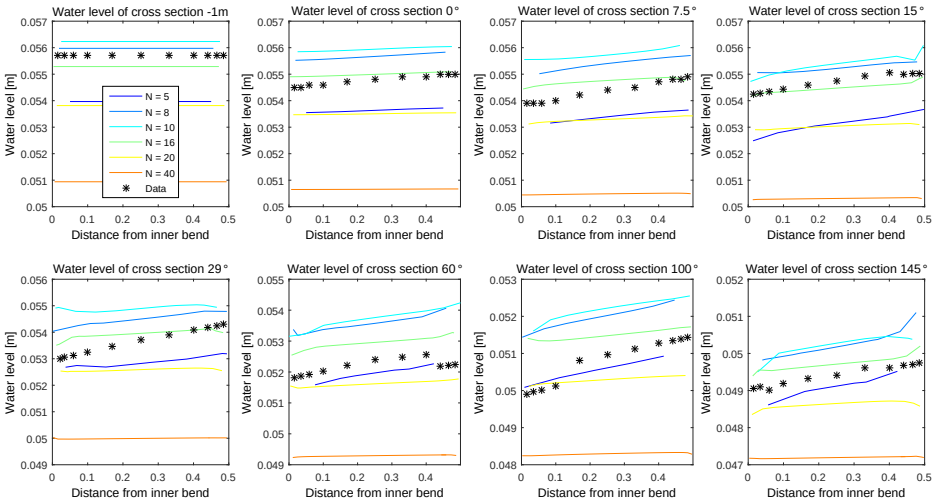

Figure 6.9: Water levels in cross sections indicated in Figure 6.1 with multiple grid resolutions in 3Di compared with measurements

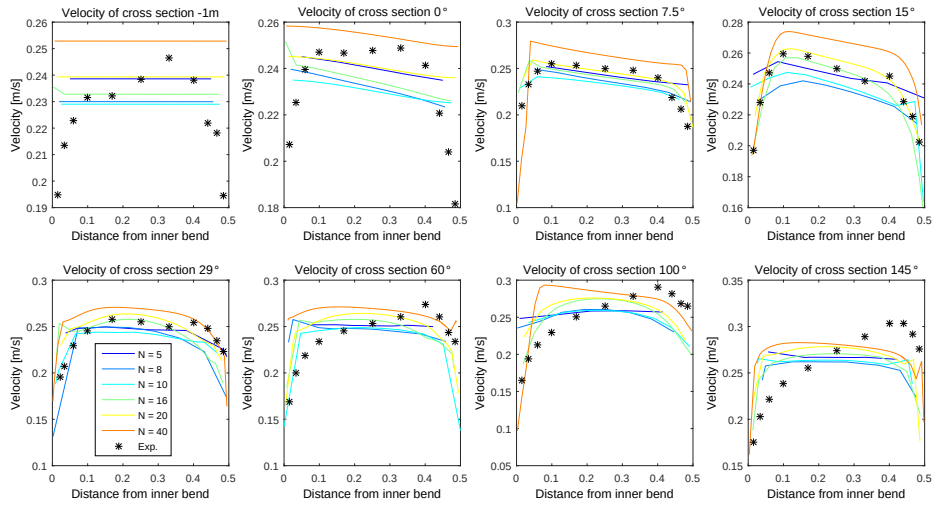

Figure 6.10: Velocities in cross sections indicated in Figure 6.1 with multiple grid resolutions in 3Di compared with measurements

ments. Here it can be seen that the profile shapes more like the data with increasing resolution. When further proceeding in the bend one can see from the data that the maximum velocity is going from the inner to the outer bend. However, for the numerical results this is not the case. The maximum velocity remains more at the inner bend. Most likely is this the results of the missing 3-dimensional processes as secondary flow. Since this package is originally developed for the simulation of flooding, where this process is compared to other processes not important, it is not taken into account. For this particular case secondary flow has more influence on the hydrodynamics compared to flooding, which results in the distinct velocity profile of the measurements compared to 3Di.

6.4.2 Simulation 1: default

Starting point for the upcoming simulations in Flexible Mesh is using only default values. Hence, free slip at the vertical, closed boundaries, no addition from secondary flow, Smagorinsky and Elder, plus the viscosity is set to $1\text{m}^2/\text{s}$. Just as in Section 6.2, these results will be compared to 3Di. The remaining simulations will only be compared with the available measurements and other simulations of Flexible Mesh. Figure 6.11 presents the water levels, whereas Figure 6.12 represents the velocities.

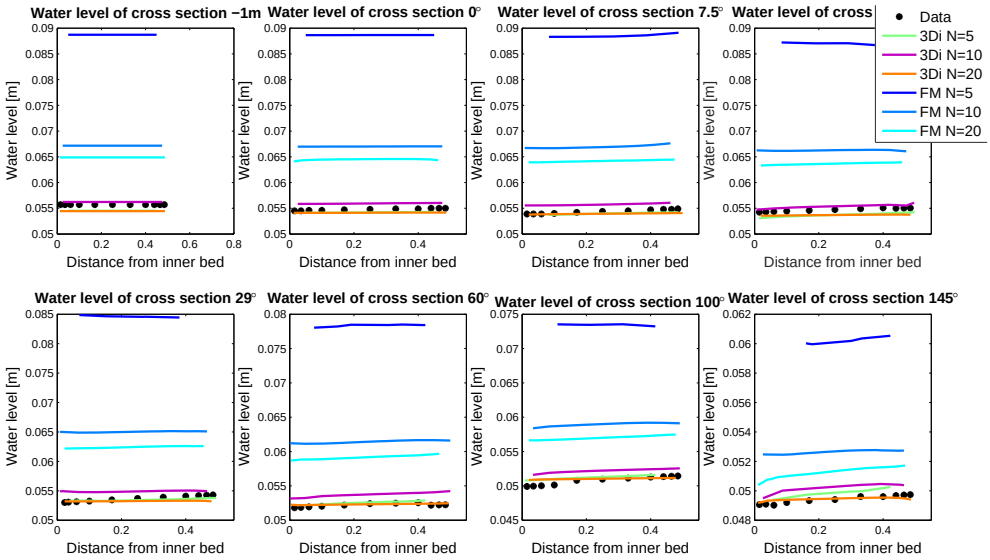

Figure 6.11: Water levels in cross sections indicated in Figure 6.1 for a curvilinear grid in FM and Cartesian grid in 3Di for multiple grid resolutions

Results show that the values of both the water levels and velocities are agreeable with the measurements, though the shape of the velocity profile is more off. The latter is the result of using a free slip condition, instead of no-slip. Section 6.3.1 has explained that, especially in a flume experiment such as this one, a no-slip condition can have a high influence on the velocity profile. The fact that a free slip condition is applied in 3Di, but a parabolic velocity profile arises, is explained in Section 6.2. Furthermore, it can be seen that the water levels of Flexible Mesh are converging to a value that is slightly lower, $\mathcal{O}(10^{-3})m$, than the measurements. This is similar to 3Di, where the value seems to converge to a lower value as well.

6.4.3 Simulation 2: Smagorinsky and no-slip

In the second simulation the constant turbulent viscosity is set to zero, while the Smagorinsky option is used to calculate the eddy viscosity. In Section 6.3.4 it is seen that this value is depended on time and space. Since these simulation will run until a steady state is reached, the eddy viscosity will only depend on space. In case both a constant turbulent viscosity and Smagorinsky is used, these values will be added together. The same applies when using Elder. Smagorinsky can be used in Flexible Mesh by setting the Smagorinsky

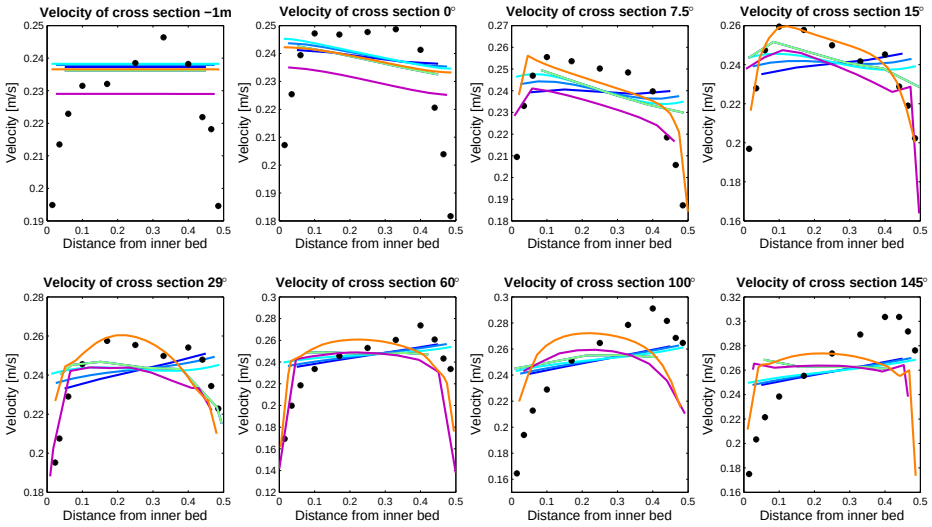

Figure 6.12: Velocities in cross sections indicated in Figure 6.1 for a curvilinear grid in FM and Cartesian grid in 3Di for multiple grid resolutions

constant. For this simulation its value is set to 0.1 (Deltares, 2015a). In combination with Smagorinsky, a no-slip condition is applied.

In Figure 6.14, where the velocities are plotted (dark blue line for this case), it can be seen that it appears as if the no-slip condition is not applied. Whether this is the result of a wrong input, or a bug, is not known. In order to investigate whether this is also the case with another value of the viscosity, a constant eddy viscosity is used that is equal to the average of Smagorinsky, $\nu_t = 1.543 \cdot 10^{-5} \mathrm{m}^2/\mathrm{s}$.

Using this combination, it can be seen that the no-slip condition is visible in the velocity profiles of Figure 6.14, where the light blue line represents the simulation with a constant viscosity. For cross section 0° till 29° the profile of the numerical model coincides quite well with the experimental data. Considering the results further downstream the bend, the velocity profile of the measurements has its maximum velocity moved to the outer bend. For the numerical results this is not the case. The same results have been visible in the simulations of 3Di and of Flexible Mesh before. Again, it can either be the result of missing 3-dimensional processing, or due to modeling in 2DH, where assumptions have been made to go from the Navier-Stokes equations to the shallow water equations that are not valid. Another observable situation is that while the velocity profiles of the first cross section coincide best with the data, the results of the water levels overlap better with the last three cross sections. At least when using a constant viscosity instead of Smagorinsky. For the other cross sections the water levels of the simulation are a bit lower than that of the experimental data. When using Smagorinsky, these are even lower than the results with a constant viscosity. Hence, in this case it seems better to use a no-slip condition in combination with a constant viscosity.

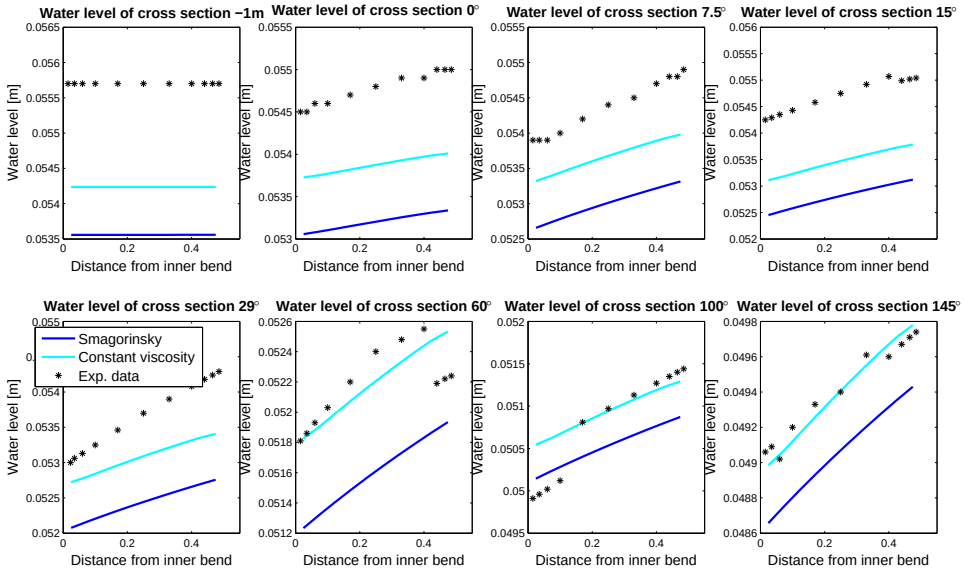

Figure 6.13: Water levels in cross sections indicated in Figure 6.1 for $N = 10$ in FM where a constant and variable viscosity is applied with free slip conditions

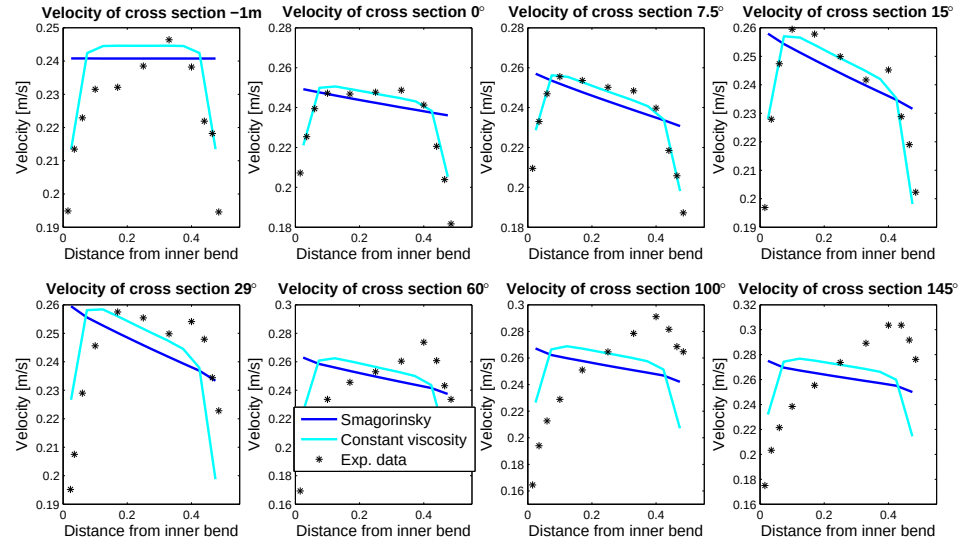

Figure 6.14: Velocities in cross sections indicated in Figure 6.1 for $N = 10$ in FM where a constant and variable viscosity is applied with free slip conditions

6.4.4 Simulation 3 & 4: Smagorinsky/constant viscosity and partial slip

In Section 6.4.3 it is seen that using Smagorinsky in combination with a no-slip condition resulted in a velocity profile that does not agree with the no-slip condition. Using a constant viscosity instead, with the average viscosity of Smagorinsky, the results are closer to the experimental data and the velocity profile is more agreeable with the no-slip

condition. In both simulation 3 and 4, a partial slip condition is used for the closed boundaries at the side. Whereas simulation 3 the Smagorinsky constant is set to 0.1 instead of zero, simulation 4 uses a constant eddy viscosity. Since these type of simulations with a no-slip condition have been compared in Section 6.4.3, they are also compared in this section. Just as before, the mean viscosity is calculated from the simulation using Smagorinsky, which is used as input for the simulation with a constant viscosity. The mean viscosity is equal to $5.7765 \cdot 10^{-6}\mathrm{m}^2/\mathrm{s}$, which is a factor 10 smaller than when using a no-slip condition. To find out the influence of this value, both a value of $10^{-6}\mathrm{m}^2/\mathrm{s}$ and $10^{-4}\mathrm{m}^2/\mathrm{s}$ is chosen as input for the viscosity.

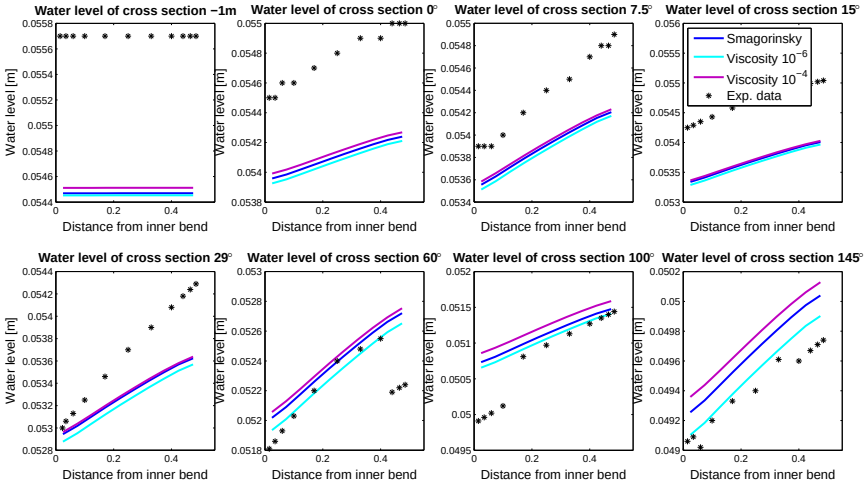

Figure 6.15: Water levels in cross sections indicated in Figure 6.1 for $N = 10$ in FM where a constant (2 values) viscosity is applied with partial slip conditions

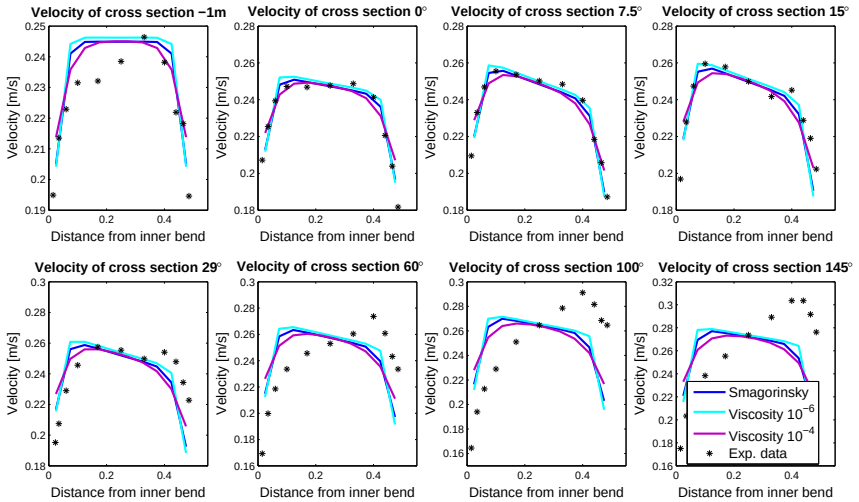

Figure 6.16: Velocities in cross sections indicated in Figure 6.1 for $N = 10$ in FM where a constant (2 values) viscosity is applied with partial slip conditions

Both the differences between the water levels and the velocities for all simulation is quite

small, and can be neglected. Comparing the velocities gives that the middle (linear) part of the profiles are more or less the same. The main dissimilarity is in the transition from the side to the middle part of the profile. With a higher viscosity the transition is smoother than lower viscosities. The viscosity of a fluid represents the measure of its resistance to flow. Hence, a higher viscosity means more resistants, resulting in a smoother profile.

6.4.5 Simulation 5: Elder, Smagorinsky and partial slip

Simulation 5 is similar to simulation 3, where Smagorinsky and the partial slip condition are applied, but with the additional process Elder. This results in an extra addition to the eddy viscosity that is already calculated by Smagorinsky, $\nu_t = \nu_t + \nu_{Elder}$. Calculating the mean viscosity of simulation 5, results in $1.2065 \cdot 10^{-4} \mathrm{m}^2/\mathrm{s}$. Though in this simulation the viscosity depends on space, results are expected to be similar to the previous results of simulation 4. Here a constant viscosity has been used of $10^{-4} \mathrm{m}^2/\mathrm{s}$. Figure 6.17 and Figure 6.18 present the results of simulation 5 in combination with the measurements and results of simulation 3. The latter are plotted as well to show the influence of adding more viscosity by using Elder. It can be seen that the differences between the velocity profiles are similar to the previous results of simulation 3 and 4, confirming the expectation. Furthermore, it seems that the velocity profiles without Elder agree more with the experimental data in the first few cross sections.

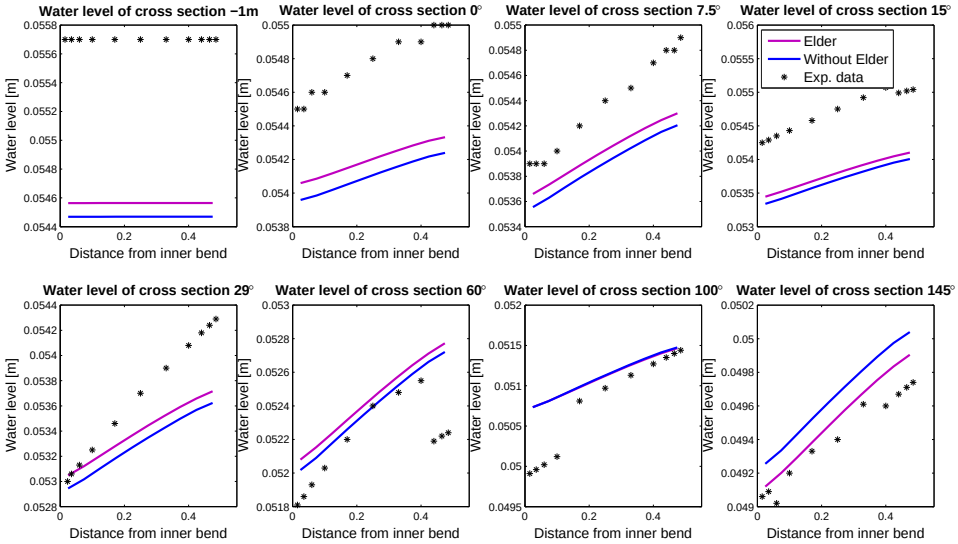

Figure 6.17: Water levels in cross sections indicated in Figure 6.1 for $N = 10$ in FM where a variable (2 values) viscosity is applied with partial slip conditions

6.4.6 Simulation 6: Secondary flow, constant viscosity and partial slip

Using the results of simulations 3-5, this simulation will be split into two variations. One of the simulations is done with a constant viscosity, set to $10^{-6} \mathrm{m}^2/\mathrm{s}$, and the other one with Smagorinsky, $C_s = 0.1$. The mean viscosity of the latter is of the same order as the

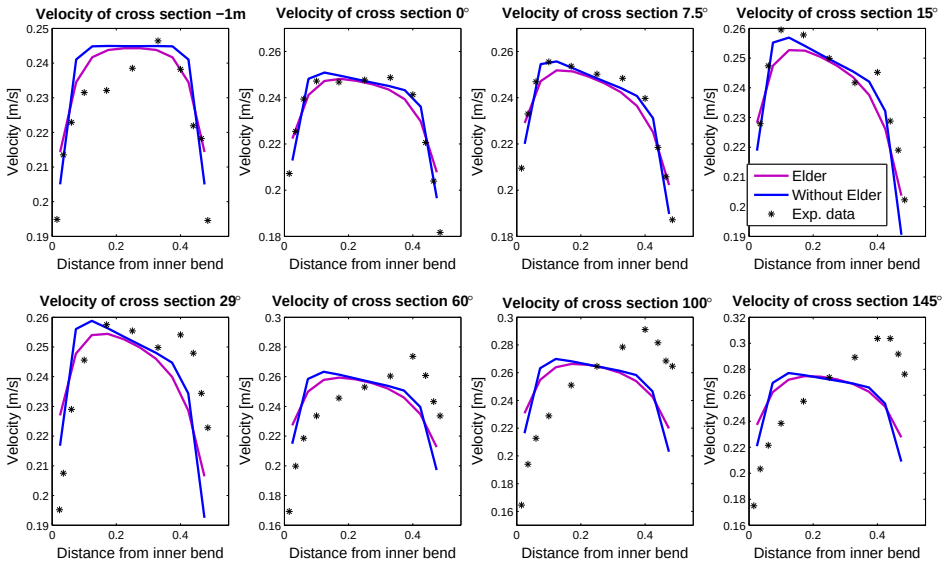

Figure 6.18: Velocities in cross sections indicated in Figure 6.1 for $N = 10$ in FM where a variable (2 values) viscosity is applied with partial slip conditions

constant viscosity. As an addition to simulation 3 and 4, an additional parameter is used to take secondary flow into account. Results are plotted in Figure 6.19 and Figure 6.20.

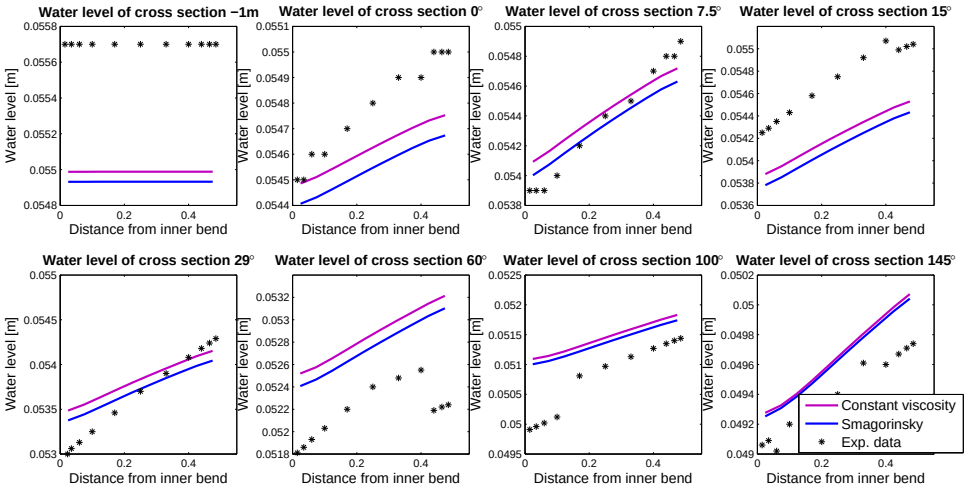

Figure 6.19: Water levels in cross sections indicated in Figure 6.1 for $N = 10$ in FM where a constant viscosity is applied in combination with secondary flow with partial slip conditions

It is interesting to see that the velocity profile agrees a bit more with the experimental data than the other simulations. The maximum velocity is still closer the inner bend than the outside bend. However, the profile in the inner bend of the numerical results matches quite well with the data. Whereas for the other simulations this was not the case. The other velocity profiles are a bit underestimated. Nevertheless, the water levels are for

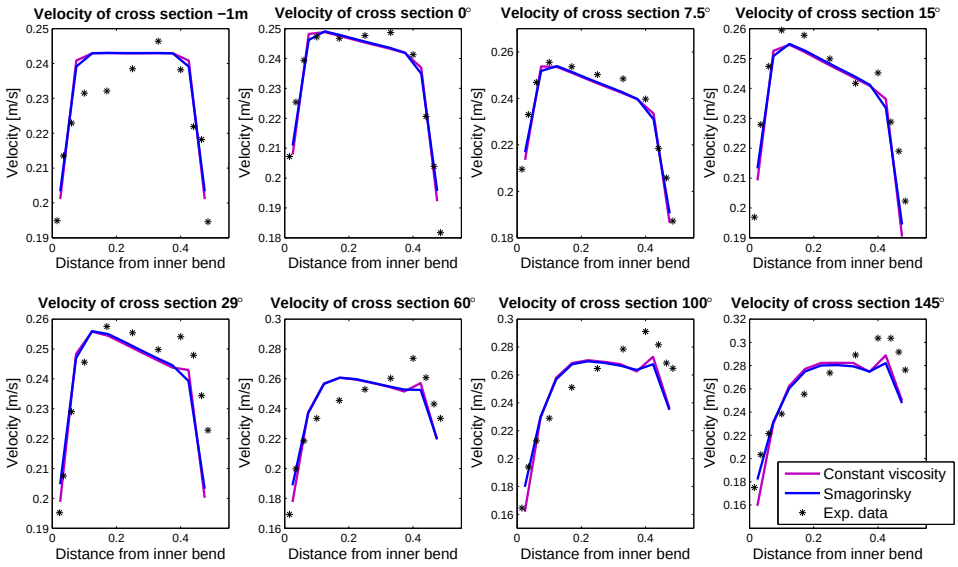

Figure 6.20: Velocities in cross sections indicated in Figure 6.1 for $N = 10$ in FM where a constant viscosity is applied in combination with secondary flow with partial slip conditions

these profiles a bit higher which result in a better estimation than before.

6.4.7 Analysis for combined results

In this section observations of all simulations in Flexible Mesh are brought together. In Sections 6.4.2 to 6.4.6 the results of Flexible Mesh have been investigated. Most results have been investigated separately. However, in some simulations there have been observations that have been seen in multiple results. One of these observations that is noticeable, can be seen in simulations 2-6. In these simulations the viscosity has been varied. An instability in the outflow part of the area can be found. With an observation station in the domain the water levels of three points are captured. The first point is in the right straight part of the bend, the second in the bend itself, and the third in the left straight part of the bend. In Figure 6.21 the course of the water level is presented. Whereas the black and red line are steady, the blue line shows instabilities. These instabilities arise as soon as the viscosity is changed. Often the viscosity is set higher than physically normal in order to prevent instabilities. However, when a higher viscosity is used, as is applied in simulation 1, the results are not agreeable with the measurements. Turning on other physical processes have not had influence on these results. With a high viscosity as in simulation 1, the resistance of the flow is too high.

Considering the viscosity itself, there are a few observations that can be made. In the simulations multiple runs have been done with a constant viscosity, while others have a variable viscosity. Using Smagorinsky, where the viscosity depends in space, it can be seen in Figure 6.22 that for each slip condition the viscosity is different. The main difference in viscosity between these conditions is near the walls. With free slip the viscosity is almost

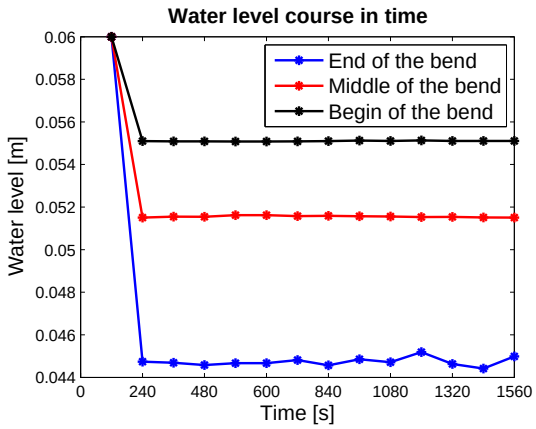

Figure 6.21: Water level course in time for three observation stations with a low turbulent viscosity set

everywhere uniform in the width. One can see a small difference between the viscosity in the straight parts and in the bend. However, in the left corner at the bottom of Figure 6.22c the viscosity seems random in size. Considering the colorbar that belongs with it, it can be seen that the difference is up to 15 times the viscosity in the parts before. This is hard to explain, since it is not occurring with the other slip conditions. If the viscosity of the no- and partial slip condition is compared with free slip than one can see that for the first two conditions the viscosity is higher near the walls than in the middle. Comparing this between the no- and partial slip gives that with the latter the viscosity against the wall is slightly lower than a bit further away from the wall. Then it decreases again when looking more away from the wall. This is not the case with a no-slip condition. Here only the nearest flow links to the wall have a higher viscosity value while all the other flow links are approximately the same. Hence, the type of boundary condition has a high influence on the viscosity when using Smagorinsky.

The viscosity itself can subsequently be used to calculate the shear velocity $\overline{u'v'}$, as is seen in Equation (7.2). Before this equation can be used, the gradient of the streamwise velocity in the $y-$direction has to be known. With the figures of velocity profiles belonging to each simulation this can be computed. Since the gradient is not a constant over the whole width when using slip conditions, only the middle part of the profile is considered where the profile is linear. With the gradient known, the shear velocity $\overline{u'v'}$ can be computed. The results are presented as the difference between the shear velocity of the experimental data and the numerical results. For each cross section the second-norm error is computed with these differences.

$$\|x - \hat{x}\|_2 = \left(\sum_{i=1}^{N} x_i - \hat{x}_i \right)^{1/2}, \tag{6.7}$$

where $N = 11$, since there are 11 points that contain experimental data. $\hat{x}$ represents the numerical data, while x the experimental data. Besides this second-norm error, the relative second-norm error is also computed. This will provide more information about how close, or far off, the numerical results are with the experimental data. This is

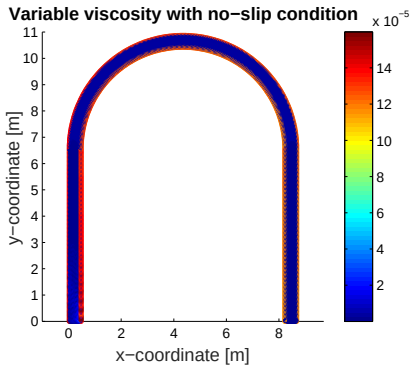

(a) Viscosity with no-slip

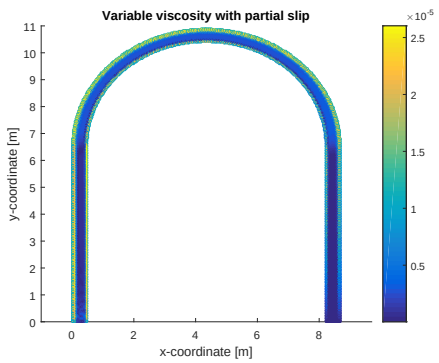

(b) Viscosity with partial slip

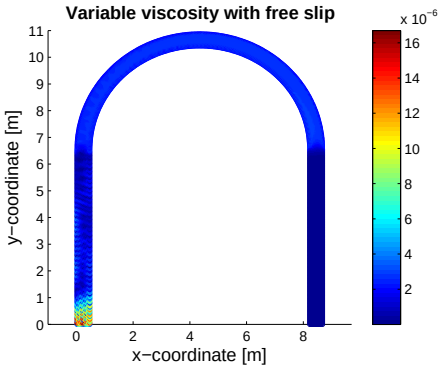

(c) Viscosity with free slip

Figure 6.22: Variable viscosity calculated with Smagorinsky for all slip conditions

calculated as

$$\frac{\|x - \hat{x}\|_2}{\|x\|_2}. \tag{6.8}$$

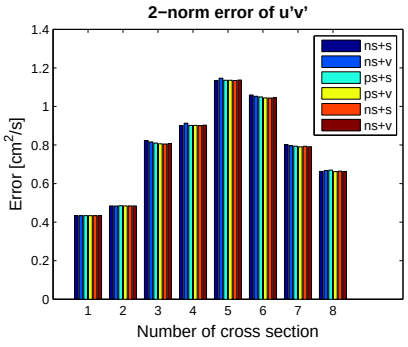

(a) Error of $\overline{u'v'}$

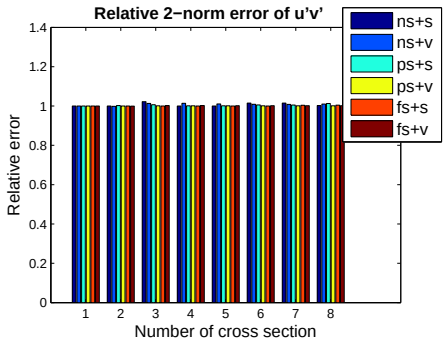

(b) Relative error of $\overline{u'v'}$

Figure 6.23: Comparing $\overline{u'v'}$ of numerical results and experimental data by calculating the (relative) 2-norm error

These errors can be found in Figure 6.23. The first thing that stands out, is the fact that

for all simulations the results are approximately the same. Both for the second-norm error as the relative second-norm error. Considering the latter, it can be seen that for each of the simulations its value is about 1. This means that the numerical results are not even near the value of the experimental data. For each of these simulations, it is seen that the water levels and velocities are quite near the ones from the experiment. However, when comparing $\overline{u'v'}$ it seems that this is not the case. The values of the numerical results are a order of 10/100 smaller. Thus, almost neglectable, which lead to

$$\frac{\|x - \hat{x}\|_2}{\|x\|_2} \approx \frac{\|x\|_2}{\|x\|_2} = 1. \tag{6.9}$$

Since the velocities are quite agreeable with the experimental results, it can be concluded that the viscosity is underestimated. Using a higher viscosity as input results, however, into a velocity profile as seen in Figure 6.18, when using both Elder and Smagorinsky. It underestimates the velocity as some points, but the gradient in the middle is approximately the same. The mean viscosity increases from $5.7765 \cdot 10^{-6}$ to $1.2065 \cdot 10^{-4}$, which could lead to a more realistic value of the shear velocity. However, this is not the case. Considering the shear velocity when using Elder, the (relative) error is larger than before. Considering only at the hydrodynamics in this case, it seems not to influence the results in a negative way, but with complexer simulations it might be.

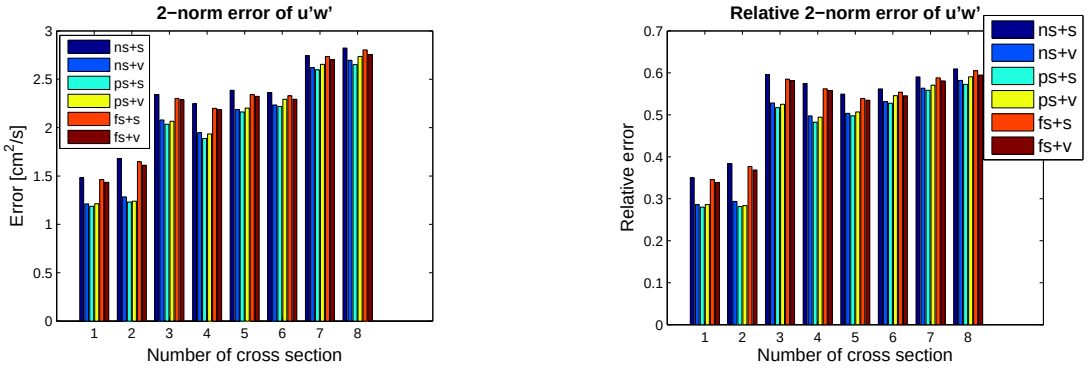

(a) Error of $\overline{u'w'}$

(b) Relative error of $\overline{u'w'}$

Figure 6.24: Comparing $\overline{u'w'}$ of numerical results and experimental data by calculating the (relative) 2-norm error

The last thing that is compared for this case is the shear velocity $\overline{u'w'}$. This can be easily calculated by

$$\overline{u'w'} = \tau/\rho. \tag{6.10}$$

The results are presented in the same way as the shear velocity $\overline{u'v'}$, and can be seen in Figure 6.24. These figures show a clear difference between the six different simulations. Both in the second-norm error and relative error the simulation with partial slip in combination with Smagorinsky results in the smallest errors. If the relative error of $\overline{u'w'}$ and $\overline{u'v'}$ are put next to each other, the shear velocity $\overline{u'w'}$ is better approximated than $\overline{u'v'}$. Its values are clearly below one. The first two cross sections have the smallest

(relative) error. The errors become larger when we look further into the bend. Since the bottom stress is depended on the velocities, which are farther off the measurements when considering cross sections more downstream, the bottom stress will also contain larger differences. Hence, resulting in a higher relative and second-norm error of $\overline{u'w'}$.

6.5 Conclusion and discussion

Two types of grids have been compared in this chapter as a starter, a Cartesian and curvilinear grid. The results for these grids in each packages were different, either in the water levels or velocities. A Cartesian grid in Flexible Mesh when simulating bends is not recommended. Although a higher resolution led soon to a much better approximation of the water levels and velocities, the errors are still higher than when applying a curvilinear grid. Although 3Di uses a Cartesian grid as well, the results are closer to the experimental data than Flexible Mesh. With a pixel subgrid that has the minimum resolution ($N_p = 10$), the differences with the experimental data are smaller than using Flexible Mesh. Using a higher resolution for the pixels improves the results quite a lot, while the sizes of the grid can be kept the same. Using a smaller grid size, while having the same resolution of pixels led only to a small improvement of the results. Thus, for similar results the computational time can be lowered due to this approach.

Whereas Flexible Mesh has multiple options to influence the simulation, 3Di has none of these options. This makes 3Di easy for usage. Since Flexible Mesh has multiple options there is the possibility to calibrate the results. This can be done in Flexible Mesh by adjusting viscosity, slip conditions, etc. This gives that Flexible Mesh has many buttons that can be turned in order to change the results to belonging. However, calibrating the results means that the same model is not necessary valid for another situation. Hence, this chapter is devoted of researching these physical variables to investigate how well these results are without any calibration.

The results of 3Di were quite dependent on the grid. Refining these grid cells have led to unexpected results. Up to a refinement factor where $N = 10$, the water levels have been increasing. Here after the water levels start to decrease as if they converge to another value than first expected. In the end it appears that the value it converges to is slightly smaller than the measurements. Even though this occurs, the results coincide quite with the experimental data, even though certain processes are not available.

Using only default values in Flexible Mesh gives almost the same results as in 3Di. Only the velocity profile is not correct, since it uses a free slip condition. Adjusting this into a no-slip or partial slip condition results into a better profile, if the viscosity is changed as well. One can use Smagorinsky and Elder for a space dependent viscosity. This has the advantage that one does not have to guess for the viscosity in order to run a simulation. Otherwise, the chance exists that the viscosity is guessed too high or low which gives results that are physical not correct. With this simulation it is seen that the viscosity is underestimated if one approaches the shear velocity $\overline{u'v'}$. Increasing the viscosity manually too high leads to a velocity profile that looks like simulation 1.

The velocity profile of the last three cross sections is for none of the results correct, whether this is in Flexible Mesh or 3Di. The secondary flow has a high influence on

the velocity profile if one proceeds further into the bend. Since this is a 3-dimensional phenomenon, it cannot be completely simulated with a 2DH model. It can be seen in the velocity profile of 3Di that maximum velocity shifts more to the outer bend, but this is not as extreme as the experimental data shows. Without turning on the secondary flow option in Flexible Mesh, 3Di plots the velocity profile nearer to the experimental data than Flexible Mesh. Though this is not due to the inclusion of secondary flow, since it is not in 3Di. When turning this option on in Flexible Mesh, one can see a slight change in the profile. It looks more as the results in 3Di after this. So, using the option secondary flow gives that the velocity profile is better approximated.

Chapter 7

Flow over weir

Before modeling the river Elbe with Flexible Mesh and 3Di, another test model is done. A straight channel with a weir is considered. This weir is modeled with two different methods. With the first method it is modeled with a supergrid model, hence, the weir is represented in the bathymetry. The second method is using a subgrid model. With an extra input file the weir can be located anywhere and a special numerical scheme is applied for horizontal advection. With an analytical solution, where hydrostatic pressure is assumed, the results of both 3Di and Flexible Mesh are compared. With these results also a convergence test is done, followed by adding physical processes one by one. This chapter ends with a conclusion and discussion that can be used for the modeling of the river Elbe. These simulations are performed with D-Flow FM Version 1.1.148.41897, and 3Di - subgrid Version 0.1.1.1958.

7.1 Flow geometry

In order to study the influence of the grid on the results, the model is as simple as possible. This gives that friction and viscosity are not taken into account. Furthermore, the bottom does not have a slope and the channel is rectangular. The water flows due to the difference in water levels at the boundary conditions. The water level on the left side of the channel is fixed at 3m, while at the right side it changes in time. Its starting point is 2.95m. Each time interval of 3 hours it goes down by 0.05m until it reaches 2.75m. This will give different submergence degrees, hence, different flow regimes. The time for each water level is chosen such that the model has enough time to become steady. With a submergence degree of 0.8 and 0.75 the flow on top of the weir is supercritical. For the other degrees this is subcritical.

In the middle of the channel a groyne is modeled. This can be done for both programs in two different ways. In one of the options, a groyne is represented in the bathymetry, while for the other option an extra input file is needed with the location of a fixed weir and the crest height. The energy loss is then calculated at that location with a special numerical

scheme. When a groyne is captured by enough grid cells, and it is represented in the bathymetry it is called a supergrid model. Usually a minimum of three grid cells on the crest is needed to solve the hydrodynamics in a detailed way. Otherwise it is better to use the extra input file, which is called subgrid modeling. When using 3Di, a third option is used which is subgrid pixel modeling. As seen in the previous chapter, a minimum of four pixels in one grid cell is needed. With these pixels the volume inside a grid cell can be calculated more precisely. The influence of these pixels will become more clear in Section 10.3, where the size will vary in each model.

When a weir is placed exactly in the middle of a cell, it is placed on both sides of the cell instead of just one, see Figure 7.1. Instead that a fixed weir is solved at the given location, it is placed near the closest face of a cell and solved there (Deltares, 2015a), see Figure 7.1. This is done so that no computational cells are cut by a weir, which makes the computation easier. In this case, it resulted in an error of 30% when the weir is placed in the middle of a cell with $dx = 12$m. So, if by accidence the weir is placed in the middle of a cell, this results in quite an error. This can be fixed by replacing the weir just a few centimeters. This will result in the top figure of Figure 7.1 instead of the bottom figure, where the cell is surrounded by the fixed weir.

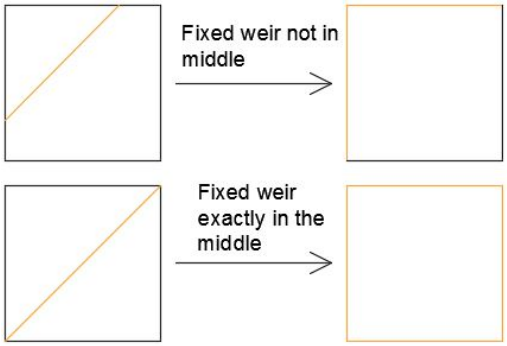

Figure 7.1: Example of how a fixed weir is located to the cell faces

The groyne that is modeled, has a crest height of 2 meters, a crest width of 3m and is in total 15m long with a slope of 1:3. Figure 7.2 shows how the groyne is presented in both Flexible and 3Di when using a grid size of $dx = 6$m and $dx = 3$m and how it is in reality (black line). In this figure the minimum amount of pixels is used to represent the bathymetry. If a higher resolution is available of the bottom one can use more pixels per grid cell. Due to these pixels the bottom of 3Di is better represented than when using Flexible Mesh. Another difference between the two figures is that the figure of Flexible Mesh contains two lines, a blue and red line. The latter is used in calculations for the volume, while the flow area and friction term depend on the values of the blue line (see Chapter 3 for these terms).

Weirs can be distinguished in roughly two types, a short-crested and broad-crested weir. With the latter streamlines on top of the weir have the space to become parallel to each other, which gives that a hydrostatic pressure distribution can be assumed. In case of a short-crested weir the streamlines stay curved, hence, this kind of distribution is not valid. If one does assume this distribution, then the velocity on top of the crest can be underestimated in case of a constant discharge, as is seen in Chapter 3 where the

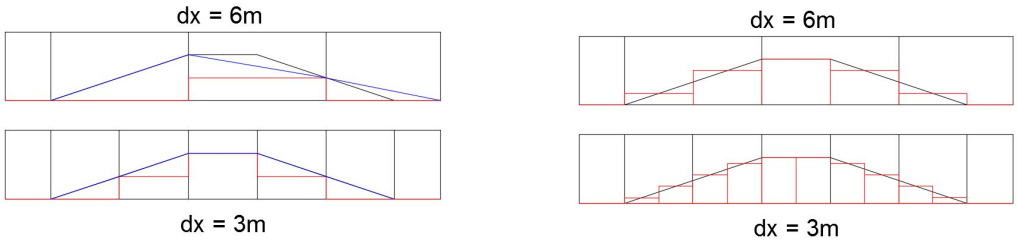

(a) Groyne representation FM

(b) Groyne representation 3Di

Figure 7.2: Groyne representation for various grid sizes in FM and 3Di

distribution is explained. To decide which type of weir we have, one has to calculate the ratio H_w/L, where H_w is the energy head above the weir and L the width of the crest. Although it differs per source between which values this ratio should be, the smallest upper limit found so far is (Boiten and Pitlo, 1982), $0.075 \leq H_w/L \leq 0.45$. It is expected, based on analytical data, that the energy head is around $1 - 1.1$ on top of the weir. This would give, in case of $H_w = 1.1$, $H_w/L = 0.36$, which is below the upper limit. However, since it is close to the upper limit and per source this upper limit is different, it might be that this value is too high in order for the hydrostatic pressure distribution to be valid.

In order for the hydraulic assumption to be valid, at least 5 cells on the crest of the weir are needed in order to create straight streamlines. For this model only one of the grid sizes that is used, satisfies this condition. It is also recommended to use this amount of cells on the crest in order to obtain a accurately answer (van Kester, 2015) In the next sections modeling obstacles in the bathymetry will be called supergrid modeling to make it easier to distinguish between the two types of modeling. However, usually it is supergrid modeling if at least 5 cells on top of the crest are used to simulate the obstacle. Which is in the case here only if $dx = 0.75$m.

7.2 Convergence study

For the convergence study multiple grid sizes are used when modeling the weir. Both models have the same sizes in grid cells: $dx = 12$, $dx = 6$, $dx = 3$, $dx = 1.5$ and $dx = 0.75$ meter. For 3Di some extra runs are done with different pixel sizes. These pixel sizes for grid cell $dx = 12$m, could differ from $dx_p = 6$m (largest value) and $dx_p = 0.75$m (smallest value). First comparisons are done with a fixed pixel size of $dx_p = 0.75$m (or $dx_p = 0.375$m if $dx = 0.75$m) and a varying grid size for 3Di and FM. In the next section pixel sizes will be varied as well. Results of the discharges for the convergence study are given in Figure 7.3. When using a grid size of $dx = 3$m, or smaller, the groyne is represented correctly in length and shape (for friction and flow area). Of course, this groyne is chosen such that it fits perfectly in certain grid cells. In this case the crest of the groyne is always on a cell face. This gives a better idea of the influence of the grid cells around a groyne or other obstacle. In the next section the results are compared if the groyne is placed 6 meters further to the right. When modeling a random river, the grid is usually not perfect aligned around obstacles, so this will show how the placement of a grids influence the result.

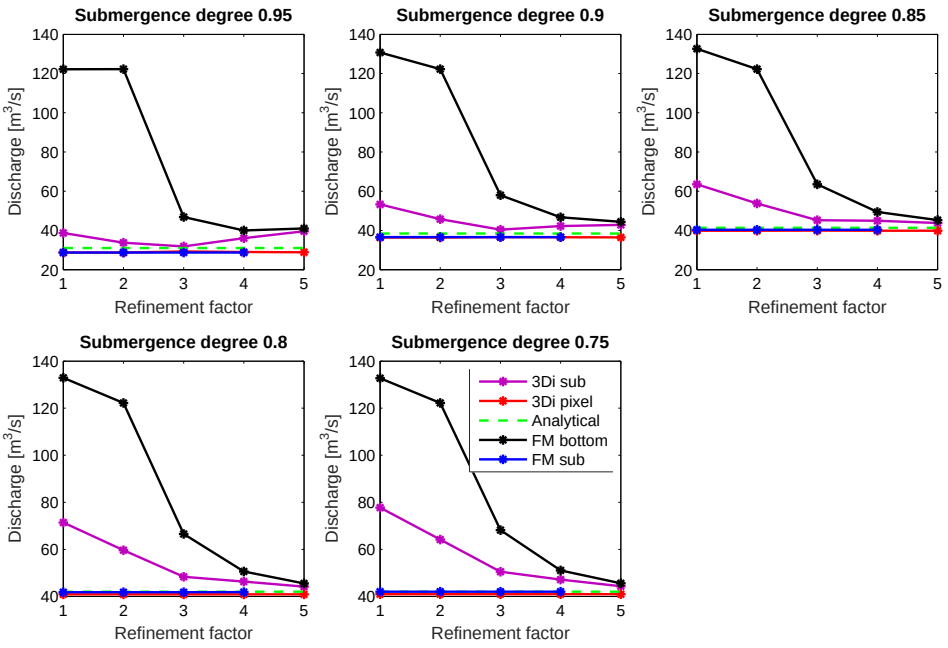

Figure 7.3: Convergence of discharges in FM and 3Di using a subgrid or supergrid model for various submergence degrees

If we first take a closer look at the figure that belongs to a submergence degree of 0.95, it can be seen that it appears that the lines belonging to a supergrid model converge to the analytical value. However, the discharge of the yellow line that belongs to the model in 3Di, increases again when a higher refinement factor than 2 is applied. The same seems to happen in FM (black line), although it is almost negligible and it happens with a higher refinement factor than 4. Both models appear to converge to another value than the analytical value. In order to find out why this happens, the most important processes of this model need to be known. With a sudden decrease in the bottom there will be a detachment point, which means that there will be energy losses. Thus, we will take a closer look at the energy head of this model in the $x-$direction. Roughly the model can be split into three parts, before the weir, on top of the weir and behind the weir. For the first two parts energy conservation should apply, while for the last two parts it is momentum conservation. In the figure below the energy head is presented. At $x = 162$, the slope of the weir starts until $x = 168$, where the crest begins. At $x = 171$ an expansion starts until $x = 177$. From here on the bottom will be flat again.

The energy head is calculated as follows,

$$E = h_1 + \frac{u_1^2}{2g} = h_2 + z_c + \frac{u_2^2}{2g}, \tag{7.1}$$

where h_1 and u_1 are respectively the water level and velocity in front of the weir, h_2 and u_2 are on top of the weir and z_c is the crest height. Both of the super- and subgrid models the energy head is plotted, together with the analytical value. Above results are from models with $dx = 1.5$m. Immediately it can be seen that the energy head

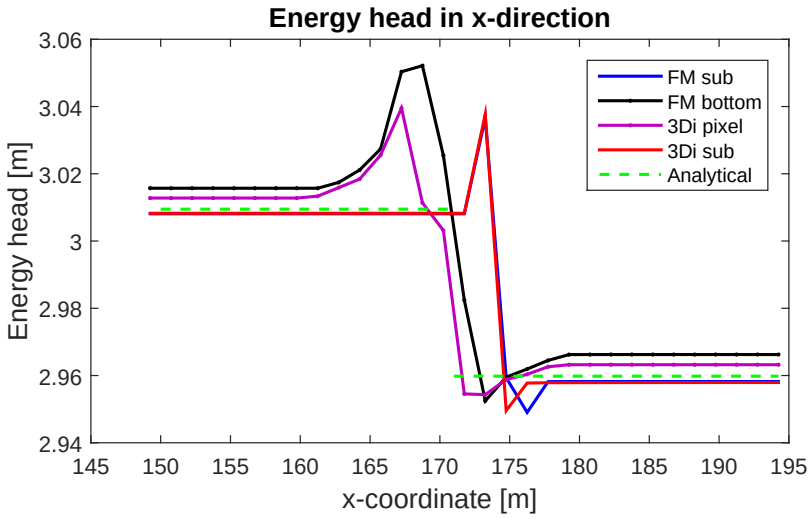

Figure 7.4: Energy head in FM and 3Di using a subgrid and supergrid model for $S = 0.95$

has an increase at the point where the weir starts. As said before, between part 1 and 2 there should be energy conservation, so both programs introduce energy while this is physically not possible. For both programs it can be due to the discretization fo the advection term. According to Stelling and Duinmeijer (2003) an increase of energy can occur if conservation of momentum is applied when using many types of advection schemes, which is a consequence of wrongly assuming a hydrostatic pressure on top of the weir. So even though the upper limit of 0.45 in Section 8.1 is not reached, it seems that this distribution is not valid for this simulation. When using the subgrid method, another advection scheme will be used locally. It is explained before that fixed weirs are placed to the nearest face of a cell. At this face conservation of energy is applied between the two neighbor cells instead of momentum. The local energy loss after the weir is calculated with the velocities in front and after the weir. For Flexible Mesh and 3Di the energy heads of subgrid modeling are quite the same. Hence, in both programs a certain energy increase can be seen, even though energy conservation is applied. This can be explained by the interpolation of velocities that takes place. Both Flexible mesh and 3Di use a staggered grid, hence, water levels on the center and velocities on the faces of a cell. When plotting the results, however, both of them are placed at the cell center. Interpolating the velocities can result in values that are not correct with the water level in the cell center, which result in an over- or underestimated energy head.

When the submergence degree decreases this additional energy increases. Since the water level is constant in front of the weir and decreases only a bit when the weir begins, the velocity has the most influence on this. With a lower submergence degree, the discharge, hence the velocity, increases since the water level is fixed. This term is squared, hence, influences the energy head even more. Even though the energy addition is higher, it appears that the convergence of discharge goes faster with a lower submergence degree. The numerical values are closer to the analytical values. Still, for both 3Di and Flexible Mesh, it seems that they are converging to a higher value than the analytical value.

Another noticeable point is that for each grid size when modeling the groyne with a fixed weir (subgrid), the discharge is almost the same. Differences are of the order 10^{-2}, hence

negligible. For both 3Di as Flexible Mesh this is the case. While the results of modeling the weir in the bathymetry is dependent on the grid size, the subgrid method is always applicable since it is independent of the cell sizes. Usually the resolution of a grid in rivers is never high enough to capture obstacles such that supergrid modeling is possible. Thus, in these cases it is better to implement fixed weirs. In order to get more insight in the energy losses and gains, three other variations of the previous model are simulated. Each of them are explained below together with their results.

Groyne with a wider basis

The first variation of the previous model is a groyne with a variable width. Together with the original width, five weirs are modeled. Each weir has the same height, but the width, hence slope, is different. With a lower slope the velocity differences between two cells in the $x-$direction are lower, hence, the advection term becomes smaller for each cell, since the cell sizes will be the same. This might result in a lower energy increase than before.

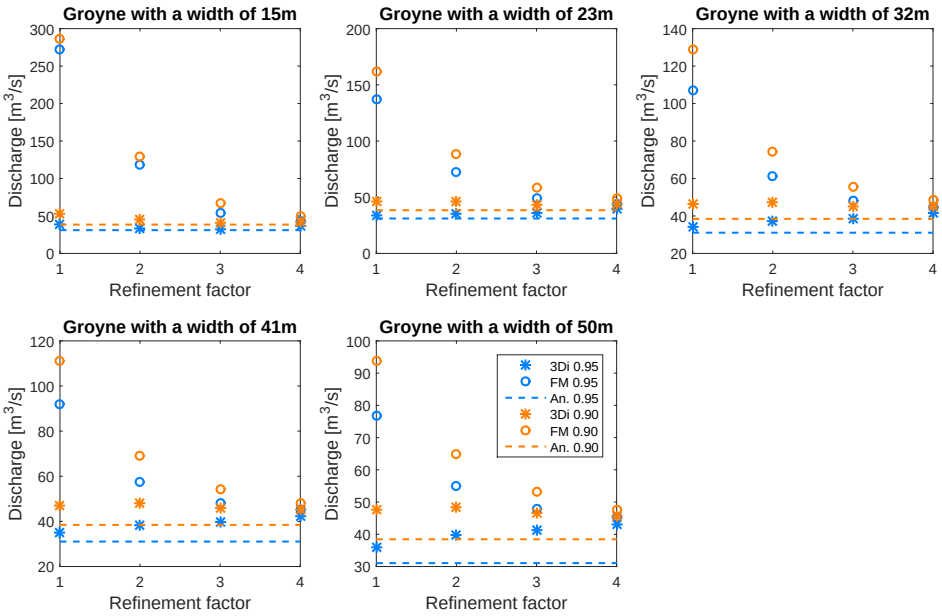

Figure 7.5: Convergence of discharges in FM and 3Di with an obstacle represented in bathymetry for $S = 0.95$ and $S = 0.9$ for various width

The obtained results are from a submergence degree $S = 0.95$ and $S = 0.90$, to see if this variable has some influence on them. In Figure 7.3 it is seen that the convergence is different between these two submergence degrees. For a lower degree the discharge appears to converge as one would expect. With $S = 0.95$ the discharge decreases up to a certain refinement factor, where after it increases. As said before, with a wider groyne the slope is smaller. Additional to this, more grid cells capture the groyne when it is wider. As a result the convergence of the discharge goes faster than with the original width, see Figure 7.5. The presumption that the values seem to converge to another value seem true for both submergence degrees. For $S = 0.95$ the discharge converges to a value around

$Q = 44\text{m}^3/\text{s}$, both for 3Di and Flexible Mesh, which is about 40% off with the analytical value. Since the discharges of 3Di increase even more than before, it can be expected that the energy level increases as well. Either the peak becomes higher, or the extra energy is smeared out over the entire length of the channel. Figure 7.6 presents the energy heads of both Flexible Mesh and 3Di. For 3Di the energy increase is mostly spread over the entire length. Hence, the velocity is overestimated for the whole model. On the other hand, for Flexible mesh the peaks decreases a bit. Over most of the length energy does not depend much on the groyne's width. From the energy head the width of the groyne can be derived. At the beginning of the groyne, where the advection term is not zero anymore, the energy increases until the crest of the groyne. This is also visible in 3Di. Although varying the width has some influence on the energy head, it does not prevent the energy increase.

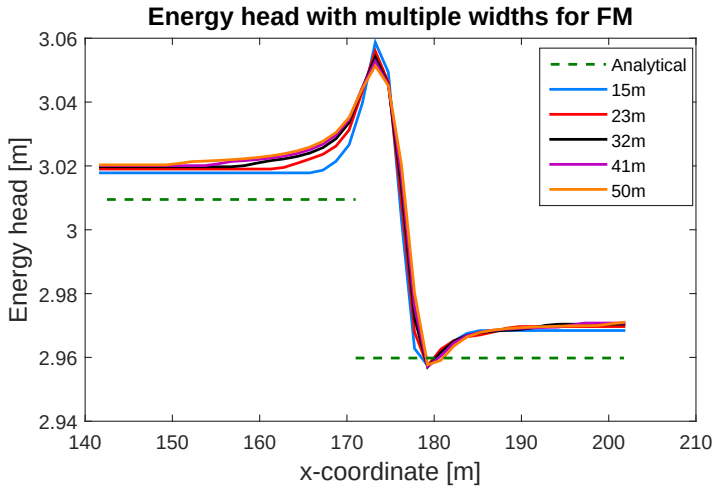

(a) Flexible Mesh

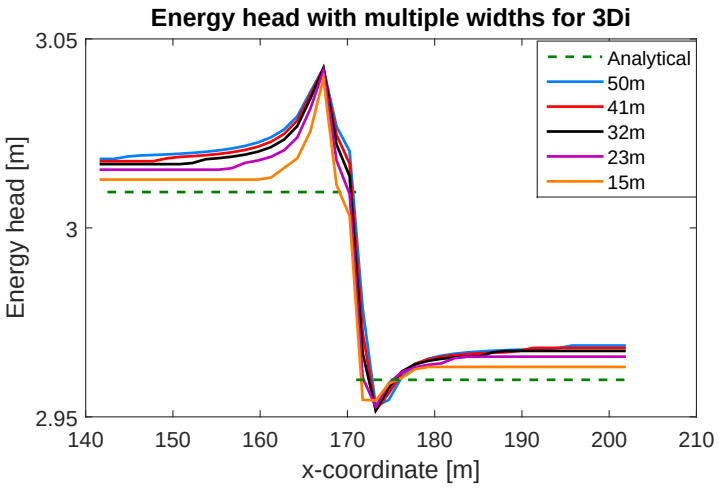

(b) 3Di

Figure 7.6: Energy head in FM and 3Di with an obstacle represented in bathymetry for $S = 0.95$ and $S = 0.9$ for various width

Groyne with a sudden expansion

This model is almost the same as the previous variation. Hence, there are multiple widths of the weir modeled and the height is the same. The only difference is that the weir has a sudden expansion instead of gradually. In the first model an energy increase is seen followed by the loss due to the expansion of the flow area. Whereas the previous model researched the effect of a slope's steepness, this model will take into account the effects of a sudden expansion. Usually when modeling a weir, it ends with a sudden expansion instead of a smooth transition. The analytical value is based on this type of weir. Using this sudden expansion gives that the model is more similar to the analytical approach.

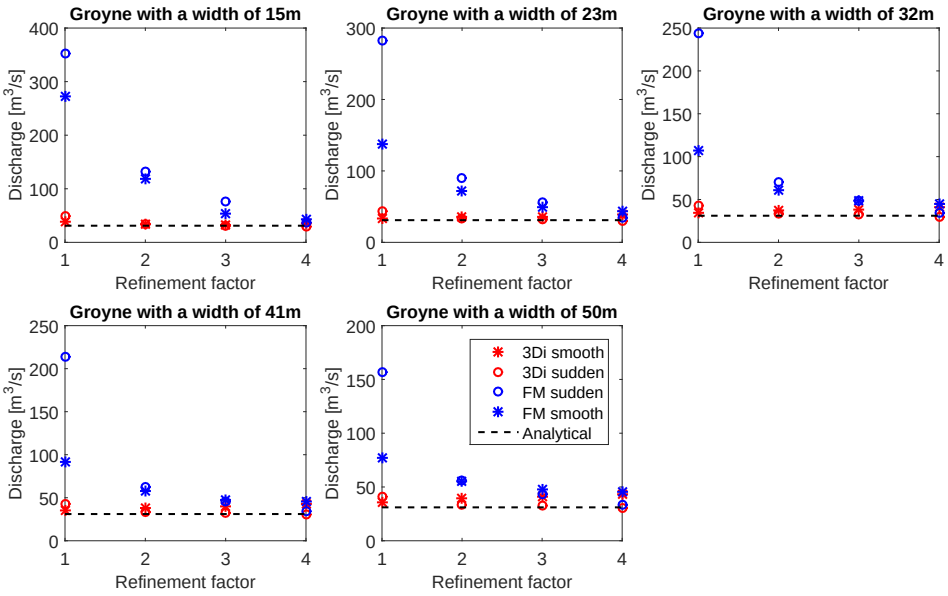

Figure 7.7: Comparison of convergence of discharge in FM and 3Di for an obstacle with a smooth or sudden expansion for $S = 0.95$ and varying width

Comparing the smooth and sudden expansion, it can be seen (especially with a width of 50m) that the discharge converges more to the analytical value for both programs. For a refinement factor of 4 the difference between two numerical values (smooth and sudden) is about 40% ($(x_{smooth} - x_{sudden})/x_{smooth}$). If we look at the energy over the length, it can be seen that the peak is smaller for a sudden expansion than a smooth expansion. Not only this peak is a bit smaller, but most of all the energy head over the length is lower with a sudden expansion. Both for Flexible Mesh and 3Di it is closer to the analytical value. Even though there is still an increase of energy locally at the groyne, hence, the velocities and/or water levels do not agree with the analytical values, they are more agreeable over the rest of the length. Physically it is expected that more energy is lost with a sudden expansion. In these cases, the energy losses for and after the groyne are the same everywhere, but locally at the groyne from the highest to lowest energy peak, energy losses are higher with a smoother bottom. With the depth-averaged equations in a model it is more difficult to distinguish depth variations, which can results in a under or overestimation of energy loss.

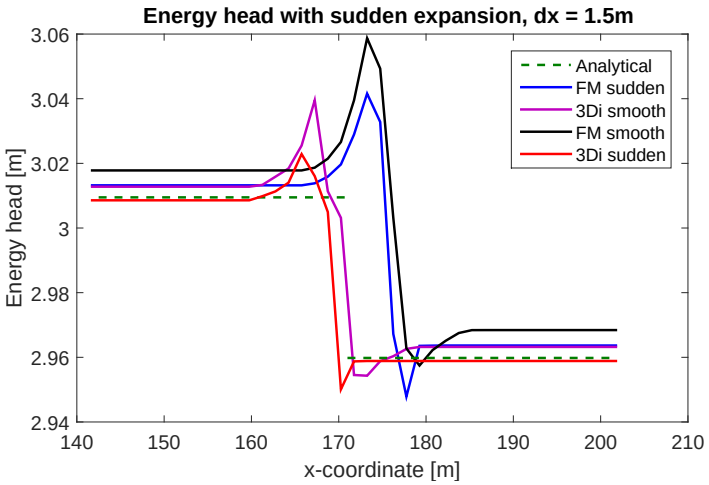

Figure 7.8: Comparison of energy head in FM and 3Di for an obstacle with a smooth or sudden expansion for $S = 0.95$ and varying width

Combination of fixed weirs and use of bathymetry

Whereas the previous variations were a continuation of the research of energy increase, this model will combine both fixed weirs and use of bathymetry (subgrid and supergrid, if the resolution is high enough to capture the weir). When modeling rivers its bathymetry is either interpolated in the net nodes (Flexible Mesh) or it is needed in a special file determining the pixel sizes and heights (3Di). Either way, the groynes and other obstacles are present in the grid. With a coarse grid these obstacles are too small to be noticed for the cells, hence, a subgrid model is needed to correctly represent these. In case of a finer grid it is possible that these obstacles are better represented by the grid. Also locally refining can result in a better represented obstacle in the bathymetry. In some cases one also wants to use a subgrid model to obtain energy conservation, as energy conservation is not valid otherwise. For both a coarse and fine grid both types of modeling are used to investigate the effects of this combination.

The fixed weir is positioned at two different places when combining bathymetry with subgrid modeling. In one of the simulations it is placed at the first face of the cell where the crest begins. In the other on the second face. For dx = 1.5m this gives that the face is placed at the beginning of the crest and in the middle. For lower resolutions they are placed at the end or even on the slope after the crest. Results of both programs when combining both models gives quite different results. Whereas for Flexible Mesh the differences between placement of the fixed weir is not that significant, the discharges for 3Di are much lower than expected. Placing a fixed weir at the beginning of the crest gives for both programs results that are near the values of only a subgrid model. Placing it at the second cell discharges are suddenly below $20\text{m}^3/\text{s}$ in 3Di. The main difference between these programs are the pixels that are present in 3Di to calculate the volume more precise. Whereas for Flexible Mesh the volume is calculated with the lowest bottom point in a cell. Thus, in Flexible Mesh the volume is probably overestimated, which might result in a higher estimation of the discharge compared to 3Di. If we look at the energy heads for $dx = 3$ and 1.5m, it can be seen that for 3Di the velocities are underestimated

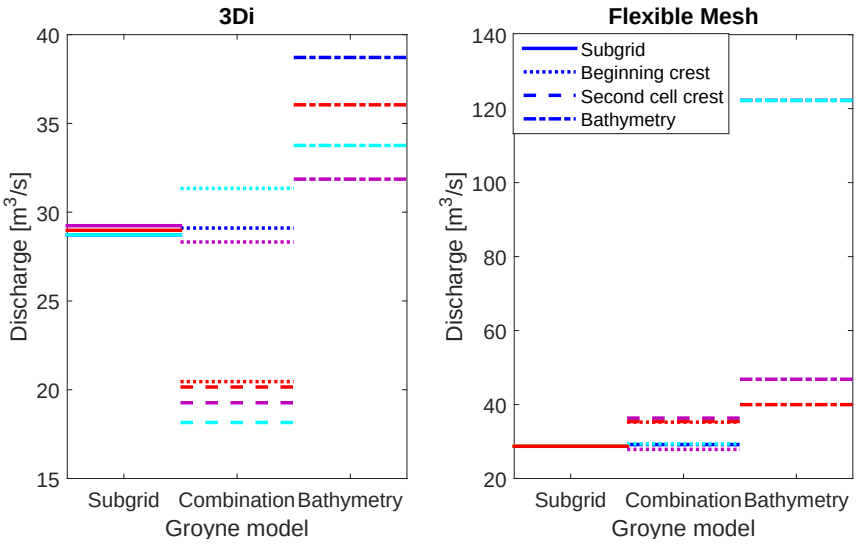

Figure 7.9: Discharge for groyne with a combination of subgrid and bathymetry compared with both models separately: blue = refinement 1, purple = refinement 2, light blue = refinement 3, red = refinement 4

as well. The energy head is below the analytical value. Also the peak is smaller for certain placements of the fixed weir in combination with the bathymetry. The same applies for Flexible Mesh.

7.2.1 Influence of grid placement

In the above models the placement of the groyne was such that the crest was adjacent to at least one face of a cell for all refinements. However, this is not always the case when modeling. Usually one does not have the luxury to place each obstacle at the face of a cell. To show the difference of results with different placements, the groyne is placed 6 meters to the right. Although the results of Figure 7.12 are only for 3Di, the same occurs in Flexible Mesh.

Figure 7.13 shows how the discharge depends on the pixel sizes for both placements. This figure clearly shows the difference for the pixel resolution for both placements.

It can be seen that for grid sizes, except for $dx = 12$m, the equilibrium discharges are closely together. For $dx = 12$m, the values seem to be far of the analytical value with increasing pixel resolution for placement 2. One would expect that for a higher pixel resolution the discharge lies closer to the analytical value that is shown in Figure 7.3. This is not the case here. With a lower resolution the groyne is better modeled than a higher resolution. One of the possibilities in 3Di is that one can give a refinement threshold. This is the maximum bathymetry difference between pixels that is allowed before the program will automatically refine the cells. For this model, locally refinements are turned off, hence, it is not possible for the model to apply this. With a grid size of $dx = 12$m, where most of the groyne is placed exactly inside one grid cell, the groyne is not taken into account for all calculations. With the computation of the volume each pixel cell is used, but for the flow area only the pixels that are adjacent to the face of

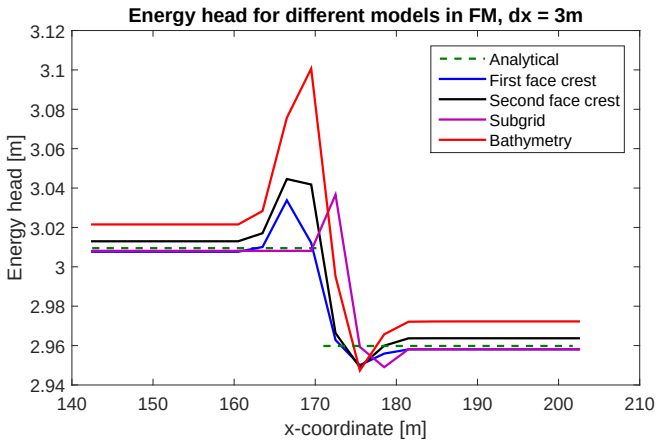

(a) dx = 3m

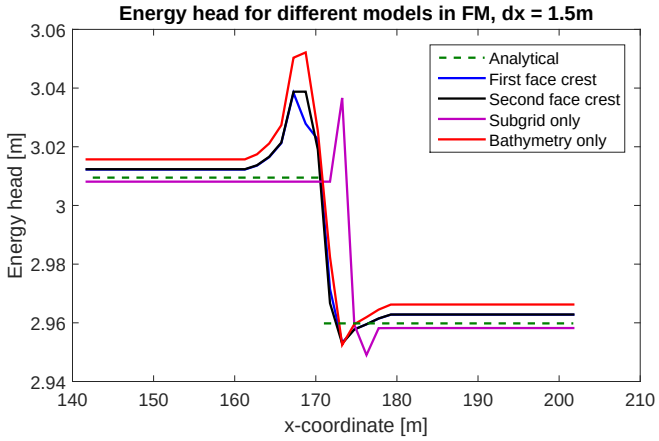

(b) dx = 1.5m

Figure 7.10: Discharge for groyne with a combination of subgrid and bathymetry compared with both models separately for Flexible Mesh

the cell are used. So, when an obstacle like this groyne is placed as in Figure 7.14, it will seem as if there is just a small obstacle when computing the flow areas. This will lead to an overestimation of the discharge. This is why the results in Figure 7.12, for $dx = 12$m, are so different.

Results of placement 1, where the crest of the weir is placed at a cell face, show that discharges for different pixel sizes are closer together than before. Also, for increasing pixel resolution the discharge is closer to the analytical value. Thus, it is recommended to not use one cell size, but use at least two sizes in combination with using the option mentioned before about a refinement threshold.

7.3 Varying model input

The previous cases are simulated without friction and physical viscosity. Numerical viscosity can be in the simulations due to numerical approximations. Chapter 8 will focus

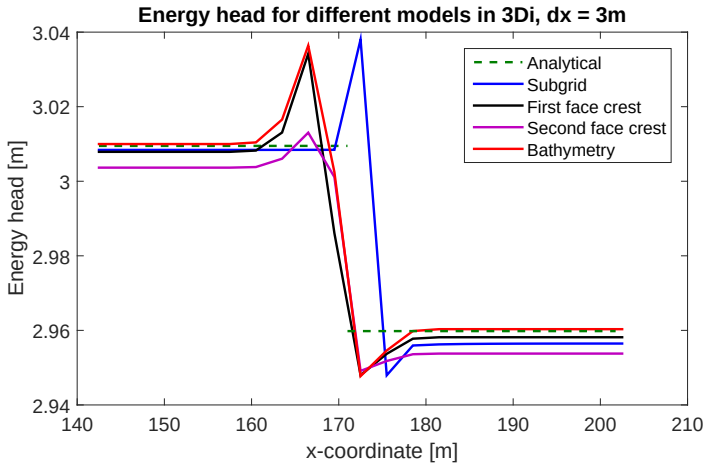

(a) dx = 3m

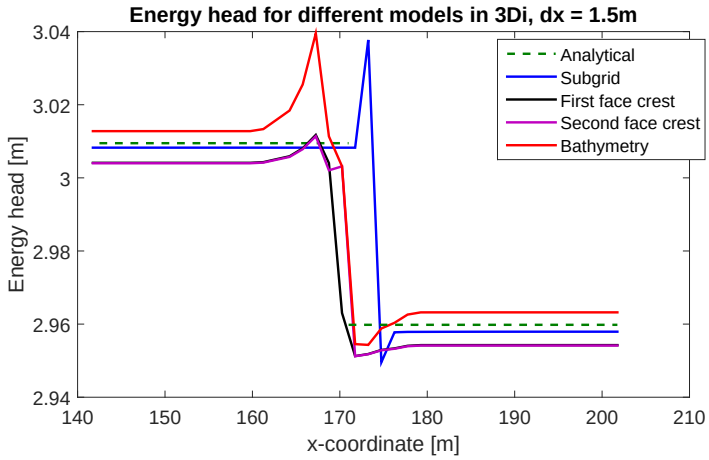

(b) dx = 1.5m

Figure 7.11: Discharge for groyne with a combination of subgrid and bathymetry compared with both models separatelyfor 3Di

more on this subject. The basic equation that applies to the previous cases is as follows,

$$u\frac{\partial u}{\partial x} + g\frac{\partial \zeta}{\partial x} = 0. \tag{7.2}$$

Hence, when the weir influences the surrounding water

$$u\frac{\partial u}{\partial x} = -g\frac{\partial \zeta}{\partial x}. \tag{7.3}$$

Further in front and behind the weir the velocity is constant and there is no gradient in the water level, thus, both terms are zero. In order to make the simulations more as a river, other processes are needed. The first added process is friction, followed by adding a slope in the bottom. These options are done for both Flexible Mesh and 3Di. Hereafter the case in Flexible Mesh is expanded with turbulent viscosity. Based on the equilibrium

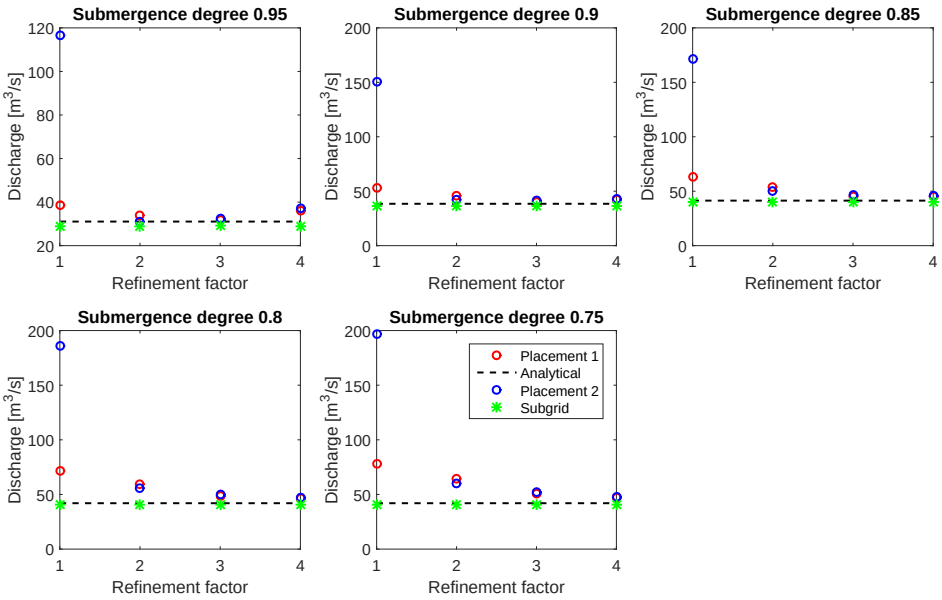

Figure 7.12: Comparison of convergence of discharge with different placements of obstacles in basin in 3Di

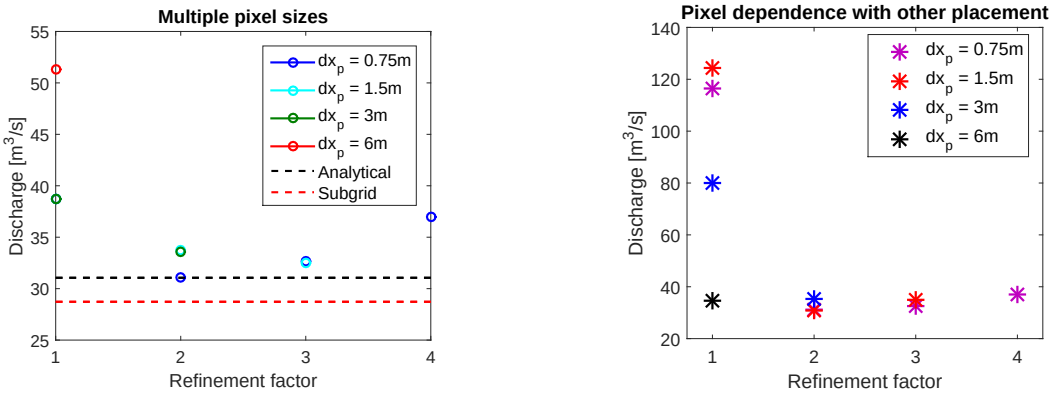

(a) Placement 1 (b) Placement 2

Figure 7.13: Comparison of convergence of discharge for multiple grid sizes and two placements

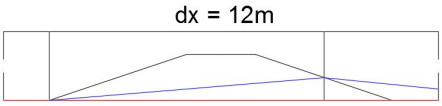

Figure 7.14: Groyne representation in FM with a grid size of $\Delta x = 12$m

discharges that are found with previous results, another inflow boundary condition is chosen. Instead of a fixed water level, a inflow discharge is chosen. When introducing a slope in the model, but still using a fixed water level that is placed at the middle of a

ghost cell, no matter the size of these cell, can lead to a small deviation in the results with multiple grid sizes. Though the deviations will be small, it might be better to keep them out of the simulations. Figure 7.15 shows that the increase of energy is still present, even with another boundary condition. Differences in the energy head that are visible are due to the overestimation of the discharge in the simulation when a water level boundary condition at the inflow is taken.

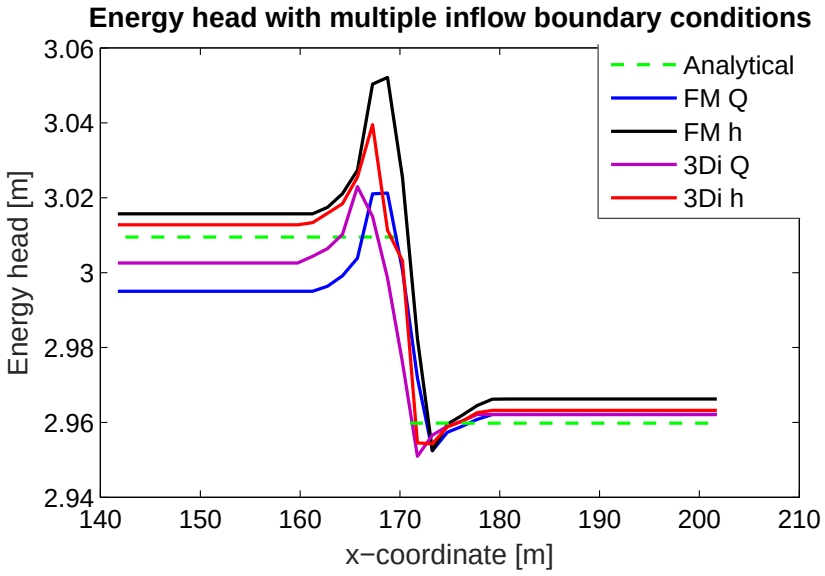

Figure 7.15: Energy head in FM and 3Di for multiple inflow boundary conditions

7.3.1 Friction

The first process that is added to the basic case that is simulated before is friction. Equation (7.2) is expended with an extra term which can be seen in Equation (7.4). In order to get a better understanding of what should differ in the results compared to the previous simulation, an arbitrary small cell that is located in front of the weir is taken. The forces that are applicable on this cell are drawn together with the cell in Figure 7.16. The cell in the top figure presents the situation of the previous simulation, a water level and bottom with no gradient. By taking a friction coefficient larger than zero a force, that is directed to the left in this case, is added. To maintain a balance of momentum in a steady state, another force directed to the right is needed. Whereas both the advection and water level gradient are zero in the first simulation, this cannot be the situation here. Thus, in order to obtain a force to the right a pressure difference, where the pressure is higher on the left side, is expected, see bottom figure of Figure 7.16. Hence, with increasing distance from the inflow boundary a lower water level can be expected. At the same time this results in an increase of the velocity by the mass balance. Furthermore, due to friction there should be an energy loss over the entire length of the model. Compared to the loss behind the weir it will be relatively small.

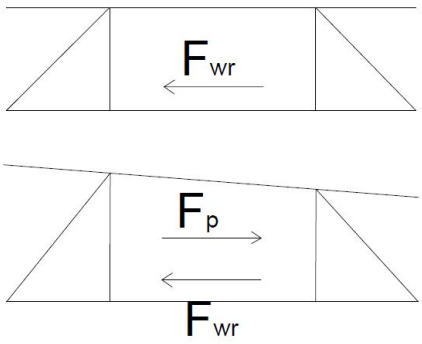

Figure 7.16: Invluence of friction on the results. Forces in cell presented

With Figure 7.16 the following equation applies,

$$u\frac{\partial u}{\partial x} + g\frac{\partial \zeta}{\partial x} + \frac{c_f}{h}u\|u\| = 0. \tag{7.4}$$

Figure 7.17 shows the gradients of both velocity and gradient. With friction as an extra force it is expected that the water level will have a negative gradient, which is indeed the case. While the order of this gradient is not that large, it is a factor 10 higher than the velocity gradient, that is directed the other way around.

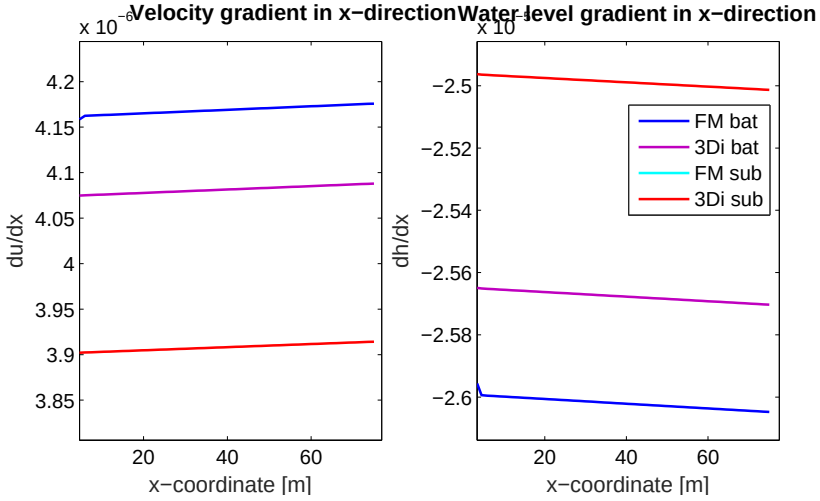

Figure 7.17: Velocity and water level gradients with friction on for subgrid models and obstacles presented in bathymetry

For now, the results that are presented have a submergence degree of 0.95. It is recommended to also investigate lower submergence degree, especially ones where the flow regime is different. In this way both a super- and subcritical flow can be compared.

Considering Figure 7.18, where the energy head is plotted against the $x-$coordinate, it can be seen that over the entire length indeed a loss of energy is present. Still, the increase of energy around the weir is present. Even though the peak belonging to Flexible Mesh bathymetry is slightly smaller compared to Figure 7.15. Friction does have some influence,

but it is not enough to prevent the energy increase. Another noticeable point, is the energy head difference for the subgrid models and implementing the weir in the bottom. Using only a subgrid model results in a higher water level than the other simulation. Although it is just a few centimeters, it might lead to higher differences when multiple weirs are being modeled. Using a Manning roughness coefficient, depended on the hydraulic radius, gives a variable friction over the simulation. Using only a fixed weir means that the hydraulic radius is the same, since the bottom height does not change. Which results in a lower friction term, hence, a higher energy head. When both type of models are combined, as in done in a previous section of this chapter, the energy head is somewhere between both values.

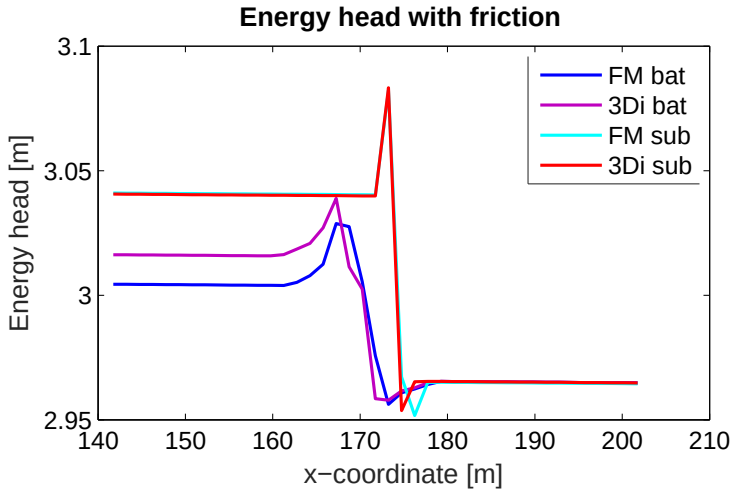

Figure 7.18: Energy head in FM and 3Di using a subgrid and supergrid model for $S = 0.95$ with friction

7.3.2 Friction + bottom slope

Adding a small slope in the bottom does not add any extra terms into the equation that is solved compared to adding only friction. The difference is, that due to a constant slope, the water level will also obtain a slope in these simulations. Each case is simulated until a steady state is reached. In this steady state the slope of the water levels in front of the weir will be the same as the bottom slope. Due to the influence of the weir, this is not applicable to water levels on and close to the weir. Further behind the weir, when its influence is not there anymore, the slope of water is expected to be the same as the bottom slope again.

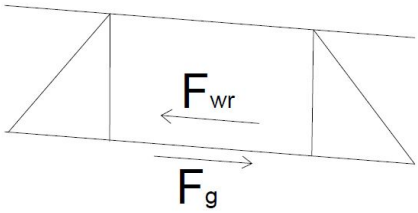

Figure 7.19: Forces in cell with friction on and a slope

With Figure 7.16 the following equation applies,

$$u\frac{\partial u}{\partial x} + g\frac{\partial \zeta}{\partial x} + \frac{c_f}{h}u\|u\| = 0. \tag{7.5}$$

Compared to the previous section, where only friction is added, the results are not changed in any significant way. Of course, by only adding a bottom slope this should also not be the case. Beside that the energy head has decreased a bit, the main difference is that the sign of the velocity gradient changed. In the previous section there is an increase of velocity, while now there is a decrease. This also gives that the waterdepth is increasing over the length. Although only the gradient of the water level is shown, which is still negative, this is not similar to the water depth anymore. Figure 7.19 shows a negative water level gradient, but a constant depth.

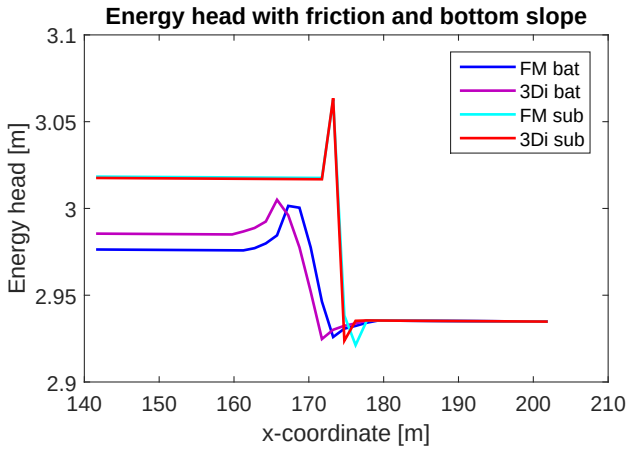

Figure 7.20: Energy head in FM and 3Di using a subgrid and supergrid model for $S = 0.95$ with friction and a bottom slope

7.3.3 Including turbulent viscosity

In Flexible Mesh the simulation is expended by including turbulent viscosity. However, it is expected that introducing a diffusion term will not have much influence on the results. The only gradient that is of importance, is $\partial u/\partial x$ due to the weir that is placed. Other gradients are negligible. The vertical processes that would be highly influenced by adding a turbulent viscosity value, are not simulated in the shallow water equations. This test

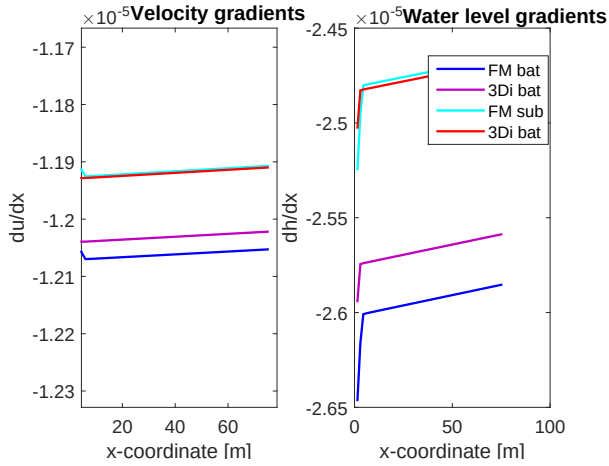

Figure 7.21: Velocity and water level gradients with friction and a bottom slope for subgrid models and obstacles presented in bathymetry

case does not contain processes where the horizontal turbulent viscosity would be of high interest. In the next chapter, this term will be of higher importance. For this test case an inflow of momentum is introduced in still water, where diffusion will be an interesting process to investigate due to this.

$$u\frac{\partial u}{\partial x} + g\frac{\partial \zeta}{\partial x} + \frac{c_f}{h}u\|u\| = \frac{1}{h}\nabla \cdot \left(\nu h \left(\nabla v + \nabla v^T\right)\right). \tag{7.6}$$

When applying viscosity, both a constant and space dependent viscosity is used. The first value is estimated as in Chapter 6, $\nu_t \sim 1.6 \cdot 10^{-3} u_m h$, while the second value is calculated by the program itself with Smagorinsky. As described before, it is not expected that both will change the results that are presented at in this chapter. Figure 7.22 shows the space depended viscosity. At places where more turbulence is expected, a higher estimation of the viscosity is taken. In this case around and on the weir. It also be seen that the value of the viscosity is dependent on the grid size. Both the velocity gradients and grid size are taken into account when the turbulent viscosity is calculated with the Smagorinsky formula (Deltares, 2015a).

As expected the results, when using multiple values for viscosity, are not that different from each other. A slight difference is present in the energy head before and on the weir, where the difference is higher when the viscosity is higher (Smagorinsky estimates almost in the whole area a higher viscosity). This gives that the diffusivity term is slightly higher as well, and the balance changes a bit. However, in the next chapter the variance can be expected to be higher, since the diffusivity is of importance in this case.

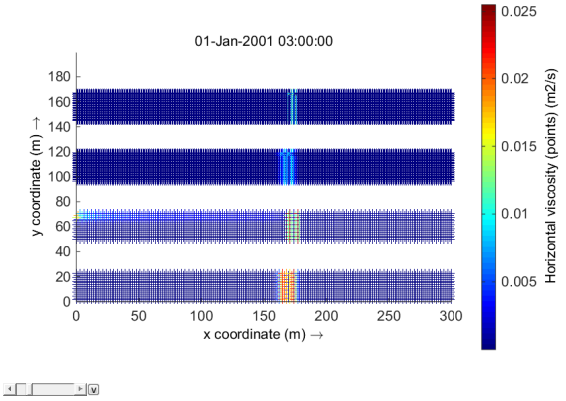

Figure 7.22: Top views of basins with a variable viscosity calculated with Smagorinsky

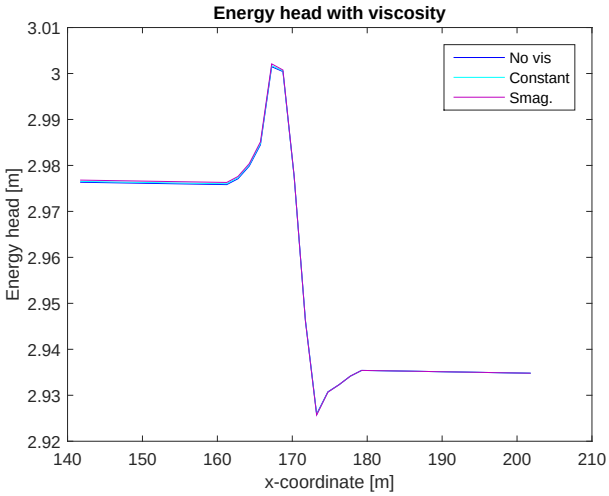

Figure 7.23: Energy head in FM and 3Di using a subgrid and supergrid model for $S = 0.95$ with friction, a turbulent viscosity model and a bottom slope

7.4 Conclusion

Investigating the convergence of the test cases in 3Di and Flexible Mesh, shows the energy increase at the weir in both packages. With a conservation of energy in front and on top of the weir and momentum on top and behind the weir, an analytical value of the discharge has been determined. 3Di and Flexible Mesh have showed convergence to a higher value of the discharge than this analytical value. Combining both supergrid and subgrid models, resulted in a smaller difference. When the river is simulated, this combination will be used as well, since the grid will be too coarse to only use bathymetry and the obstacles will not be correctly represented. The groynes in this simulation will only be partly overflowed, hence, it is expected that these differences will be even smaller. Hence, it will not have a high influence on the results. When plotting the energy head over the $x-$direction, it shows that from the beginning of the weir the energy head increases. According to Stelling and Duinmeijer (2003) an increase of energy can occur, when the wrong type of conservation is used. Over the entire domain a conservation of momentum is assumed,

while only conservation of energy is applied when a subgrid model is used. It might also be the result of wrongly assuming a hydrostatic pressure. For further research it is recommended to create a weir where the hydrostatic pressure is valid to investigate the origin of the energy increase.

By changing the geometry of the weir (lower slope, sudden expansion) the energy increase is slightly brought down. Combining both the bathymetry and subgrid model resulted in lower energy increases for all simulations. This is because the subgrid model assumes conservation of energy at the first part of the weir instead of conservation of momentum over the entire model. The grid size influence the results in this situation as well. As soon as the resolution is high enough to represent the weir in high detail in bathymetry, this combination can result in an underestimated discharge. This is due to the way how the subgrid model is implemented. It is depended on the grid size and its surrounded bathymetry. When a fixed weir is placed on top of the weir, where on one side the bottom level is still equal to the crest height, this value is used for the calculation of the depth. This results in an underestimation of this value. Though the energy increase seems quite high in this chapter, this is not the case. With an increase of around 3cm with a water depth of 3m in front of the weir, it is just an increase of 1%.

Adding more processes, as friction, has also not resulted in a lower energy increase. However, they do results in a better representation of a simulation in reality. Based on a theoretical analysis it is seen that the processes are well represented. The addition of viscosity is the only process that does not influence the results. Since there are no processes that are highly depended on the horizontal viscosity, this is expected.

The focus of this chapter has been mainly about a submergence degree of 0.95. To get a better idea of the result it is recommended to also investigate other degrees, especially the ones with another flow regime.

Chapter 8

Turbulent jet

In Chapters 6 and 7 the influence of 3-dimensional processes and flow over structures are investigated. Before a part of the River Elbe is simulated, more insight needs to be obtained about the horizontal viscosity. Viscosity can be divided into molecular and turbulent viscosity, where the first is a property of the fluid itself and the latter a property of the flow. For water this molecular viscosity is of the order 10^{-6}, while the turbulent viscosity is dependent on space and time. In applications as rivers the Reynolds number is usually high, which means that the flow is turbulent. Turbulent stresses, hence the turbulent viscosity, are in this case much higher than the molecular viscosity which can be neglected. In rivers it is common that flows with different velocities come together, where transfer of momentum takes place. Viscosity is an important term in these cases. In Chapter 2 it is seen that the diffusivity term is missing in the shallow water equations for 3Di, hence, viscosity is not taken into account. In this chapter a turbulent jet is simulated to investigate the effect of the missing term. Two test cases are used. The second test case follows from the first one where the results are not as expected. First the numerical viscosity is explained. Then the first test case is explained with its flow geometry and the results. Hereafter the second test case is built based on the results of the first case. This chapter ends with a conclusion and discussion of the results. These simulations are performed with D-Flow FM Version 1.1.191.47288, file format 1.05 and 3Di - subgrid Version 0.1.1.1958.

8.1 Numerical viscosity

In this section the truncation errors are investigated. To make it a bit easier to calculate these truncation errors in the whole area, no limiters are used in Flexible Mesh. Thus, for both 3Di and FM an upwind scheme is used to calculate the velocities. The starting point of the momentum equation is as follows,

$$\frac{\partial u}{\partial t} + u\frac{\partial u}{\partial x} = 0. \tag{8.1}$$

From here on friction is neglected, and there are no (or negligible) water level gradients. Furthermore, momentum is only introduced in the $x-$direction, hence $v = 0$. When this equation is discretized in space, an extra term is introduced, which is a diffusion term.

$$\frac{\partial u}{\partial t} + u\frac{u_{n+1} - u_n}{\Delta x} = \frac{1}{2}|u|\Delta x\frac{\partial^2 u}{\partial x^2}. \tag{8.2}$$

The term in front of the second order derivation is called numerical viscosity.

8.2 Simulation 1

8.2.1 Flow geometry

In a basin, with a length of 10 meters and a width of 4 meters, a turbulent jet is modeled. The length and width are chosen, after some considerations, to match the ratio L/B_s (see Figure 8.1) between groynes in rivers. Usually a ratio of 3-4 is taken to make optimal use of them. The jet is a plane jet of 1 meter wide, which introduces momentum into still water that is in the basin. The right side of the basin, where the water flows out, is also 1 meter wide and placed on the same $y-$coordinates as the inflow boundary. Another version has an open boundary condition in the total width that has a water level boundary condition. The second version is chosen to investigate the mixing layer that is then not limited by a small opening. The depth at these outflow boundaries is set to 0.20m. The boundary condition for the inflow is $Q = 7.1l/s$. These values for this case are based on a experiment of Dewals et al. (2008). Instead of the whole symmetric basin just half of it is modeled. In this way the grid can be made with a higher resolution. However, because of this the test case cannot be compared with this experiment anymore. Also the inflow and outflow area are larger. The grid cells are for each simulation the same and have a size of $dx = dy = 0.05m$. Due to this high resolution the mixing layer can be simulated in quite detail, which will give more insight in the diffusivity of both packages.

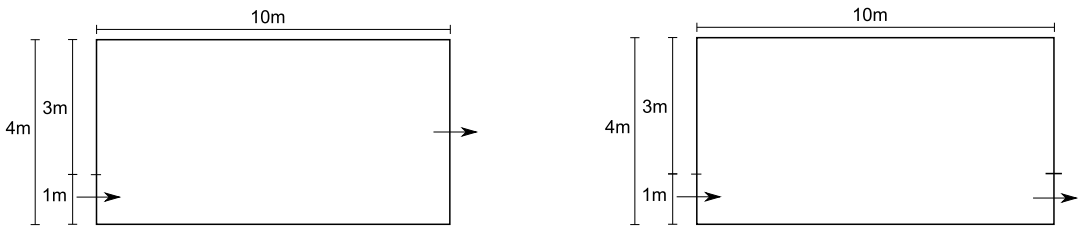

(a) Flow geometry with an open boundary over the entire width

(b) Flow geometry with an open boundary of 1 meter

Figure 8.1: Top view of flow geometry of test case "Turbulent jet"

8.2.2 Results

Unfortunately the simulation contains some assumptions that are not completely justified. On the whole right side of the model an open boundary is taken where a fixed water level

is assumed. The combination of the boundary conditions are taken from an experiment that is explained in Section 8.2.1. Using this boundary condition at the whole right side of the area instead of just a small part as in the experiment, might have influenced it such that is takes a long time before the model gets steady. This is due to reflection waves that are introduced. In previous cases the time it took them to become steady was quite short. Hence, when this simulation did not become steady the results were misinterpreted for turbulence. The velocity profile for each timestep looked as if the mixing layer contained eddies.

With this interpretation of the results, the idea is to find the time-averaged and fluctuating velocities $\bar{u}$ and $u'v'$. The first can be used to find the velocity profile in the cross section and is calculated with Equation (8.3), where N should be large enough (around $\mathcal{O}(10^{3-4})$). Using these values for multiple fixed $y-$coordinates and variable $x-$coordinates the development of this profile can be viewed. A uniform velocity profile is introduced for the inflow boundary. Hereafter, due to viscosity, transfer of momentum takes place and the uniform velocity profile slowly changes into a Gaussian profile.

$$\bar{u} = \frac{1}{N}\sum_{i=1}^{N} u(t_i) \tag{8.3}$$

The mixing layer, where the largest gradients of velocity are, grows with increasing distance from the inflow point. This gradient can be used, together with the averaged fluctuation velocities $\overline{u'v'}$, to calculate the turbulent viscosity as is done in the equation below.

$$\tau_t = \rho\overline{u'v'} = -\rho\nu_t\frac{\partial u}{\partial y} \tag{8.4}$$

The averaged fluctuation velocities $\overline{u'v'}$ can be obtained in the same way as the mean velocity. Since the velocities are known, and the mean velocities have been calculated in the previous step, the fluctuating part of the velocity can simply be found by subtracting the mean from total velocity.

$$\overline{u'v'} = \frac{1}{N}\sum_{i=1}^{N} u'(t_i)v'(t_i) \tag{8.5}$$

$$u'(t_i) = u(t_i) - \bar{u} \tag{8.6}$$

$$v'(t_i) = v(t_i) - \bar{v} \tag{8.7}$$

These steps are only allowed when the total velocity, $u = \bar{u} + u'$, is simulated, which is wrongly assumed in this case. Flexible Mesh and 3Di solve the mean velocity $\bar{u}$ and $\bar{v}$ with the shallow water equations. These equations are derived from the Reynolds-averaged Navier Stokes equations, hence, the velocity is already split into both parts. The shallow water equations in Flexible Mesh contain a diffusion term where the turbulent properties of the fluid are included by closing the system of equations with assuming Equation (8.4). In the cases that are simulated, the turbulent viscosity is set to zero to match the

equations with 3Di. Hence, τ_t is equal to zero, and all the transfer of momentum is due to the kinematic and numerical viscosity. Figure 8.2 presents in its top figure the total velocity, $u = \bar{u} + u'$, of a flow, while in the bottom figure the time-averaged velocity $\bar{u}$ is presented.

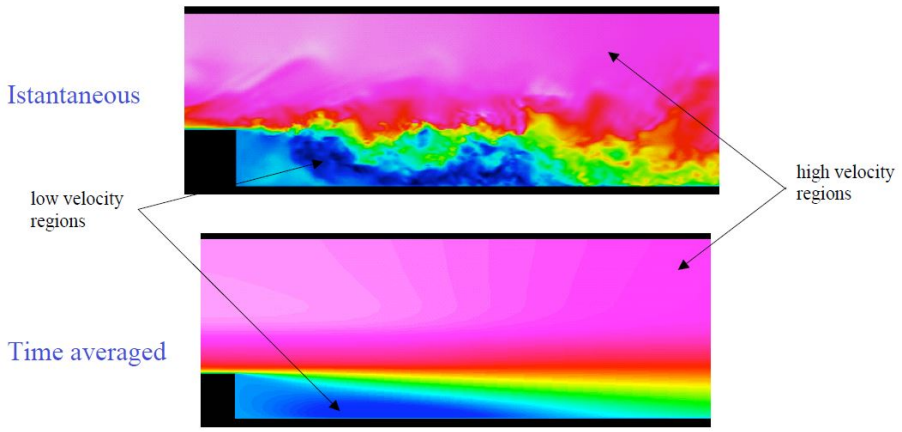

Figure 8.2: Difference between an instantaneous ($u = \bar{u} + u'$) and time-averaged ($\bar{u}$) flow field[1]

8.3 Simulation 2

Returning to Equation (8.4), which is implemented in Flexible Mesh to take into account turbulent effects, there is the possibility to give a value for ν_t. This can either be a constant value, or a variable that is calculated with Smagorinsky or Elder (both explained in Chapter 6) methods. Since the turbulent viscosity is usually not a constant value, the latter methods are more realistic. The given, or calculated, turbulent viscosity is added to the kinematic viscosity. Together these viscosities define the diffusivity. As seen in Section 8.1, beside these two viscosities, numerical viscosity also plays a part in diffusivity. So summarizing, there are three types of viscosity that need to be taken into account, where the turbulent viscosity can be controlled. In Table 8.1 an overview of the simulations is given. The variable options are friction and turbulent viscosity for Flexible Mesh, and only friction for 3Di. For now a constant turbulent viscosity is chosen in Flexible Mesh. The flow geometry of the second simulation is the same as the first simulation, see Figure 8.1.

Options	Flexible Mesh				3Di	
Experiment number	1	2	3	4	5	6
Manning coefficient	0	0.022	0	0.022	0	0.022
Turbulent viscosity	0	0	0.0001	0.0001	0	0

Table 8.1: Overview of the simulated models

[1] 13-09-'16 https://web.stanford.edu/class/me469b/handouts/turbulence.pdf

The value of the turbulent viscosity is roughly estimated by $v_t \approx 1.6 \cdot 10^{-3} h u_m \approx 10^{-4}$ (Uijttewaal, 2015). The numerical viscosity is approximately $0.5 \cdot 0.35 \cdot 0.05 \approx 8 \cdot 10^{-4}$, which is larger than the turbulent viscosity. Due to numerical viscosity it can be expected that the mixing layer will be wider if it is compared to experiments. Flexible Mesh has numerical limiters to prevent this, but they are not used in this simulation, since 3Di does not have these options. The simulations given in Table 8.1 are both for a partly and completely open boundary on the right side.

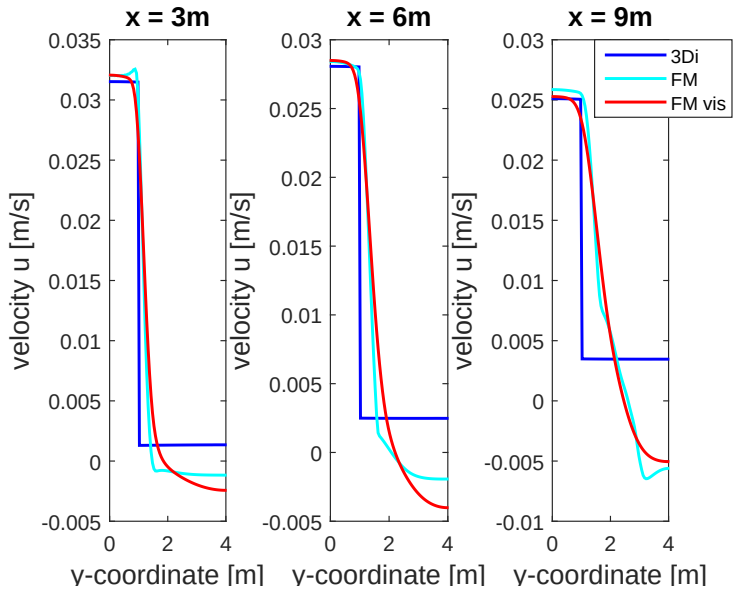

(a) With friction

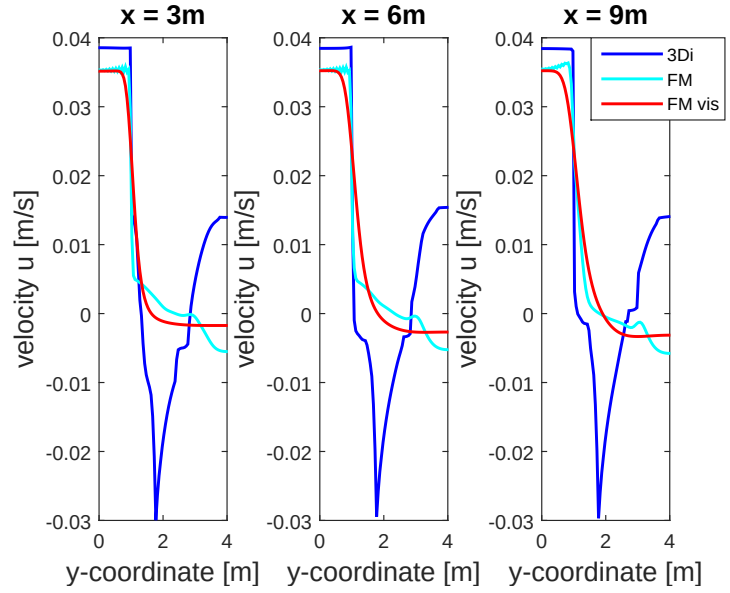

(b) Without friction

Figure 8.3: Velocity profiles at cross sections $x = 3, 6, 9$m for 3Di and FM (both with and without a turbulence model) with an open boundary

8.3.1 Results

The experiments where friction is set to zero, have not reached a steady state, which might be the result of the continuous input of momentum and reflection waves that are not damped. Figure 8.3 presents the cross sections of the completely open boundary models, where the abbreviation FM vis means the experiment from Flexible Mesh with a turbulent viscosity larger than zero. These cross sections are captured at $x = 3$, 6 and 9m in order to see the development of the velocity profile in the $x-$direction. The same cross sections for a partly open boundary are used. A distinction is made between the

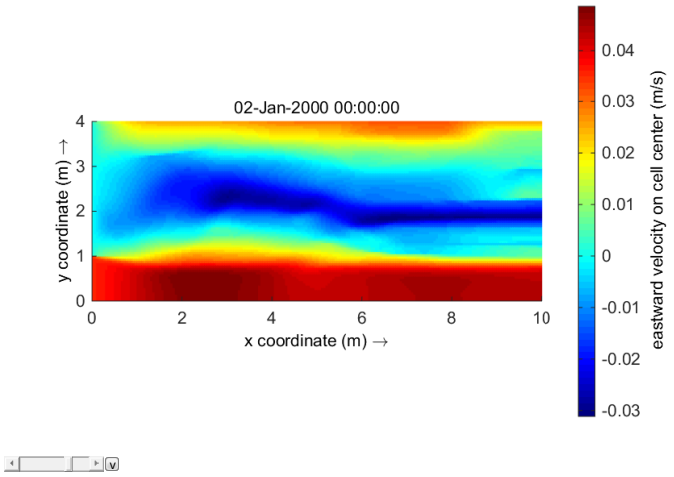

(a) Without friction

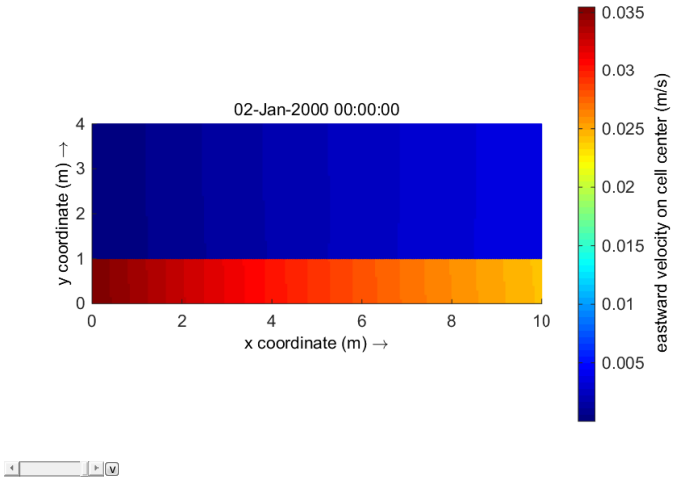

(b) With friction

Figure 8.4: Top view, represented in Figure 8.1, with eastward velocities in 3Di where an complete open boundary is used on the right side

cases with and without friction. Modeling with no friction (experiments 1, 3 and 5 of Table 8.1) has the disadvantaged in these simulations, that due to the continues input of momentum, and probably the reflection waves due to the boundary condition as well, it is

difficult to get them into a steady state. These shocks are usually damped due to friction, which is set to zero. Even while the simulations without friction have a simulation time that is twice as long compared to the simulation time of experiments including friction (at least 24 hours), they have not reached a steady state yet.

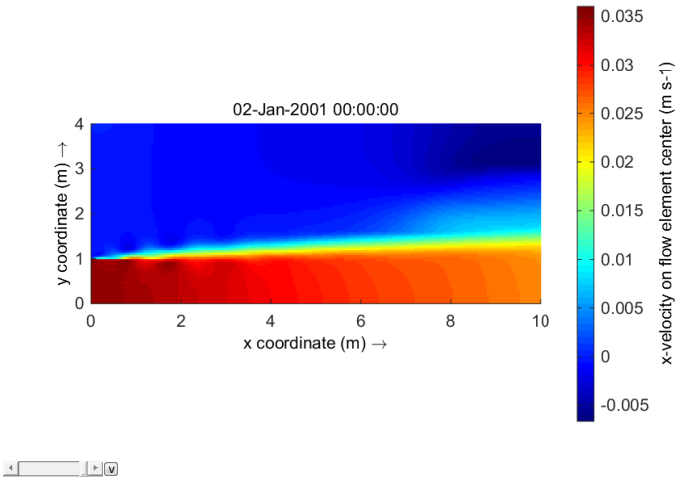

(a) Without turbulent viscosity

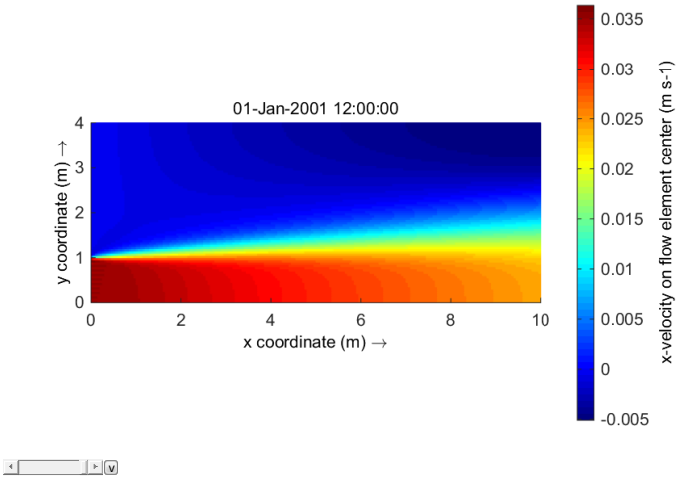

(b) With turbulent viscosity

Figure 8.5: Top view, represented in Figure 8.1, with eastward velocities in FM where an complete open boundary is used on the right side

The velocity profiles of Flexible Mesh and 3Di are quite different from each other, considering Figure 8.3. In Flexible Mesh the process of diffusion is visible based on the smoother velocity profile with respect to 3Di. With increasing distance from the inflow boundary the profile becomes smoother, whether turbulent viscosity is set to zero or not. If it is turned on the profile becomes more quickly smoother than without turbulent viscosity as one would expect. However, for 3Di the profile still looks discontinuous, even in the last cross section. Though the velocity between $y = 0$ and $y = 1$ decreases and between $y = 1$ and $y = 4$ it increases, hence it appears as if there is diffusion, there is no visible mixing

layer.

The decrease of the velocity is most likely due to the friction, since the same velocity in Figure 8.3b is not decreasing. The models with and without friction of 3Di are not completely comparable, since the one without friction has not reached a steady state. Figure 8.4 presents the top views of these simulations. Differences between the unsteady and steady state are clearly visible. Though in Flexible Mesh the differences are less, they are present and can be seen in the different cross sections. Even though the simulations have not reached a steady state, the influence of the turbulent viscosity is still visible. The profile is again smoother.

Not only friction, but also the turbulent viscosity influences the time it takes for the simulation to become steady. Figure 8.5 shows a top view of the models in Flexible Mesh where the mixing layers are visible. It also appears that the viscosity influences the time it takes for the simulation to become steady. It can be seen in Figure 8.5a that there are some unsteady features near the inflow of the area, while it is not present in Figure 8.5b where the simulation time is even shorter. Apparently due to the extra diffusion, even if it is smaller than numerical viscosity, the simulation reaches its steady state faster.

The results for the simulation with a partly open boundary are quite similar to the results where a complete open boundary is applied. The most important difference are the full gyres that will arise. With an open boundary also return flow is expected. Investigating these for both Flexible Mesh and 3Di will be helpful to understand the results when simulating the river Elbe. Just as with the open boundary, the results that do not contain friction will not be steady yet. Except for a full eddy between the closed boundary parts ($y = 1$ and $y = 4$m), the results are expected to be much alike the ones with the completely open boundary, since nothing else changed. Figure 8.6 shows the cross sections of the results.

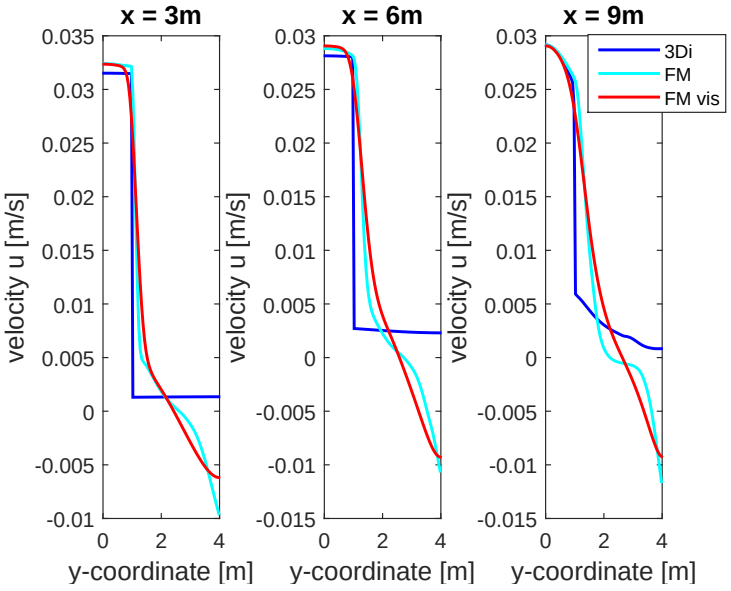

(a) With friction

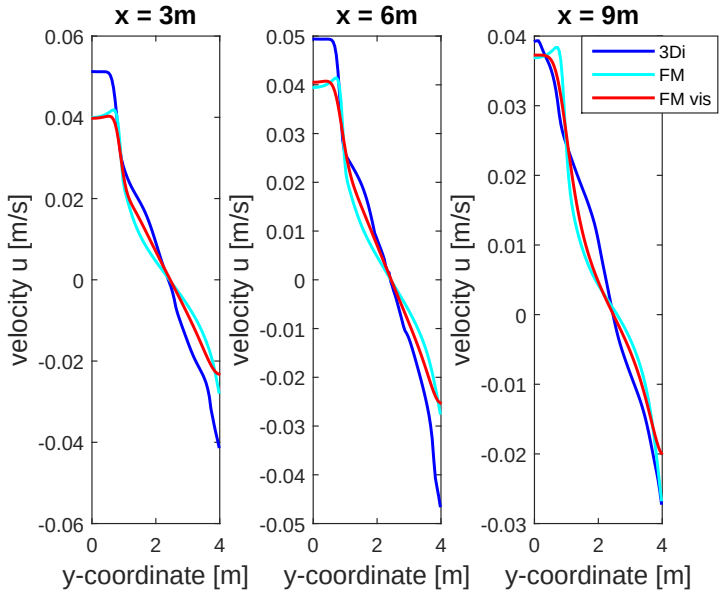

(b) Without friction

Figure 8.6: Velocity profiles at cross sections $x = 3, 6, 9$m for 3Di and FM (both with and without a turbulence model) with a partly open boundary

In Figure 8.6a it can be seen that the flow near the outgoing boundary ($x = 9$m) shows the largest differences compared to the results of an open boundary for 3Di. The results of 3Di look almost exactly the same as in the previous simulation, for a fiction coefficient larger than zero, except for the last cross section. This is due to the flow that has to go trough a smaller part. What also can be noticed is that the velocity is nowhere negative. Hence, there is no flow that goes back. Figure 8.7 compares the velocities in the $y-$direction of both 3Di and Flexible Mesh. These figures have a completely different

profile. Combining the cross sections results and the velocities in the $y-$direction, it becomes clear that whereas there is an eddy with Flexible Mesh, it is not present in 3Di. After the inflow it flows directly upwards and follows the shape of the domain. In the results of Flexible Mesh the diffusion process is visible together with one eddy. It cannot be explained where these differences come from. Even when there is no turbulent viscosity in Flexible Mesh, there is still an eddy present. The inflow discharge is small, hence, it might be possible that due to the slow inflow velocity the flow can be easily directed upwards. However, this would need further research by changing the inflow values. Unfortunately, there is not enough time to investigate this further.

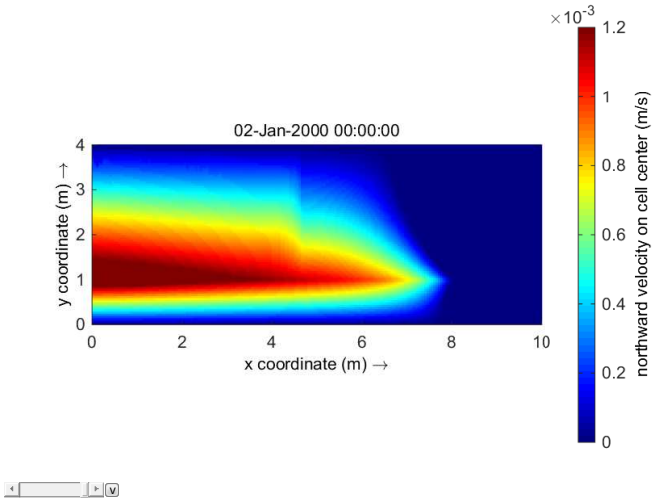

(a) 3Di

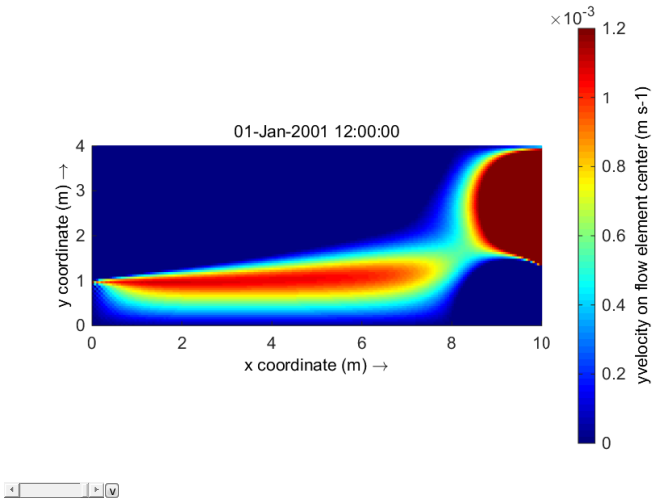

(b) Flexible Mesh

Figure 8.7: Top view, represented in Figure 8.1, with northward velocities in FM and 3Di where an complete open boundary is used on the right side

8.4 Conclusion

Comparing 3Di and Flexible Mesh shows quite some differences between the results. First of all, there is no visible mixing layer in 3Di, which gives rise to the question if there is any diffusion at all. Though the velocity profile in the cross section seems to change when increasing the distance from the inflow boundary, it is not clear whether this is a result of the right boundary or the friction that is present. Results from the simulation without friction are difficult to interpret, since it has no steady state. As a recommendation for further research, it can be checked whether a steady state will be reached by adjusting the simulation time again. Due to the lack of time, this is not accomplished. Furthermore, simulating cases with multiple velocities would give more insight whether the velocity influences the missing eddy in 3Di. When the river is simulated, a higher velocity is used. Thus, it can be partly investigated with that case. However, besides the velocity also another geometry and friction coefficient will be used, so this is not a good comparison with this simulation. It would be better to make the changes just in this simulation.

Estimating a constant value for the turbulent viscosity can be quite difficult, since usually not much information about the flow is known beforehand. Also, this viscosity depends on time and space. Because of these difficulties it might be easier to use the Smagorinsky and Elder method. However, also here the coefficients are only estimated. Thus as with a constant value, some calibration would be needed. This makes it all quite difficult to make a numerical model without doing any calibrations. It is recommended to have an experiment where the term $\overline{u'v'}$ is measured. If from this experiment the gradients are also known, the turbulent viscosity can be calculated. Making the same simulation with Flexible Mesh, either an average turbulent viscosity can be used, where after with the gradients $\overline{u'v'}$ can also be calculated and compared. Another option is to use Smagorinsky or Elder and compare the turbulent viscosities that are calculated with these options.

It would be interesting to find out more about the influence of numerical viscosity. Above experiments are done with one inflow value. With another value the velocity changes, hence the numerical viscosity changes as well. When the influence and order of numerical viscosity are known, it might be easier to predict what the influence of turbulent viscosity will be. The grid size also determines the order of the numerical viscosity. Refining the grid, or even making it coarser, will help to gain more knowledge about the numerical viscosity.

Chapter 9

Synthesis of both parts

After the literature study the report is split up in two parts, where Part I is focused on the mathematics and Part II on the physical aspects. The final study where the river Elbe is simulated, combines both parts. Before this is done, a synthesis of both parts is presented in this chapter. This will give the reader a better understanding of the research that will be done with the river. Additional, this chapter takes the results of all test cases into consideration in order to derive hypotheses for the results of the river. Hence, with these test cases a better understanding can be obtained of the results of the Elbe.

In total four test cases have been investigated, a flume experiment, a U-bend with sinusoidal profile, a rectangular channel with a weir and a turbulent jet. In Table 9.1 an overview of the test cases is given together with what subject of each study. With an exception of the turbulent jet, each case consisted of a convergence study as starting point. Since this is done for almost each case, it is not added in the table.

Test case	Physical aspects	Mathematics	Chapter
1. Flume experiment	3-dimensional processes Grid comparison	Grid comparison	3 & 6
2. U-bend		Local refinement in the middle of the bend	4
3. Flow over weir	Energy losses	Local refinement as a function of x	5 & 7
4. Turbulent jet	Horizontal viscosity		8

Table 9.1: Overview test cases

Test case "Mildly curved flow experiment in flume"

Two types of grids have been compared when simulating the flume experiment, a Cartesian and curvilinear grid. The results for these grids in each package were different, either in the water levels or velocities. A Cartesian grid in Flexible Mesh when simulating bends is not recommended. Although a higher resolution led soon to a better approximation of the

hydrodynamics, the differences are still higher compared to a curvilinear grid. Although 3Di uses a Cartesian grid as well, the results are closer to the experimental data than Flexible Mesh. Using a high resolution for the pixels improves the results quite a lot, while the sizes of the grid are the same. When simulating the river in Flexible Mesh a curvilinear grid will be taken as the main grid, since the results of this grid are more likely to simulate the river with more precision. However, since a river is not completely comparable to an experiment, it is interesting to investigate whether a Cartesian grid indeed lead to results that are far of the ones in 3Di and Flexible Mesh with a curvilinear grid. For this reason the first step in simulating the river will be done with both grids. One of the final outstanding points in 3Di is the converging of the water levels. In the cross sections it is noticed that when increasing the resolution the water levels increase as well. Until a certain refinement, whereafter the water levels decrease again. While it also occurs in the test case with a weir, it is not significant in the test case U-bend. Thus, certain aspects of this case will be applied in the flume experiment, such as the bed profile and another friction coefficient. This is applied in Chapter 10.

The added processes in Flexible Mesh for the same experiment will not be used completely. Most of the processes have not had a significant influence on the hydrodynamics. Furthermore, the condition no-slip or partial slip will also not be used. In an experimental flume, where there are vertical walls that have a high influence on the flow, it is needed to use these options to obtain results that are more related to the experiment. When a river is simulated, it is of less importance, since there are, usually, no vertical walls present. Only the friction and horizontal viscosity are variables of interest in this river simulation. Though the latter had limited influence of the water level in the flume experiment, it is an important variable in the test case "Turbulent jet".

Test case "Turbulent jet"

Besides the numerical viscosity, the turbulent viscosity has an effect on the mixing layer, since it both determines the amount of viscosity. Results of this simulation for 3Di are not as expected. There is no eddy present, but the flow simply follows the walls. However, since the geometry, dimensions and Reynolds number will be higher, the latter due to a higher velocity, there is a probability that it does not occur in the groyne fields. One of the reasons why this is happening in 3Di, might be the low velocity.

Test case "Flow over weir"

The main point of interest in simulating the weir is the energy loss and the placement of local refinement. The first is investigated in Part II and the second in Part I. It is seen that in each case where the weir is simulated in the bathymetry, an increase of energy is found. For both packages it is thought to be due to the discretization of the advection term. According to Stelling and Duinmeijer (2003) an increase of energy can occur, when the wrong type of conservation is used. It might also be the result of wrongly assuming a hydrostatic pressure. By changing the geometry of the weir (lower slope, sudden expansion) the energy increase is investigated to find out what influences it the most. The best solution, in case of a river, is the combination of bathymetry and subgrid modeling. In the test cases the mesh sizes could be small enough to properly represent the weir. In a river, the resolution is most of the time not high enough due to computational limits, hence, the lowest resolution of the test case is the most representative for the river. Combining both the bathymetry and subgrid model resulted in lower energy increases for

all cases. However, only for the lower resolutions the discharge is estimated closely to the analytical value. For a more extensive explanation references are made to Chapter 5 and 7.

Local refinements in test cases "Flow over weir" and "U-bend"

Local refinements of the weir case, but also the U-bend, has led to visible differences in the hydrodynamics. In the U-bend a local refinement is only placed at one side of the domain, where the transition of one grid size to another is placed in the middle of the bend. In case of the test case "Flow over weir" this transition is done at multiple places. For the U-bend it is interesting to see the effects of this transition in the middle of a bend, where not only a velocity is present in one direction, but in both directions. In the weir case only a velocity in the $x-$direction is present. With this case there a sudden variation in the main flow direction, resulting in larger gradients, that influences the results when refining. In both cases a sudden increase or decrease in the water levels/velocities is visible locally where the transition is. After the transition the flow still contains some differences compared to a grid with no refinement, but these go slowly to zero where the boundary condition is set. Without the boundary condition there would be a small differences of the order of a few centimeters over the entire domain. In the weir case results have lead to the conclusion that an error is only introduced if there are gradients in the velocity or water level present. In a river these gradients are always present, hence, local refinement would certainly give rise to other results. The order of these errors depends on the value of the gradients. For the river, where groyne fields will be considered, it is recommended to place a refinement in front of groyne. Preferably one field before the field of interest, such that the largest errors are not present in the area of interest.

In each case that is simulated there has been multiple differences between 3Di and Flexible Mesh. When a discharge as an inflow boundary is set, the water level in Flexible Mesh is always simulated lower than in 3Di. If as an inflow boundary a water level is set, the discharge is estimated higher in Flexible Mesh. Simulating the river it can thus be expected that for the same input values, such as friction, the water levels for 3Di will be higher than in Flexible Mesh. Thus, the water slope of both programs differ. When calibrating the simulation by adjusting the friction coefficient, a higher coefficient will be needed in Flexible Mesh compared to 3Di.

Chapter 10

Applying the geometry of test case "U-bend" to the test case "Flume experiment"

In Chapter 6 a flume experiment is simulated to get more insight in the 3-dimensional processes and the grid types of 3Di and Flexible Mesh. Plotting the water levels of certain cross sections has given rise to some uncertainties of the results in 3Di. When the resolution is increased, the water levels are until a certain refinement factor increased as well. However, after a certain refinement factor the water level decreases, where for $N = 40$ it is resulting in a water level that is lower than for $N = 5$. In Chapter 4 another bend is simulated based on Stelling (2012). Results of this test case show less changes in the convergence of discharge. Thus, it might be interesting to use this test case to find out why the water levels are changing as they do in the flume experiment. Since the flow geometry of both cases is already known, this chapter will only consist of the results when adding other processes and a conclusion. These simulations are performed with D-Flow FM Version 1.1.148.41897, and 3Di - subgrid Version 0.1.1.1958

10.1 Addition of bottom profile and friction for the flume experiment

Comparing the U-bend with the flume experiment there are three main differences. The first is the dimensions of both bends. The latter is smaller, since it is an experiment, while the other is based on the dimensions of a river. Besides the difference in dimensions it is also possible to distinguish bends on their ratio of bend curvature to channel width. While the river bend has a low ratio (≈ 1), the flume experiment can be considered a stronger bend with a ratio of approximately 8. However, this ratio has probably a higher influence on the morphology of a river and the momentum distribution. In this case, where the water level is the main interest, it is not necessary important. Of course, to

make a better comparison the ratio should be closer together. For now the focus is on the other two differences, the bottom profile and friction. For the flume experiment a flat bottom is used, with no bottom slope and a low friction coefficient. On the other hand, for the river bend a higher friction coefficient is taken combined with a sinusoidal bed profile in the cross section and a bottom slope in the downstream direction. By applying this first separately and then together, the influence of these process will be clearer. Perhaps this will also give more insight in the convergence of the flume experiment. The results are plotted in Figure 10.1. Instead of the cross sections that are plotted in Chapter 6, the middle part of the flume is followed in streamwise direction.

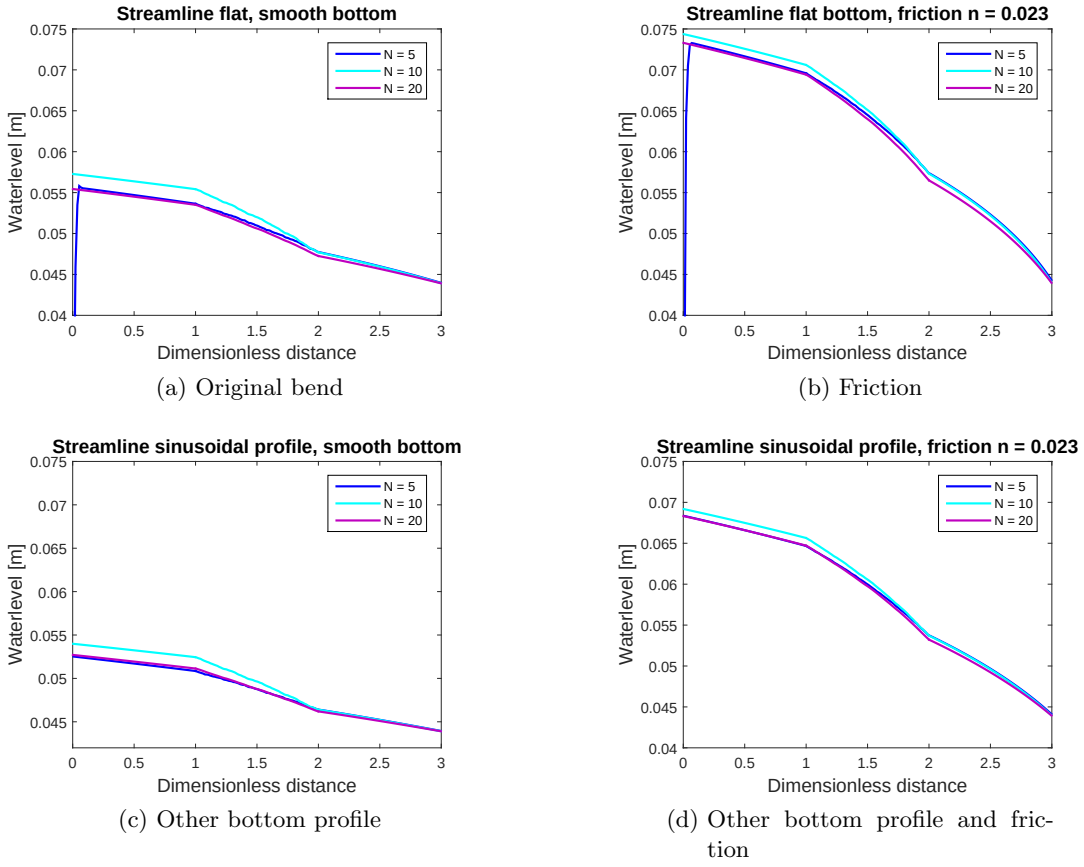

(a) Original bend

(b) Friction

(c) Other bottom profile

(d) Other bottom profile and friction

Figure 10.1: Water levels in 3Di for multiple resolutions with varying bed profile and friction coefficient

Although the results are not much influenced by the adjustments, there is one noticeable difference when another bottom profile is used. Since in the previous results of the flume experiment only the cross sections are taken into account, the sudden low water level at the beginning has not been visualized. It appears that it is only happening at the inflow of the domain and with the coarsest grid size. When another bottom profile is taken than the flat bottom, it is also not appearing anymore. It seems though, that is does not influence the results further downstream. For now, it is not investigate any further.

10.2 Conclusion

Adjusting the flume such that it is more similar to the U-bend has not resulted in additional knowledge. Though with friction the results of $N = 5/20$ and $N = 10$ are closer together, the water levels are still increasing up to $N = 10$, whereafter they decrease again. Although it is more pronounced in this simulation, the same phenomenon has occurred in some of the other cases. At the weir discharges (a water level is used instead of a discharge inflow) are either increasing or decreasing until a certain refinement factor. After this factor it will decrease if it was increasing before or the other way around. With the weir it depends on the submergence degree if this is visible. In this case also other processes are added or the weir's geometry is changed. For the U-bend and the flume experiment the changing point lies closely together. Figure 4.23 presents the convergence of discharges for 3Di and Flexible Mesh. It can be seen that after a refinement factor 3 the discharge does not increase anymore. With this refinement roughly 16 cells are used for the width of the bend. For the flume experiment, the changing point is around $N = 10$. These values are quite close together. It might be interesting to find out where the changing point really lies, which will give more insight in the convergence path of 3Di. It is possible that with a lower grid resolution certain processes are not completely solved, since they are more important with a higher resolution. Or that with a lower resolution the results are not precise enough. This can both lead to this changing point in either the discharge or water level that is seen.

Chapter 11

River Elbe

In part I and II multiple test cases are performed. These are done in order to obtain more insight in both the processes of Flexible Mesh and 3Di. Chapter 9 consists of a summary of these results. Due to this test cases it will be easier to interpret the results of the river Elbe that is simulated in this chapter. While the test cases were divided into two parts, this chapter will consist both of the physical properties and a refinement study. This chapter begins with a description of the numerical model, where the grid generation is explained together with the calibration. Also a part is dedicated to the Cartesian grid of Flexible Mesh. Hereafter the convergence is investigated, followed by the research of the physical processes in groyne fields. We conclude with investigating the influence of local refinements and a conclusion. These simulations are performed with D-Flow FM version 1.1.191.47288 and 3Di - subgrid Version 0.1.1.1958.

11.1 Numerical model

A previous project of the BAW (Bundesanstalt für Wasserbau) on the Elbe river at Lenzen has resulted in a large data set with both measurements and information of the bathymetry. In this project the dike has been relocated such that the river has more space in case of high water. In this project a detailed data set of the bathymetry, roughly measured at areas of two by two meters, is obtained, as well as water levels and velocity profiles in groyne fields. Furthermore the discharge is measured, which is set at $Q = 768\text{m}^3/\text{s}$. All the data used in this chapter is provided by the BAW. With the measured water levels an estimation of the water slope is made, in order to set a water level boundary condition at the outgoing boundary. Also the friction coefficient is not known, hence, it should be found with calibration. Even though the basic idea is to analyse the results of both simulations with (almost) no calibration, this leads to bad results. Thus, after the water level boundary condition is estimated, the grid is generated, and a calibration is done in order to estimate the friction coefficient. Figure 11.1 presents the part of the river that is modeled. In this figure the interpolated bathymetry is shown. The domain of interest, where measurements are done in the groyne fields, is marked with

a squared area. In this area the domain of interest is enlarged. Furthermore, in Figure 11.5 the two groyne fields of interest are marked. Notice that the flow in the river is from right to left (east to west).

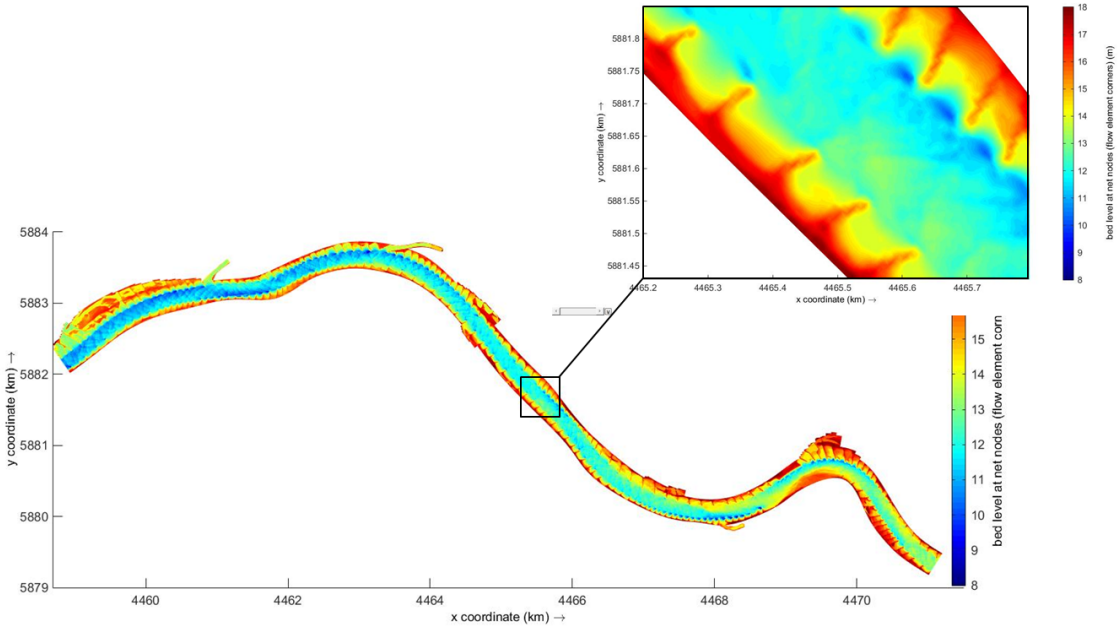

Figure 11.1: Bathymetry of river Elbe with indicated domain of interest

11.1.1 Grid generation

Generating a grid for the river is done in various ways for both packages. Chapters 3 and 6 have shown that a curvilinear grid for Flexible Mesh obtains results that are more precise than using a Cartesian grid. In 3Di only a Cartersian grid is possible, but results show that this grid does not limit the results the same way as in Flexible Mesh. Nonetheless, for a coarse grid both a curvilinear and Cartesian grid in Flexible Mesh are used. This is done to make a better comparison between both grids. It is expected that the results will not be as far off the data as seen in Chapter 3 or 6, where the results of Flexible Mesh with a Cartesian grid are 50% off when a coarse grid is used (20% when using a fine grid). This is expected due to the fact that the geometry is different, both for the bends and bottom, and that there are other physical processes present, such as friction.

Since bathymetry is available at a high resolution, the smallest mesh sizes are based on this resolution. For 3Di this means that a pixel subgrid has to be created with this data, that will be the same resolution for each simulation. Hence, independent from the mesh size, the pixels will be one by one meter. This implies that the smallest mesh size possible is two by two meter. In total four different sizes are used, thus $\Delta x = \Delta y = 2$, 4, 8, and 16m. Even with a mesh size of $\Delta x = 16$m, the results are expected to be quite close to the results of $\Delta x = 2$m, since the pixel subgrid is fine. With the interpolation function of Matlab, where it is assumed that the bathymetry is linearly varying between two data points, the data are interpolated to a uniform grid of one by one meter.

In Flexible Mesh a curvilinear grid is built of the main channel, whereas the side channels consist of triangles that are connected to the curvilinear grid. The cells of the curvilinear grid vary slightly in size compared to the cells of a Cartesian grid. The cell lengths in the stream direction are approximately twice as large as in the transversal direction. Furthermore, these cells will adjust to the geometry of the river. Hence, at other points this ratio can be higher or lower. Since the grid has a fixed number of cells in the width and length of the channel, they will be more squeezed together in the inner side of a bend, while in the outer bend they are more stretched. A Cartesian grid is created in a simple way, and just placed on top of the sample points. With the interpolation function of Flexible Mesh itself the sample points are placed at the cell nodes.

11.1.2 Calibration

The only aspect that is unknown is the friction coefficient, which will be derived in this section. For a channel the Manning coefficient usually takes a value between $n = 0.022$ and $n = 0.033$ (Arcement and Schneider), depending on the type of material on the bottom and its roughness. As a starting point a value of $n = 0.022$ is taken. The numerical results can be partly compared with the available data that are taken over a part of the river (between 480km and 485km).

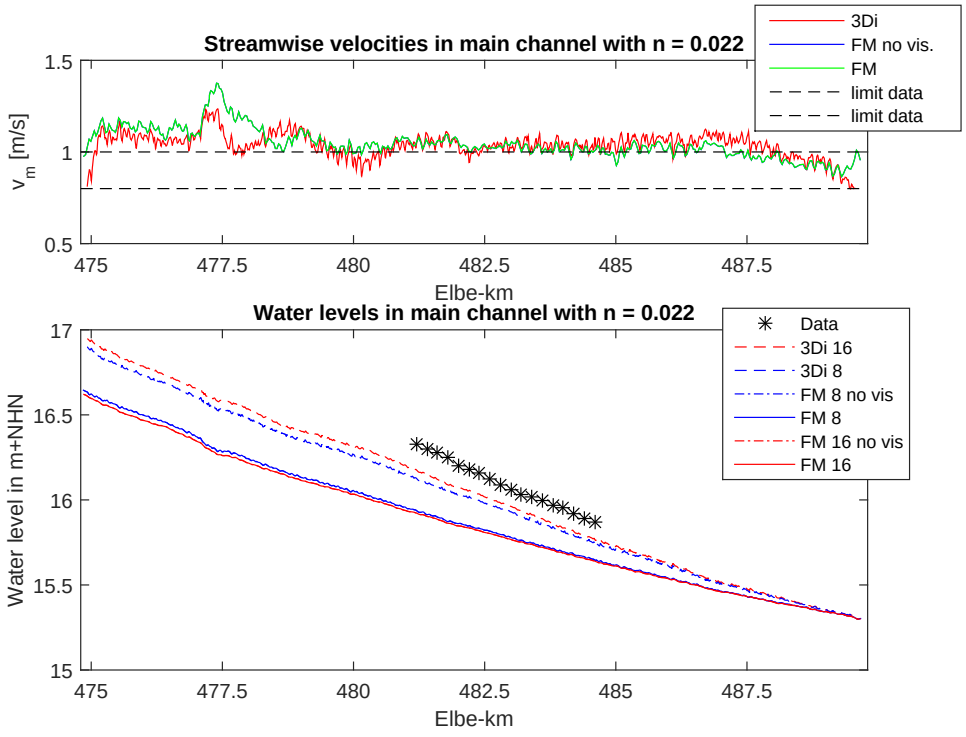

Figure 11.2: Steamwise velocities (upper figure) and water levels (bottom figure) in main channel with n = 0.022. No vis. means no viscosity and the numbers represent mesh sizes

Based on the first results, presented in Figure 11.2, it appears that Flexible Mesh underestimates the water levels more than 3Di does. Also the convergence direction differs.

Whereas with Flexible Mesh the water level increases when increasing the resolution, they decrease in 3Di. These differences are also observed when simulating the test case "Flow over weir" in Chapter 5 and 8, although it is simulated with an inflow water level boundary condition instead of an inflow discharge. In these cases 3Di underestimates the equilibrium discharge, while Flexible Mesh overestimates it (the water levels at the boundaries are fixed). In order for the water levels to increase when using Flexible Mesh, while the velocity needs to decrease, a higher friction coefficient than before needs to be taken. This is seen in Chapter 7.3.2, which is the test case most representative for a river, since it contains friction and a bottom slope. So, in the next experiment a value of $n = 0.03$ (Manning friction coefficient) is used.

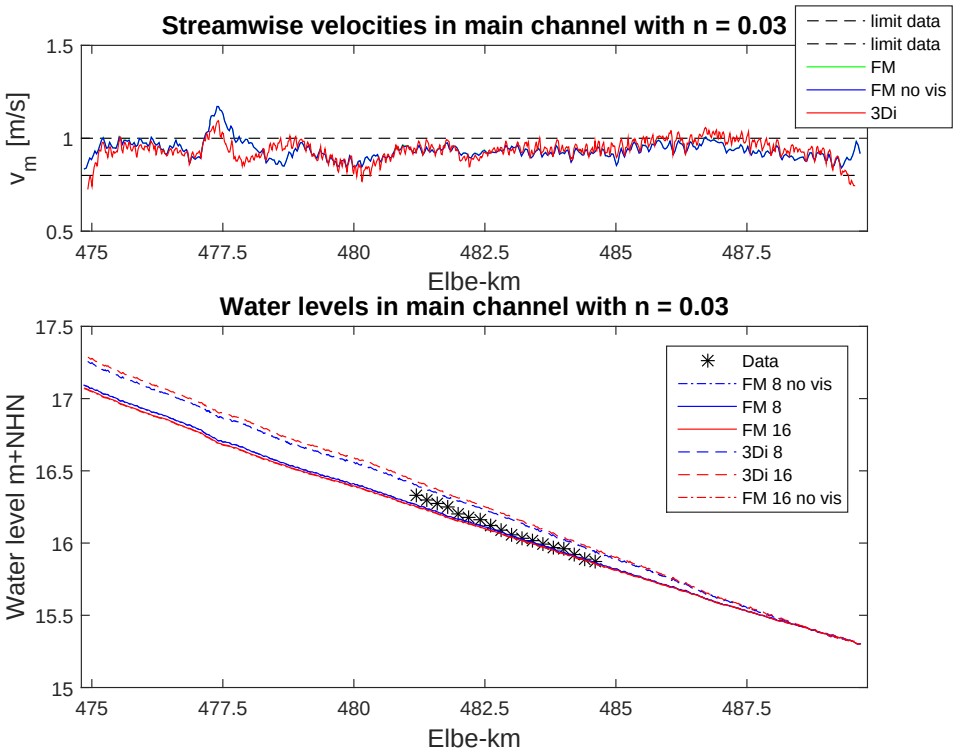

Figure 11.3: Steamwise velocities (upper figure) and water levels (bottom figure) in main channel with n = 0.03. No vis. means no viscosity and the numbers represent mesh sizes

Figure 11.3 shows that this value for the Manning coefficient appears to be suitable for the case in Flexible Mesh. However, for 3Di a slightly lower value is taken, since the results are further of the data compared to Flexible Mesh. In the simulations of 3Di a value of $n = 0.0285$ will be used. With these values for the Manning coefficients, the flows are simulated in the upcoming sections.

11.1.3 Cartesian grid Flexible Mesh

Though in the test cases it is concluded that a curvilinear grid appears to be more suitable for Flexible Mesh, it is interesting to investigate how a Cartesian grid differs in results

compared to a curvilinear grid. Simulating a flume experiment that consisted of a bend only in Chapter 3 and 6, resulted in a water level slope that is larger compared to the data and results of using a curvilinear grid in the bend (in the straight parts the slope is similar). In this test case only 5 to 20 cells are used over the flume width. In the river the coarsest mesh size is $\Delta x = \Delta y = 16$m for a Cartesian grid in 3Di, resulting in (depending on where the cross section is taken) a number of cells between 20 and 25 over the width, which is slightly more than in the test case. In Figure 11.4 the water levels and velocities of a Cartesian grid with $\Delta x = 16$ and 8m are compared with the results of a curvilinear grid where the mesh size in the transverse direction of the stream is approximately 16 and 8m, while in the streamwise direction 32 and 16m.

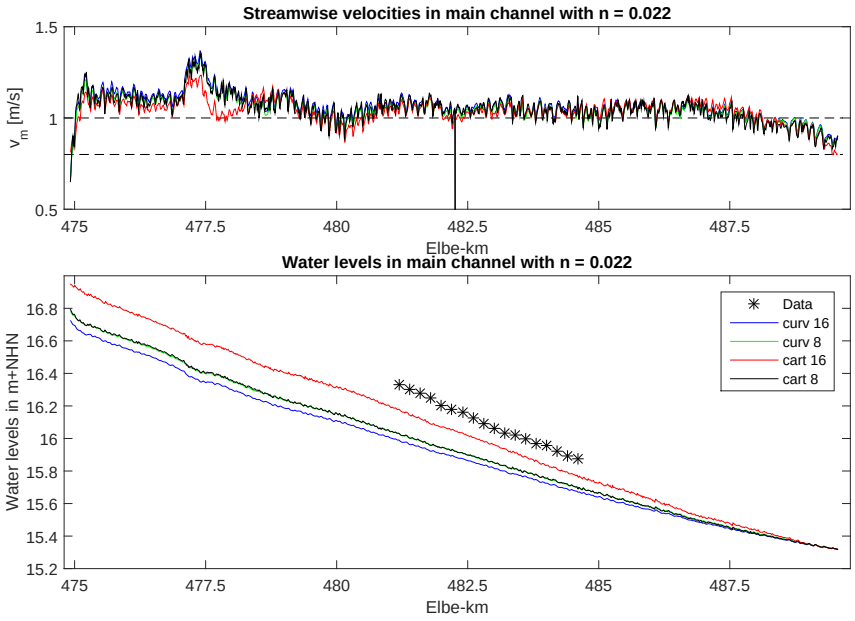

Figure 11.4: Steamwise velocities (upper figure) and water levels (bottom figure) in main channel with n = 0.022 in FM. Cart stands for Cartesian grid, curv stands for curvulinear grid, and the numbers represent mesh sizes

The results presented in Figure 11.4 display a larger water slope when using a Cartesian grid compared to a curvilinear grid, while this difference is almost zero when a higher resolution is used. With the coarsest grid one can see that the results of a Cartesian and curvilinear grid are quite different. The water level slope of the simulation with a Cartesian grid is estimated higher than for a curvilinear grid, which is seen in the test case (Chapter 3 and 6) as well. However, the results are almost similar to each other when a higher resolution is used. The water slopes for all simulations, shown in Figure 11.4, are estimated lower than the measurements. However, a value of $n = 0.022$ is used for the Manning friction coefficient instead of $n = 0.03$ that is found in Section 11.1.2.

Comparing the velocity profiles in a groyne field of a Cartesian and curvilinear grid, differences between the angle and magnitude can be found, which might be the result of dissimilar resolutions. These differences are plotted in Figure 11.6, and the groyne fields are defined in Figure 11.5. Since the mesh sizes are not exactly the same, these differences

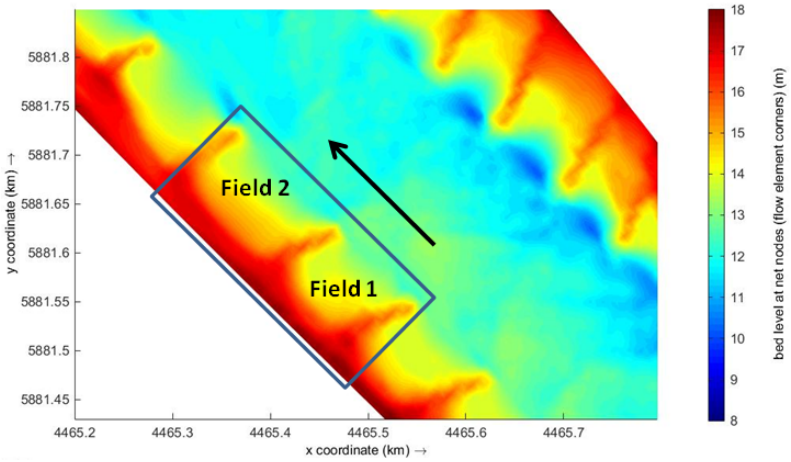

Figure 11.5: Bathymetry of the Elbe with the groyne fields, where measurements are taken, indicated. Flow direction given by arrow

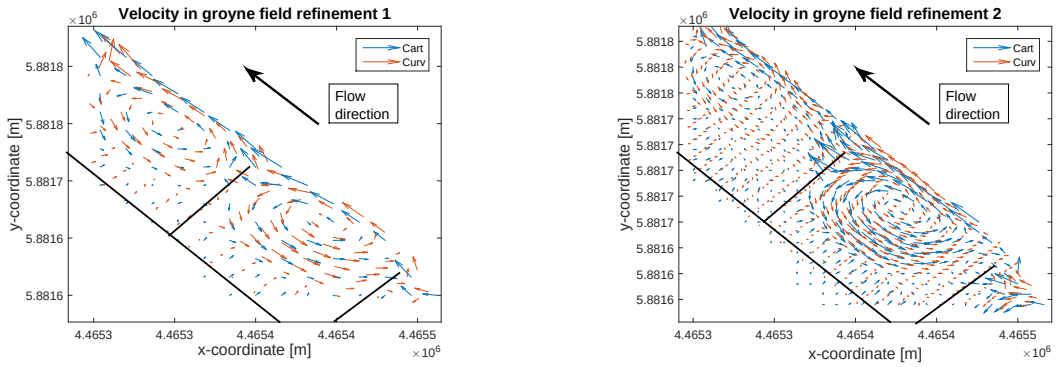

(a) Refinement factor 1

(b) Refinement factor 2

Figure 11.6: Velocity in indicated groyne fields of Figure 11.5 for a curvilinear (curv) and Cartesiant (cart) grid in FM

in angle can arise from the fact that with a resolution of the Cartesian grid, multiple gyres can be distinguished which coincide with the data, while for a curvilinear grid it is only one gyre. Increasing the resolution of this grid also results in additional gyres, having a total of two gyres in the flow field. Since there is not enough time to apply both type of grids, a curvilinear grid is used in the upcoming sections for the simulations in Flexible Mesh. Though the results of a Cartesian grid appear to coincide well with the measured data from the river, this is not seen in Chapter 3 and 6 when a Cartesian grid has been used. Furthermore, it will be easier to investigate the effects of local refinements when a curvilinear grid is applied.

11.2 Convergence

In Section 11.1.2 the friction coefficient is chosen based on the first results obtained with the coarsest mesh sizes. Observing the convergence of these two grids and the results

of convergence in the previous chapters the coefficients are chosen. When the results of Flexible Mesh are observed, it appears that the friction coefficient results in a numerical result that lies close to the data points. Hence, the numerical results seem to converge closely to the data points. However, for 3Di it seems as if the difference between each refinement is the same. In the test cases it is already seen that the convergence of 3Di can be hard to predict. Also for Flexible Mesh the distance between the results of refinement 2 ($\Delta x_1 = 2\Delta x_2$) and 3 ($\Delta x_2 = 2\Delta x_3$) are larger than the ones of 1 and 2, and 3 and 4.

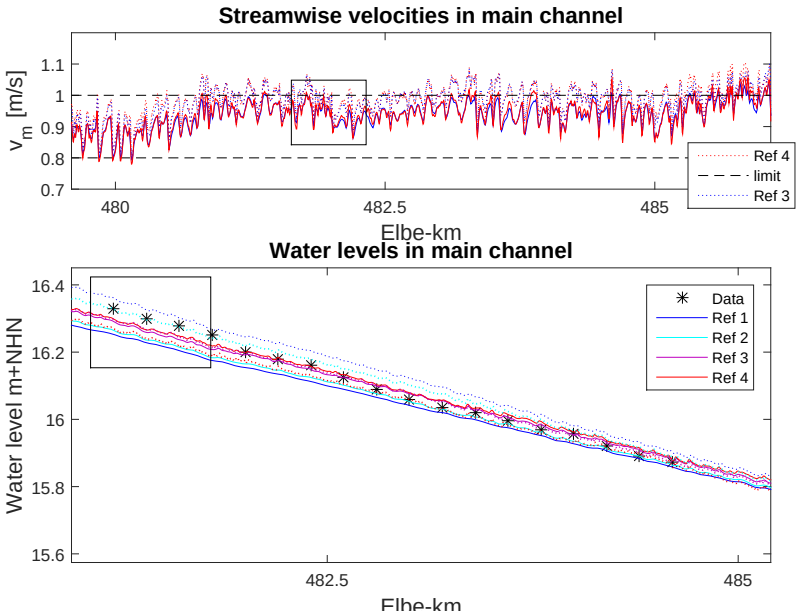

(a) Steamwise velocities and water levels in main channel for FM and 3Di with indicated area that is zoomed in

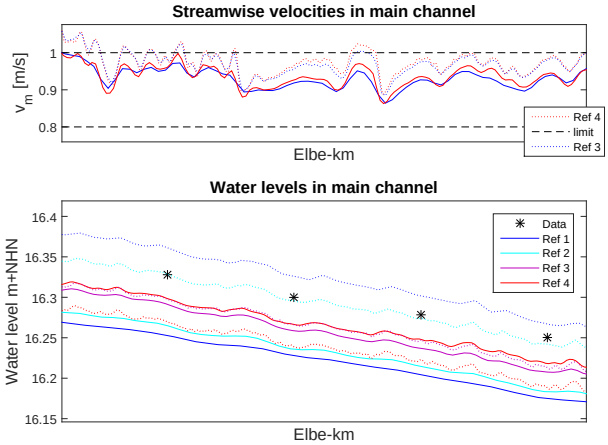

(b) Steamwise velocities and water levels in main channel for FM and 3Di zoomed in

Figure 11.7: Steamwise velocities (upper figure) and water levels (bottom figure) in main channel for FM (continuous line) and 3Di (dashed line). Ref. is short for refinement factor

Since it is not possible to refine any further (due to limitations in the computer's capacity), it is recommended to make a coarser grid in order to investigate the convergence of both packages in more detail. For now it is assumed that the results of both Flexible Mesh and 3Di are close to the values they converge to with refinement factor 4. However, the computational time of the simulation with this refinement makes it not possible to run multiple simulations. For this reason a refinement factor of three is taken for the simulations in the upcoming sections. The results for this refinement factor are close to the ones of refinement factor 4, and coincide well with each other for both packages. Furthermore, with the water level slope and velocities in the main channel similar, the comparison between both packages will be easier.

11.3 Physical processes in groyne fields

In this section the physical processes in groyne fields (the groyne fields as defined in Figure 11.5) are investigated, where the groynes are slightly flooded (only the tips) with a $Q_{in} = 768\text{m}^3/\text{s}$. As noted in Section 11.1.2, this research is done with refinement factor 3. Using this resolution the gyres, diffusivity and other processes are better represented than when a factor 1 or 2 is taken. Also the hydrodynamics in the main channel of both 3Di and Flexible Mesh are most similar with this refinement. In the test cases the focus has been on energy and viscosity (diffusivity). Hence, using the results of the test cases in Chapter 7 and 8, both aspects are further investigated for this more complicated case.

11.3.1 Energy losses

It is seen in Chapter 7 that there is an energy increase, which should not be present, when the flow goes over an obstacle that is fixed in the bathymetry. Combining both the bathymetry and subgrid model resulted in lower energy increases for all cases. This is because the subgrid model assumes conservation of energy at the upstream part of the groyne instead of conservation of momentum over the entire domain. This combination is taken to simulate the flow over groynes.

Thought the energy increase is still present in the results of this simulation, the increase is relatively small compared to the energy head before and after the increase and might be neglected. Figure 11.9 presents the energy head and bathymetry over a polygon. The polygon, shown in Figure 11.8, is taken over the tips of the groynes, where they are flooded. Water levels, velocities and bed heights are interpolated from surrounding center points of grid cells to points of this polygon. Since the grid of 3Di and Flexible Mesh do not match, the used bathymetry based on the sample points will not be the same. This is quite clear in Figure 11.9, where the highest point of the groynes differ up to one meter. The water levels, and consequently the energy head, are almost equal to each other. Similar to the test case of Chapter 5 and 7, an energy increase is found over the groynes. Where in the test case this increase is already quite small, a few centimeters over a depth of 1 meter on the weir, it is even less over these groynes. Both packages show, independent of which groyne, an energy increase around 1/1.5 cm. Without zooming in on the energy head it would not even be visible. The circles in Figure 11.9 show where the energy increases are. Just as with the test case, the increase begins at the moment

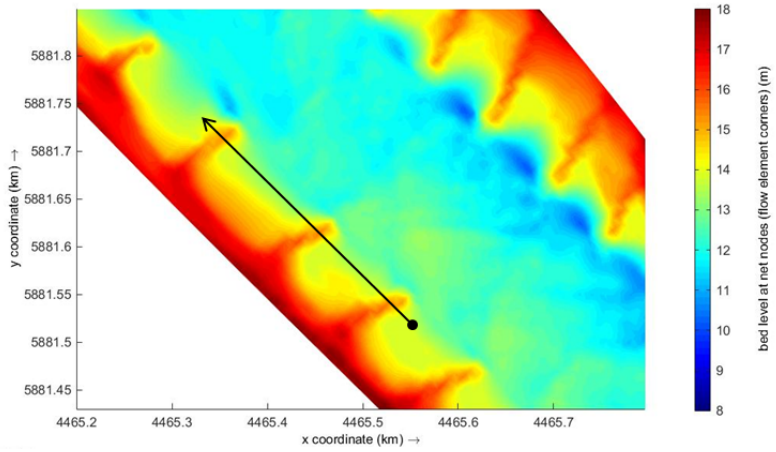

Figure 11.8: Bathymetry of river Elbe with an arrow indicating the $x-$axis location in Figure 11.9

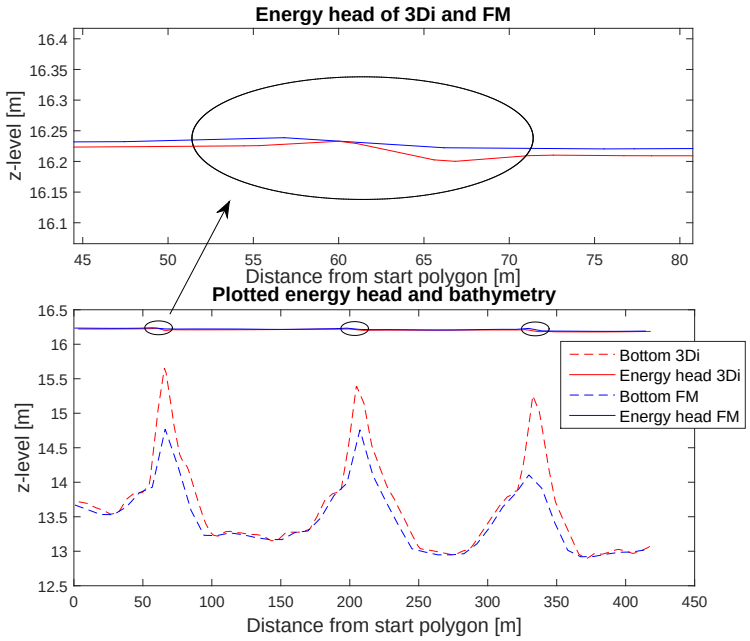

Figure 11.9: Plotted energy head and bottom level at the arrow of Figure 11.8

where the bed height increases. Though it is physically not correct, it will not have much influence on the other results, since it is so small. With the test case "Flow over weir" multiple variations have been taken into account that lowered the energy increase, but in none of the simulations the energy increases is prevented.

11.3.2 Viscosity

Starting point for this section is setting the viscosity for Flexible Mesh at zero, and compare the results with 3Di. In Chapter 8 a turbulent jet is simulated, where it is seen

that the results of 3Di are different to those of Flexible Mesh. Where for Flexible Mesh a gyre is found in combination with a mixing layer, the fluid in 3Di has none. Next, a constant turbulent viscosity is set, where this viscosity is approximated by $\nu_t \sim 1.6 \cdot 10^{-3} h u_m$, Uijttewaal (2015). This approximations give an idea of the order of magnitude of the turbulent viscosity. The water depth and mean velocity are taken from the results that have no turbulent viscosity. Another option is a variable turbulent viscosity, that is calculated either by Elder (Elder, 1959) or Smagorinsky (Smagorinsky, 1963). Both options are used separately. Before each of these options are investigated, a total overview is given of the locations of gyres. The circles in Figure 11.10 indicate the locations of the gyres centers. The colors are defined as follows:

Color	Model
Red	Data
Black	3Di
Purple	FM: no turb. viscosity
Green	FM: constant turb. viscosity
Blue	FM: variable turb. viscosity

Table 11.1: Definition of colors in Figure 11.10

Thus, the center of these gyres are highlighted with a colored circle. This overview shows how the turbulent viscosity influences the velocity in the groyne fields. A first remark has to be made about the gyres in the corners. They are located at places where there are no measurements. In the simulations the groyne fields are a bit more flooded than in the river, which results in another location for a gyre.

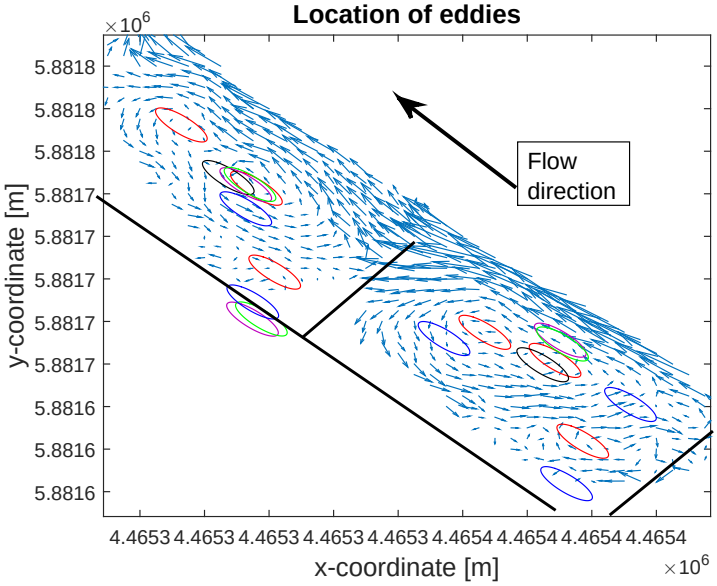

Figure 11.10: Plotted velocities of measurements in indicated groyne fields of Figure 11.5 with centers of gyres displayed for various turbulence models given in Table 11.1

With the turbulent viscosity equal to zero for Flexible Mesh, the velocity field between

groynes is quite similar to the results of 3Di. In Figure 11.5 the groyne fields have been presented and are given a number. In field 2 of Figure 11.10, the center of the gyres are close to each other. In field 1 the center of the gyre in Flexible Mesh is closer to the main channel. What strikes is that for 3Di there is a rotating flow in the groyne field, since in the test case "Turbulent Jet" it was not present. With a velocity in the main channel of approximately 1 m/s opposite to the inflow velocity of 0.035m/s in the test case, it seems that the velocity influences this result as expected. Since the water also flows partly over the groyne, and there is another bottom profile, it is not completely comparable. To be sure, another inflow boundary of the test case needs to be taken, which is recommended to do for further research.

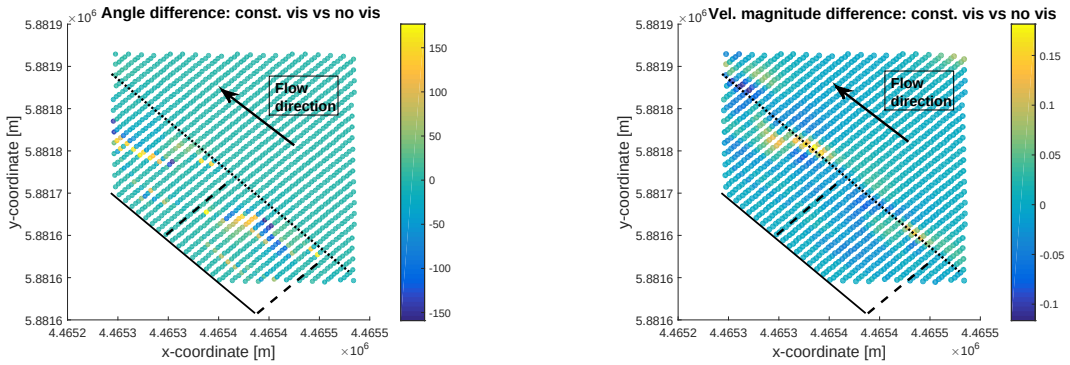

(a) Angle differences

(b) Velocity magnitude differences

Figure 11.11: Differences between a turbulent model with a constant viscosity and no turbulent model

The differences in velocity and water level between a simulation with and without a constant viscosity are minimal, and the location of the gyre is approximately the same. It was already expected that the results using Flexible Mesh, with and without a constant turbulent viscosity, will not differ that much. Chapter 8 showed that the mixing layer is mostly affected by changing the turbulent viscosity to a constant value, while the location of the gyre's center is quite the same. This can indeed be seen in Figure 11.10. The difference in the location of the gyre is insignificant, though it does result in some distinction between the angles and velocity magnitudes, see Figure 11.11. With increasing distance from the center of a gyre the velocity magnitude increases. So if the center is not the same, these differences will result and consequently are largest near the center of a gyre.

For the third option a variable turbulent viscosity is used, calculated either by Elder (Elder, 1959) or Smagorinsky (Smagorinsky, 1963). Though the values in the main channel are completely different as can be seen in Figure 11.12, the turbulent viscosity inside a groyne field is approximately the same and of the order $\mathcal{O}(10^{-1})$. The centers of the gyres are almost located at the same place. Furthermore, the differences between the hydrodynamics are minimal. Since the focus is on the groyne fields, we will not investigate these differences in the main channel further.

Considering the gyres in the groyne fields (Figure 11.10) when a variable turbulent viscosity is used, it can be seen that for both the measurements and simulation results multiple

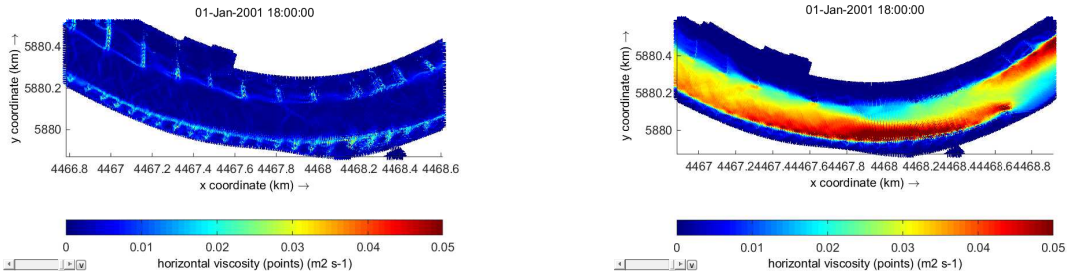

(a) Variable viscosity calculated with Smagorinsky

(b) Variable viscosity calculated with Elder

Figure 11.12: Turbulent viscosity plotted in part of the river based on two options

gyres can be found, but the centers of them do not match. In field 1 (Figure 11.5) it can be seen that for the measurements three gyres are found, two arise approximately in the middle of the groyne field, while the third is a secondary gyre in the corner of the field. The same number of gyres apply with a variable turbulent viscosity. However, the centre of the gyre closest to the right groyne originates much closer to the groyne than the measurements. Using the results of test case "Turbulent Jet", Chapter 8, there might be an explanation. In this test case it is seen that with an additional turbulent viscosity, where the numerical viscosity is already present, the mixing layer is wider with increasing distance from the inflow than without this addition. The center of the gyre of the simulation with additional viscosity is closer to the inflow boundary, what is also seen in the groyne field 1 of the river. Hence, the turbulent viscosity might be overestimated compared to the data. Since so many other factors, like bathymetry, measurement errors, interpolation, influence the results, it is difficult to determine which factor is most important.

11.4 Local refinement

In Section 11.3 the physical processes in groyne fields have been investigated. With Flexible Mesh this includes varying the turbulent viscosity to analyse its influences on the velocity pattern in the groyne field. With a turbulent viscosity higher than zero, more than one gyre is found in the groyne fields for Flexible Mesh, which is more similar to the measurements. However, with the inclusion of diffusion in Flexible Mesh the shallow water equations of Flexible Mesh and 3Di are dissimilar. Hence, instead a ν_t of zero is taken in Flexible Mesh for this section, which results in identical shallow water equations for both packages. Furthermore, it is seen in Chapter 5 that multiple options are available to refine in Flexible Mesh. In this section a local refinement is applied using triangles as shown in Figure 5.19. In this case refinement Type 1 is applied, where both in the streamwise and transverse direction the cell is refined, and the local refinement is only applied to the area of interest.

The transition of a coarse to fine grid is located at various locations in order to investigate the influence of distance to the results. These transitions can be found in Figure 11.13.

The first placement is just in front of the domain of interest. It is expected that this will influence the results in that area the most, since it is seen in Chapter 4 and 5 that locally at the transition the highest differences arise. The second transition is one groyne field further upstream, and the third two groyne fields. The results will be compared by looking at the differences between a uniform grid and a grid with local refinements for each package.

The advantage of using a local refinement instead of refining the complete domain, is the reduction of the computational time. When a local refinement is applied at the area of interest, less computational cells are present in the simulations, which reduces the simulation time.

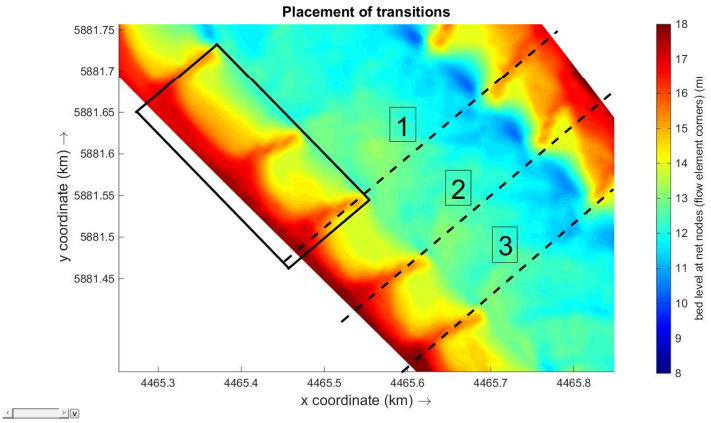

Figure 11.13: Bathymetry of the Elbe with placement of transitions indicated by dotted lines and area of interest by a rectangle

Comparison of the results is done in the same way as in Figure 11.11. The velocity (angle and magnitude) and water level differences are taken into account. They are plotted in Figure 11.14 for 3Di and in Figure 11.15 for Flexible Mesh. Since for each refinement three plots result, only the first transition is presented in this chapter of both Flexible Mesh and 3Di. The other figures are given in Appendix G.

The angle and magnitude differences appear to be mostly influenced by the using a local refinement, which is due to the shift of the gyre. This leads to large differences. The largest differences of both the angle and magnitude are located approximately at the same place. At the entire length of the groyne, where the transition of the local refinement is set (see Figure11.13, number 1), it can be seen that the angles of the velocity vectors differ up to 150 degrees. Also, from the tip of the groyne, or at the place where the water just flows over the groyne, to the center of the gyres these differences are high as well.

Analyzing the results of transition 2 and 3 (Figure 11.13) it can be observed that for both groyne fields differences between the uniform grid and the grid with local refinement are present. In Chapter 4 and 5 it is already seen that differences between these two grids are introduced over the entire domain. However, this is only the case when the transition is placed where gradients in water levels and velocities exist. Considering a river, these gradients are always present, resulting in differences over the entire domain due to applying a local refinement.

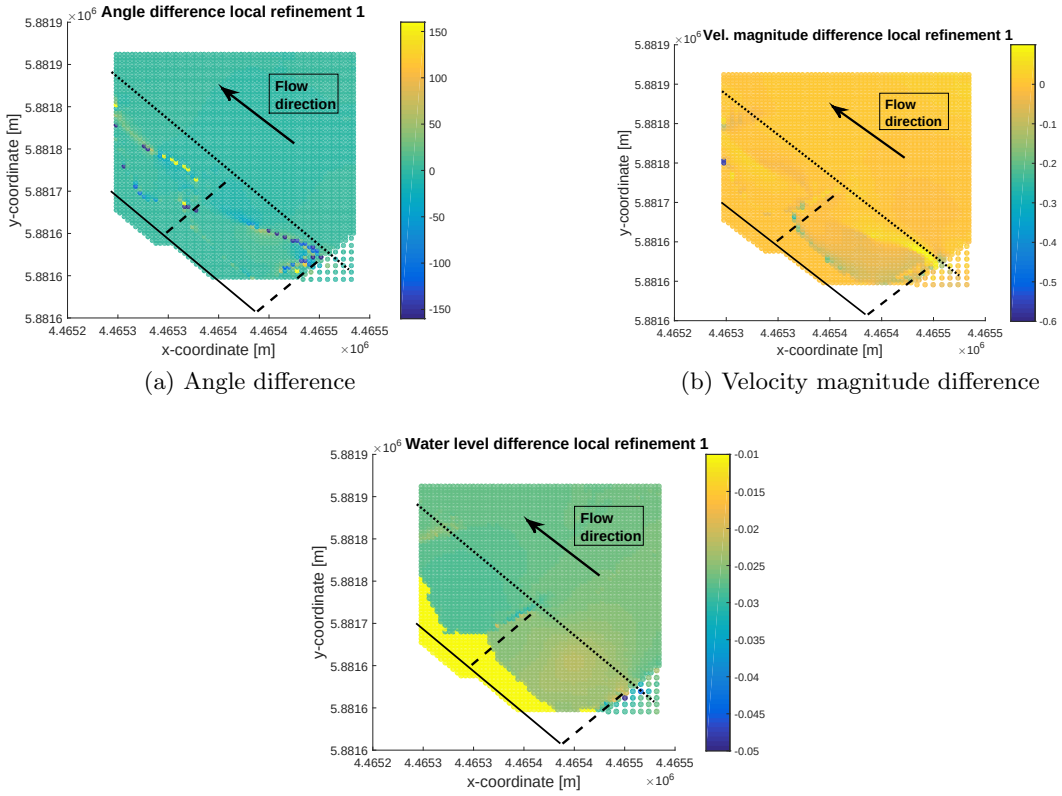

(a) Angle difference

(b) Velocity magnitude difference

(c) Water level difference

Figure 11.14: Differences in the groyne fields of Figure 11.5 between a fine uniform grid and a grid with local refinements with transition at line 1 in 3Di

Considering the results of transition 2 and 3 in Figure G.1 and Figure G.2 one can observe that the figures appear approximately similar to each other, which is indeed the case. Hence, locally at the transition the highest differences between a uniform grid and a grid with local refinements arise, whereas over the remaining domain these differences in velocities and water levels appear constant. The observations made for 3Di apply for Flexible Mesh as well, where the results are presented in Figure 11.15, Figure G.3, and Figure G.4.

Thus, it can be concluded that the placement of transition influences the hydrodynamics. Locally at the transition the largest differences in velocity, both angle and magnitude, and water level arise. Placing this transition further upstream of the domain of interest reduces the differences between a uniform grid and a grid with local refinement at this area. Furthermore, it is recommended to estimate where the smallest water level or velocity gradients arise, in order to place the transition there. In Chapter 5 it is seen that these gradients are one of the main factors that influence the hydrodynamics when applying a local refinement.

Considering the same polygon as in Figure 11.8, it can be seen in Figure 11.16 that a small additional energy increase in 3Di or decrease in Flexible Mesh is present when transition 1 is applied (black line presents the placement of transition). The difference in 3Di and Flexible Mesh (increase or decrease) arises due to the fact that in 3Di the energy head

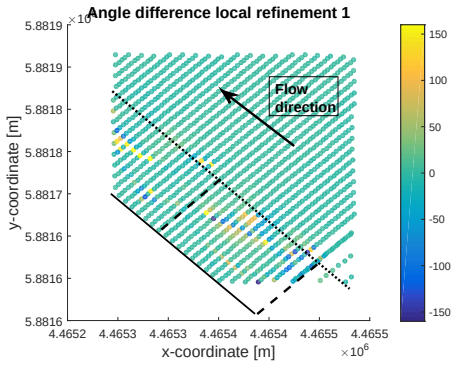

(a) Angle difference

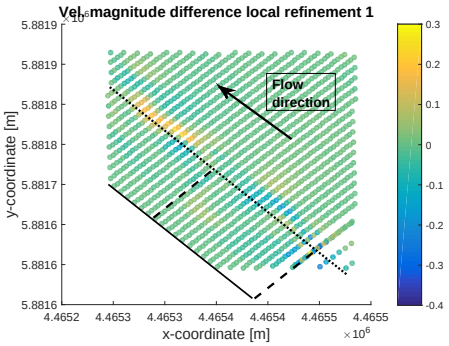

(b) Velocity magnitude difference

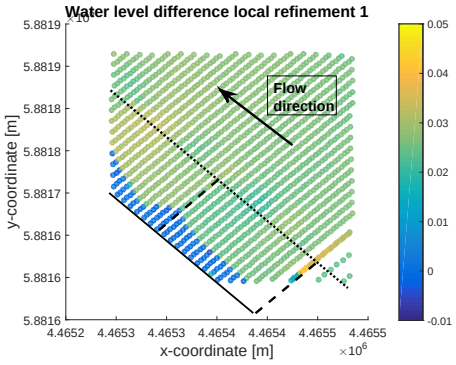

(c) Water level difference

Figure 11.15: Differences in the groyne fields of Figure 11.5 between a fine uniform grid and a grid with local refinements with transition at line 1 in FM

is higher when a local refinement is used, while it is lower in Flexible Mesh. This results from different estimation of the water levels. It can be seen in Figure 11.14c and Figure 11.15c that this is the case for the water levels as well, which determine the value of the energy head together with the velocity magnitude in a given direction.

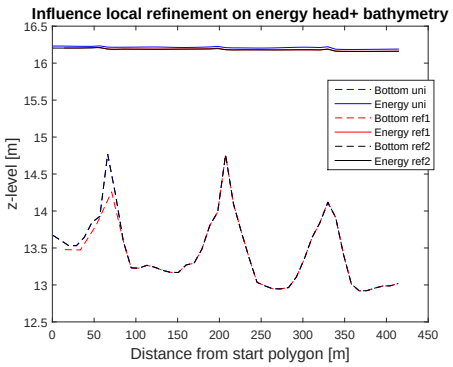

(a) Results of Flexible Mesh

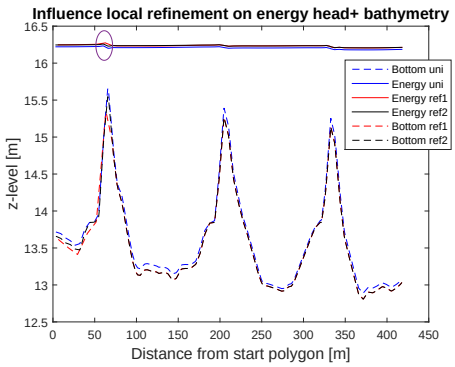

(b) Results of 3Di

Figure 11.16: Plotted energy head and bottom level at the arrow of Figure 11.8

11.5 Conclusion

The focus in this case is on physical aspects, diffusivity and energy losses, and mathematical aspects. The multiple options for a turbulence model in Flexible Mesh have lead to results that are more similar to the velocity field measurements. Hence, the diffusivity is better represented in Flexible Mesh. In both 3Di and Flexible Mesh small energy increases can be found at flow over obstacles. Though this increase is physically not correct, it is small enough to be neglected. The order of magnitude is in both packages approximately similar. Applying local refinements resulted in local errors. In this specific case it is seen that large differences in the velocity fields are found, since the location of the gyre is slightly changed. In most cases this small change can be acceptable, and results in a large decrease of the computational time in case of a large simulation with a relatively small area of interest.

Chapter 12

Discussion

This study has revealed that the many choices that can be made with the use of numerical models for depth averaged simulations have great consequences for the resolved hydrodynamics. The considered choices in this research are related to grid resolution, boundary conditions, and turbulence models. Based on these choices there are considerations that need to be taken into account, which are the representation of physical processes, accuracy and computational effort. Each of the choices and considerations will have consequences for the depth averaged simulations. This research investigates the importance of these considerations and consequences for the suitability of results for specific problems. The consequences that are of interest in this investigation are convergence, robustness, and validity.

With the focus on software packages 3Di and D-Flow Flexible Mesh, multiple cases are simulated in order to analyze the results based on the made choices. Starting point of this research is simulating test cases that are used to analyze the considerations and choices step by step. Hereafter a river reach is simulated where it is more difficult to analyze the considerations and choices separately.

First a literature study is set up. In this study the main differences between Flexible Mesh and 3Di have been described. One of the differences between these packages is the mesh generation. 3Di generates a Cartesian grid based on the sub-grid method with quadtrees, while Flexible Mesh works with an unstructured grid that combines the curvilinear grid and triangles. Though it also has the possibility to use a Cartesian grid. The other main difference is the inclusion of diffusion in Flexible Mesh.

The first test case that is considered, is based on a mildly curved flow experiment in the flume (Blokland, 1985). It is chosen because many measurements are available. These measurements make it possible to compare the influence of the additional physical processes in Flexible Mesh such as secondary flow and turbulent viscosity. In addition the results for the multiple grids of Flexible Mesh are compared with each other and with the Cartesian grid of 3Di. For this comparison the shallow water equations of both packages are identical, hence, the turbulent viscosity and diffusivity in Flexible Mesh are set to zero just as other additional processes. Whereas in 3Di the results coincide well with the

experimental data, this is not the case for a Cartesian grid in Flexible Mesh. Even with a higher resolution the results are further off than for a curvilinear grid.

The comparison of the second test case, U-bend with sinusoidal bed profile, is done by using a curvilinear grid for Flexible Mesh instead of Cartesian grid, because of the results of the first test case. This test case is based on a paper of Stelling (2012), and is chosen due to the varying bottom profile in both the $x-$ and $y-$direction. As a result a better understanding of processing bathymetry in both packages can be obtained. Furthermore, a refinement is placed on the left side of the bend, where the transition of a coarse to fine grid is placed in the middle of the bend. Unlike the first test case, the curvilinear grid is not quite comparable to the Cartesian grid. The cells in the streamwise direction are twice as long as the ones in the transversal direction.

The main point of interest in simulating the weir is the energy loss and the placement of local refinement. It is seen that in each simulation where the weir is modeled in the bathymetry, an increase of energy is found. For both packages it is thought to be due to the discretization of the advection term. According to Stelling and Duinmeijer (2003) an increase of energy can occur, when the wrong type of conservation is used. Over the entire domain a conservation of momentum is assumed, while only conservation of energy is applied when a subgrid model is used. It might also be the result of wrongly assuming a hydrostatic pressure. For further research it is recommended to create a weir where the hydrostatic pressure is valid to investigate the origin of the energy increase.

Outcomes of the test cases have made it easier to understand the results of the river. However, some of the outcomes do not coincide with the expectations based on the test cases. This applies for the Cartesian grid of Flexible Mesh. Based on the test case it is recommended to use a curvilinear grid in Flexible Mesh instead of a Cartesian grid, since these results differ more with the experimental data.

In the test case "Turbulent jet" it is seen that with an additional turbulent viscosity, where the numerical viscosity is already present, the mixing layer is wider with increasing distance from the inflow than without this addition. With additional viscosity the center of the gyre is also closer to the inflow boundary, what can also be seen in the groyne field of the river. Hence, the turbulent viscosity might be overestimated compared to the river. Since so many other factors, like bathymetry, measurement errors, interpolation, influence the results, it is difficult to know which factor is important.

Though in each case certain choices are made, multiple decisions have already been made before considering these cases. Each numerical model consists of the shallow water equations, which gives that certain assumptions are already made.

Some limitations of the packages have been that both of them were quite new, hence, not many people have expertise in these programs. Doing this research partly at Deltares has helped to understand results that were sometimes due to bugs in the packages or self-created due to misunderstandings.

Chapter 13

Conclusions

This study has revealed that the many choices that can be made with the use of numerical models for depth averaged simulations have great consequences for the resolved hydrodynamics. The considered choices in this research are related to grid resolution, boundary conditions, and turbulence models.

With the focus on software packages 3Di and D-Flow Flexible Mesh, multiple cases are simulated in order to analyze the results based on the made choices. Starting point of this research is simulating test cases that are used to analyze the considerations and choices step by step. Hereafter a river reach is simulated where it is more difficult to analyze the considerations and choices separately. The conclusions of the most important choices, considerations and consequences for each case are presented.

Flow over broad-crested weir

An obstacle can be modeled in two ways, either with a supergrid or subgrid model. For the first it is important to have a resolution where at least 5 cells on the crest of the weir are needed. Otherwise, with a subgrid model, the resolution is of less importance for a simple rectangular channel. Considering a flat bottom, no friction, the results can be compared with an analytical solution and are quite accurate, though the energy head is overestimated for both packages. The computational effort can be decreased by applying a local refinement on the obstacle. For both FM and 3Di this results in local differences compared to a grid where the high resolution is applied uniformly. In FM it is seen that the usage of triangles results in errors in the equilibrium discharge than are up to 30% but decrease when having a finer grid.

Mildly and sharply curved bend

Two of the cases consisted of simulating a bend, where one is mildly curved and the other one sharply curved. The latter is more focused on mathematical aspects, such as local refinements, while in the mildly curved bend multiple physical processes are analyzed in Flexible Mesh. Each physical process resulted in hydrodynamics that are more accurate to the measurements. However, without calibrating it is almost impossible to obtain results

that are similar to the measurements. In 3Di these physical processes, expect friction, are not implemented, resulting in easier usage, but might also result in less accurate results.

For the sharply curved bend local refinements are introduced. These refinements result in a lower computational time, but also additional errors in the results compared to a uniform grid. The local error at the transition of a coarse to fine grid are in both packages approximately of the same error. However, it is seen that the overall differences in the hydrodynamics are larger in 3Di than Flexible Mesh.

Turbulent jet

In this case only one fine resolution is chosen such that the diffusivity is well represented. In Flexible Mesh a constant turbulent viscosity is chosen in one simulation and it is set at zero in another simulation. For all results it is expected that there is numerical viscosity present, however, this is only visible in the results of Flexible Mesh. Though it appears as if diffusivity is present in 3Di due to numerical viscosity by northward directed velocities that are present, when only an eastward directed velocity is introduced, there is no mixing layer or gyre in the results. More research will be needed in order to obtain more insight in this process, which is partly provided by the river reach.

River reach

The focus in this case is on physical aspects, diffusivity and energy losses, and mathematical aspects. The multiple options for a turbulence model in Flexible Mesh have lead to results that are more similar to the velocity field measurements. Hence, the diffusivity is better represented in Flexible Mesh. In both 3Di and Flexible Mesh small energy increases can be found at flow over obstacles. Though this increase is physically not correct, it is small enough to be neglected. The order of magnitude is in both packages approximately similar. Applying local refinements resulted in local errors. In this specific case it is seen that large differences in the velocity fields are found, since the location of the gyre is slightly changed. In most cases this small change can be acceptable, and results in a large decrease of the computational time in case of a large simulation with a relatively small area of interest.

Synthesis

Overall, it appears that the rate of convergence in 3Di is higher than in Flexible Mesh for the cases that are taken into account. In most cases a high resolution for the pixel subgrid model is used, which has the advantage of a more precise volume balance while it is possible to maintain a coarser grid. Though the rate of convergence is high, the converge itself is more unexpected, which is seen in each case where a variable grid is used. By changing the resolution the results are unexpected, making it more difficult to interpret them.

Furthermore, in both 3Di and Flexible Mesh the placement of transition from a coarse to fine grid is important. When this transition is placed where gradients are present, local errors are introduced. A larger gradient will results in higher errors. It is recommended to place this transition a distance further upstream from the area of interest in order to avoid these errors in that area. When multiple areas of interest are closely together it might be better to refine the complete area in order to avoid unnecessary errors.

Besides some differences, both packages behave quite similar in either physical processes that influence the hydrodynamics or when applying a local refinement. Based on the cases

that are solved in this thesis a better overview of the choices in each package is obtained for specific problems, together with the most important considerations and consequences.

13.1 Further research

The aim of simulating the test cases before a more complex model such as the river, is to get a better understanding of both Flexible Mesh and 3Di. Though the test cases are helpful, they raised some questions for further research. For each test case the convergence of 3Di behaves a bit unexpected. It appears that it underestimates the discharge or overestimates the water level, depended on the inflow boundary condition, whereas for Flexible Mesh it is the other way around. However, after a certain refinement factor the values that converge suddenly de-/increase after they are respectively increasing or decreasing before this factor. The geometry as well as the important processes differ for each test case, hence, there must be some other connection and origin for this occurrence. If more information about it would be available, it is easier to predict and understand the results of 3Di when refining the grid.

Simulating a turbulent jet has given more insight in the diffusion process in Flexible Mesh and 3Di. Viscosity influences the diffusion process, whether this is turbulent viscosity or numerical viscosity. It would be interesting to find out more about the influence of numerical viscosity. This test case is done with one inflow value. With another value the velocity changes, hence the numerical viscosity changes as well. Also adjusting the grid size will influence the numerical viscosity. When the influence and order of numerical viscosity are known, it might be easier to predict what the influence of turbulent viscosity will be. Furthermore it is recommended to have an experiment where the term $\overline{u'v'}$ is measured. When from this experiment the gradients are also known, the turbulent viscosity can be calculated. This turbulent viscosity can then be used to implement in the Flexible Mesh. When the velocity gradients from the results of the simulation in Flexible Mesh are known, the Reynolds stresses can be calculated. These stresses can be compared to the experimental $\overline{u'v'}$ values. Hence, more insight will be obtained about the diffusion term in Flexible Mesh. Another option is to use Smagorinsky or Elder and compare the turbulent viscosities that are calculated with these options. With more insight in these variables, it can be better explained why the center of the gyres in the groyne field appear at a certain location.

Bibliography

Arcement, G. and Schneider, V. *Guide for Selecting Manning's Roughness Coefficients for Natural Channels and Flood Plains.* US.

Blokland, T. (1985). *Turbulentie-metingen in een gekromde goot.* M.Sc. Thesis, Delft University of Technology.

Boiten, W. and Pitlo, R. (1982). The V-shaped broad-crested weir. *Journal of the Irrigation and Drainage*, 108: .

Borsboom, M. (2013). Construction and analysis of D-FLOW FM-type discretizations. Tech. rep., Deltares Memorandum.

Casulli, V. (2009). A high-resolution wetting and drying algorithm for free-surface hydrodynamics. *International Journal for Numerical Methods in Fluids*, 60: 391–408.

Chatterjee, A. (2004). Novel multi-block strategy for CAD tools for microfluidics type applications. *Advances in Engineering Software*, 35: 443–451.

Deltares (2015a). *Delft3D Flexible Mesh Suite: D-Flow Flexible Mesh Technical Reference.* Delft.

Deltares (2015b). *Delft3D Flexible Mesh Suite: D-Flow Flexible Mesh User Manual.* Delft.

Dewals, B., Kantoush, S., Erpicum, S., Pirotton, M., and Schleiss, A. (2008). Experimental and numerical analysis of flow instabilities in rectangular shallow basins. *Environmental Fluid Mechanics*, 8: 31–54.

Elder, J. (1959). The dispersion of a marked fluid in a turbulent shear flow. *Journal of Fluid Mechanics*, 5: 544–560.

Hagen, E. T. (2014). *Hydrodynamic river modelling with D-Flow Flexible Mesh.* M.Sc. Thesis, University of Twente.

Ji, Z.-G. (2008). *Hydrodynamics and water quality: modeling rivers, lakes and estuaries.* Cambridge Aerospace Series. Cambridge University Press, Cambridge.

Jirka, G. H. and Uijttewaal, W. S. J. (2004). *Shallow Flows*. Balkema, Leiden.

Kernkamp, H., van Dam, A., Stelling, G., and van der Pijl, S. (2011a). D-flow flexible mesh: Hydrodynamic modelling using structured and unstructured meshes. Powerpoint.

Kernkamp, H. W. J., van Dam, A., Stelling, G. S., and de Goede, E. D. (2011b). Efficient scheme for the shallow water equations on unstructured grids with application to the Continental Shelf. *Ocean Dynamics*, 61: 1175–1188.

Liseikin, V. D. (2004). *A computational differential geometry approach to grid generation*. Springer-Verlag, Berlin.

Madsen, P., Rugbjerg, M., and Warren, I. (1988). Subgrid Modelling in Depth Integrated Flows. *Coastal Engineering*, page .

Perot, B. (2000). Conservation properties of unstructured staggered mesh schemes. *Journal of Computational Physics*, 159: 58–89.

Smagorinsky, J. (1963). General circulation experiments with the primitive equations. I. The basic experiment. *Monthly weather review*, 91: 99–164.

Stelling, G. (2012). Quadtree flood simulations with sub-grid digital elevation methods. *Water Management*, 165: 567–580.

Stelling, G. and Duinmeijer, S. (2003). A staggered conservative scheme for every Froude number in rapidly varied shallow water flows. *International Journal for Numerical Methods in Fluids*, 43: 1329–1354.

Stelling, G. S. and Duinmeijer, S. P. A. (2003). A staggered conservative scheme for every Froude number in rapidly varied shallow water flows. *International Journal for Numerical Methods in Fluids*, 43(12): 1329–1354.

Uijttewaal, W. S. J. (2015). Turbulence in hydraulics. Lecture Notes.

van Kester, J. (2015). *Memo Deltares: afhandeling van overlaten*. Delft.

Vreugdenhil, C. B. (1994). *Numerical Methods for Shallow-Water Flow*. Kluwer Academic Publishers, Dordrecht.

Vuik, C., van Beek, P., Vermolen, F., and van Kan, J. (2006). *Numerieke Methoden voor Differentiaalvergelijkingen*. VSSD, Delft.

Wang, J. P., Borthwick, A. G. L., and Taylor, R. E. (2004). Finite-volume type VOF method on dynamically adaptive quadtree grids. *International Journal for Numerical Methods in Fluids*, 45(5): 1–22.

Appendix A

Description of the mathematical model

The starting point of modeling rivers are the Navier-Stokes equations, which describe the evolution of a fluid. The shallow water equations that are used in the programs 3Di and D-Flow Flexible Mesh are derived from the NS equations, which are treated in this chapter. Another important point to introduce is grid generation. Besides the NS equations also a short introduction on different mesh types is given.

A.1 Navier-Stokes equations

The Navier-Stokes equations govern the motion of a viscid fluid and describe the conservation of mass and momentum. In the next subsections both conservations are given. The equations are given for a Cartesian coordinate system. Figure A.1 shows the coordinate system and the boundaries in the z-direction with ζ the surface elevation above reference plane (dotted lines) and z_b the bottom level above reference plane.

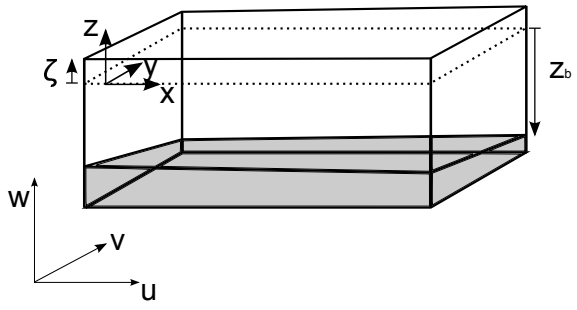

Figure A.1: Coordinate system

A.1.1 Conservation of mass

The basic point for the derivation of the mass-conservation equation is a mass balance for a fluid particle, given below.

Rate of change of mass in fluid particle = Ingoing flux of mass - Outgoing flux of mass

Using this mass balance leads to the continuity equation for a compressible fluid (A.1). In Appendix E a full derivation of the mass-continuity equation can be found.

$$\frac{\partial \rho}{\partial t} + \frac{\partial \rho u}{\partial x} + \frac{\partial \rho v}{\partial y} + \frac{\partial \rho w}{\partial z} = 0 \tag{A.1}$$

In the case of water it is usually assumed that the fluid is incompressible, hence, has a constant density. According to Vreugdenhil (1994) the only point where you have to use the actual density is at the gravitational acceleration, since density variations are important there. This is called the Boussinesq approximation and results in the continuity equation for an incompressible fluid.

$$\frac{\partial u}{\partial x} + \frac{\partial v}{\partial y} + \frac{\partial w}{\partial z} = 0 \tag{A.2}$$

A.1.2 Conservation of momentum

The basic of the momentum equations is the second law of Newton. In Appendix E a full derivation of the momentum equations can be found with starting point Newton's second law. The general form of the momentum equations is as follows (Ji, 2008),

$$\rho \frac{D\mathbf{v}}{Dt} = \frac{\partial \rho \mathbf{v}}{\partial t} + \nabla \cdot (\rho \mathbf{v}\mathbf{v}) = \rho \mathbf{g} - \nabla p + \overline{f_{\text{vis}}}. \tag{A.3}$$

Beside the absence of some external forces in the above equation, the viscous force is not yet defined. Water is known as an Newtonian fluid, which means that the stresses are linear proportional to the rate of deformation (Ji, 2008). Together with the Boussinesq approximation these viscous forces can be written as

$$\overline{f_{\text{vis}}} = \nabla \cdot \boldsymbol{\tau} \tag{A.4}$$

where the water shear stress is expressed as

$$\begin{aligned} \tau_{xx} &= 2\mu \frac{\partial u}{\partial x} & \tau_{xy} &= \tau_{yx} = \mu \left(\frac{\partial u}{\partial y} + \frac{\partial v}{\partial x} \right) \\ \tau_{yy} &= 2\mu \frac{\partial v}{\partial y} & \tau_{xz} &= \tau_{zx} = \mu \left(\frac{\partial u}{\partial z} + \frac{\partial w}{\partial x} \right) \\ \tau_{zz} &= 2\mu \frac{\partial w}{\partial z} & \tau_{zy} &= \tau_{yz} = \mu \left(\frac{\partial w}{\partial y} + \frac{\partial v}{\partial z} \right) \end{aligned} \tag{A.5}$$

with μ the dynamic viscosity, and where the first subscript denotes the plane on which the stress are working and the second the direction on which the stress works. Substituting expression (A.4) for the viscous forces and considering the Coriolis effect Equation A.3 transforms in the full set of momentum equations in 3 dimensions.

$$\frac{\partial \rho u}{\partial t} + \frac{\partial \rho u^2}{\partial x} + \frac{\partial \rho uv}{\partial y} + \frac{\partial \rho uw}{\partial z} = -\frac{\partial p}{\partial x} + \rho f v + \left[\frac{\partial \tau_{xx}}{\partial x} + \frac{\partial \tau_{yx}}{\partial y} + \frac{\partial \tau_{zx}}{\partial z}\right] \tag{A.6}$$

$$\frac{\partial \rho v}{\partial t} + \frac{\partial \rho vu}{\partial x} + \frac{\partial \rho v^2}{\partial y} + \frac{\partial \rho vw}{\partial z} = -\frac{\partial p}{\partial y} - \rho f u + \left[\frac{\partial \tau_{xy}}{\partial x} + \frac{\partial \tau_{yy}}{\partial y} + \frac{\partial \tau_{zy}}{\partial z}\right] \tag{A.7}$$

$$\frac{\partial \rho w}{\partial t} + \frac{\partial \rho wu}{\partial x} + \frac{\partial \rho wv}{\partial y} + \frac{\partial \rho w^2}{\partial z} = -\frac{\partial p}{\partial z} - \rho g + \left[\frac{\partial \tau_{xz}}{\partial x} + \frac{\partial \tau_{yz}}{\partial y} + \frac{\partial \tau_{zz}}{\partial z}\right] \tag{A.8}$$

with $f = 2\Omega \sin \phi$ the Coriolis parameter. Ω is the angular velocity of rotation of the Earth and ϕ represents the latitude in degrees. In order to solve the equations, boundary conditions are needed. However, the equations are simplified in Chapter 3 which means that the boundary conditions are needed for the simplified equations. Hence, in Chapter 3 the boundary conditions are given for the simplified equations.

A.2 Grid generation

One of the basic steps of creating a numerical model is the generation of a grid (or mesh) of the area that one is interested in. A grid consists of grid cells that can have various forms. The simplest form is a triangular cell in two-dimensional volumes and a tetrahedral cell in three-dimensional volumes (Liseikin, 2004). This is due to their pertinence to all sorts of domain structures. Figure A.2 displays these grid cells as an example for the definitions.

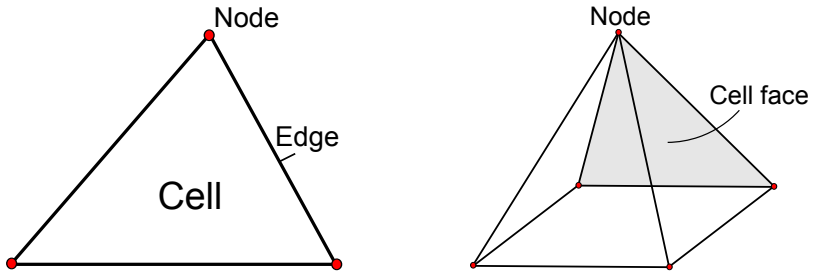

(a) 2-dimensional (b) 3-dimensional

Figure A.2: Grid cell definitions

It is assumed that the grid cells do not intersect each other. Hence, there cannot be a node of one cell lying in the middle of another cell. When also each node of a cell is either the same node of another cell or belongs to the boundary it is called an admitted intersection. Figure A.3 displays both admitted and nonadmitted intersections. Number 2 and 3 show a node that is on the edge of another cell. This node is known as a hanging node. When a grid is locally refined it is possible that these hanging nodes occur.

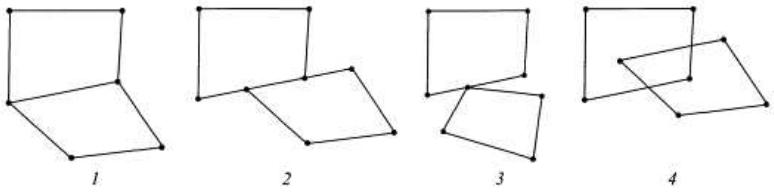

Figure A.3: Admitted (1) and nonadmitted (2, 3, 4) intersections of neighboring quadrilateral cells (Liseikin, 2004)

Another important point is the grid organization. In order to form and solve the discretized equations that originate from the differential equations, it should be known where the neighboring points and cells are. Some organization is needed for this. The generation of grids can be done in multiple ways. The two fundamental classes are the structured and unstructured grid generation, both are discussed below.

A.2.1 Structured grid

A structured grid (looking in 2D) can consist of a rectangular or curvilinear grid. The left grid of Figure A.4 shows how a curvilinear grid looks and the right a rectangular grid. Note, this figure displays the transformation of a grid from the physical to the logical space, which is done to solve the model in an easier way. With a structured grid one has an ordered layout of grid points. All the cells are arranged and the location of each cell is known in a way given in Figure A.4. Due to this arrangement of the cells the computational time is faster compared to an unstructured grid, since finding the value of each cell is much easier. However, looking at modeling rivers, a rectangular grid is often not the best option. The kind of grid is not able to follow the geometry of a river. The result would be a river with a stairway land boundary. So, usually a curvilinear grid is used. Delft 3D Flow uses this grid for example.

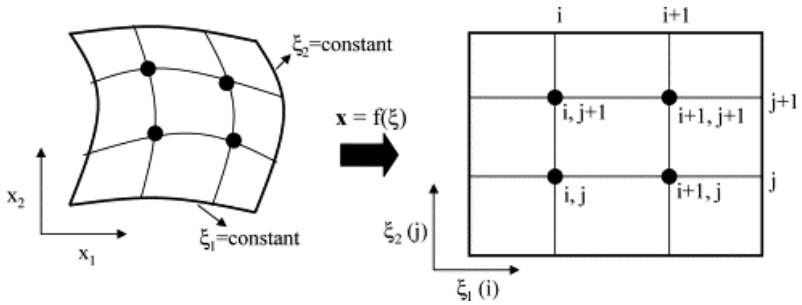

Figure A.4: Layout of grid points in a structured grid (Chatterjee, 2004)

3Di uses a sub-grid method that is arranged as stated by quadtrees (Stelling, 2012), see Figure A.5. It can be seen that this method consist of squares in different sizes, where a larger square can be divided into quarters. Hence, a rectangular grid is used even though it is known this is not the best option for rivers. In Chapter 4 this method will be explained in detail.

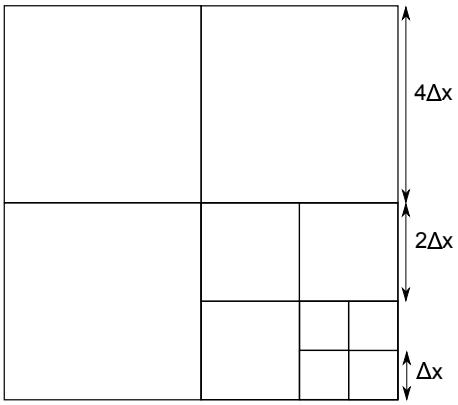

Figure A.5: Sub-grid with quadtrees

A.2.2 Unstructured grid

Usually, an unstructured grid consist of triangles. However, also other geometric forms are possible. These triangles have the ability to take complex geometries into account. The disadvantages if one uses only triangles, are that the computational time is higher and it uses more memory. The advantage of a structured grid where the location of each cell is known is not there for the triangular grid. The information of the location has to be kept in a table, which uses more memory, and finding the right cells is time consuming.

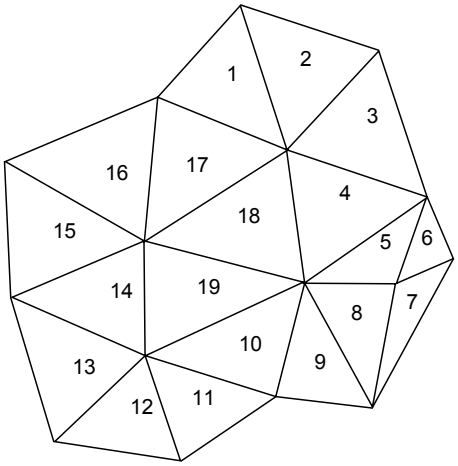

Figure A.6: Unstructured grid

D-Flow Flexible Mesh uses a combination of triangles and a curvilinear grid (Deltares, 2015a), which is sometimes called a hybrid grid since it uses both structured as unstructured grids. When there are complex geometries present in a river (or somewhere else), the triangles can be used to model this far more accurate than when one uses only a curvilinear grid. Where the geometry is less complex the curvilinear grid can be used which has the advantage of a faster computational time and using less memory than working with only a triangular grid. A more detailed explanation is given in Appendix C for this type of grid.

Appendix B

Shallow water equations

Both D-Flow Flexible Mesh and 3Di work with the 2-dimensional depth-averaged equations, also called the 2D Saint-Venant equations or shallow water equations. They originate from the Navier-Stokes equations. The latter are however not easy to solve. Thus, most of the time, simplifications are used based on various assumptions. Making these assumptions means that some 3-dimensional processes are not modeled in the programs, or are not modeled in a correct way. In this thesis only the shallow water equations are used, since 3Di cannot model 3-dimensional. This chapter describes the derivation from the Navier-Stokes equations to the shallow water equations together with all the used assumptions. For an extensive explanation reference is made to Vreugdenhil (1994), Chapter 2. The first three sections in this thesis are a summary of Chapter 2 Vreugdenhil (1994).

B.1 Reynolds averaged Navier-Stokes equations

The scale of motion has a wide range when working in flows like rivers. Solving all fluctuations on these scales is impossible, since it would require enormous computational force. Usually, the interest is only in the large-scale features. Hence, the small-scale features should be isolated in order to solve the other characteristics. This can be done by decomposing the velocity vector and pressure into a mean value and a fluctuating value.

$$u = \bar{u} + u' \tag{B.1}$$

Since there is no information yet whether the flow is stationary or time-dependent, the mean value can be best determined by ensemble averaging instead of time-averaging (Uijttewaal, 2015). If the flow is stationary both averaging processes are equal to each other if the averaging period is long.

The decomposition is substituted into the Navier-Stokes equation followed by averaging. The result is the Reynolds averaged Navier-Stokes equations (RANS). Appendix B gives a full derivation of these equations.

$$\frac{\partial \rho\bar{u}}{\partial t} + \nabla \cdot (\rho\bar{u}\bar{\mathbf{v}}) + \nabla \cdot \left(\rho\overline{u'\mathbf{v}'}\right) = -\frac{\partial \bar{p}}{\partial x} + \rho f\bar{v} + \nabla \cdot (2\mu\nabla^s\bar{u}) + \bar{F}_x \tag{B.2}$$

$$\frac{\partial \rho\bar{v}}{\partial t} + \nabla \cdot \left(\rho\bar{v}\bar{\mathbf{v}'}\right) + \nabla \cdot \left(\rho\overline{v'\mathbf{v}}\right) = -\frac{\partial \bar{p}}{\partial y} - \rho f\bar{u} + \nabla \cdot (2\mu\nabla^s\bar{v}) + \bar{F}_y \tag{B.3}$$

$$\frac{\partial \rho\bar{w}}{\partial t} + \nabla \cdot \left(\rho\bar{w}\bar{\mathbf{v}'}\right) + \nabla \cdot \left(\rho\overline{w'\mathbf{v}}\right) = -\frac{\partial \bar{p}}{\partial z} - \rho g + \nabla \cdot (2\mu\nabla^s\bar{w}) \tag{B.4}$$

where $\nabla^s = \frac{1}{2}\nabla(\cdot) + \frac{1}{2}\nabla(\cdot)^T$, the symmetric operator, and F_i other driving forces that might occur. These equations look like the Navier-Stokes equations except for one extra term in each of the equations. These terms can be seen as stresses, called the Reynold stresses, and represent the exchange of momentum by turbulent motion.

In the next sections the bar over the variables will be omitted in the equations. However, it should be noted that it is still about the Reynolds averaged quantities.

B.2 Boundary conditions

Solving a partial differential equation means one needs boundary conditions. These conditions are applied at the boundary of a domain of interest. In a river boundary conditions are needed at the bottom, surface and both upstream and downstream of the area of interest. The latter are not treated here, since these boundaries are not defined yet. The conditions at the bottom and surface can be divided into kinematic and dynamic boundary conditions. The first state that no water particle can pass the boundary, while the second are related with the force balance.

- Kinematic boundary condition at solid bottom:

$$u\frac{\partial z_b}{\partial x} + v\frac{\partial z_b}{\partial y} - w = 0 \qquad \text{at } z = z_b \tag{B.5}$$

  where $z_b = \zeta - h$ the bottom level above reference level, and ζ the water level above reference level (Figure A.1).

- Kinematic boundary condition at free water surface:

$$\frac{\partial \zeta}{\partial t} + u\frac{\partial \zeta}{\partial x} + v\frac{\partial \zeta}{\partial y} - w = 0 \qquad \text{at } z = \zeta \tag{B.6}$$

- Dynamic boundary condition at solid bottom:

$$u = v = 0 \qquad \text{at } z = z_b \tag{B.7}$$

  the "no-slip" condition. It can be seen as viscous fluid that sticks to the boundary, in this case the bottom (Vreugdenhil, 1994).

- Dynamic boundary condition at free water surface:

$$p = p_a \qquad \text{at } z = \zeta, \tag{B.8}$$

  where p_a is the atmospheric pressure.

B.3 Scaling

To go from the RANS equations to the shallow water equations it is assumed that any vertical scale H is much smaller than the horizontal scales L. This results into a flow that can be seen as a boundary-layer form. Using dimensionless numbers the vertical momentum equation can be written in its non-dimensional form. The advantage of this technique is that it is easy to find the order of magnitude of each term. Hence, determining which terms can be neglected and which are important.

Let the terms x and y be of order L and z of the order H, whereas the velocities u and v are of order U. The continuity equation gives that the scale of the vertical velocity w should be of the order UH/L. Using these scales in the vertical momentum equation results into the following ratios:

$$\begin{aligned} \text{local acceleration} \quad & \frac{FrH^2}{L^2} \\ \text{advective terms} \quad & \frac{Fr^2H^2}{L^2} \\ \text{stress gradients} \quad & \frac{Fr^2H}{ReL} \end{aligned} \tag{B.9}$$

where Fr is the Froude number and Re the Reynolds number.

$$Fr = \frac{U}{\sqrt{gH}}, \qquad Re = \frac{UH}{\nu} \tag{B.10}$$

In rivers the Reynolds number can have orders of 10^5, while the Froude number usually has a small order, 10^{-1}. Using these values in the above ratios these will be relative small compared to the gravitational term. This results in two remaining terms, the pressure gradient and the gravitational acceleration.

$$\frac{\partial p}{\partial z} = -\rho g \tag{B.11}$$

This balance is known as the hydrostatic pressure distribution. Integration over the waterdepth results in an expression for the pressure. This expression is only valid if the density assumed constant over the depth, otherwise the pressure gradient will depend on z.

$$p = \rho g(\zeta - z) + p_a \tag{B.12}$$

with p_a the atmospheric pressure. Substitution into the momentum equations leads to

$$\frac{\partial u}{\partial t}+\frac{\partial u^2}{\partial x}+\frac{\partial uv}{\partial y}+\frac{\partial uw}{\partial z}-fv+g\frac{\partial \zeta}{\partial x}+\frac{g}{\rho_0}(\eta-z)\frac{\partial \rho}{\partial x}+\frac{1}{\rho_0}\frac{\partial p_a}{\partial x}-\frac{1}{\rho_0}\left(\frac{\partial \tau_{xx}}{\partial x}+\frac{\partial \tau_{yx}}{\partial y}+\frac{\partial \tau_{zx}}{\partial z}\right)=0 \tag{B.13}$$

$$\frac{\partial v}{\partial t}+\frac{\partial uv}{\partial x}+\frac{\partial v^2}{\partial y}+\frac{\partial vw}{\partial z}+fu+g\frac{\partial \zeta}{\partial y}+\frac{g}{\rho_0}(\eta-z)\frac{\partial \rho}{\partial y}+\frac{1}{\rho_0}\frac{\partial p_a}{\partial y}-\frac{1}{\rho_0}\left(\frac{\partial \tau_{xy}}{\partial x}+\frac{\partial \tau_{yy}}{\partial y}+\frac{\partial \tau_{zy}}{\partial z}\right)=0$$

where ρ_0 is the reference density.

B.4 2D shallow-water equations

The final step is to integrate Equations (B.13) and the continuity equation over the depth $h=\zeta-z_b$. The depth averaged values are defined as:

$$\bar{u}=\frac{1}{h}\int_{z_b}^{\zeta} u dz. \tag{B.14}$$

Integration of the continuity equation is given as an example. The other integrations are fully described in Appendix B.

$$\begin{aligned}\int_{z_b}^{\zeta}\frac{\partial u}{\partial x}+\frac{\partial v}{\partial y}+\frac{\partial w}{\partial z}dz =&\frac{\partial}{\partial x}\int_{z_b}^{\zeta} u dz-u^s\frac{\partial \zeta}{\partial x}+u^b\frac{\partial z_b}{\partial x}+\frac{\partial}{\partial y}\int_{z_b}^{\zeta} v dz-..\\ &..-v^s\frac{\partial \zeta}{\partial y}+v^b\frac{\partial z_b}{\partial y}+w^s-w^b\\ =&\frac{\partial \zeta}{\partial t}+\frac{\partial h\bar{u}}{\partial x}+\frac{\partial h\bar{v}}{\partial y}=0\end{aligned} \tag{B.15}$$

where the Leibniz Integral Rule is used at the first line and boundary conditions (B.5) and (B.6) at the second line. s and b stand respectively for surface and bottom in the above equation. Using similar operations for the momentum equations and omitting the overbar, the resulting shallow water equations are

$$\frac{\partial hu}{\partial t}+\frac{\partial hu^2}{\partial x}+\frac{\partial huv}{\partial y}-fhv+gh\frac{\partial h}{\partial x}+\frac{gh^2}{2\rho_0}\frac{\partial \rho}{\partial x}-\frac{1}{\rho_0}\tau_{bx}-\frac{\partial}{\partial x}\left(hT_{xx}\right)-\frac{\partial}{\partial y}\left(hT_{xy}\right)=F_x \tag{B.16}$$

$$\frac{\partial hv}{\partial t}+\frac{\partial huv}{\partial x}+\frac{\partial hv^2}{\partial y}+fhu+gh\frac{\partial h}{\partial y}+\frac{gh^2}{2\rho_0}\frac{\partial \rho}{\partial y}-\frac{1}{\rho_0}\tau_{by}-\frac{\partial}{\partial x}\left(hT_{yx}\right)-\frac{\partial}{\partial y}\left(hT_{yy}\right)=F_y$$

with $F_{x,y}$ the driving forces including wind, radiation stresses, and the atmospheric pressure gradient and T_{ij} the lateral stresses that include viscous friction, turbulent friction and differential advection (Vreugdenhil, 1994):

$$T_{ij}=\frac{1}{h}\int_{z_b}^{\zeta}\left(\nu\left(\frac{\partial u_i}{\partial x_j}+\frac{\partial u_j}{\partial x_i}\right)-\overline{u_i'u_j'}+(u_i-\overline{u_i})(u_j-\overline{u_j})\right)dz \tag{B.17}$$

These equations are usually not the "standard" form of the shallow water equations. The "standard" form is obtained by neglecting some of the processes and assuming a few parameterizations. However, these are not explained here but in the next section together with the equations used in FM and 3Di.

B.5 Assumptions

The shallow water equations that are used in FM and 3Di are different from the one that were derived above, except for the conservation of mass. The differences between both momentum equations, together with an explanation of new terms, are described after the next equations. Conservation of momentum for both programs is as follows ((Deltares, 2015a), (Stelling, 2012)),

$$\text{3Di } x-\text{direction} \quad \frac{\partial u}{\partial t}+u\frac{\partial u}{\partial x}+v\frac{\partial u}{\partial y}+g\frac{\partial \zeta}{\partial x}+\frac{c_f}{h}u\|u\|=0 \tag{B.18}$$

$$y-\text{direction} \quad \frac{\partial v}{\partial t}+u\frac{\partial v}{\partial x}+v\frac{\partial v}{\partial y}+g\frac{\partial \zeta}{\partial y}+\frac{c_f}{h}v\|u\|=0 \tag{B.19}$$

$$\text{FM } x-\text{direction} \quad \frac{\partial u}{\partial t}+u\frac{\partial u}{\partial x}+v\frac{\partial u}{\partial y}+g\frac{\partial \zeta}{\partial x}+\frac{c_f}{h}u\|u\|=\frac{1}{h}\nabla\cdot\left(\nu h\left(\nabla u+\nabla u^T\right)\right) \tag{B.20}$$

$$y-\text{direction} \quad \frac{\partial v}{\partial t}+u\frac{\partial v}{\partial x}+v\frac{\partial v}{\partial y}+g\frac{\partial \zeta}{\partial y}+\frac{c_f}{h}v\|u\|=\frac{1}{h}\nabla\cdot\left(\nu h\left(\nabla v+\nabla v^T\right)\right) \tag{B.21}$$

which is the non-conservative form of the shallow water equations, whereas the equations in Section 3.4 are in conservative form. It can be seen when Equation (B.16) and the above are compared many terms are missing or different. Hence, there are some processes that are neglected and some that are simplified. Below these are described together with assumptions that were needed to go from the Navier-Stokes equations to the 2D shallow water equations (Vreugdenhil, 1994).

Boundary layer form

A boundary layer form is assumed. Hence, all terms except the pressure gradient in the vertical momentum equations are small relative to the gravitational acceleration. This results in a pressure that is hydrostatic distributed and the simplified terms $\left(g\frac{\partial \zeta}{\partial x}, g\frac{\partial \zeta}{\partial y}\right)$ instead of $\left(\frac{\partial p}{\partial x}, \frac{\partial p}{\partial y}\right)$. Looking at a river one can assume that the acceleration and eddy viscosity terms are much smaller than the gravitational acceleration. However, when there are structures in a river, like groynes, these terms cannot always be neglected. Consequences are that the velocity is underestimated, since acceleration in the vertical direction is neglected.

Driving forces

Driving forces (F_x, F_y) are neglected:

- The atmospheric pressure gradient $\left(\frac{\partial p_a}{\partial x}, \frac{\partial p_a}{\partial y}\right)$ can be important when a storm surge is simulated. Looking only at rivers it can be neglected.
- Wind stresses are not present in the shallow water equations. In both programs there is however the possibility to turn it on.
- It was assumed that the density is constant in the vertical direction, since the depth-averaged equations are used. This led to a linear relation between pressure and density (Equation (3.12)). When there is no stratification, or it is negligible, this will be no problem. Otherwise, a 2DH model will not suffice anymore. This does not mean that the density is constant in the horizontal plane. These density gradient s$\left(\frac{\partial \rho}{\partial x}, \frac{\partial \rho}{\partial y}\right)$, present in Equation (3.16), usually have a small influence compared with other terms and are therefor often neglected.
- Radiation and tidal stress are of less importance in modeling rivers than in coastal areas or oceans. Neglecting these terms will therefor not have a large impact.

Coriolis force

The Coriolis effect in Equation (3.16) is left out. Whether this assumption is acceptable can be seen with the Rossby number, Ro= U/fL. It represents the ratio between inertia and Coriolis terms. When it is of the order 1 or higher, the Coriolis effect can be neglected, since it is of minor importance. In the case of rivers, the length scale is of the order of $10^3 - 10^4$ m and the velocity of order 1 m/s. Looking at rivers in countries like the Netherlands or Germany gives a Coriolis parameter of order 10^4. Using these values gives a Rossby number of the order 1. Hence, the assumption of neglecting the Coriolis force is acceptable.

Bottom stress

The bottom stress is expressed as $\tau_{bx}/\rho = c_f u\|u\|$, where $\|\cdot\|$ is the L2-norm. Hence, $\|u\| = \sqrt{u^2 + v^2}$. This parameterized form is needed to have a closed system of equations. It originates from the similarities with the equilibrium between turbulent boundary layers. Thus, if the fluid has a analogous flow this supposition is assumed correct. The coefficient c_f is a standard friction coefficient which depends on the wall roughness. It can for example be approximated by Chezy, or Manning.

Lateral stresses

Lateral stresses T_{ij} where $i, j = x, y$:

- The viscous stresses are neglected. In realistic situations the order of magnitude is small compared to the other therms, hence, consequences of neglecting the viscous stresses will be small.
- A river bend has a secondary flow that results from centrifugal and pressure forces in the intersection. Looking at a cross section of the river in a bend, see Figure B.1, it can be seen that in the upper part the flow is directed towards the outer bend and in the lower part towards the inner bend. When the bend is only mildly curved the amount of water flowing outwards is almost equal to the inwards water flow. Usually the main velocity has a profile that is more or less a logarithmic

distribution. Hence, the mean velocity is higher at the upper part than the lower part. Combining the secondary flow and the main velocity results in a helical flow, Figure B.2. It can be seen that there is more momentum transported to the outer

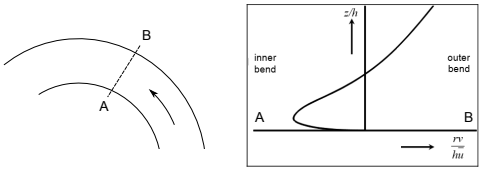

Figure B.1: Secondary flow in a bend

part of the bend than the inner part. It results in a higher velocity at the outer part of the bend which is at the cost of the flow velocity at the inner bend. This is known as differential advection (Jirka and Uijttewaal, 2004). If it is not taken into account it would mean that the flow velocity at the outer bend is underestimated, while the velocity at the inner bend is overestimated.

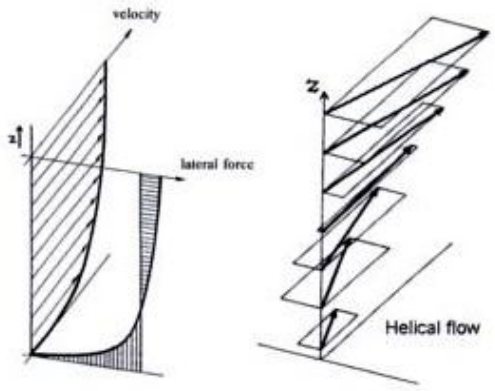

Figure B.2: Helical flow (Jirka and Uijttewaal, 2004)

- One of the processes that is neglected in 3Di but not in Flexible Mesh is the diffusivity. Consequences are that turbulent processes are not modeled in 3Di. In Civil Engineering applications almost all flows are turbulent, including river flows. If only information about the mean flow is needed the absence of turbulence is of less importance compared to information needed about velocity profiles behind groynes. In FM turbulent shear stress is approximated similar to viscous shear stress. This results in one missing expression for the turbulent viscosity. Flexible Mesh uses Elder to estimate the horizontal turbulence viscosity.

B.6 Difference in processes in 3Di and Flexible Mesh

At this moment the possibilities in Flexible Mesh are greater than in 3Di. Of course, it is important to know both differences and similarities. In this section the processes of interest are shortly described.

Friction

Flexible Mesh and 3Di have different options to model bottom friction. In the previous section it was already seen that the bottom stress is expressed as $\tau = \rho c_f u \|u\|$, with c_f a standard friction coefficient. This coefficient can be determined with the following formulations.

Chezy:

$$u = C\sqrt{Ri} \tag{B.22}$$

where C is the Chezy coefficient, R the hydraulic radius en i the bed slope. It can be related to c_f by $C = \sqrt{g/c_f}$. This formulation originates from the fact that there is a balance between the force driving flow and the total friction force and that the latter is a function of a roughness coefficient and the velocity squared.

Manning:

$$u = \frac{1}{n} R^{2/3} \sqrt{i} \tag{B.23}$$

with n the Manning coefficient. This coefficient has the following relation with the Chezy coefficient, $C = R^{1/6}/n$. Manning's formulation is most commonly used in open channel flows

White-Colebrook:

$$\frac{1}{\sqrt{c_f}} = -2 \log \left(\frac{\epsilon}{14.8R} + \frac{2.51}{Re\sqrt{c_f}} \right) \tag{B.24}$$

a formula that calculates directly the friction coefficient with ϵ the roughness height. It is only present in Flexible Mesh and not in 3Di. Above a relation with the Chezy coefficient was already given. Looking at this formula it is seen that there is a log function. Thus, a logarithmic velocity profile is assumed in the vertical direction. Of course, when using the depth-averaged equations this profile is spread over the depth. However, it is physically not correct anymore to use these formulas. Using 2-dimensional models instead of 3-dimensional implies implicitly that the flow is fully developed. When modeling rivers it should be kept in mind whether these formulas are physically correct when used.

Diffusivity

This term is neglected in 3Di as seen before. In Flexible Mesh it is calculated by the term

$$\nabla \cdot \left(\nu h(\nabla u + \nabla u^T)\right). \tag{B.25}$$

In Section 3.1 the Reynolds-averaged Navier-Stokes equations were derived. The $x-$direction is taken as an example to see where this diffusion term arises from. There are two terms in Equation (3.2) that represent stresses,

$$\nabla \cdot (\overline{\rho u' v'}), \text{ and } \qquad \nabla \cdot (2\mu \nabla^s \bar{u}). \tag{B.26}$$

Remember that the overline in this case represents the time-averaged. These terms can be taken together. Then,

$$\begin{aligned} \frac{\partial}{\partial x}\tau_{xx} &= \frac{\partial}{\partial x}\left(\rho\overline{u'u'} + 2\mu\frac{\partial u}{\partial x}\right) \\ \frac{\partial}{\partial y}\tau_{xy} &= \frac{\partial}{\partial y}\left(\rho\overline{u'v'} + \mu\left(\frac{\partial u}{\partial y} + \frac{\partial v}{\partial x}\right)\right) \end{aligned} \tag{B.27}$$

In order to close the equation system, the turbulent shear stress needs to be approximated by a relation proportional with the mean velocity field. This is done as follows,

$$\begin{aligned} \tau_{t,xx} &= \rho\overline{u'u'} = -2\rho\nu_t\frac{\partial u}{\partial x}, \\ \tau_{t,xy} &= \rho\overline{u'v'} = -\rho\nu_t\left(\frac{\partial u}{\partial y} + \frac{\partial v}{\partial x}\right) \end{aligned} \tag{B.28}$$

where ν_t is the turbulent viscosity, or eddy viscosity. When there is a high Reynolds number, the flow is highly turbulent. This implies that the molecular viscosity shear stresses are much smaller than the turbulent shear stresses. For flows near a wall this is not true. Hence, they can be neglected, giving

$$\begin{aligned} \frac{\partial}{\partial x}\tau_{xx} &= \frac{\partial}{\partial x}\left(-2\rho\nu_t\frac{\partial u}{\partial x}\right) \\ \frac{\partial}{\partial y}\tau_{xy} &= \frac{\partial}{\partial y}\left(-\rho\nu_t\left(\frac{\partial u}{\partial y} + \frac{\partial v}{\partial x}\right)\right). \end{aligned} \tag{B.29}$$

Or, generally written in the shallow water equations,

$$\nabla \cdot \left(\nu h(\nabla u + \nabla u^T)\right). \tag{B.30}$$

Notice that the kinematic viscosity is thus the turbulent viscosity, and not the molecular viscosity which is much smaller in turbulence flows.

Grid

Grid differences were shortly mentioned in Chapter 2. Chapter 4 en 5 will continue with describing this grid generation of both programs. It will not be treated here.

The goal with these differences and similarities is to first make models that are as similar as possible in order to compare them in the same situation. The grid will, however, not be the same since this is what both tools make unique. Possible differences in both programs can then hopefully be reduced to grid generation. It is clear that Flexible Mesh has more options in the modeling. The second step will be to use other processes to run models and compare them with the results where both models were made as similar as possible.

Appendix C

D-Flow Flexible Mesh

One of the main differences between Flexible Mesh and 3Di is the way a grid is generated. Whereas 3Di generates a Cartesian grid, Flexible Mesh uses a combination of an unstructured and structured grid. The latter can consist of a curvilinear or rectangular grid. This combination makes it possible to model numerically complex geometries in a more precise way. When equations are discretised Flexible Mesh has several options to choose from. It will be made clear when this appears together with an explanation of the choice made. This chapter will explain the grid generation of Flexible Mesh, together with the discretisation of the shallow water equations. The main part of this chapter is from the Technical Reference of Delft3D D-Flow Flexible Mesh (Deltares, 2015a).

C.1 Grid generation

Before the discretisation of the shallow water equations is done, an introduction of some notations and properties that are important for this discretisation is given. Flexible Mesh works both with a structured and unstructured grid. Generating an unstructured or curvilinear grid can be complicated compared to a Cartesian grid. There are two important properties that have to be taken into account. These are orthogonality and smoothness. The orthogonality is measured by taking the cosinus of the angle between the netlink and flowlink. See Figure C.1 for the definitions of these terms. Smoothness is defined by the ratio of two adjacent cell areas. In a perfect grid generation both of these parameters would be equal to one. Hence, the netlink has an angle of 90° with the flowlink. An example of both parameters that are ideal is given in Figure C.2. It can be seen that the flowlink is a line between two flownodes. Flownodes are the centers of a cell, that can be defined in different ways. These are explained later in this chapter.

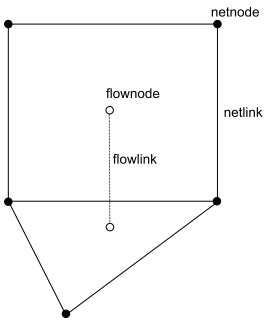

Figure C.1: Net (domain discretisation)

The discretisation is done with a staggered grid, hence, water levels are calculated at the cell center while velocities are calculated at the cell faces' midpoints. For a rectangle the cell center is easy to see. However, looking at a triangle there are multiple ways to define a cell center.

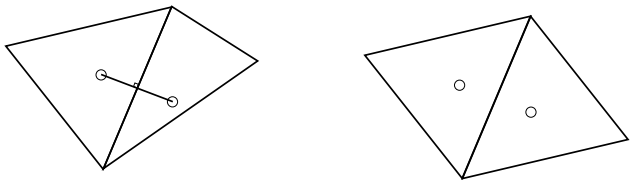

Figure C.2: Perfect orthogonality (left) and perfect smoothness (right)

One of them is the center of a circle that intersects the triangle at each node. The other possibility is the gravity point of the triangle itself, the mass center. Flexible Mesh uses the first possibility, since with this option the orthogonality property is easier to fulfil. One of the disadvantages of using a circumcenter is that the center can lie outside the triangle. When Flexible Mesh construct a grid automatically this usually will not happen. Otherwise, there are many options that can be performed, like changing the minimal and maximal angle of a triangle. In this way triangles with an outlying circumcenter are easier to avoid. Another disadvantage is that the flow link can approach zero. Hence, the flownodes of two adjacent cells are too close together, see Figure C.3a. It shows that the white dots, cell centers, inside the red circle are almost on top of each other. The flow link that connects both cell centers will be very small, which leads to high errors. This can be solved by removing that certain flowlink as seen in Figure C.3b. Notice that the two white dots are not connected with each other.

Removing a flowlink, as is done in Figure C.3b, has consequences for the flow and the grid. The common face between these two cells is removed from the grid. Instead, an invisible, infinite high wall arises where no water can go through. Figure C.4 shows what happens. If the flowlink was not removed, the velocity vectors would be only directed in the $x-$direction, since there are no obstacles. Now, one can see that the flow is going around something invisible. If this happens, the velocity profile resulting from a model is physically not correct. This is why the cell centers should be inside the triangles and not too close to their edges.

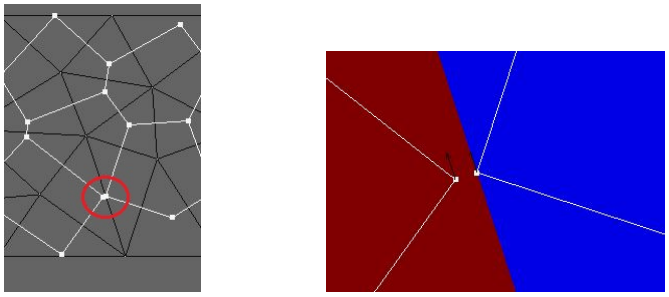

(a) Grid with flowlinks

(b) Removed flowlink

Figure C.3: Small flowlinks

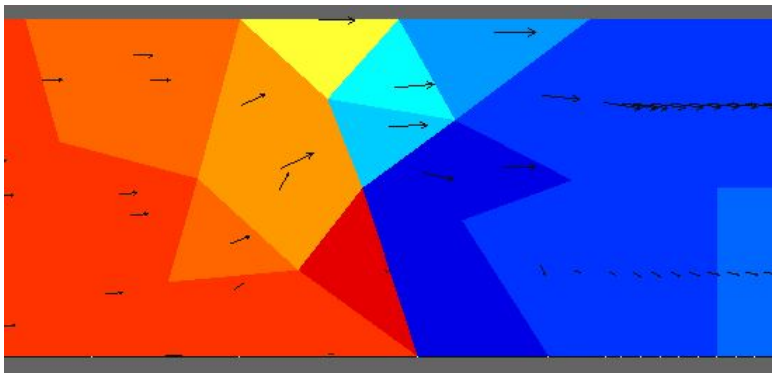

Figure C.4: Behaviour of the flow when a flowlink misses

C.1.1 Connectivity

In this subsection a few important expressions are introduced. These are needed in order to understand the following part of the report. Figure A.2 showed a 3-dimensional cell together with some definitions. The cells in Flexible Mesh can take multiple forms, like rectangular, curvilinear, and triangular prism but also a prism with more than four nodes on top and bottom base. The most common shape in Flexible Mesh are the first three. Since it is easy to extend the following definitions to a rectangular prism, only the triangular prism is taken as an example, also in the remainder of this chapter.

All vertical faces j of a cell k are contained in a set $\mathcal{J}(k)$. The mesh nodes i of a cell k are in a set $\mathcal{I}(k)$. Each face j has mesh nodes $i_{L(j)}, i_{R(j)}$. It depends on the orientation of face j which node belongs to $i_{L(j)}$ or $i_{R(j)}$. The same applies to the neighbour cells $L(j), R(j)$ for face j. This orientation can be taken into account by $1_{j,k}$, which is

$$1_{j,k} = \begin{cases} 1, & L(j) = k \quad (\mathbf{n}_j \text{ is outward normal of cell k}) \\ -1, & R(j) = k \quad (\mathbf{n}_j \text{ is inward normal of cell k}). \end{cases} \tag{C.1}$$

$\mathbf{n}_f$ is the normal vector of face j (Deltares, 2015a). If we take two cells as in Figure C.5, then $\mathcal{J}(1) = \{1, 2, 3\}$ and $\mathcal{J}(2) = \{4, 5, 1\}$. The set of mesh nodes is given by $\mathcal{I}(1) = \{1, 2, 3\}$ for cell $k = 1$ and $\mathcal{I}(2) = \{1, 2, 4\}$ for cell $k = 2$. For face 1 an outward normal vector is found for cell $k = 1$. Hence, $L(1) = 1$, $R(1) = 2$ and $i_L(1) = 2$, $i_R(1) = 1$.

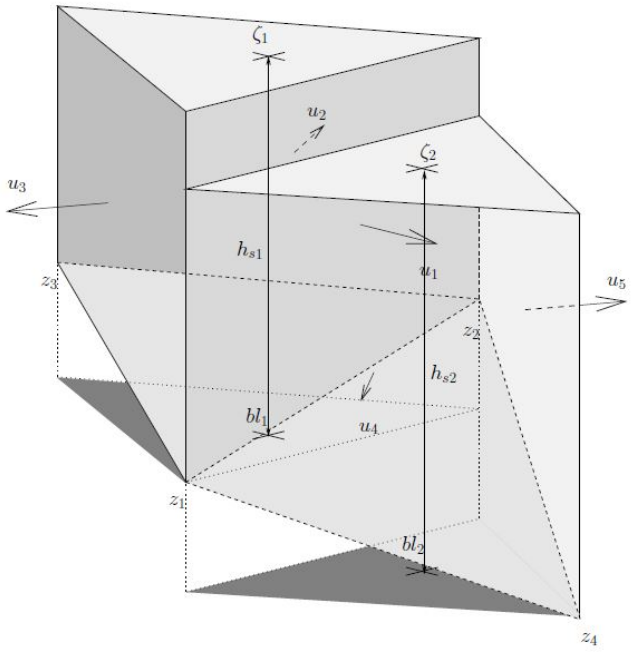

Figure C.5: Example of notations (Deltares, 2015a)

C.1.2 Bed geometry

In Flexible Mesh there are multiple options to define the bed geometry. In Section 4.1.1 the cell-based bed level was already shown in Figure C.5. Its value depends on the type of bed level one chooses. For all available options one can go to the Technical Reference of Deltares (2015a). In this thesis bed level type 3 is chosen in combination with a conveyance type ≥ 1, explained below. This results in the possibility to model the bottom linearly. Usually a uniform bed representation is used. However, a linearly representation gives a more accurate description of the total wet cross sectional area.

$$\begin{aligned} bob_{1,2_j} &= z_{i_{L,R}(j)} \\ bl_k &= \min_{j \in \mathcal{J}(k)} [\min(bob_{1j}, bob_{2,j})] \end{aligned} \tag{C.2}$$

with $bob_{1,2_j}$ the face-based bed-levels and z_i the node-based bed levels. Choosing bed-level type 3 in combination with conveyance ≥ 1 gives that the face- and node-based bed levels are the same. The type of conveyance gives how the friction is defined. When a bottom is linearly modelled in a cell, the water depth is a function inside this cell. This also means that the velocity is not constant, hence, the bed stresses differ inside this cell. If a closer look is taken at the friction term,

$$\text{friction} = \frac{gu\|u\|}{C^2\hat{h}} \tag{C.3}$$

with $\hat{h}$ the hydraulic radius. It can be seen that it depends both on the normal and tangential velocity. Both are variable for the width of a cell. For the conveyance there are 3 types that are possible that are ≥ 1:

Type of conveyance	Normal velocity	Tangential velocity	Water depth	Friction coefficient	Note
1	$u(y)$	$v(y)$	$\hat{h}(y)$	C	All terms are linear varying over the width.
2	$u(y)$	zero	$\hat{h}(y)$	C	Only applicable for a curvilinear grid aligned with the flow.
3	constant	constant	$h = A/P$	C	With a sufficient resolution of a gully in the grid just as good as 1 and 2. However, computational time is 10% faster.

A is the wet cross sectional area and P the wet perimeter.

With the type of bed level known, the wet cross-sectional can be calculated as well. This is the area of a cell face that is wet. When looking at this area there are two possibilities. The first is that the cell face is entirely wet (Figure C.6), while the second is that it is only partly wet.

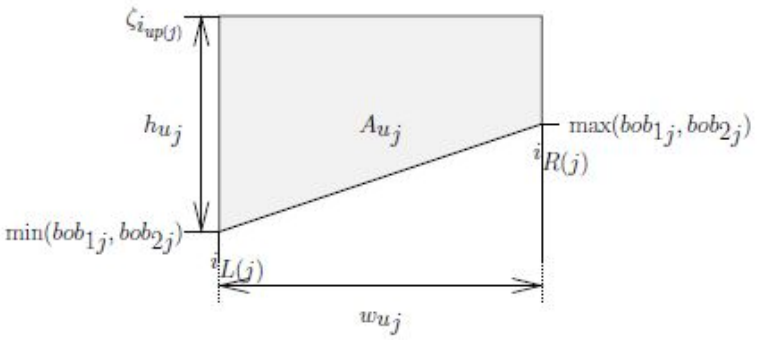

Figure C.6: Flow area A_{uj} and face-based water depth h_{uj} (Deltares, 2015a)

Let $\Delta b_j = \max(bob_{1j}, bob_{2j}) - \min(bob_{1j}, bob_{2j})$, and

$$h_{uj} = \begin{cases} \zeta_{L(j)} - \min(bob_{1j}, bob_{2j}), & u_j > 0 \quad \text{or} \quad u_j = 0 \text{ and } \zeta_{L(j)} > \zeta_{R(j)} \\ \zeta_{R(j)} - \min(bob_{1j}, bob_{2j}), & u_j < 0 \quad \text{or} \quad u_j = 0 \text{ and } \zeta_{L(j)} \leq \zeta_{R(j)} \end{cases} \tag{C.4}$$

where the water level $\zeta_{L,R}$ is obtained by first order upwinding. Hence, there is an error

of second order. This is one of the main disadvantages of using unstructured grids. They usually do not have a high-order accuracy (Perot, 2000). Using these expressions the wet cross-sectional can be defined as

$$A_{uj} = \begin{cases} w_{uj} h_{uj}, & \Delta b_j < 10^{-3} w_{uj} \\ w_{uj} h_{uj} \min(\frac{h_{uj}}{\Delta b_j}, 1) \left(1 - \frac{1}{2} \min(\frac{\Delta b_j}{h_{uj}}, 1)\right), & \text{otherwise} \end{cases} \tag{C.5}$$

with w_{uj} the width. When $\frac{h_{uj}}{\Delta b_j} < 1$ one obtains the rule of calculating areas of triangles. If $\frac{\Delta b_j}{h_{uj}} < 1$ it is a rule for a trapezium.

C.2 Discretisation of shallow water equations

In Section 3.5 the shallow water equations were given like they are implemented in Flexible Mesh. The following subsections contain the spatial and temporal discretisation of these equations.

C.2.1 Spatial discretisation

For cell k the following continuity equation is found,

$$(V_k)_t + \sum_{j \in \mathcal{J}(k)} A_{uj} u_j 1_{j,k} = 0 \tag{C.6}$$

where, as said before, $1_{j,k}$ takes into account the orientation of face j with respect to cell k, and A_{uj} is the wet cross-sectional area. Since the finite volume method is used to discretize the continuity equation it is guaranteed that there is mass conservation. This can be easily seen in the discretized continuity equation. At each cell face there is an incoming or outgoing flux (depended on the value of $1_{1,k}$). At the neighbouring cell this is exactly the opposite sign. Hence, the mass fluxes cancel each other inside the domain channel (Borsboom, 2013). Thus, leaving only the fluxes at the boundary.

Discretisation of the momentum equations is a bit harder than the continuity equation, since it takes place at the faces of a cell.

$$(u_j)_t + \mathcal{A}_{ij} u_j + \mathcal{A}_{ej} + \frac{g}{\Delta x_j} \left(\zeta_{R(j)} - \zeta_{L(j)}\right) + \frac{g \|u_j\|}{C^2 \hat{h}} u_j = 0 \tag{C.7}$$

with $\hat{h}$ the hydraulic radius. The second and third terms are the discretized advection and diffusion term, where $\mathcal{A}_{ij}$ denotes the implicit terms and $\mathcal{A}_{ej}$ explicit terms. They will be better explained below. The fourth term is the water level gradient. By assuming an orthogonal grid the water level gradient can be determined by central differencing, which results in a second order local error.

$$g \nabla \zeta|_j \cdot \mathbf{n}_j \approx \frac{g}{\Delta x_j} (\zeta_{R(j)} - \zeta_{L(j)}) + \mathcal{O}(\Delta x_j^2) \tag{C.8}$$

where Δx_j is the distance between the two circumcenter points where the water levels are defined. It has been observed in Chapter 3 that the bottom friction is an unknown variable which has to be expressed in the mean velocity field and a friction coefficient. Section 3.6 gave the possibilities to determine this friction coefficient. Notice that in Equation (C.7) the Chezy formulation is used.

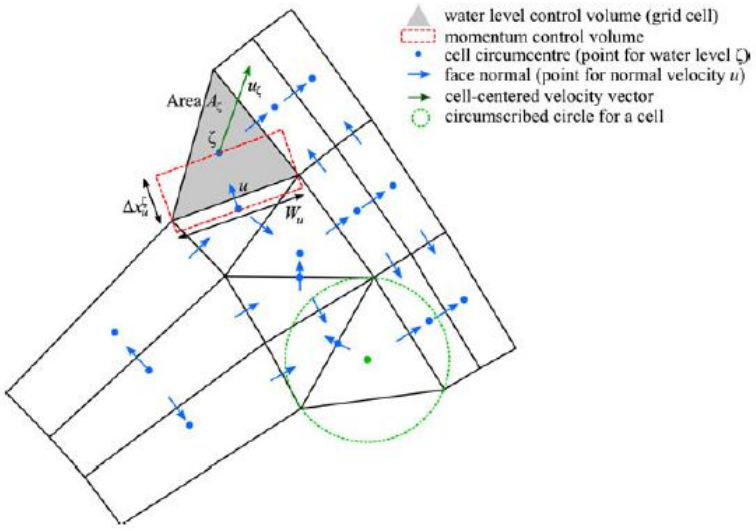

Figure C.7: Control volumes of triangular grid (Kernkamp et al., 2011b)

Whereas for mass there is both local and global conservation, this cannot be said for momentum. Only global conservation of momentum can be proven (Borsboom, 2013). This is the result of the control volumes of momentum. Figure C.7 shows among other things the momentum control volume for a face-normal velocity. It can be seen that it is a rectangle which has in one direction the length between common grid points and in the other direction a length of the distance between the circumcenters of both cells. If in this way the momentum control volume for another adjacent cell of the triangular cell is taken, one would see that they overlap. In order to prove local momentum conservation it is needed to discretize the momentum equation for non-overlapping control volumes, which is not possible for arbitrary triangular cells (or even all quadrilateral grid cells). When there is a rectangular grid, the control volumes will not overlap and there will be local momentum conservation.

Momentum advection

The momentum equations are solved in the face-normal directions, hence, not the complete momentum vector is solved. It was said before that momentum conservation is locally not conservative. Flexible Mesh is not able to define conservative fluxes, since only the face-normal velocity is solved. Following the method of Perot (2000), who achieved momentum conservation for unstructured staggered mesh schemes, multiple advection schemes are thought of. However, none of these schemes is conservative as the method of Perot (2000). The idea behind Perot's method is to reconstruct face-normal velocities to cell-centered velocities. Here a discretisation is performed, whereafter these velocities

are interpolated back to the faces. The final step is to project these velocities in the face-normal direction. This thesis will not elaborate further on the method of Perot (2000). A more detailed idea is given in Deltares (2015a). The advection term as implemented in FM is given by

$$\begin{aligned}\mathcal{A}_{ej} =& \frac{\alpha_j}{\alpha_j V_{L(j)} + (1-\alpha_j)V_{R(j)}} \sum_{l \in \mathcal{J}(L(j))} q_{al} 1_{l,L(j)} \mathbf{u}_{ul} \cdot \mathbf{n}_j - q_{al} 1_{l,L(j)} u_j + .. \\ & .. + \frac{1-\alpha_j}{\alpha_j V_{L(j)} + (1-\alpha_j)V_{R(j)}} \sum_{l \in \mathcal{J}(R(j))} q_{al} 1_{l,R(j)} \mathbf{u}_{ul} \cdot \mathbf{n}_j - q_{al} 1_{l,R(j)} u_j \\ \mathcal{A}_{ij} =& 0,\end{aligned} \tag{C.9}$$

where $\mathbf{u}_{ul}$ is the reconstructed full velocity at the faces obtained by upwinding the cell-centered velocities. The discrete cell-centered approximation is first-order accurate unless the mass and center point (here circumcenter) are close together. In this case it is a second order approximation. Further, q_{al} fluxes, u_j the face-normal velocity and α_j the non-dimensional distance from the left cell center to the face.

Momentum diffusion

Discretisation of diffusion has the same approach as the momentum advection. The term is first discretised at the cell centers whereafter it is interpolated to the faces and then projected in the face normal direction. Section 3.5 showed the diffusion term as it is in the momentum equation. In Flexible Mesh this term is a bit altered,

$$\frac{1}{h^p} \nabla \cdot (\nu h^p (\nabla \mathbf{u} + \nabla \mathbf{u}^T)) \tag{C.10}$$

with

$$p = \begin{cases} 1, & \text{istresstype} = 3 \\ 1, & \text{istresstype} = 5 \\ 0, & \text{otherwise.} \end{cases} \tag{C.11}$$

This gives that if istresstype $\neq 3 \wedge \neq 5$ the momentum diffusion does not depend on the water depth. This is, however, incorrect. In this thesis the value 3 will be used. In this way the diffusion term is still dependent on the depth. Another advantage is that in modelling the viscosity coefficient Elder's formula can be used or a Smagorinsky model, not further explained here.

C.2.2 Time discretisation

Time discretisation of the momentum equation is semi-implicit and is as follows

$$\frac{u_j^{n+1} - u_j^n}{\Delta t} + \mathcal{A}_{ij} u_j^{n+1} + \mathcal{A}_{ej} u_j^n + \frac{g\theta_j}{\Delta x_j}(\zeta_{R(j)}^{n+1} - \zeta_{L(j)}^{n+1}) + \frac{g(1-\theta_j)}{\Delta x_j}(\zeta_{R(j)}^{n} - \zeta_{L(j)}^{n}) + \frac{g\|\hat{u}_j\|}{C^2 h} u_j^{n+1} = 0. \tag{C.12}$$

As determined before $\mathcal{A}_{ij} = 0$ and $\mathcal{A}_{ej}$ consists of momentum advection and diffusion. θ_j is a value between 0 and 1 which determines whether the equation is fully implicit, explicit or semi-implicit. Usually its value is around 0.5.

$$u_j^{n+1} = -f_{u_j}^n(\zeta_{R(j)}^{n+1} - \zeta_{L(j)}^{n+1}) + r_{u_j}^n \tag{C.13}$$

with

$$f_{u_j}^n = \frac{1}{B_u}\frac{g\theta_j}{\Delta x_j}, \qquad B_u = \frac{1}{\Delta t} + \frac{g}{C^2 h}\sqrt{(\hat{u}_j^*)^2 + (v_j^n)^2} \tag{C.14}$$

where $\hat{u}_j^*$ is the face normal velocity that follows from a few iterations by taking $\theta = 0$ and solving the momentum equation for $\hat{u}_j$. Further

$$r_{u_j}^n = \frac{1}{B_u}\left(\frac{u_j^n}{\delta t} - \mathcal{A}_{ej} - \frac{g(1-\theta_j)}{\Delta x_j}(\zeta_{R(j)}^n - \zeta_{L(j)}^n)\right). \tag{C.15}$$

The continuity equation is discretized in time as

$$\frac{V_k^{n+1} - V_k^n}{\Delta t} + \sum_{j\in\mathcal{J}(k)} A_{u_j}^n(\theta_j u_j^{n+1} + (1-\theta_j)u_j^n)1_{j,k} = 0. \tag{C.16}$$

Substituting the momentum equation into this equations yields the following system for the water column volume,

$$\frac{V_k^{n+1} - V_k^n}{\Delta t} + \sum_{j\in\mathcal{J}(k)} A_{u_j}^n\theta_j f_{u_j}^n \zeta_k^{n+1} - \sum_{j\in\mathcal{J}(k)} A_{u_j}^n\theta_j f_{u_j}^n \zeta_{O(k,j)}^{n+1} = -\sum_{j\in\mathcal{J}(k)} A_{u_j}^n(\theta_j r_{u_j}^n + (1-\theta_j)u_j^n)1_{j,k} \tag{C.17}$$

where $O(k,j)$ represents the cell that shares face j with cell k. After the water volume is expressed in terms of water levels (not explained here, for technical details see Deltares (2015a)) these equations can be solved by a preconditioned Conjugate Gradient method.

Appendix D

3Di

In Appendix C.5 the shallow water equations as used in 3Di were treated. In order to solve these equations numerically the domain has to be approximated by a grid. The way this grid is generated is new in the world of hydraulic engineering. It consists of a coarse grid that can be locally refined by using a quadtree method (further explained in this chapter). This coarse grid is linked to a sub-grid that is able to solve bottom friction and storage on a grid with a high resolution. This gives that the possible errors in both should be reduced, hence, reproduce a better view of reality. This chapter describes the 3Di grid generation together with a detailed description of all important components. All definitions given in this chapter are from the article of Stelling (2012).

D.1 Quadtrees

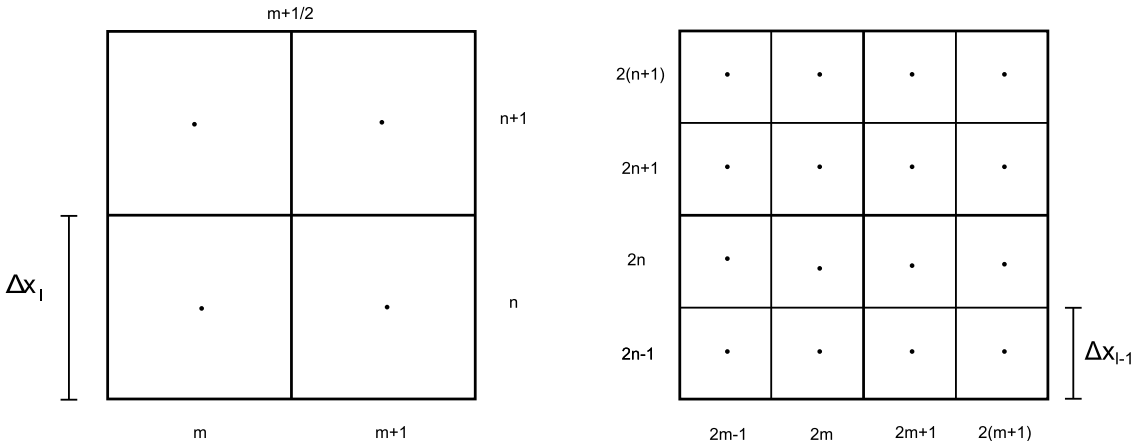

Figure D.1: Grid cell numbering in two layers

A Cartesian grid is often the most simple grid that can be used for making a numerical model. It has many advantages. One of them is the simplicity. The numerical equations

that are involved are quite simple and the generation of a grid is very easy and quick comparable to other grids. In the past years the disadvantages, see Section B.2.1, are partly removed by using flow solvers that have the ability to manage with arbitrary and moving boundaries. Adjusting the grid by using quadtrees is a possibility. A quadtree grid distinguishes itself from other grids due to the fact that each square cell can be subdivided into four child cells. Each of these child cells will be of equal size. Hence, a grid using this method can be refined in an easy way. Since multiple methods are combined to create a new method as used in 3Di, the quadtree grid is used a bit different than it is normally used. Using the quadtree method "normal" would mean that the whole domain of interest is placed inside one square, called the root square (Wang et al., 2004). The root square is divided into four child cells and each of the cells is checked to see if it should be divided again. In case of the 3Di grid the root square is the largest grid cell that is used. When there are l layers its grid size is $\Delta x_l \times \Delta y_l$, where $\Delta x_l = \Delta y_l$. Looking at a subdivision level the grid size is $\Delta x_{l-1} \times \Delta y_{l-1}$. Figure D.1 shows an example of two levels with their grid cell size and the numbering. These are however two different grids. Combining them would look like Figure D.2. This is how the grid is used in 3Di. It is important that the subdivision level difference between two adjacent cells has a maximum of 1. This results in a balanced quadtree, and only one hanging node (a node on the face between the two cells which does not belong properly to both of the cells) per edge of a cell (Figure A.5).

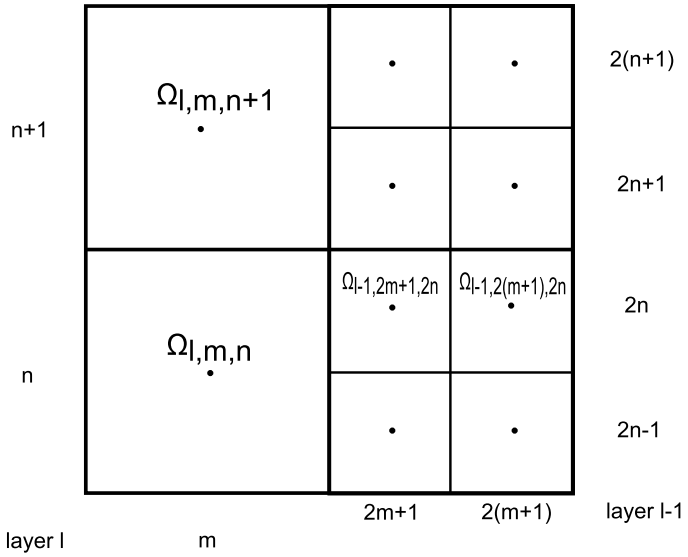

Figure D.2: Grid cell numbering

D.2 Subgrid

Another change in the flow solver that is used to take out the disadvantages of the Cartesian grid is using a digital element model (DEM), which is a second grid with a different resolution. In this way it is possible to use detailed bathymetry data on a fine Cartesian grid. This fine grid contains the bottom values, while the coarse grid holds the water levels and velocities. Figure D.3 shows a coarse cell $\Omega_{l,m,n}$ with a sub-grid that

consist of pixels $P_{i,j}$, for $i = j = 1, ..., 4$. Other terms in this figure that are not defined yet, will be explained in Section 5.2.1.

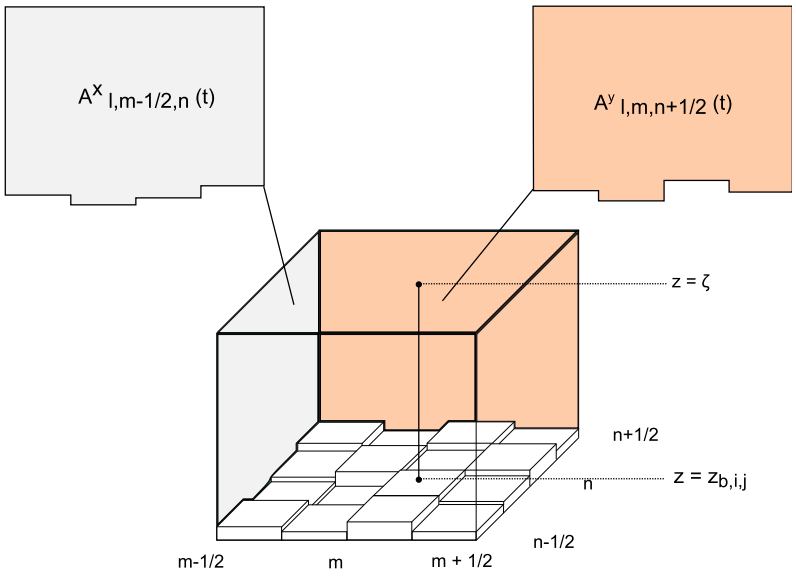

Figure D.3: Coarse cell with sub-grid

The DEM pixels are the smallest grid cells in the model with a size defined by $\delta x \times \delta x$. Each of the cells are of equal size, while cells of the coarse grid are a multiple of these pixels, see Figure D.4, where $\Gamma \geq 1$ and $l \geq 0$ are integers. If Figure D.4 is taken as an example with $l = 2$, then $\Delta x_2 = \Gamma 2^2 \delta x = 4\Gamma \delta x$. Thus, the coarse cell consists of $\Gamma 2^l \times \Gamma 2^l$ DEM pixels. It can be seen from the figure that the cell consist of 8×8 DEM pixels, hence, $\Gamma = 2$ in this example.

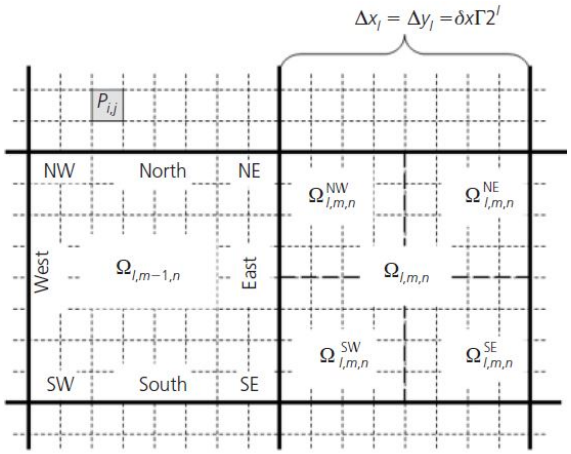

Figure D.4: Coarse grid sub-domains (Stelling, 2012)

D.2.1 Integration of the grids

The two sub-domains are denoted by Ω for the coarse cell and P for a pixel. Both are continuous domains and they are defined as

$$\begin{aligned} P_{i,j} &= [(i-1)\delta x, i\delta x] \times [(j-1)\delta x, j\delta x] \\ \Omega_{l,m,n} &= [(m-1)\Delta x_l, m\Delta x_l] \times [(n-1)\Delta x_l, n\Delta x_l]. \end{aligned} \tag{D.1}$$

In order to integrate both grids with each other step functions that are based on a indicator function χ_D are defined.

$$\chi_D(x,y) = \begin{cases} 1 & \text{if } (x,y) \in D \\ 0 & \text{if } (x,y) \notin D \end{cases} \tag{D.2}$$

With these definitions, functions of the bottom z_b, water level ζ and water depth h can be approximated. Note that the approximated functions can be recognized by the tilde.

$$z_b(x,y) \approx \tilde{z}_b(x,y) = \sum_{i=1}^{I} \sum_{j=1}^{J} z_{b,i,j} \chi_{P_{i,j}}(x,y) \tag{D.3}$$

$$\zeta(x,y) \approx \tilde{\zeta}(x,y) = \sum_{m=1}^{M} \sum_{n=1}^{N} \zeta_{l,m,n}(t) \chi_{\Omega_{l,m,n}}(x,y) \tag{D.4}$$

$$h(x,y) \approx \tilde{h}(x,y) = \max[0, \tilde{\zeta}(x,y,t) - \tilde{z}_b(x,y)]. \tag{D.5}$$

Notice the difference between summation of water levels and bottom levels. Whereas the bottom level is defined at each pixel in a coarse cell, the water levels are given at coarse cells. 3Di works with a staggered grid. Hence, the water levels are calculated at the center of a cell while the velocities are calculated at the middle of a edge on the coarse grid. Since it is possible that there are cells of two sizes adjacent to each other, it is meant at the middle of an edge of the smallest cell. Velocity domains also depend on the level difference between two adjacent cells. This can be notated by defining the quarter sub-domains in terms of compass directions, see Figure D.4.

$$\Omega^{SW}_{l,m,n} = [(m-1)\Delta x_l, (m-1/2)\Delta x_l] \times [(n-1)\Delta y_l, (n-1/2)\Delta y_l] \tag{D.6}$$

$$\Omega^{NW}_{l,m,n} = [(m-1)\Delta x_l, (m-1/2)\Delta x_l] \times [(n-1/2)\Delta y_l, n\Delta y_l] \tag{D.7}$$

$$\Omega^{SE}_{l,m,n} = [(m-1/2)\Delta x_l, m\Delta x_l] \times [(n-1)\Delta y_l, (n-1/2)\Delta y_l] \tag{D.8}$$

$$\Omega^{NE}_{l,m,n} = [(m-1/2)\Delta x_l, m\Delta x_l] \times [(n-1/2)\Delta y_l, n\Delta y_l] \tag{D.9}$$

$$\tag{D.10}$$

If one compares Figure D.4 with Figure D.2 it can be seen that the sub-domains in terms of compass directions overlap with the quarter cells at a different level: $\Omega_{l-1,2m+1,2n} =$

$\Omega^{NW}_{l,m+1,n}$, etc. Velocity domains, $\Omega_{l,m+1/2,n}$ or $\Omega_{l,m,n+1/2}$, can be constructed with these quarter cells. Generally,

$$\Omega_{l,m+1/2,n} = \Omega^E + \Omega^W \tag{D.11}$$

where there are multiple options for Ω^E and Ω^W, depending on the level difference between cells.

$$\Omega^E = \begin{cases} \Omega^{NW}_{l+1,m/2+1,n/2} & l^E > l, \quad n = \text{ even} \\ \Omega^{SW}_{l+1,m/2+1,(n+1)/2} & l^E > l, \quad n = \text{ odd} \\ \Omega^{SW+NW}_{l,m+1,n} & l^E = l \end{cases} \tag{D.12}$$

$$\Omega^W = \begin{cases} \Omega^{NE}_{l+1,m/2,n/2} & l^W > l, \quad n = \text{ even} \\ \Omega^{SE}_{l+1,m/2,(n+1)/2} & l^W > l, \quad n = \text{ odd} \\ \Omega^{SE+NE}_{l,m,n} & l^W = l \end{cases} \tag{D.13}$$

where l^E, l^W are the level layer of the cell. If level layers of the adjacent cells are equal, then the number of quarter cells that are used is equal to four. Otherwise, it is equal to three: two quarters of the smallest cell and one quarter of the larger cell. The same steps can be done for $\Omega_{l,m,n+1/2} = \Omega^N + \Omega^S$. Now that the domains are defined it is possible to describe the following discrete variables.

Cross sections in the $x-$ and y-direction respectively (Figure D.4)

$$A^x_{l,m+1/2,n} = \int_{(n-1)\Delta y_l}^{n\Delta y_l} \tilde{h}(m\Delta x_l, y, t)dy = \delta x \sum_{j=j_0}^{j=j_1} \max(0, {}^*\zeta_{l,m+1/2,n} - z_{b,i+1/2,j}) \tag{D.14}$$

$$A^y_{l,m,n+1/2} = \int_{(m-1)\Delta x_l}^{m\Delta x_l} \tilde{h}(x, n\Delta y_l, t)dx = \delta x \sum_{i=i_0}^{i=i_1} \max(0, {}^*\zeta_{l,m,n+1/2} - z_{b,i,j+1/2}). \tag{D.15}$$

It is allowed to go from the integrals to summations due to the fact that coarse cells are composed of pixels which are simply step functions. Notice the new value ${}^*\zeta_{l,m+1/2,n}$. This is the water depth at the interface. Since it is only defined in the center of a cell first-order upwinding is applied to find this value. Hence, second order errors are obtained.

$${}^*\zeta_{l,m+1/2,n} = \max\left(0, \frac{u_{l,m+1/2,n}}{|u_{l,m+1/2,n}|}\right)\zeta_{l,m,n} - \min\left(0, \frac{u_{l,m+1/2,n}}{|u_{l,m+1/2,n}|}\right)\zeta_{l,m+1,n} + \mathcal{O}(\Delta x_l^2) \tag{D.16}$$

Further, if we look at the cross section in the $x-$direction

$$z_{b,i+1/2,j} = \max(z_{b,i,j}, z_{b,i+1,j}) \tag{D.17}$$

$$i = 2^l \Gamma m \tag{D.18}$$

$$j_0 = 2^l \Gamma (n-1) + 1 \tag{D.19}$$

$$j_1 = 2^l \Gamma n. \tag{D.20}$$

Based on this information elements of the cross section in the $y-$direction should be clear as well.

Volume of water in cell $\Omega_{l,m,n}$:

$$V_{l,m,n}(t) = \int_{\Omega_{l,m,n}} \tilde{h}(x,y,t)d\Omega = \delta x^2 \sum_{i=i_0}^{i=i_1} \sum_{j=j_0}^{j=j_1} \max(0, \zeta_{l,m,n} - z_{b,i,j}). \tag{D.21}$$

in which

$$i_0 = 2^l \Gamma(m-1) + 1 \tag{D.22}$$

$$i_1 = 2^l \Gamma m \tag{D.23}$$

and j_1, j_0 as defined in (5.19) and (5.20).

Volume of water in a velocity domain $\Omega_{l,m+1/2,n}$:

$$\begin{aligned} V_{l,m+1/2,n}(t) &= \int_{\Omega_{l,m+1/2,n}} \tilde{h}(x,y,t)d\Omega \\ &= \int_{\Omega^E} \tilde{h}(x,y,t)d\Omega + \int_{\Omega^W} \tilde{h}(x,y,t)d\Omega \end{aligned} \tag{D.24}$$

where Ω^E, Ω^W are defined in (5.12) and (5.13). This summation is not the same as for the volume cell $\Omega_{l,m,n}$, where just one water level $\zeta_{l,m,n}$ is needed. In this case the summation consists of two parts, where summation of the east cell is done with the water level $\zeta_{l,m,n}$, while for the west cell it is done with the water level $\zeta_{l,m+1,n}$.

Volume-averaged velocity:

$$u_{l,m+1/2,n} \approx \frac{\int_{\Omega_{l,m+1/2,n}} u(x,y,t)h(x,y,t)d\Omega}{\int_{\Omega_{l,m+1/2,n}} h(x,y,t)d\Omega} \tag{D.25}$$

Discharge:

$$Q^x_{l,m+1/2,n}(t) = A^x_{l,m+1/2,n}(t) u_{l,m+1/2,n}(t) \tag{D.26}$$

$$Q^y_{l,m,n+1/2}(t) = A^y_{l,m,n+1/2}(t) u_{l,m,n+1/2}(t) \tag{D.27}$$

Now that everything is defined, the shallow water equations can be discretized in the next section.

D.3 Discretisation of the shallow water equations

The shallow water equations are discretized with the finite volume method (FVM). The mesh over which spatial discretization is performed was already defined in the previous sections. In each cell of this mesh the integrals are approximated by the discrete variables that were described in Section 5.2.1. With each time step these variables are modified. The following sections treat the spatial discretization and time discretization.

D.3.1 Spatial discretisation

First of all the shallow water equations are rewritten for just one cell Ω. In case of the continuity equation this cell of interest is $\Omega_{l,m,n}$, whereas for the momentum equations this is the velocity domain $\Omega_{l,m+1/2,n}$.

$$(V_{l,m,n})_t + \sum_f Q\mathbf{n}_f = 0, \tag{D.28}$$

the continuity equation with f the faces of $\Omega_{l,m,n}$ and $\mathbf{n}_f$ the outward directed normal for a face. The number of faces, hence discharges, is dependent on the ordering of local quadtrees. Looking at a velocity domain $\Omega_{l,m+1/2,n}$ the momentum equation in the $x-$direction is given by

$$(uV)_t + \sum_{\delta\Omega} {}^*u\bar{Q}\mathbf{n}_f + \int_\Omega \tilde{h}g\frac{\partial\zeta}{\partial x}d\Omega + \int_\Omega \frac{\tau_b^u}{\rho}d\Omega = 0 \tag{D.29}$$

which is in conservative form. The first term can be simplified by rewriting $(uV)_t = u_tV + uV_t$. Substituting into the above equation, dividing by V and letting $\hat{\tau} = \tau/\rho$ the following equation is obtained from the conservative momentum equation,

$$u_t + \frac{1}{V}\left(\sum_{\delta\Omega} {}^*u\bar{Q}\mathbf{n}_f + uV_t\right) + \frac{1}{V}\left(\int_\Omega \tilde{h}g\frac{\partial\zeta}{\partial x}d\Omega\right) + \frac{1}{V}\left(\int_\Omega \frac{\tau_b^u}{\rho}d\Omega\right) = 0 \tag{D.30}$$

for $\Omega_{l,m+1/2,n}$. Note that there is a new velocity ${}^*u$ appearing in the equation. This is the velocity on the edge of a velocity domain. These edges are different from the edges where velocity is defined. So, they are computed by upwinding. The terms between the brackets are from left to right known as advection, pressure (hydrostatic) and bottom friction. Each of them is discretized separately in the following parts.

Hydrostatic pressure

Starting with the hydrostatic pressure, it is assumed that the pressure gradient $\frac{\partial\zeta}{\partial x}$ is constant. Hence, between the water levels calculated at the center of the coarse cell a linear relation is assumed.

$$\begin{aligned}\frac{-F_{hp}^x}{V} &= \frac{\int_\Omega \tilde{h}g\frac{\partial\zeta}{\partial x}d\Omega}{V} \\ &= \frac{g\frac{\partial\zeta}{\partial x}\int_\Omega \tilde{h}d\Omega}{V} \\ &= g\frac{\partial\zeta}{\partial x} = g\frac{\zeta^E - \zeta^W}{(\Delta^E + \Delta^W)/2}.\end{aligned} \tag{D.31}$$

The values of ζ^E, ζ^W depend on the level difference between the two adjacent cells. In case of the same level $l^E = l^W$

$$\zeta^E = \zeta_{l,m+1,n}, \quad \zeta^W = \zeta_{l,m,n}. \tag{D.32}$$

If there is a difference in the level layer it gets a bit more complicated. If $l^E > l^W$ then the following two options are possible,

$$\zeta^E = \begin{cases} \zeta_{l+1,m/2+1,n/2}, & n = \text{ even} \\ \zeta_{l+1,m/2+1,(n+1)/2}, & n = \text{ odd} \end{cases}, \quad \zeta^W = \begin{cases} \frac{1}{2}(\zeta_{l,m,n} + \zeta_{l,m,n-1}), & n = \text{ even} \\ \frac{1}{2}(\zeta_{l,m,n} + \zeta_{l,m,n+1}), & n = \text{ odd} \end{cases} \tag{D.33}$$

When $l^E < l^W$ the following water levels are used,

$$\zeta^E = \begin{cases} \frac{1}{2}(\zeta_{l,m+1,n} + \zeta_{l,m+1,n-1}), & n = \text{ even} \\ \frac{1}{2}(\zeta_{l,m+1,n} + \zeta_{l,m+1,n+1}), & n = \text{ odd} \end{cases}, \quad \zeta^W = \begin{cases} \zeta_{l+1,m/2,n/2}, & n = \text{ even} \\ \zeta_{l+1,m/2,(n+1)/2}, & n = \text{ odd} \end{cases} \tag{D.34}$$

Advection

The advection term is given by

$$-\hat{F}^x_{adv} = \sum_f {}^*u\bar{Q}\mathbf{n}_f + uV_t. \tag{D.35}$$

As said before, ${}^*u$ represents velocities on edges of the velocity cell which are computed by upwinding. It remains to find a way to compute the discharges $\bar{Q}$ at the faces of a velocity domain. Figure D.5 shows discharges at the faces of such a cell. In this cell the mass conservation law has to be fulfilled.

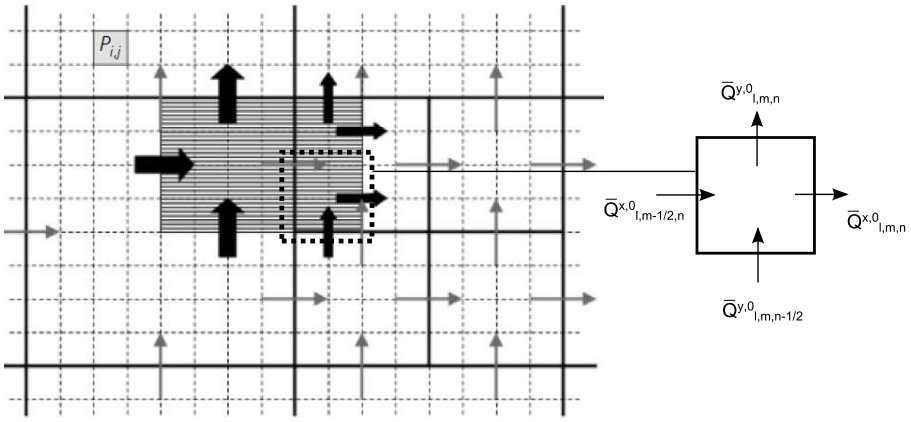

Figure D.5: Discharges for momentum transport (Stelling, 2012)

Not all discharges at the faces of sub-volumes are known. It is known that each velocity domain consists of three or four quarters of sub-volumes. For each of these sub-volumes a mass-continuity equation is used to compute the sub-grid discharges.

$$(V^{SW}_{l,m,n})_t = \bar{Q}^{x,0}_{l,m-1/2,n} - \bar{Q}^{x,0}_{l,m,n} + \bar{Q}^{y,0}_{l,m,n-1/2} - \bar{Q}^{y,0}_{l,m,n} \tag{D.36}$$

where $\bar{Q}^{x,0}_{l,m-1/2,n}, \bar{Q}^{y,0}_{l,m,n-1/2}$ are the external discharges and the other two internal discharges of $V_{l,m,n}$. The external discharges are computed by assuming

$$\bar{u}^0_{m-1/2,n} = \bar{u}^1_{m-1/2,n} = u_{m-1/2,n} \tag{D.37}$$

such that

$$\bar{Q}^{x,1}_{l,m-1/2,n} = u_{l,m-1/2,n} A^{x,1} = u_{l,m-1/2,n} \int_{(n-1/2)\Delta y_l}^{n\Delta y_l} \tilde{h}\left((m-1)\Delta x_l, y, t\right) dy. \tag{D.38}$$

The same can be done for the other external discharge. The problem in computing discharges lies in the internal discharges. Using Equation (D.36) for all sub-volumes of $\Omega_{l,m,n}$ four equations are obtained with the four unknown internal discharges. The resulting system does not have a unique solution however. Stelling (2012) solved this by replacing one of the four equations by a requirement. Which is that the following expression should be minimal at (l, m, n),

$$E_Q = \left(\frac{\bar{Q}^{x,0}}{A^{x,0}}\right)^2 + \left(\frac{\bar{Q}^{x,1}}{A^{x,1}}\right)^2 + \left(\frac{\bar{Q}^{y,0}}{A^{y,0}}\right)^2 + \left(\frac{\bar{Q}^{y,1}}{A^{y,1}}\right)^2. \tag{D.39}$$

Once the fourth equation is replaced by this equation the solution can be attained by a linear least-squares method. Advection of momentum can now be written as

$$-\hat{F}^x_{adv} = \sum_f {}^*u\bar{Q}\mathbf{n}_f + uV_t = \sum_f ({}^*u - u)\bar{Q}\mathbf{n}_f. \tag{D.40}$$

The summation will consist of inflowing momentum only. For outflowing momentum the value for ${}^*u$ is equal to u when first-order upwinding is used. Furthermore, it is assumed that the flow is hydrostatic, hence, in case of strong contractions in the flow there will be errors. To counter these errors a correction has to be applied that is thought of by Stelling and Duinmeijer (2003). The advection term can now be written as

$$adv(u) = \frac{1}{V} \sum_f ({}^*u - u)\bar{Q}\mathbf{n}_f \tag{D.41}$$

Bottom friction

The last term that needs to be discretized is the bottom friction force $\hat{F}^x_{bot}$.

$$-\hat{F}^x_{bot} = \int_\Omega \frac{\tau^u_b}{\rho} d\Omega = \int_\Omega c^f u \|u\| d\Omega \tag{D.42}$$

The cell of interest is still $\Omega_{l,m+1/2,n}$, since the momentum equations is defined on this cell. The velocity in this cell is not known, except at $(l, m+1/2, n)$. It is possible to assume a constant velocity in the entire cell. However, looking at shallow flows that can contain locally relative deep parts this will lead to deviation in gravity-driven flows. It leads to an overestimation of the velocity, hence friction, and an underestimation of conveyance. The following assumptions are done to find a function $\tilde{u}(x, y)$.

Note, these assumptions are not valid when instead of gravity the flow is driven dominantly by wind.

In each quarter of a computational cell it is assumed that the friction slope S^f, rate at which energy is lost along a given length of channel, is constant. Second, a constant direction of the flow is taken. These assumptions are done in order to keep the computational time small. Without these assumptions one would need to compute each velocity for a pixel one by one. Of course, this would be very expensive. Since the flow is gravity-driven the dominant terms in the momentum equation are the pressure term and friction term. These terms are used to compose an expression for the friction slope for a quarter cell $\Omega = \Omega^{SW,\ldots,NE}_{l,m,n}$,

$$|S^f| = \frac{c^f \|\tilde{u}\|^2}{g\tilde{h}} = \text{constant if } (x, y) \in \Omega \tag{D.43}$$

with $\tilde{h} = \tilde{h}(x, y)$, the water depth that depends on the water and bottom level at point (x, y). The following velocity is one calculated within a quarter of a computational cell. Hence at SW,..., NE of (l, m, n).

$$\|\tilde{u}\| = \frac{1}{V} \int_\Omega \tilde{h}(\tilde{u}(x, y)^2 + \tilde{v}(x, y)^2)^{1/2} dxdy = \frac{1}{V} \int_\Omega \tilde{h} \|\tilde{u}(x, y)\| dxdy \tag{D.44}$$

where the velocity inside the integral is a cell varying velocity, while the one being calculated is a cell average velocity of a quarter cell. If two points $(x, y), (x', y')$ are taken, both in Ω, then

$$\frac{c^f(x, y)(\tilde{u}(x, y)^2 + \tilde{v}(x, y)^2)}{g\tilde{h}(x, y)} = \frac{c^f(x', y')(\tilde{u}(x', y')^2 + \tilde{v}(x', y')^2)}{g\tilde{h}(x', y')}, \tag{D.45}$$

so

$$\|\tilde{u}(x, y)\| = \|\tilde{u}(x', y')\| \left(\frac{c^f(x', y')}{\tilde{h}(x', y')}\right)^{1/2} \left(\frac{\tilde{h}(x, y)}{c^f(x, y)}\right)^{1/2}. \tag{D.46}$$

Both assumptions are used to come to this expression. That is why it is only valid when both points are inside the same cell. A last assumption that is made is

$$\|\tilde{u}(x', y')\| = \frac{\|u\|}{\alpha(x', y')} \tag{D.47}$$

with u the calculated velocity on the edge of a cell. If, for example, $\Omega = \Omega^{NW}_{l,m,n}$, then

$$u = u^{NW}_{l,m,n} = \begin{cases} u_{l,m-1/2,n} \\ \text{or} \\ u_{l-1,2m-3/2,2n} \end{cases} \tag{D.48}$$

$$v = v^{NW}_{l,m,n} = \begin{cases} v_{l,m,n+1/2} \\ \text{or} \\ v_{l-1,2m-1,2n+1/2} \end{cases} . \tag{D.49}$$

Working out α' which is used in the final step to obtain the bottom friction,

$$\begin{aligned} \alpha' &= \frac{\|u\|}{\|\tilde{u}'\|} = \frac{\int_\Omega \|\tilde{u}\|\tilde{h}dxdy}{\|\tilde{u}'\|V} \\ &= \frac{\|\tilde{u}'\| \int_\Omega \tilde{h}(\tilde{h}/c^f)^{1/2}dxdy}{\|\tilde{u}'\|V(\tilde{h}'/c^{f'})^{1/2}} \\ &= \frac{\int_\Omega \tilde{h}(\tilde{h}/c^f)^{1/2}dxdy}{V} \left(\frac{c^{f'}}{\tilde{h}'}\right)^{1/2} \end{aligned} \tag{D.50}$$

where $c^{f'} = c^f(x', y')$, $\tilde{h}' = \tilde{h}(x', y')$, $\alpha' = \alpha(x', y')$. Now the bottom friction can be defined with the function $\tilde{u}(x, y)$ instead of a constant velocity in the entire cell.

$$-\hat{F}^x_{bot} = \int_\Omega \frac{\tau^u_b}{\rho} d\Omega = \int_\Omega c^f \tilde{u}\|\tilde{u}\| d\Omega. \tag{D.51}$$

Substituting Equation (D.47) and subsequently writing out α by using Equation (D.50) the bottom friction is now defined by

$$\begin{aligned} -\hat{F}^x_{bot} &= \int_\Omega c^f \tilde{u}\|\tilde{u}\| d\Omega = u\|u\| \int_\Omega \frac{c^f}{\alpha^2} dxdy \\ &= u\|u\| \int_\Omega \frac{c^f}{c^f \cdot \left(\int_\Omega \tilde{h}(\tilde{h}/c^f)^{1/2}dxdy\right)^2} V^2 \tilde{h} dxdy \\ &= u\|u\| \frac{V^3}{\left(\int_\Omega \tilde{h}(\tilde{h}/c^f)^{1/2}dxdy\right)^2} \end{aligned} \tag{D.52}$$

for a quarter cell $\Omega = \Omega_{l,m,n}^{SW,\ldots,NE}$. For a velocity domain the friction force will be the sum of all quarter sub-domains. If $l^E = l^W$, then four quarter sub-domains are taken. Otherwise, only three quarter sub-domains. This was already explained in Section 5.2.1. Suppose that the levels of adjacent cells are equal, then

$$\begin{aligned} -\left(\frac{\hat{F}_{bot}^x}{V}\right)_{l,m+1/2,n} &= \frac{(\hat{F}_{bot}^x)_{l,m+1/2,n}^{W+E}}{-V_{l,m+1/2,n}} \\ &= \frac{(F_{bot}^x)_{l,m,n}^{NE+SE} + (F_{bot}^x)_{l,m+1,n}^{NW+SW}}{-V_{l,m+1/2,n}} \\ &= \frac{u_{l,m+1/2,n}}{V_{l,m+1/2,n}} \left(f_{l,m,n}^{NE+SE} + f_{l,m+1,n}^{NW+SW}\right) \end{aligned} \tag{D.53}$$

with f defined as a friction factor and h^f as the roughness depth.

$$f = V\frac{\|u\|}{h^f}, \qquad h^f = \left[\frac{\int_\Omega \tilde{h}(\tilde{h}/c^f)^{1/2}dxdy}{V}\right]^2. \tag{D.54}$$

Using this friction factor makes it very easy to compute the bottom friction force. For each sub-domain the friction factor is computed, which can also be used for the force in $y-$direction. It might look like this way uses a lot of memory.

D.3.2 Time discretisation

Discretisation in time is done with the semi-implicit theta method. For the bottom friction some predictor-corrector is also applied, which is necessary to model large-area flooding problems (Stelling, 2012). Respectively for the continuity and momentum equations the time integration is as follows,

$$\frac{V(\zeta^{k+1}) - V(\zeta^k)}{\Delta t} + \sum_f A^k u^{k+\theta} \mathbf{n}_f = 0 \text{ at } (l,m,n) \tag{D.55}$$

$$\frac{u^{k+1} - u^k}{\Delta t} + \text{adv}(u^k) + g\frac{\partial \zeta^{k+\theta}}{\partial x} + \frac{u^{k+1}}{V(\zeta^k)}(f^k)^{E+W} = 0 \text{ at } (l,m+1/2,n)(l^E = l^W) \tag{D.56}$$

with $p^{k+\theta} = (1-\theta)p^k + \theta p^{k+1}$ and $\theta \in [\frac{1}{2}, 1]$ (Casulli, 2009). If the level layers are not the same, the pressure gradient takes another form. Describing the hydrostatic pressure term in Section 5.3.2, it is seen that there are four other possibilities, see (5.34) and (5.35). One of these pressure terms, $l^W > l^E$ is taken with $n =$ even, is taken as an example at the end of this section. Solving the equations u^{k+1} has to be eliminated from the mass

conservation equation. Taking the case $l^E = l^W$ as an example, Equation (D.56) has to be rewritten such that an expression for u^{k+1} is found.

$$u^{k+1} = \frac{1}{B}\left(u^k - \Delta t(adv(u^k) + g\frac{\partial \zeta^{k+\theta}}{\partial x})\right) \tag{D.57}$$

with

$$B = 1 + \frac{\Delta t}{V(\zeta^k)}(f^k)^{E+W}. \tag{D.58}$$

Substituting this into the mass equation results in

$$\begin{aligned} V(\zeta^{k+1}) - g\Delta t^2\frac{\theta^2}{B}\sum_f \frac{\partial \zeta^{k+1}}{\partial x}A^k\mathbf{n}_f =& V(\zeta^k) - \Delta t\sum_f A^k\mathbf{n}_f\left[\theta\frac{\Delta t}{B}\left(adv(u^k) + ..\right.\right. \\ & \left.\left.. + g(1-\theta)\frac{\partial \zeta^k}{\partial x}\right) + (1-\theta)u^k\right]. \end{aligned} \tag{D.59}$$

This equation can be written in a vector notation

$$\mathbf{V}(\zeta) + \mathbf{T}\zeta = \mathbf{b} \tag{D.60}$$

which is solved by an iterative scheme where it is assured that the system converges under physically compatible assumptions (Casulli, 2009). This is done based on a Newton iteration. Note that the system in nonlinear because of the water volumes (defined at ...). The water volume V is assumed strictly positive, since a value of zero would lead to the trivial solution.

When $l^E \neq l^W$ the system differs in the pressure terms as seen before. If $l^W > l^E$ is taken with $n =$ even, then the pressure term is

$$\begin{aligned} \frac{\partial \zeta}{\partial x} &= \frac{\frac{1}{2}(\zeta_{l,m+1,n} - \zeta_{l,m+1,n-1}) - \zeta_{l+1,m/2,n/2}}{\frac{1}{2}(\Delta x_{l+1} + \Delta x_l)} \\ &= \frac{\zeta_{l,m+1,n-1} - \zeta_{l,m+1,n}}{\Delta x_{l+1} + \Delta x_l} + \frac{\zeta_{l,m+1,n} - \zeta_{l+1,m/2,n/2}}{\frac{1}{2}(\Delta x_{l+1} + \Delta x_l)} = \frac{\partial \zeta}{\partial x} - d_y\zeta + d_y\zeta. \end{aligned} \tag{D.61}$$

The term $d_y\zeta$ is added to avoid stability problems. The difference with Equation (5.56) can be seen if the time integrations are compared. For the latter the time integration is given by

$$\frac{u^{k+1} - u^k}{\Delta t} + \mathrm{adv}(u^k) + g(\frac{\partial}{\partial x} - d_y)\zeta^{k+\theta} + gd_y\zeta^k + \frac{u^{k+1}}{V(\zeta^k)}(f^k)^{E+W} = 0. \tag{D.62}$$

If n = odd, then

$$\frac{u^{k+1}-u^k}{\Delta t} + \text{adv}(u^k) + g(\frac{\partial}{\partial x} + d_y)\zeta^{k+\theta} - gd_y\zeta^k + \frac{u^{k+1}}{V(\zeta^k)}(f^k)^{E+W} = 0. \tag{D.63}$$

It can be seen that the plus and minus sign are different for the pressure term. This gives that their arises anti-symmetry in the system which avoids stability problems due to the explicit $d_y\zeta$ term. This system is solved with a method that combines the Conjugate Gradient method and Gaussian elimination.

Appendix E

Derivation of mass and momentum equations

In this appendix the full derivation of both the conservation of mass and momentum is given. It starts in both cases with a small cubic fluid particle as given in Figure E.1 with forces working on the faces and in- and outgoing fluxes in all three directions.

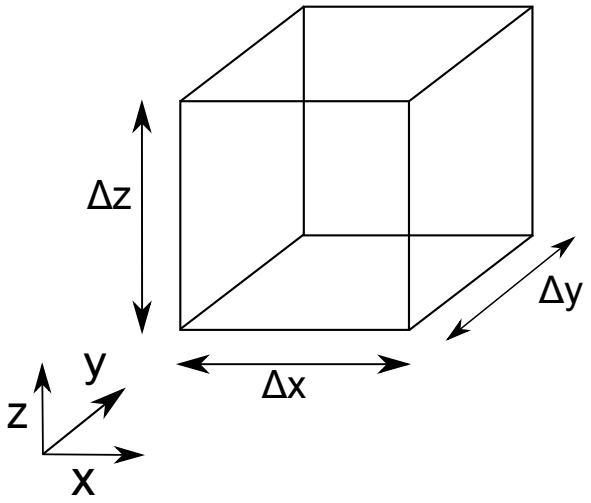

Figure E.1: Fluid particle

E.1 Conservation of mass

A mass balance for a fluid particle is the basic point for the derivation of the mass-conservation equation.

Rate of change of mass in fluid particle = Ingoing flux of mass - Outgoing flux of mass

The rate of change of mass of the fluid particle in Figure can be written as

$$\frac{\rho\Delta x\Delta y\Delta z|_{t+\Delta t} - \rho\Delta x\Delta y\Delta z|_t}{\Delta t} \tag{E.1}$$

The net flux are given as "ingoing flux - outgoing flux"

$$\begin{aligned} x-\text{direction: } & \rho\Delta y\Delta z u|_x - \rho\Delta y\Delta z u|_{x+\Delta x} \\ y-\text{direction: } & \rho\Delta x\Delta z v|_y - \rho\Delta x\Delta z v|_{y+\Delta y} \\ z-\text{direction: } & \rho\Delta x\Delta y w|_z - \rho\Delta x\Delta y w|_{z+\Delta z} \end{aligned} \tag{E.2}$$

Together this gives the mass balance

$$\begin{aligned} \frac{\rho\Delta x\Delta y\Delta z|_{t+\Delta t} - \rho\Delta x\Delta y\Delta z|_t}{\Delta t} =& \rho\Delta y\Delta z u|_x - \rho\Delta y\Delta z u|_{x+\Delta x} + ... \\ & ... + \rho\Delta x\Delta z v|_y - \rho\Delta x\Delta z v|_{y+\Delta y} + ... \\ & ... + \rho\Delta x\Delta y w|_z - \rho\Delta x\Delta y w|_{z+\Delta z} \end{aligned} \tag{E.3}$$

Dividing by $\Delta x, \Delta y, \Delta z$

$$\frac{\rho|_{t+\Delta t} - \rho|_t}{\Delta t} = \frac{\rho u|_x - \rho u|_{x+\Delta x}}{\Delta x} + \frac{\rho v|_y - \rho v|_y + \Delta y}{\Delta y} + \frac{\rho w|_z - \rho w|_z + \Delta z}{\Delta z} \tag{E.4}$$

The final step is taking the limit of $\Delta x, \Delta y, \Delta z, \Delta t$, which gives us the mass-continuity equation.

$$\lim_{\Delta x,\Delta y,\Delta z,\Delta t\to 0} \frac{\rho|_{t+\Delta t} - \rho|_t}{\Delta t} = \lim_{\Delta x,\Delta y,\Delta z,\Delta t\to 0} \left(\frac{\rho u|_x - \rho u|_{x+\Delta x}}{\Delta x} + \frac{\rho v|_y - \rho v|_{y+\Delta y}}{\Delta y} + \frac{\rho w|_z - \rho w|_{z+\Delta z}}{\Delta z} \right) \tag{E.5}$$

$$\frac{\partial \rho}{\partial t} + \frac{\partial \rho u}{\partial x} + \frac{\partial \rho v}{\partial y} + \frac{\partial \rho w}{\partial z} = 0 \tag{E.6}$$

E.2 Conservation of momentum

The basic of the momentum equations is the second law of Newton, $F = m \cdot a$, where m is mass and a acceleration. The first is equal to density times the volume of the element, while the latter is equal to the Laplace derivative.

$$\rho\Delta x\Delta y\Delta z \frac{D\mathbf{v}}{Dt} = \text{sum of forces on element} \tag{E.7}$$

Looking in the x-direction, the sum of forces consist of the net pressure force and the viscous force, also known as the surface forces. The same forces work in the y-direction and the z-direction. Besides the surface forces, there are also body forces like gravity. The gravitational force is directed downwards, hence only in the z-direction an term for the gravity is found.

When looking at waters at large scales, the Coriolis effect also plays a part in the x- and y-direction. Since a general case is treated, it cannot be neglected. Combining all the terms give the following equations.

$$\begin{aligned}
\rho\Delta x\Delta y\Delta z\frac{Du}{Dt} =&\Delta y\Delta z\left(p|_x - p|_{x+\Delta x}\right) + \rho f v\Delta x\Delta y\Delta z + \Delta y\Delta z\left(\tau_{xx}|_x - \tau_{xx}|_{x+\Delta x}\right) + ... \\
&... + \Delta x\Delta z\left(\tau_{yx}|_y - \tau_{yx}|_{y+\Delta y}\right) + \Delta y\Delta x\left(\tau_{zx}|_z - \tau_{zx}|_{z+\Delta z}\right) \\
\rho\Delta x\Delta y\Delta z\frac{Dv}{Dt} =&\Delta x\Delta z\left(p|_y - p|_{y+\Delta y}\right) - \rho f u\Delta x\Delta y\Delta z + \Delta y\Delta z\left(\tau_{xy}|_x - \tau_{xy}|_{x+\Delta x}\right) + ... \\
&... + \Delta x\Delta z\left(\tau_{yy}|_y - \tau_{yy}|_{y+\Delta y}\right) + \Delta y\Delta x\left(\tau_{zy}|_z - \tau_{zy}|_{z+\Delta z}\right) \\
\rho\Delta x\Delta y\Delta z\frac{Dw}{Dt} =&\Delta x\Delta y\left(p|_z - p|_{z+\Delta z}\right) - \rho g\Delta x\Delta y\Delta z + \Delta y\Delta z\left(\tau_{xz}|_x - \tau_{xz}|_{x+\Delta x}\right) + ... \\
&... + \Delta x\Delta z\left(\tau_{yz}|_y - \tau_{yz}|_{y+\Delta y}\right) + \Delta y\Delta x\left(\tau_{zz}|_z - \tau_{zz}|_{z+\Delta z}\right)
\end{aligned} \tag{E.8}$$

Dividing all three equations by $\Delta x\Delta y\Delta z$ and then taking the limit as is done in the previous section gives

$$\begin{aligned}
\rho\frac{Du}{Dt} &= -\frac{\partial p}{\partial x} + \rho f v + \left[\frac{\partial\tau_{xx}}{\partial x} + \frac{\partial\tau_{yx}}{\partial y} + \frac{\partial\tau_{zx}}{\partial z}\right] \\
\rho\frac{Du}{Dt} &= -\frac{\partial p}{\partial y} - \rho f u + \left[\frac{\partial\tau_{xy}}{\partial x} + \frac{\partial\tau_{yy}}{\partial y} + \frac{\partial\tau_{zy}}{\partial z}\right] \\
\rho\frac{Du}{Dt} &= -\frac{\partial p}{\partial z} - \rho g + \left[\frac{\partial\tau_{xz}}{\partial x} + \frac{\partial\tau_{yz}}{\partial y} + \frac{\partial\tau_{zz}}{\partial z}\right]
\end{aligned} \tag{E.9}$$

The term on the left hand side can be rewritten for all three directions, however, only for the x-direction this is shown.

$$\begin{aligned}
\rho\frac{D\mathbf{v}}{Dt} =&\rho\left(\frac{\partial\rho}{\partial t} + u\frac{\partial u}{\partial x} + v\frac{\partial u}{\partial y} + w\frac{\partial u}{\partial z}\right) \\
=&\frac{\partial\rho u}{\partial t} + \frac{\partial\rho u^2}{\partial x} + \frac{\partial\rho uv}{\partial y} + \frac{\partial\rho uw}{\partial z} - u\left(\frac{\partial\rho}{\partial t} + \frac{\partial\rho u}{\partial x} + \frac{\partial\rho v}{\partial y} + \frac{\partial\rho w}{\partial z}\right) \\
=&\frac{\partial\rho u}{\partial t} + \frac{\partial\rho u^2}{\partial x} + \frac{\partial\rho uv}{\partial y} + \frac{\partial\rho uw}{\partial z}
\end{aligned} \tag{E.10}$$

The final step can be done by using the conservation of mass, equation (E.6). Substituting this in (E.8) gives the equations that represent the conservation of momentum.

$$\begin{aligned}
\frac{\partial \rho u}{\partial t} + \frac{\partial \rho u^2}{\partial x} + \frac{\partial \rho uv}{\partial y} + \frac{\partial \rho uw}{\partial z} &= -\frac{\partial p}{\partial x} + \rho f v + \left[\frac{\partial \tau_{xx}}{\partial x} + \frac{\partial \tau_{yx}}{\partial y} + \frac{\partial \tau_{zx}}{\partial z} \right] \\
\frac{\partial \rho u}{\partial t} + \frac{\partial \rho vu}{\partial x} + \frac{\partial \rho v^2}{\partial y} + \frac{\partial \rho vw}{\partial z} &= -\frac{\partial p}{\partial y} - \rho f u + \left[\frac{\partial \tau_{xy}}{\partial x} + \frac{\partial \tau_{yy}}{\partial y} + \frac{\partial \tau_{zy}}{\partial z} \right] \\
\frac{\partial \rho u}{\partial t} + \frac{\partial \rho wu}{\partial x} + \frac{\partial \rho wv}{\partial y} + \frac{\partial \rho w^2}{\partial z} &= -\frac{\partial p}{\partial z} - \rho g + \left[\frac{\partial \tau_{xz}}{\partial x} + \frac{\partial \tau_{yz}}{\partial y} + \frac{\partial \tau_{zz}}{\partial z} \right]
\end{aligned} \tag{E.11}$$

Appendix F

Derivation of the shallow water equations

F.1 RANS equations

The momentum equation in the x-direction is taken as an example for the derivative of the RANS equations.

$$\frac{\partial \rho u}{\partial t} + \frac{\partial \rho u^2}{\partial x} + \frac{\partial \rho uv}{\partial y} + \frac{\partial \rho uw}{\partial z} = -\frac{\partial p}{\partial x} + \rho f v + \left[\frac{\partial \tau_{xx}}{\partial x} + \frac{\partial \tau_{yx}}{\partial y} + \frac{\partial \tau_{zx}}{\partial z}\right] \tag{F.1}$$

Substitute $u = \bar{u} + u'$, $v = \bar{v} + v'$, $w = \bar{w} + w'$, and $p = \bar{p} + p'$ in the momentum equation in the x-direction.

$$\frac{\partial \rho(\bar{u} + u')}{\partial t} + \frac{\partial \rho(\bar{u} + u')^2}{\partial x} + \frac{\partial \rho(\bar{u} + u')(\bar{v} + v')}{\partial y} + \frac{\partial \rho(\bar{u} + u')(w = \bar{w} + w')}{\partial z} = -\frac{\partial \bar{p} + p'}{\partial x} + ... \tag{F.2}$$
$$... + \rho f(\bar{v} + v') + \nabla \cdot \left(2\mu \nabla^s (\bar{u} + u')\right)$$

The next step is to average this equation. By doing this the following rules are used

$$\overline{\bar{u}} = \bar{u}, \qquad \overline{u'} = 0, \qquad \overline{\bar{u}\bar{v}} = \bar{u}\bar{v}, \qquad \overline{u'v'} \neq 0, \qquad \overline{\bar{u} + u'} = \bar{u} \tag{F.3}$$

Thus, averaging Equation (B.2) and using above rules give the RANS for the x-direction. The same steps can be done for the other directions. These will not be done here.

$$\frac{\partial\overline{\rho(\bar{u}+u')}}{\partial t}+\frac{\partial\overline{\rho(\bar{u}+u')^2}}{\partial x}+\frac{\partial\overline{\rho(\bar{u}+u')(\bar{v}+v')}}{\partial y}+\frac{\partial\overline{\rho(\bar{u}+u')(w=\bar{w}+w')}}{\partial z}=-\frac{\partial\overline{\bar{p}+p'}}{\partial x}+... \tag{F.4}$$

$$...+\overline{\rho f(\bar{v}+v')}+\overline{\nabla\cdot(2\mu\nabla^s(\bar{u}+u'))}$$

$$\frac{\partial\rho(\overline{\bar{u}}+\overline{u'})}{\partial t}+\frac{\partial\rho(\overline{\bar{u}^2}+2\overline{\bar{u}u'}+\overline{u'u'})}{\partial x}+\frac{\partial\rho(\overline{\bar{u}\bar{v}}+\overline{\bar{u}v'}+\overline{\bar{v}u'}+\overline{u'v'})}{\partial y}+\frac{\partial\rho(\overline{\bar{u}\bar{w}}+\overline{\bar{u}w'}+\overline{\bar{w}u'}+\overline{u'w'})}{\partial z}= \tag{F.5}$$

$$-\frac{\partial\overline{\bar{p}}+\overline{p'}}{\partial x}+\rho f(\overline{\bar{v}}+\overline{v'})+\nabla\cdot\left(2\mu\nabla^s(\overline{\bar{u}}+\overline{u'})\right)$$

$$\frac{\partial\rho\bar{u}}{\partial t}+\frac{\partial\rho(\bar{u}\bar{u}+\overline{u'u'})}{\partial x}+\frac{\partial\rho(\bar{u}\bar{v}+\overline{u'v'})}{\partial y}+\frac{\partial\rho(\bar{u}\bar{w}+\overline{u'w'})}{\partial z}=-\frac{\partial\bar{p}}{\partial x}+\rho f\bar{v}+\nabla\cdot(2\mu\nabla^s\bar{u}) \tag{F.6}$$

$$\frac{\partial\rho\bar{u}}{\partial t}+\nabla\cdot(\rho\bar{u}\bar{\mathbf{v}})+\nabla\cdot\left(\rho\overline{u'\mathbf{v}'}\right)=-\frac{\partial\bar{p}}{\partial x}+\rho f\bar{v}+\nabla\cdot(2\mu\nabla^s\bar{u}) \tag{F.7}$$

F.2 Scaling

Applying scaling technique to the vertical momentum equations gives insight in the order of magnitude of all terms. Let the terms x and y be of order L and z of the order H, whereas the velocities u and v are of order U. Using the continuity equations gives the order of the velocity w as follows. Write all components as a dimensionless number (recognized by the tilde) times the order of scale.

$$u=U\tilde{u} \tag{F.8}$$
$$v=U\tilde{v} \tag{F.9}$$
$$w=\alpha\tilde{w} \tag{F.10}$$
$$x=L\tilde{x} \tag{F.11}$$
$$y=L\tilde{y} \tag{F.12}$$
$$z=H\tilde{z} \tag{F.13}$$

where α is an unknown order that needs to be derived. Substituting these terms in the continuity equation gives

$$\frac{U}{L}\frac{\partial\tilde{u}}{\partial\tilde{x}}+\frac{U}{L}\frac{\partial\tilde{v}}{\partial\tilde{y}}+\frac{\alpha}{H}\frac{\partial\tilde{w}}{\partial\tilde{z}}=0 \tag{F.14}$$

The first two terms usually do not cancel one another out, hence, α should be such that the third term is of the same order as the first two. This gives that $\alpha=HU/L$. Now these terms can be substituted into the vertical momentum equation. However, it is easier to rewrite the local acceleration and advection terms.

$$\frac{\partial \rho w}{\partial t} + \frac{\partial \rho w u}{\partial x} + \frac{\partial \rho w v}{\partial y} + \frac{\partial \rho w^2}{\partial z} = \rho \frac{\partial w}{\partial t} + \rho u \frac{\partial w}{\partial x} + \rho v \frac{\partial w}{\partial y} + .. \tag{F.15}$$

$$.. + \rho w \frac{\partial w}{\partial z} + w \frac{\partial \rho}{\partial t} + w \frac{\partial \rho u}{\partial x} + w \frac{\partial \rho v}{\partial y} + w \frac{\partial \rho w}{\partial z}$$

$$= \rho \frac{\partial w}{\partial t} + \rho u \frac{\partial w}{\partial x} + \rho v \frac{\partial w}{\partial y} + \rho w \frac{\partial w}{\partial z} \tag{F.16}$$

since $\frac{\partial \rho}{\partial t} + \frac{\partial \rho u}{\partial x} + \frac{\partial \rho v}{\partial y} + \frac{\partial \rho w}{\partial z} 0$.

$$\rho \frac{HU}{LT} \frac{\partial \tilde{w}}{\partial \tilde{t}} + \rho \frac{HU^2}{L^2} \tilde{u} \frac{\partial \tilde{w}}{\partial \tilde{x}} + \rho \frac{HU^2}{L^2} \tilde{v} \frac{\partial \tilde{w}}{\partial \tilde{y}} + \rho \frac{HU^2}{L^2} \tilde{w} \frac{\partial \tilde{w}}{\partial \tilde{z}} = -\frac{\partial p}{\partial z} - \rho g + \nu \rho \frac{HU}{L^3} \frac{\partial^2 \tilde{w}}{\partial \tilde{x}^2} + .. \tag{F.17}$$

$$.. + \nu \rho \frac{HU}{L^3} \frac{\partial^2 \tilde{w}}{\partial \tilde{y}^2} + \nu \rho \frac{U}{LH} \frac{\partial^2 \tilde{w}}{\partial \tilde{z}^2} + ..$$

$$.. + \nu \rho \frac{U}{LH} \frac{\partial^2 \tilde{u}}{\partial \tilde{x} \partial \tilde{z}} + \nu \rho \frac{U}{LH} \frac{\partial^2 \tilde{v}}{\partial \tilde{y} \partial \tilde{z}}$$

The only term that is not scaled is the pressure term, since it is not known what order this will be. Next, divide the equation by ρg.

$$\frac{HU}{LTg} \frac{\partial \tilde{w}}{\partial \tilde{t}} + \frac{HU^2}{gL^2} \tilde{u} \frac{\partial \tilde{w}}{\partial \tilde{x}} + \frac{HU^2}{gL^2} \tilde{v} \frac{\partial \tilde{w}}{\partial \tilde{y}} + \frac{HU^2}{gL^2} \tilde{w} \frac{\partial \tilde{w}}{\partial \tilde{z}} = -\frac{1}{\rho g} \frac{\partial p}{\partial z} - 1 + \nu \frac{HU}{gL^3} \frac{\partial^2 \tilde{w}}{\partial \tilde{x}^2} + .. \tag{F.18}$$

$$.. + \nu \frac{HU}{gL^3} \frac{\partial^2 \tilde{w}}{\partial \tilde{y}^2} + \nu \frac{U}{gLH} \frac{\partial^2 \tilde{w}}{\partial \tilde{z}^2} + ..$$

$$.. + \nu \frac{U}{gLH} \frac{\partial^2 \tilde{u}}{\partial \tilde{x} \partial \tilde{z}} + \nu \frac{U}{gLH} \frac{\partial^2 \tilde{v}}{\partial \tilde{y} \partial \tilde{z}}.$$

Notice that the stress gradient terms with second derivatives in the horizontal direction differ with a factor $(L/H)^2$ from the other stress gradient terms. Thus, these can be neglected. If $T = L/\sqrt{gH}$, then each factor in front of a term can be written as the following ratios

$$\begin{aligned} \text{local acceleration} \quad & \frac{FrH^2}{L^2} \\ \text{advective terms} \quad & \frac{Fr^2H^2}{L^2} \\ \text{stress gradients} \quad & \frac{Fr^2H}{ReL} \end{aligned} \tag{F.19}$$

where Fr is the Froude number and Re the Reynolds number.

$$Fr = \frac{U}{\sqrt{gH}}, \qquad Re = \frac{UH}{\nu} \tag{F.20}$$

F.3 Depth integration

The final step is to integrate Equations (B.13) and the continuity equation over the depth $h = \zeta - z_b$. The depth averaged values are defined as:

$$\bar{u} = \frac{1}{h}\int_{z_b}^{\zeta} u dz. \tag{F.21}$$

Integration of the continuity equation is given as follows,

$$\begin{aligned}\int_{z_b}^{\zeta} \frac{\partial u}{\partial x} + \frac{\partial v}{\partial y} + \frac{\partial w}{\partial z} dz =& \frac{\partial}{\partial x}\int_{z_b}^{\zeta} u dz - u^s \frac{\partial \zeta}{\partial x} + u^b \frac{\partial z_b}{\partial x} + \frac{\partial}{\partial y}\int_{z_b}^{\zeta} v dz - .. \\ & .. - v^s \frac{\partial \zeta}{\partial y} + v^b \frac{\partial z_b}{\partial y} + w^s - w^b \\ =& \frac{\partial \zeta}{\partial t} + \frac{\partial h\bar{u}}{\partial x} + \frac{\partial h\bar{v}}{\partial y} = 0\end{aligned} \tag{F.22}$$

where the Leibniz Integral Rule is used at the first line and boundary conditions (B.5) and (B.6) at the second line. Since the difference in momentum equations in $x-$ and $y-$direction are not that large, integration is only done for the $x-$direction. Integration of the Coriolis and pressure term is quite easy.

$$\int_{z_b}^{\zeta} f v dz = h f \bar{v} \tag{F.23}$$

$$\int_{z_b}^{\zeta} g \frac{\partial \zeta}{\partial x} dz = h \frac{\partial \bar{\zeta}}{\partial x} \tag{F.24}$$

Looking at the stress gradients, the same approach is used as for the continuity equation: using the Leibniz Integral Rule and then applying boundary conditions.

$$\begin{aligned}\int_{z_b}^{\zeta} \left(\frac{\partial \tau_{xx}}{\partial x} + \frac{\partial \tau_{xy}}{\partial y} + \frac{\partial \tau_{xz}}{\partial z} \right) dz =& \frac{\partial}{\partial x}\int_{z_b}^{\zeta} \tau_{xx} dz + \frac{\partial}{\partial y}\int_{z_b}^{\zeta} \tau_{xy} dz - .. \\ & .. - [\tau_{xx}\frac{\partial h}{\partial x} + \tau_{xy}\frac{\partial h}{\partial y} - \tau_{xz}]_{z=h} + [\tau_{xx}\frac{\partial z_b}{\partial x} + \tau_{xy}\frac{\partial z_b}{\partial y} - \tau_{xz}]_{z=z_b} \\ =& \frac{\partial \bar{\tau}_{xx} h}{\partial x} + \frac{\partial \bar{\tau}_{xy} h}{\partial y} + \tau_{wind,x} + \tau_{b,x}\end{aligned} \tag{F.25}$$

When integrating the local acceleration and advection terms it is a bit trickier. Also using the same approach as the continuity equation results in an expression that contains nonlinear terms.

$$\begin{aligned}\int_{z_b}^{\zeta}[\frac{\partial u}{\partial t}+\frac{\partial uu}{\partial x}+\frac{\partial uv}{\partial y}+\frac{\partial uw}{\partial z}]dz =& \frac{\partial}{\partial t}\int_{z_b}^{\zeta}udz+\frac{\partial}{\partial x}\int_{z_b}^{\zeta}uudz+\frac{\partial}{\partial y}\int_{z_b}^{\zeta}uvdz-.. \quad \text{(F.26)}\\ & .. - u^s\left(\frac{\partial \zeta}{\partial t}+u^s\frac{\partial \zeta}{\partial x}+v^s\frac{\partial \zeta}{\partial y}-w^s\right)+u^b\left(\frac{\partial z_b}{\partial t}+u^b\frac{\partial z_b}{\partial x}+v^b\frac{\partial z_b}{\partial y}-w^b\right)\\ =& \frac{\partial h\bar{u}}{\partial t}+\frac{\partial h\bar{u}\bar{u}}{\partial x}+\frac{\partial h\bar{u}\bar{v}}{\partial y}+..\\ & .. + \frac{\partial}{\partial x}\int_{z_b}^{\zeta}(u-\bar{u})^2dz+\frac{\partial}{\partial y}\int_{z_b}^{\zeta}(u-\bar{u})(v-\bar{v})dz\end{aligned}$$

where the boundary conditions are applied at the second line. Resulting shallow water equations can be found in Chapter 3.

Appendix G

River Elbe local refinement results

In this Appendix the remaining figures of Chapter 14 are presented.

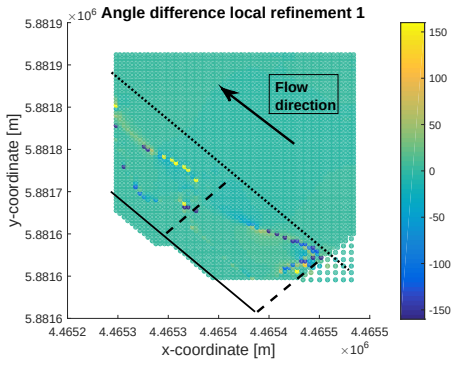

(a) Angle difference

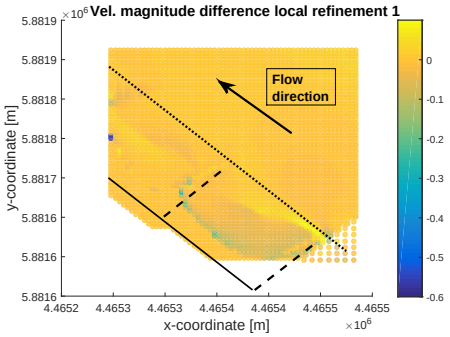

(b) Velocity magnitude difference

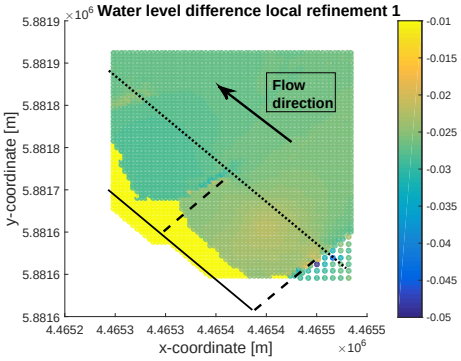

(c) Water level difference

Figure G.1: Differences between refinement 2 and uniform grid for 3Di

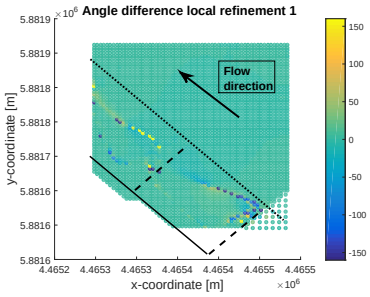

(a) Angle difference

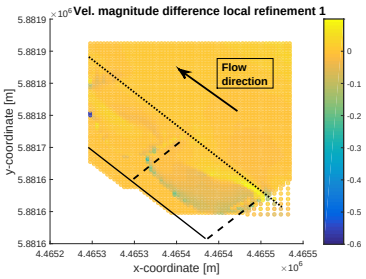

(b) Velocity magnitude difference

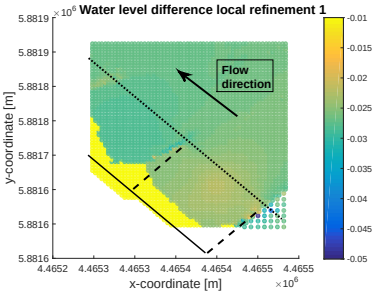

(c) Water level difference

Figure G.2: Differences between refinement 3 and uniform grid for 3Di

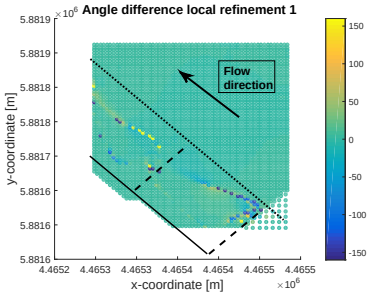

(a) Angle difference

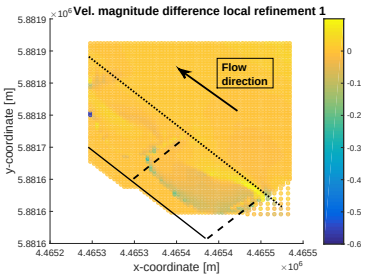

(b) Velocity magnitude difference

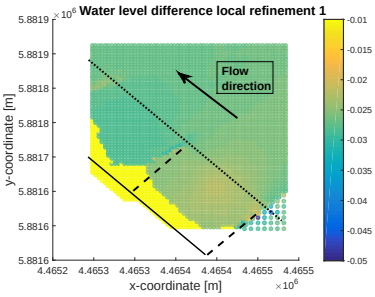

(c) Water level difference

Figure G.3: Differences between refinement 2 and uniform grid for Flexible Mesh

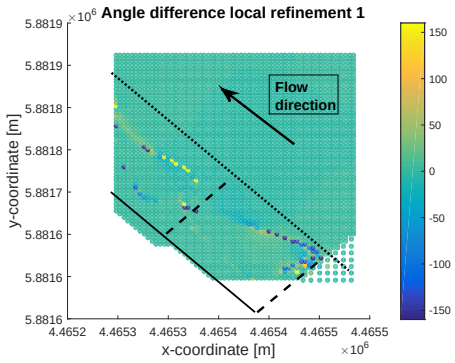

(a) Angle difference

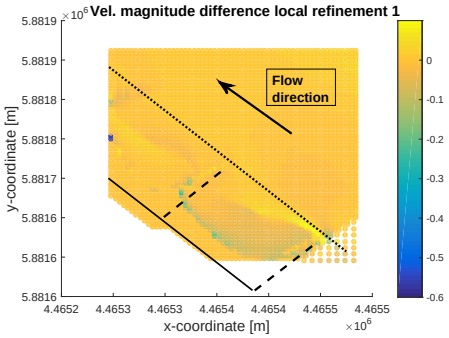

(b) Velocity magnitude difference

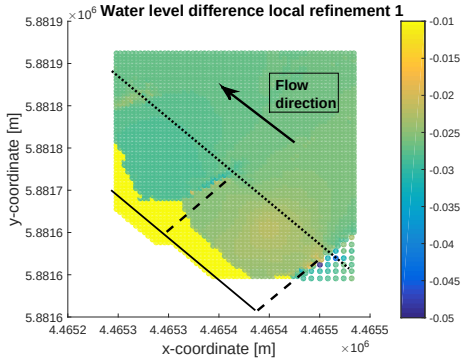

(c) Water level difference

Figure G.4: Differences between refinement 3 and uniform grid for Flexible Mesh